THE UNIVERSITY *of* EDINBURGH

Numerical investigation of granular flow and dynamic pressure in silos

Yin Wang

School of Engineering

The University of Edinburgh

Doctor of Philosophy

April 2012

Declaration

This thesis entitled “Numerical investigation of granular flow and dynamic pressure in silos” is submitted to the College of Science and Engineering, The University of Edinburgh, for the degree of Doctor of Philosophy.

The research work described and reported in this thesis was completed solely by Yin Wang, under the supervision of Prof. Jin Y. Ooi, Prof. Yong Lu and Prof. Yunming Yang. Where other sources were used, full reference are given.

Yin Wang

April 2012

Abstract

Although the flow of granular material in silos and the pressure acting on the silo walls have been studied for over a century, many challenges still remain in silo design. In particular, during the discharge process some dynamic phenomena in silos can often be observed to display large, self-induced and dynamic pulsations which may endanger the stability of the silo structure. The aim of this thesis is to study the flow and pressure in silos using numerical modelling and analytical methods, and to further understand the mechanical behaviour of granular material and mechanism of dynamic phenomena during silo discharge.

The Finite Element (FE) method can be used to analyse the behaviour of the granular material in silos by considering the material as a continuum. In this thesis, FEM modelling of silo flow was developed using the Arbitrary Lagrangian-Eulerian (ALE) formulation in the Abaqus/Explicit program and the key parameters that affect the predictions of the flow and pressure during discharge were identified.

Using the ALE technique, almost the entire silo discharge process can be simulated without mesh distortion problems. The mass flow rate and temporally averaged discharge pressure predicted by the FE model were first investigated in a conical hopper and were found to be in good agreement with those from the most commonly quoted theoretical solutions. The transient dynamic pressure fluctuations during incipient silo discharge were predicted and the causes for these dynamic events have been investigated which led to the conclusion that the stress wave propagation and the moving shear zone

phenomena within the bulk solid were responsible for the dominant higher and lower frequencies effects respectively.

A one-dimensional dynamic model of granular columns subject to Coulomb wall friction was developed to investigate the propagation of stress waves, focusing on the effect of geometry by examining converging and diverging tapered columns. The analytical solutions of this model are compared to the FE model based on the ALE formulation. This FE model was first validated using the known behaviour for cylindrical columns. In all cases, the stress impulse set off by incipient discharge at the silo outlet grew with the distance travelled up the column, however the rate was shown to depend on the half-angle of the taper. Over a range of small angles, the proposed analytical model was found to accurately predict this behaviour.

After the successful application of the ALE technique for a conical hopper, the FE model was extended to simulate the granular flow in a flat-bottomed model silo. The FE predictions were compared with the silo pressure measurements in a model silo (Rotter et al, 2004). Pressure cells mounted along a vertical line on the silo walls were used to measure the pressure distribution in the silo tests using dry sand.

The FE model was further extended to simulate the granular flow in a model silo consisting of a cylindrical section with a conical hopper. The prediction was compared with the experimental observations from a model silo (Munch-Andersen et al, 1992), together with the well-known theoretical solutions. Two numerical issues were addressed in some detail: one is the numerical treatment of the abrupt transition between

the cylinder section and the conical hopper, the other is the interaction between the granular solid and the silo walls that was modelled using a dynamic friction model. In addition, the dynamic pressure events during discharge were examined and plausible explanations were given.

Finally, this thesis deployed a non-coaxial elastoplastic constitutive model to explore the effect of non-coaxiality on silo phenomena. The non-coaxial FE modelling was performed on three problems: a simple shear test under various initial conditions, a steep hopper and a flat-bottomed silo. The results show that non-coaxiality did not influence the prediction of wall pressure during filling and storing, on the other hand, the discharge pressure was predicted to be larger when non-coaxiality is considered.

Acknowledgements

I would like to express my deeply-felt thanks to my three great supervisors: Prof. Jin Y. Ooi, Prof. Yong Lu and Prof. Yunming Yang, for their excellent supervision, expert guidance and continuing support in this research endeavour but also for giving me tremendous inspiration and confidence both to tackling what others said would be impossible problem and to carry it through to fruition. It is a gift to study under their esteemed supervision that I will always treasure and one which I will never take lightly. I have benefited and achieved significant progress from their guidance, which made the past four years I spent at The University of Edinburgh the most remarkable and rewarding time in my life.

I am extremely grateful to the brilliant guidance and advice from Dr. Christohper Wensrich without whom I could not accomplish the excellent results in this thesis. Sincere thanks also go to Dr. Zhijun Zhong and Dr. Craig Warren for their great guidance and support in conducting the laboratory work.

Acknowledgement is also given to my other colleagues, particularly Dr. Jianfei Chen, Dr. Jin Sun, Dr. Jun Ai for their useful directions and advices; Porf. Michael Rotter for constant sources of keen insight and sharing his tremendous knowledge in silo structure; and Dr. Vijayabaskar Narayanamurthy, J.P. Morrisey for beneficial discussions and help. Help in various forms received from Prof. Mike Forde, Dr. Rein Guillermo, Dr. Tim Stratford, Joan Birse is gratefully acknowledged.

Many thanks to my longstanding and treasured friends who deserved a special mention: Chong Zhou, Ying Liu, Xiaoqin Li, Shiqing Li, Yi Tao, Fengchen An, Noel Conlisk, Colin Brett for their nice friendship; Shanshan Zhang, Yigui Ma, Rui Huang, Xiantong Zou, Xiaoyi Sun, Song Hou for their harmonious collaboration in the work at Edinburgh University Chinese Student and Scholar Association.

I am extremely grateful to the full financial support from China State-Sponsored Scholarship Programme for Advanced Scholarship without which this dissertation would not have been possible. This distinguished fellowship is sponsored by The University of Edinburgh and Chinese Scholarship Council (CSC).

Finally and most importantly, my special thanks reserve to my family, particularly my parents for their measureless love and supports, and my wife Yidan for her amazing understanding and encouragement during my PhD study in UK. To them I dedicated this thesis.

Publications

The following publications are based on the research presented in this thesis:

Wang, Y., Wensrich, C., Ooi, J.Y. (2012). "Rarefaction wave propagation in tapered granular columns." *Chemical Engineering Science*, 71: 32-38.

Wang, Y., Lu, Y., Ooi, J.Y. (2011). "Numerical calculations of dynamic pressure during hopper discharge using the Arbitrary Lagrangian-Eulerian formulation." *Engineering Structures*, under review.

Yang, Y., Ooi, J.Y., Rotter, J.M., **Wang, Y**. (2011). "Numerical analysis of silo behavior using non-coaxial models." *Chemical Engineering Science*, 66: 1715-1727.

Yang, Y., Ooi, J.Y., Rotter, J.M., **Wang, Y**. (2011). "Flow channel boundaries in silos." *Chemical Engineering Technology*, 34(8): 1295-1302.

Wang, Y., Lu, Y., Ooi., J.Y. (2011). "Numerical calculation of dynamic pressures during silo hopper discharge using ALE formulation." *Proceedings of the 19th UK Conference of the Association for Computational Mechanics in Engineering*, Edinburgh, UK.

Wang, Y., Lu, Y., Ooi, J.Y. (2012). "Finite element modeling of dynamic pressure and flow in hopper discharge using arbitrary Lagrangian Eulerian formulation." *Proceedings of 5th Asian Technology Symposim*, Singapore.

Contents

List of Figures

List of Tables

Nomenclature

The definitions of the symbols used in this thesis are listed below. Roman characters are given first, followed by Greek characters, and the commonly used subscripts and superscripts. The symbols are defined where they first appear in the text. In the few cases where more than one definition has been assigned to a symbol, the meaning will be evident from the context in which it is used.

Roman Characters	
a	A material constant for a unified form of MC and DP models
a_i	Material acceleration in ALE description
A	Constant (in Ch.5)
A_i	Area of mesh element
b	Exponential growth constant
b_j	Force per unit volume
B	Constant (in Ch.5)
c	Convective velocity between material and mesh motion in ALE description
c_0	Cohesion of material
c_d	Dilatational wave speed
c_{el}	Elastic wave speed
C	Constant for mass flow rate in hoppers

d	Particle size of material
d_t	Vertical displacement of the solid top surface
D	Outlet diameter of the truncated column
D_0	Orifice diameter of the container
e	Void ratio
E	Young's modulus
f_0	Scale factor
f_n	Frequency of longitudinal wave travelling within the granular solid
F	Ratio of normal wall pressure to vertical stress at the hopper wall
F^V	Applied load vector
g	Acceleration due to gravity
G	Constant shear modulus
h	Height of the silo
h_0	Maximum height material measured vertically from the apex of hopper
H_{nc}	Non-coaxial plastic modulus
I	Coaxial plastic flow direction
I_1	First invariant of the Cauchy stress
$I(x)$	Integration factor with respect to x
I^V	Internal force vector
J_2	Second invariant of the deviatoric part of the Cauchy stress

k	Material constant (in Ch.4)
	Lateral pressure ratio (in Ch.5)
	A material constant for a unified form of MC and DP models (in Ch.8)
$\dot{k}$	Rate of hardening parameter
K	Elastic bulk modulus
K_p	Coaxial plastic modulus
l_i	Characteristic length
ℓ_i	Boundary velocity in ALE description
$L_{\min}$	Smallest element dimension
m	Walker pressure relationship exponent
M	Slope of the critical-state line in the p'-q plane
M^{NV}	Mass matrix
N	Number of edges
p	Normal stress within the solid
p'	Mean effective stress
p_c'	Preconsolidation pressure
p_{wn}	Wall normal pressure
p_{ws}	Wall shear pressure
P_h	Horizontal pressure

P_i	Pressure at the *i*th point
P_n	Normal pressure
q	Deviatoric stress
Q_0	Uniform surcharge at the top surface of hopper
r	Radial Coordinate emanating from the apex of the cone
R	Radius of smooth curvature at the transition
R_0	Radius of the outlet
R_X	Material domain in ALE description
R_x	Spatial domain in ALE description
R_χ	Referential domain in ALE description
s_{ij}	Deviatoric stress tensor
S	Surface area
S_0	Representative deviation
t	Time
T_i	Boundary traction in ALE description
d^N	Degree of freedom of node *N* (in Ch.3)
u_0	Discharge velocity at the outlet
u_{inc}	Displacement of the solid adjacent to the wall
u_i	Material point velocity in ALE description
$\tilde{u}_i$	Referential point velocity in ALE description

V_{dis}		Discharge volume percentage of material
$V^{'}$		Transient discharge volume of material
V_0		Volume of stored material prior to discharge
W		Mass flow rate
χ		Quantity related to the evolution of hardening parameter
X		Mesh node
X_0		Janssen's characteristic depth
Θ		Tangential stiffness of the material
	Greek	Characters
α		Hopper apex half angle
δ		Stress-related component (in Ch.3)
δ_{ij}		Kronecher delta
ε		Angle (in Ch.7)
ε_{ij}		Strain tensor
ϕ		Effective angle of internal friction of bulk solid (in Ch.4)
ϕ_d		Angle between the stagnant zone boundary and the horizontal
ϕ_i		Internal angle of friction
ϕ_w		Angle of wall friction
γ		Specific density (in Ch.6 and 7)
		Shear strain (in Ch.8)
$\dot{\gamma}$		Sliding velocity

γ_i	Allowable elastic slip
$\tilde{\lambda}$	Lames first constant
$\tilde{\mu}$	Lames second constant
μ	Coefficient of sliding friction
μ_d	Dynamic coefficient of friction
μ_s	Coefficient of static friction
μ_k	Coefficient of kinetic friction
μ_w	Coefficient of wall friction
κ	Parameter for active/passive stress case (in Ch.4)
ν	Poisson's ratio
ϖ	Decay coefficient considering dynamic coefficient of friction
ρ	Bulk density (in Ch.3)
σ_1	Major principal stress
σ_2	Intermediate principal stress
σ_3	Minor principal stress
σ_{ij}	Stress tensor
σ_{hh}	Vertical stress
$\hat{\sigma}$	Background stress state (in Ch.5)
σ^+	Small disturbance in stress
σ_0^+	Initial magnitude of small disturbance in stress

τ	Shear stress
τ_{crit}	Critical shear stress
ω	Angle in Mohr's circle
$\omega_{\max}$	Highest frequency
ω_{ij}	Normal to the yield surface
$\xi_{\max}$	Fraction of critical damping in the mode with the highest frequency
ψ	Dilatancy angle of the solid

Chapter 1

Introduction

1.1 General background

Silos are used widely and provide a buffer between one transport activity or industrial process and another. They are used in a wide variety of industries including mining, power generation, steel making, plastics, chemical processing, food processing, farming and agriculture. With the rising demands in these industries, the sizes of silos have been steadily growing to capacities of up to 100,000 tonnes. Building such massive structures bring however many challenges for the design engineer. These challenges are multidisciplinary with their backgrounds in civil engineering (safety of structures), mechanical engineering (equipment for handling and transportation), process engineering (processes involving storage in silos), and specialist areas such as experimental mechanics, dust explosion, numerical simulations, etc (Brown and Nielsen, 1998). Due to the complexity of characteristics of both the stored bulk solid and the structure, a full understanding of silo problems remains elusive.

Granular pressures in silos were subject to many studies for over a century. The pressures acting on the silo walls during filling and storing are now reasonably well understood using a variety of classical theories such as the Janssen type pressure equation (Rotter, 2001); however an accurate prediction of pressure during discharge remains a difficult challenge for silo design. The pressures during discharge tend to

exhibit time and space variation, which have often been observed in silo experiments. With the general lack of understanding and information with regard to the dynamic events, silo design standards in different countries with the assumptions and simplifications tend to give conservative predictions.

The finite element method has become well established in silo research in recent decades. Due to its versatility a great variety of silo problems can be studied. Not only has the calculations with the bulk material at rest been achieved, the ones with flowing material are possible with the help of some new computational techniques based on the extended finite element method. The behaviour of granular materials in silos is rather complex. Therefore, all relevant parameters for the interaction between the structure and the stored material, the constitutive relations of the materials, the initial state and the flowing state must be checked carefully.

1.2 Objectives and methodologies

The aim of this research is to improve the understanding of the underlying mechanism of the dynamic pressure phenomenon during silo discharge and also investigate its implications on silo quaking and silo honking issues. The main objectives of this research are as follows:

1) To develop an effective strategy for modelling the dynamic pressure phenomenon using the finite element (FE) method based on the Arbitrary Lagrangian-Eulerian formulation, and to identify the key parameters that affect the pressures during silo

discharge. Also, the finite element results will be compared with the theoretical solutions and observations of some laboratory silo tests.

2) To propose a one-dimensional dynamic model of the Janssen theory in cylindrical column subject to Coulomb wall friction. It is used to examine the propagation of rarefaction waves in granular columns which is considered as one main cause of dynamic pressure in silos. In addition, this dynamic model will be validated by means of the finite element method.

3) To discuss the characteristics of several constitutive models based on continuum mechanics. In particular, the effect of non-coaxial plastic model on the wall pressure and bulk solid behaviour in silos is to be investigated.

1.3 Structure of the thesis

This thesis is divided into nine chapters including this introduction chapter, a literature review chapter, five core chapters followed by a conclusion chapter. A brief overview of these chapters is described as follows.

Chapter 1 presents the general background, objectives and methodologies of this research.

Chapter 2 reviews the literature relevant to this thesis. It introduces the dynamic events, such as silo quaking, dynamic pressure in silos, and briefly outlines the mechanisms that must be understood in order to understand the phenomena. This chapter also outlines the FEM models for simulating silo discharge.

Chapter 3 describes a wide range of different aspects and factors that are involved in modelling of silo behaviour using the finite element method based on the Arbitrary Lagrangian-Eulerian (ALE) formulation. The issues include the ALE formulation, uncoupled ALE solution, explicit dynamic analysis, numerical implementation of initialisation state, boundary conditions, algorithm of interaction between contact surfaces, optimization of mesh etc. Besides, advantages of ALE formulation in modelling of the large deformation problems can be embodied through this chapter.

Chapter 4 develops the FE model for simulating the conical hopper discharge problem. The behaviour of the stored solid is modelled using the continuum mechanics approach based on an Arbitrary-Eulerian (ALE) formulation. The temporally averaged discharge pressures obtained from the FE model are compared with those from the most commonly quoted theoretical solutions and found to be in good agreement. Meanwhile, the dynamic events of transient pressures fluctuations are analysed, which provides useful insight into such dynamic phenomenon often observed in silo experiments.

Chapter 5 proposes a one-dimensional dynamic model of Janssen model in tapered columns subject to Coulomb wall friction. It is used to examine the propagation of rarefaction waves in a similar system to that during silo discharge. In addition, this dynamic model is validated for a range of small cone half angles by means of the finite element method.

Chapter 6 describes an experimental investigation on loads acting on the walls in a flat-bottomed silo. The normal pressure distributions at the end of filling process and during discharge process are measured and used to compare with the FE predictions. Through comparisons, the FE model developed in previous chapter is validated against the predictions of pressures in silos. Additionally, FE model has predicted the semi-mass flow and the transient development of flow channel boundary in the flat-bottomed model silo.

Chapter 7 develops the FEM model for simulating the silos consisting of a cylindrical barrel and a conical bottom. Firstly, the experimental observations carried out by researchers in Demark are used to validate this FE model, together with those well-known theoretical solutions. Two further points are addressed: one is the numerical treatment of the transition between the cylinder part and the conical part, the other is the interaction between the solid and the silo walls using a dynamic friction model. Meanwhile, the dynamic events of pressure fluctuations during silo discharge are explained on basis of the observations noted in Chapter 4.

Chapter 8 introduces an elastoplastic non-coaxial model and investigates its effect on simulated stress-strain behaviour of granular solid subject to simple shearing under various initial conditions. Further, simulations are performed using the non-coaxial model on a steep hopper and a flat-bottomed silo to investigate the influence of non-coaxiality on the wall pressure distribution. Accordingly, the conclusions are drawn that non-coaxiality does not influence the prediction of wall pressure after filling, whilst the

predicted pressure with non-coaxial considerations are larger than those without it for the discharge simulations. In addition, its mechanism is discussed in this chapter.

Chapter 9 summaries the most salient contributions and findings of this thesis. Further research related to the current work is identified and some recommendations on useful studies to improve the current understanding of the dynamic pressure phenomenon are discussed.

Chapter 2

Literature review

2.1 Introduction

Silos are the most commonly used structure for the storage of bulk solids in many industries including chemical, agriculture, mining and food processing. Silo problems are multidisciplinary with their backgrounds in civil engineering (safety of structures), mechanical engineering (equipment for handling and transportation), chemical engineering (processes involving storage in silos), and specialist areas such as experimental mechanics, dust explosion, simulations, etc (Brown and Nielsen, 1998). Due to the complexity of characteristics of both bulk solid stored and structures, a full understanding of silo problems remains elusive.

A steady flow of material in a silo is desirable when the stored material is being discharged from a silo. However, it is sometimes found that the material does not flow steadily but rather in short sharp bursts of motion (Wensrich, 2002). At industrial scales the erratic motion exhibited by these silos produces significant dynamic loads. These dynamic loads can develop so large so as to endanger the stability of the silo structure and the surrounding structures, as well as producing noise pollution that can disturb residents in the neighbourhood or can interfere with the health of personnel nearby.

The answer to the question on how a granular body within a silo can create such a dynamic problem lies within the same mechanism known as slip-stick friction that is responsible for the dynamic nature of the Earths' tectonic plates (Wensrich, 2002). Slip-stick friction is an extremely common phenomenon that can be observed in many physical systems where surfaces are sliding against each other. Slip-stick leads to spontaneous, jerking movements or self-excited oscillations with constant or varying frequency.

This chapter reviews the current literature on granular flow and dynamic pressure in silos and is divided into four sections: numerical modelling of silo behaviour, experimental studies of silo dynamic phenomena, stress wave propagation in granular material and slip-stick motion. The first two sections outline the dynamic phenomena observed in silos and traditional analysis tools to study these dynamic phenomena. The latter two sections provide a review of mechanisms to explain the dynamic phenomena in silos.

2.2 Brief review on numerical modelling of silo behaviour

Over the last decades, a major effort from researcher and engineers around the world has been put into developing computational models for the behaviour of granular solids in silos (Bishara et al., 1977, 1981; Eibl and Rombach, 1988; Ooi and Rotter, 1990; Tejchman and Gudehus, 1993; Lu et al, 1997; Rombach and Eibl, 1998; Ayuga et al, 2001; Vidal et al., 2005; Wojcik and Tejchman, 2009; Yang et al, 2011). The progress in

computational modelling for quantitative silo calculations provides promising practical predictor of silo flow and silo pressures, compared to the experimental studies or theoretical modelling which may prove to be difficult to obtain repeatable and trustworthy results.

2.2.1 Comparison of FE with DEM method

In recent years considerable progress has been made in the field of numerical modelling of the granular solid behaviour in silos. The numerical modelling, which can be based on a continuum or a discrete mechanics approach, lends itself to rigorous parametric studies, allows exploration of technological innovations, and guides the structural design for the engineers. The finite element (FE) method is used in region where the material behaves as a continuum. Another numerical technique is the discrete element method (DEM), which takes into account the particulate nature of the medium instead of treating it as a continuum.

The two methods have different characteristics. The FE models can give credible quantitative predictions of silo pressures. However, most of the FE models assume rather simple material behaviour, and do not properly deal with the dynamic discharge process in silos. They also have difficulty with the boundary conditions at the transition corners. By contrast, the DEM can give acceptable qualitative predictions of several dynamic silo phenomena, such as the development of flow patterns, arch formation, and shear bands. However, as the inherent scatter due to the microscopic behaviour of the solid, DEM tends to obtain obscure global pressure patterns, which means that very

large numbers of particles are needed if it is to be used for quantitative silo calculations (Rotter et al., 1998).

2.2.2 FE modelling of silo discharge

It has been proved that FE modelling can give predictions of silo pressures which are in good agreement with both theoretical results and experimental results in last two decades (Ooi and Rotter, 1990; Tejchman, 1998; Chen et al., 2010). However, FE modelling of silo discharge is relatively rare and requires more fundamental research.

Most existing FE models cannot simulate the entire discharge process due to the mesh distortion problem, which is caused by the large deformation when the material inside is emptied. Instead, they often consider only a very incipient discharge process in the FE simulations by adopting the remeshing-rezoning operation (Martinez et al., 2002; Vidal et al., 2005). Usually, the FE computations of silo discharge are performed in two stages. The first stage is the silo filling that sets up the initial state of stress in the material. To achieve this initial state, several methods can be used. Ding et al. (2003) and Wensrich (2003) prescribed the stresses at the top surface with the outlet boundary condition obtained from the theoretical formula for the silo's active stress. Keiter and Rombach (2001), and Ayuga et al. (2001) performed a static analysis. The second stage is the silo discharge that corresponds to the dynamic problem. This stage can be carried out by eliminating the constraints at the silo outlet to simulate its instantaneous opening (Martinez et al, 2002; Wojcik et al., 2003; Vidal et al., 2005), or by prescribing a maximum velocity as a kinematic boundary condition at the silo outlet, i.e. starting from

zero and reaching the maximum velocity after an opening period of a certain interval (Ostendorf et al., 2003). As far as the interaction between the solid and silo walls is concerned, there are several methods adopted in FE simulations of silo discharge. The contact surfaces used in the interaction are mostly modelled by complying with Coulomb friction law with a constant wall friction angle (Martinez et al., 2002; Wojcik et al., 2003; Vidal et al., 2005; Wojcik and Tejchman, 2009). In some FE models (Keiter and Rombach, 2001; Ayuga et al., 2001), the interface elements, which can slide with friction, are imposed between the flowing material and stagnant walls. Various constitutive models for granular solids are employed in FE models to simulate silo discharge process, including Drucker-Prager model, Mohr-Coulomb model, viscoplastic model, Lade's model, dilatant double shearing model, non-local hypoplastic model, non-coaxial model, etc. (Nielsen, 1998; Elaskar et al., 2000; Böhrnsen et al., 2004; Zhu et al, 2007; Wojcik and Tejchman, 2009; Yang et al., 2011). In spite of the use of various models, a realistic constitutive model that can describe the many phenomena of flowing solids in silos remains an important open problem in the field of FE models (Rycroft et al., 2009; Kamrin, 2010). Detailed accounts of the FE modelling principles for silo discharge will be given in following chapters of this thesis.

2.2.3 ALE in modelling of silo discharge

In terms of computational methods of FE simulation, they can be categorized into the purely Lagrangian formulation, the purely Eulerian formulation, and the Arbitrary Lagrangian-Eulerian (ALE) formulation. The ALE formulation of continuum mechanics

was initially developed in the context of fluid dynamics (Donea and Huerta, 2003), aiming at overcoming the limitations of the Lagrangian and Eulerian formulations. The basic idea is to allow the computational mesh to move in an arbitrary manner, independent of material motion. By doing so, it is possible to avoid the severe mesh distortion of a purely-Lagrangian formulation which is the conventional method in continuum mechanics. In resent researches (Guines et al., 2002; Wojcik and Tejchman, 2009; Yang et al., 2011; Wang et al., 2011; Wang et al., 2012), the ALE method becomes frequently used to simulate the long-time silo discharge process because of its particular strength in avoiding mesh distortion.

Wojcik and Tejchman (2009) carried out FE calculations based on the ALE formulation to study the dynamic discharge processes in a flat-bottomed silo and a conical hopper, which had been observed in their silo experimental tests. The shape of the material in the silo was controlled by Lagrangian boundaries where the computational mesh followed the material in the direction normal to the material surfaces. The silo outlet was defined as an Eulerian boundary, where the material was allowed to flow through the mesh by assuming a constant vertical velocity (termed controlled flow). With the help of the ALE technique, it was able to simulate almost the entire silo discharge process. Emphasis of their FE analyses was given to the propagation of multiple shear zones in the interior of flowing sand, the effect of wall roughness and silo geometry on the shear zone pattern. Rare quantitative results of dynamic silo pressures were given in their FE analyses.

Yang, et al. (2011) performed FE analyses of silo behaviour using the ALE formulation. In their numerical work, the identical ALE boundaries to those in the FE model of

Wojcik and Tejchman (2009) were set up with the exception that a free flow was taken into account by removing the outlet boundary constraint instantaneously at the start of discharge. And the full filling and the onset of discharge were taken into account in their numerical simulations, as they were well recognized to be the critical state of silo behaviour. A steep hopper and a flat-bottomed silo characterized by a mass flow and a semi-mass flow, respectively, were simulated to study the influences of the elastoplastic non-coaxial models on predictions of wall pressure distributions. In addition, the effect of wall roughness on the wall pressures was numerically investigated by varying the Coulomb wall friction coefficient.

Since the ALE formulation is still a new method in FE modelling of silo behaviour, there are few cases available to highlight its or silo simulations. Nevertheless, extensive researches of the ALE application in geomechanics and geotechnical engineering can be found in the literature (Hu and Randolph, 1998; Susila and Hryciw, 2003; Konuk et al., 2005; Savidis et al., 2008; Nagy et al., 2010). A detailed description of the ALE formulation in the FE simulation of silo discharge will be given in Chapter 3.

2.2.4 Constitutive model in FE simulations

In vast FE simulations of granular flow during silo discharge, the most important of which is the constitutive models for the granular materials. Flowing granular materials exhibit both solid-like and liquid-like behaviour. Due to its distinct characteristics, granular flow has attracted growing interest from physics, chemistry, and engineering communities (Jaeger and Nagel, 1992; Jaeger et al., 1996; Brown and Nielsen, 1998).

Due to this complex behaviour, it is evident that modelling granular flow would require a fusion of ideas from solid and fluid mechanics (Tardos, 1997; and Zhu et al., 2006). A general constitutive law for granular flow remains an important open problem for these communities (Kamrin, 2010).

Starting from the speculations of Bagnold (1954, 1966) on the flow of granular solid, three regimes of flow have been identified: (1) the dilute or rapid flowing regime where instantaneous particle collisions dominate the flow characteristics, which has been successfully studied by modified kinetic theories of granular flows (Jenkins and Savage, 1983); (2) the quasistatic regime, describing the stress-strain relations by classical plasticity theories (Schofield and Worth, 1968; Schaeffer, 1987; Martinez et al., 2002; Vidal et al., 2005); and (3) the intermediate, dense regime, in which both collisional and frictional interaction between particles must be considered and the shear dilatancy occurs (Midi, 2004; Artoni et al., 2009; Kamrin, 2010).

The latter two flow regimes are commonly encountered in silo discharge. Quasistatic flow is usually simulated using the continuum models based on elasto-plastic theories with various yield criteria, such as Mohr-Coulomb, Druker-Prager and critical state models, and numerous advanced models originated from these classical models. The hypoplastic model widely applied in FE simulations of silo discharge, are capable of describing the non-linear stress-strain relationship, dilatant and contractant behaviour, pressure dependence, density dependence, dependence on deformation direction and strain softening (Kolymbas, 1988; Wojcik and Techman, 2009). The non-coaxial model describes the non-coincidence between principal stresses and principal plastic strain

rates, induced by the principal stress rotation which is large during silo discharge (Yang et al., 2011).

Dense flow can be simulated using the constitutive relations analogous to those for complex fluids, with the hypothesis that the granular solids, intrinsically multiphasic, can be treated as a pseudo-fluid with a suitable viscosity. A hydrodynamic model (Artoni et al., 2009) was presented with phenomenological parameters i.e. fluid viscosity, porosity, and granular temperature and successfully applied to the simulation of a mass-flow silo with converging hopper. The model is capable of predicting not only stress state, but flow rate. The elasto-viscoplastic models (Haussler and Eibl, 1984; Karlsson et al., 1998; Wieckowsk, 2003) also introduce fluid viscosity parameters to describe the shear strain rate-dependent behaviour of granular solids. The dilatant double shearing model (Zhu et al., 2006; Zhu et al., 2007) is a more advanced viscoplastic model and can describe the unequal shearing rate along the two slip directions as a consequence of incorporating the effects of fabric appropriate for materials exhibiting anisotropy.

2.3 Experimental studies of silo dynamic phenomena

Silo dynamic phenomena can occur in the form of strong vibrations when a silo is discharging. The strong vibrations are often accompanied by a booming sound with a fundamental frequency of several hundred Hertz, sometimes called silo music (Tejchman and Gudehus, 1993; Muite et al., 2004; Buick et al., 2005; Dhoriyani et al.,

2006; Wilde et al., 2008), or by repeated shocks called silo quaking (about a few Hertz) (Tejchman and Gudehus, 1993; Tejchman, 1998; Wensrich, 2002; Muite et al., 2004). These highly dynamic phenomena have been recorded in terms of pressures, displacement, velocity or acceleration of stored granular solid under various conditions, e.g., in large full scale silos, small experimental models, during mass, funnel or expanded flow, during controlled or free outlet, and in cohesionless, or cohesive granular silo fills.

The strong dynamic phenomena create noise pollution that can disturb people residing in the neighbourhood or can cause hearing damage to workers nearby. They may also bring about earthquake-type movements which endanger surrounding structures and contribute to fatigue of joints and connections of the silo structures. In the most extreme case, rapid vibrations can cause silo failures. Nevertheless, there are no simple solutions that can systematically reduce silo vibrations without large structural modifications (Wilde et al., 2008). Moreover, in spite of extensive experimental studies, silo music and silo quaking are still not well understood.

The dynamic phenomenon of silos was first observed in granular materials during flow by Philips (1910) during the flow of dry sand from a cylindrical perspex model silo fitted with an orifice. He suggested that motion of the sands was jerky and that this was responsible for source of silo music. Later, the phenomenon was extensively investigated at the universities and research units: in Karlsruhe (Tejchman, 1987; Nielsen and Ruckenbrod, 1988; Tejchman and Gudehus, 1993; Ruckenbrod, 1995; and Renner, 1996), Braunschweig (Schulze, 1998; Hardow et al., 1998), Newcastle (Roberts,

1995; and Wensrich, 2002), Edinburgh (Buick et al., 2004; Buick et al., 2005), Gdansk (Tejchman, 1998; Niedostatkiewicz and Tejchman, 2003; Wilde et al., 2010), Princeton (Muite et al., 2004) and Bengalore (Dhoriyani et al., 2006), Academia Sinica (Li and Kwauk, 1989).

Several sources of the extensive dynamic phenomena have been proposed on the basis of experimental observations, including: slip-stick behaviour between stored solids and silo walls (Roberts, 1995; Wensrich, 2002; Muite et al., 2004; Buick et al., 2004; Buick et al., 2005), alternating flow patterns during flow (Schulze, 1998), propagation of longitudinal stress waves due to a resonant interaction between the granular material and the low part of the silo structure (Tejchman, 1987; Nielsen and Ruckenbrod, 1988; Niedostatkiewicz and Tejchman, 2003; Wilde et al., 2010), acceleration and deceleration of the granular material at the transition between parallel section and converging section (Hardow et al., 1998), internal slip-stick of stored solid (Buick et al., 2004), the dilation of bulk solid during flow (Moriyama and Jimbo, 1988; Roberts, 1995), and the shear zone in the converging region during flow (Blair-Fish and Bransby, 1973; Michalowski, 1987).

The following case studies outline several experimental investigations where silo quaking phenomenon has presented a significant problem. These experimental investigations were carried out first to illustrate the occurrence of the dynamic phenomenon and then to explore the mechanism and causes of quaking. It is not possible to highlight all the cases due to the huge amount of experimental observations on silo

quaking so far. Therefore, a few cases closely relating to the present study are outlined here.

Tejchman and Gudehus (1993) found that the dynamic phenomena of silos during the flow of sand from a slender Perspex cylinder fitted with an orifice. The fundamental frequency of vibration of the silo was measured using a geophone transducer fixed to the outer surface of the silo wall near the outlet. It was found that silo music occurred during emptying dry sand with a frequency of 25~45 Hz initially, and of 60~80 Hz later. During flow of weakly cohesive sand, it was registered that silo music with a frequency of 40~70 Hz occurred at the beginning and silo quaking with a basic frequency of a few Hertz took place later. Besides, they have investigated the specific outlet size for the silo music and quake to occur.

As reported in the TUNRA test silo by Roberts (1996), silo quaking is known to occur in tall mass-flow silos when the height of fill is above a critical height (see Fig. 2-1), approximately equal to the diameter of the silo. Pressure disturbances caused by this quaking were registered and grew with the position in a tall mass-flow silo (see in Fig. 2-2). Later, Roberts and Wensrich (2002) stated that as the velocity profile across the cross-section was changed from uniform to converging in the region of transition between cylindrical section and converging section, the flow pressure formed and led a dilation effect of bulk solid in the hopper. As a result of this dilation effect, the vertical supporting pressure decreased slightly thus reducing the support given to the plug of bulk solid in the cylinder. Subsequently, this caused the plug to drop momentarily giving rise to a load pulse. The cycle could be then repeated in the discharge process.

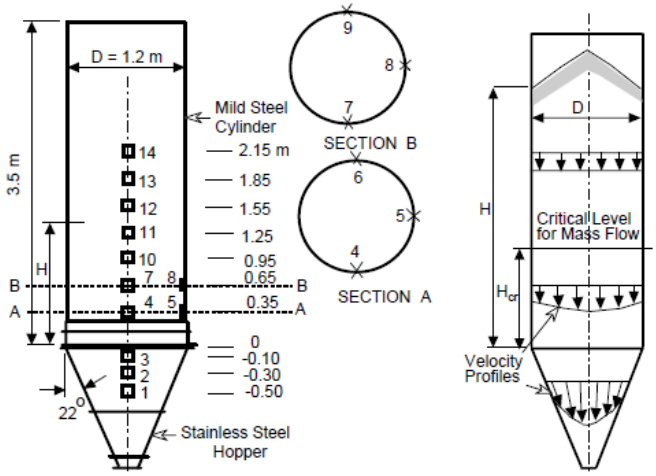

(a) **(b)**

Fig. 2-1 Tall mass-flow test silo (after Roberts, 1996): (a) load cell locations; (b) velocity profiles

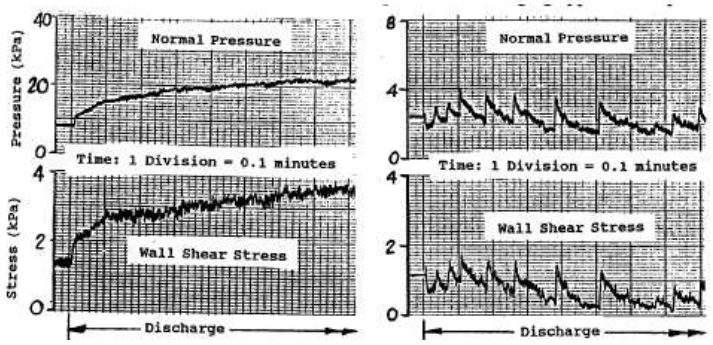

Fig. 2-2 Sample of normal pressures and shear stress at two locations in the TUNRA test silo (after Roberts, 1996): (a) results for location 5; and (b) results for location 14

Wensrich (2002) examined silo quaking using data acquired from two small Perspex silo models. Here, the smaller 90-mm test rig is taken as an example (as shown in Fig. 2-3), in which slow discharge velocity was varied (0.08 mm/s~0.4 mm/s) to investigate its relationship to the quake. In these tests, the acceleration of the sand at various depths below the free surface was measured using accelerometers buried within the column. By

doing so, it was found that the acceleration signal consisted of large quakes separated by oscillations of much smaller amplitude (see Fig. 2-4), implying that the stress-wave propagation took place. Meanwhile, the amplitude of the acceleration had an exponential growth rate with the height above the base, as shown in Fig. 2-5. Besides, an inversely-proportional relationship between discharge velocity and time interval between the large quakes was confirmed by the acquired data. Wensrich suggested that the pulsation was caused by compression and rarefaction waves in the granular material, which in turn were created by the slip-stick behaviour between the stored solids and the silo walls.

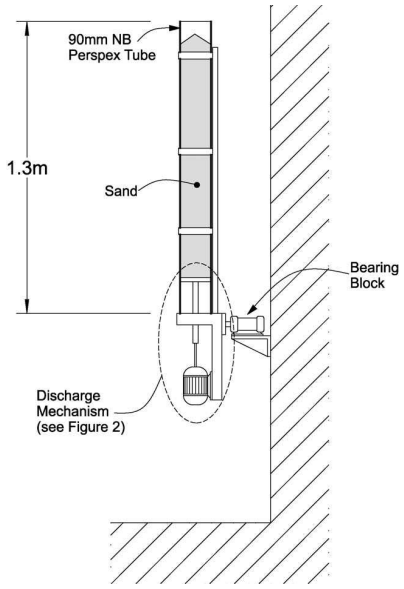

Fig. 2-3 Experimental setup of the Perspex model silo (after Wensrich, 2002)

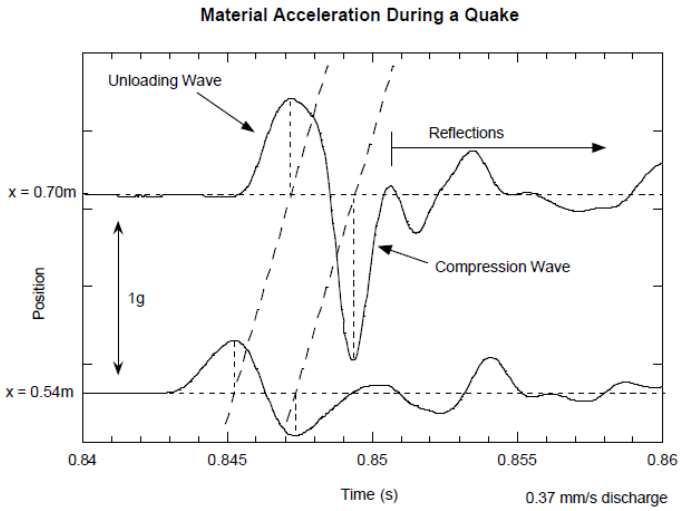

Fig. 2-4 Acceleration measurements at two different positions in the material column (the 90-mm test rig) showing the transmission of quake waves (after Wensrich, 2002)

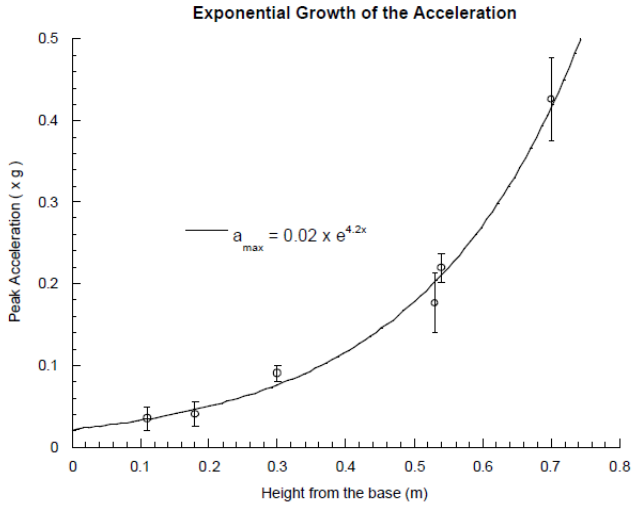

Fig. 2-5 Peak acceleration during a quake as a function of the measurement position (in the 90-mm test rig) (after Wensrich, 2002)

Muite et al. (2004) investigated the silo quaking in tall and narrow silos (see Fig. 2-6). A series of tests had been conducted using different combinations of granular materials (e.g., crushed glass, glass beads and sand) and silo wall materials (e.g., acrylic,

aluminum and plain steel). By measuring the vertical acceleration on the base of silo (see Fig. 2-7) and vertical acceleration of granular material (see Fig. 2-8), it was concluded that the pulsating motion of granular material drives the oscillatory motion of the silo. However, the large upward acceleration recorded is attributed to stress waves created by each pulsation of the granular material. From explaining that the pulsation of granular material is caused by the collapse of arch which forms as a part of force chain in the low part of the silo, Muite et al. stated that the frequency of pulsation of granular material was independent of the discharge velocity unlike in Wensrich's study (2002). Contrary to Wensrich's observation (2002), the granular material accelerations recorded in Muite et al.'s experiments with the accelerometer at a fixed depth below the free surface did not change appreciably as the bed height decreased during discharge.

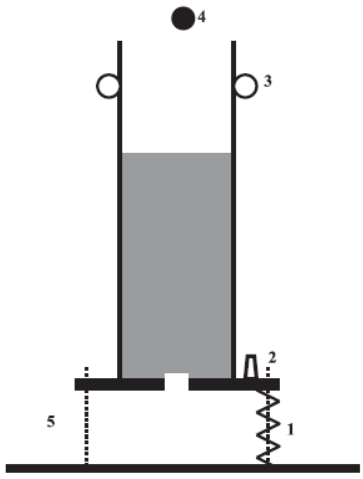

Fig. 2-6 Experimental setup for vertical acceleration and sound measurements (after Muite et al., 2004). The number indicates: 1-spring on positioning slider, 2-accelerometer, 3-positioning roller, 4-microphone, 5-positionning slider

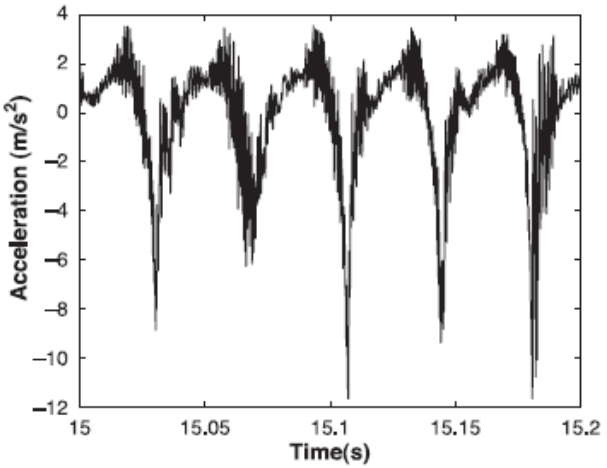

Fig. 2-7 Vertical acceleration measurements on the base of the aluminium silo during discharge of crushed glass through a 1.9-cm orifice (after Muite et al., 2004)

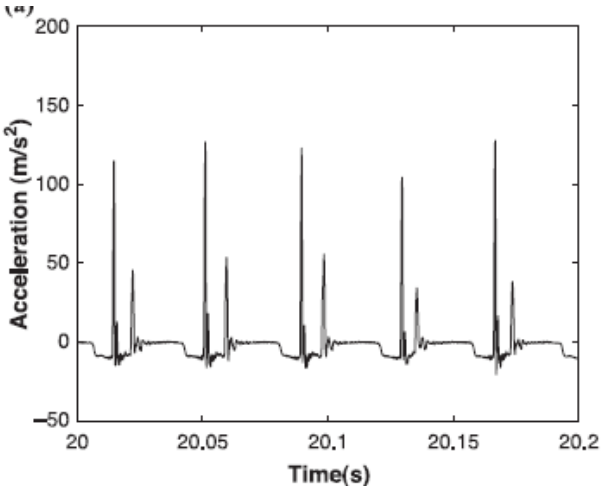

Fig. 2-8 Vertical acceleration measurements made when the accelerometer was embedded in the crushed glass (after Muite et al., 2004)

2.4 Stress wave

The study of stress waves in granular medium is of great interest in many industrial applications. Since the propagation of longitudinal stress waves due to a resonant

interaction between the granular material and the silo structure can contribute to the dynamic phenomena in silos (Tejchman, 1987; Nielsen and Ruckenbrod, 1988; Niedostatkiewicz and Tejchman, 2003; Wilde et al., 2010), a good understanding of the propagation of stress waves in granular media is required for the study of the silo dynamic phenomena including silo quaking and silo music.

The transmission of stress waves within granular medium is a complicated issue because of the heterogeneity and nonlinearity inherent in these systems. In last decades, propagation of stress waves in granular medium has been extensively studied and reported in the literature. These treatments range from analytical method (Gregor and Rumpf, 1975; Ocone and Astarita, 1995; Weir, 2001), to experimental investigation (Liu and Nagel, 1992; Ben-Dor et al, 1997; Hardin and Richart, 1963; Musmarra et al., 1995; Tournat et al., 2004) and to more recent studies using numerical simulation (Melin, 1994; Berezin et al., 2001; Hostler and Brennen, 2005; Oveisy et al., 2009; Mouraille et al., 2009).

Wensrich (2002) proposed that the pulsations or vibrations in silos are due to the propagating compression and rarefaction waves in the granular materials, which are caused by the slip-stick motion between the granular material and the silo walls. In his analytical model, a simple dynamic version of Janssen's silo model was used and showed the relationship between the wall friction and the growth of rarefaction waves.

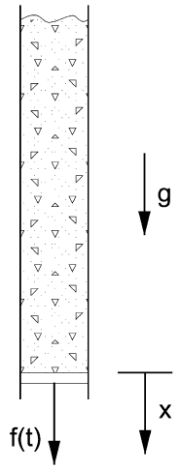

Fig. 2-9 One-dimensional column of granular material studied by Wensrich (2002)

In this model (see Fig. 2-9) it was assumed that the material was initially in a state such that friction was fully mobilised in the upward direction (akin to Janssen's original model). The action of the rarefaction wave overcomes friction and motivates the flow of initially stationary material. From this model it was shown that a rarefaction wave initially of magnitude σ_0 grows with the following form:

$$\sigma(x,t) = \sigma_0 e^{-\frac{x}{2X_0}} \tag{2-1}$$

where σ is the principal stress in the axial (x) direction, $X_0 = D/4\mu k$ is the characteristic depth of the column, D is the diameter of the column, μ is the coefficient of friction between the material and the column walls, and k is the coefficient of lateral pressure.

Using this one-dimensional dynamic version of Janssen's silo model, it is shown that the action of wall friction has an important role in the growth of rarefaction waves travelling in the granular medium. There is a positive feedback cycle between them as the

exponential growth of the wave further decreases the pressure thus reducing the wall friction, which allows the wave to grow larger. Further, the increasing rarefaction wave may induce significant dynamics which can lead to silo quaking.

Furthermore, the trigonometric form of wave dispersion was given by Wensrich (2002) as follows:

$$\Omega = A\cos(\omega(x-\lambda t)) + B\sin(\omega(x-\lambda t)) \tag{2-2}$$

where A and B are constants, and the frequency of oscillation, ω, is given by:

$$\omega = \sqrt{3(\frac{2\mu k}{D})^2 \frac{c^2}{\lambda^2 - c^2}} \tag{2-3}$$

According to this solution of travelling wave, it is concluded that the frequency of the travelling solution is related to the speed of propagation, i.e, the components travel with a speed, λ, close to the wave speed, c, are those with high frequencies.

To investigate the role of wall friction, Boutreux et al. (1997) proposed a dynamic version of the Janssen model. Based on this model a linear elastic behaviour of the material was considered and wave propagation was examined in a horizontal cylinder without considering the gravitational effects (see Fig. 2-10). In their model, friction was mobilised by the travelling wave and it was shown that the amplitude decayed exponentially in this case.

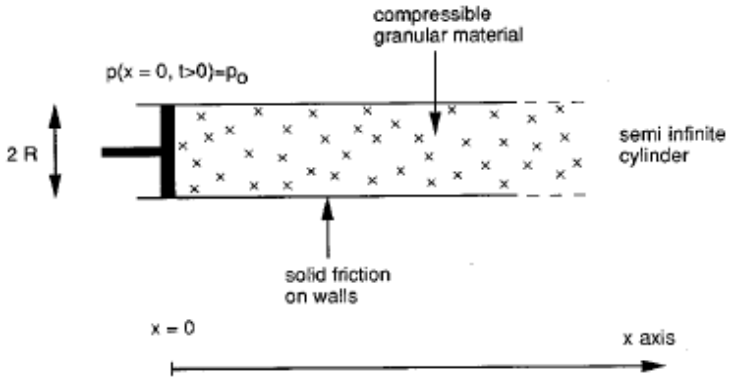

Fig. 2-10 Water hammer model for a granular material (after Boutreux et al., 1997): at t=0, a pressure step at the end of the horizontal cylinder

Despite the similar exponential form of the stress-wave growth to that proposed by Wensrich (2002), the model gave more rapid growth because of taking into account both dynamic and static friction. The exponential function is shown as follows

$$\sigma(x,t) = \sigma_0 e^{-\frac{x}{2\xi X_0}} \tag{2-4}$$

where σ is the principal stress in the axial (x) direction, $X_0 = D/4\mu k$ is the characteristic depth of the column and ξ is determined by the mobilised friction between the granular material and the container.

Borzsonyi and Kovacs (2011) reported experimental observation of sound waves in a granular material during a resonant test-scale silo discharge (see Fig. 2-11). The grain motion was tracked by high-speed imaging while the resonance of the silo was detected by piezoelectric accelerometers and acoustic method. Their major observation was that the wave velocity was not constant throughout the silo but increased considerably toward the transition zone in the lower end of the silo. In this region, the strong stress oscillations were observed where the flow was changing from cylindrical to converging

flow. Moreover, the amplitude of the oscillations increased with height and led to slip-stick motion in the upper part of the silo. This conclusion supports the viewpoint of Roberts and Wensrich (2002), and Wensrich (2002).

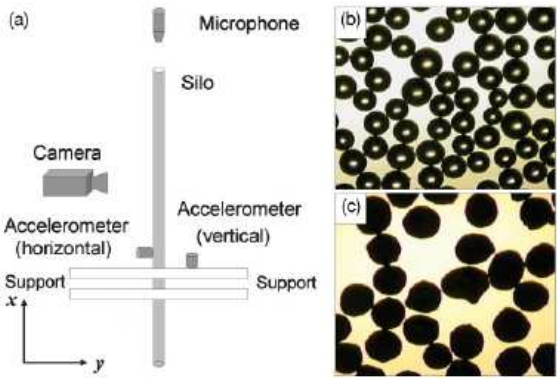

Fig. 2-11(a) Schematic illustration of the experimental setup and microscopic images of the material used: (b) glass beads with mean diameter of *d*=0.15±0.05 mm; (c) copper particles with *d*=0.15±0.05 mm (after Borzsonyi and Kovacs, 2011)

2.5 Slip-stick motion

Slip-stick motion is an extremely common phenomenon that can occur in huge variety of mechanical systems between surfaces of rigid bodies, within a bulk solid (internal friction), and between a bulk solid and the surface of a rigid body (wall friction). Slip-stick friction has been studied from a variety of perspectives over the past decades (Ibrahim, 1994). In recent years, studies based on slip-stick motion become more and more popular in explaining the physical mechanism of the dynamic phenomena in silos (Wensrich, 2002; Muite et al., 2004; Buick et al, 2004; Buick et al., 2005; Dhoriyani et al., 2006).

Fig. 2-12 shows a simplified mechanical system where a mass coupled with an elastic spring, is being pulled along *x* direction at a constant velocity *v*. The normal stress σ acting on the contact plane results from the self-weight of mass *m*. To move the solid bodies across each other, the friction between them has to be overcome and, thus, a sufficient shear stress τ must be applied.

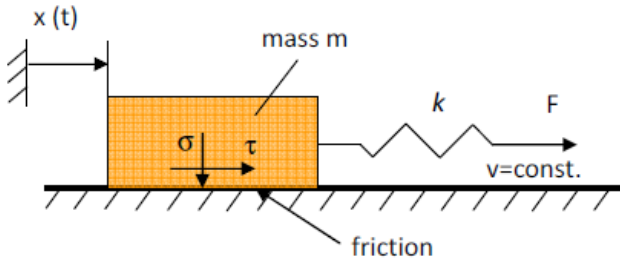

Fig. 2-12 Friction between solid bodies (redrawn after Schulze, 2007)

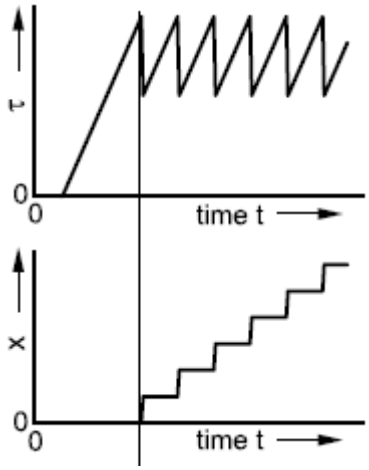

Fig. 2-13 Shear stress and displacement of moving body in the presence of slip-stick friction (after Schulze, 2007)

Fig. 2-13 shows slip-stick oscillations which are created by alternating slipping and sticking of surfaces being in contact and moved parallel across each other as shown in

Fig. 2-12. During a stick period, the shear stress τ increases until the static friction is overcome (see Fig. 2-13). Thus, the mass suddenly starts to move, which is accompanied by a sudden decrease of shear stress τ due to the change from static friction to usually smaller kinematic friction. Meanwhile, the sudden decrease of shear stress is associated with an abrupt displacement in *x* direction as shown in Fig. 2-13 (Schulze, 2007). Slip-stick oscillations can only emerge in a specific situation where the coefficient of kinematic friction μ_k (as shown in Fig. 2-14), is smaller than that of static friction μ_s; additionally, the system must have the ability to oscillate, e.g. damping must be sufficiently small (Wensrich and Roberts, 2000; Schulze, 2003). Therefore, generally slip-stick motion is a result of both material and system properties.

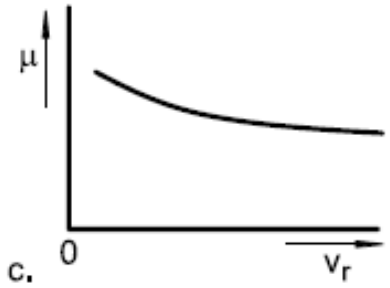

Fig. 2-14 Coefficient of friction vs. relative velocity (after Schulze, 2007): $\mu \neq const.$

The extensive studies on the role of slip-stick behaviour in silo quaking have been conducted in resent years. Wensrich (2006) performed an analysis of the slip-stick phenomenon in simple one-dimensional discrete systems (see Fig. 2-15) and uncovered a very important non-dimensional number that defines the boundary between slip-stick and smoothing sliding, as a function of the damping ratio of this system (see Fig. 2-16). Through an investigation of the motion of a single mass, the number was found to be

very important in the occurrence of slip-stick in more complicate systems with multiple degrees of freedom, as in the situation as silo quaking.

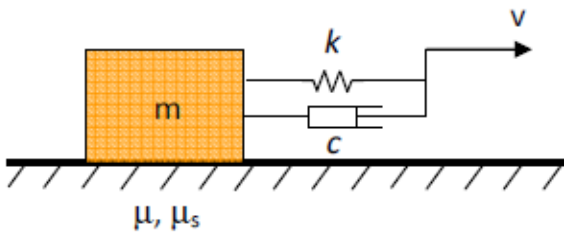

Fig. 2-15 A simple one degree-of-freedom mass spring-damper system (redrawn after Wensrich, 2006)

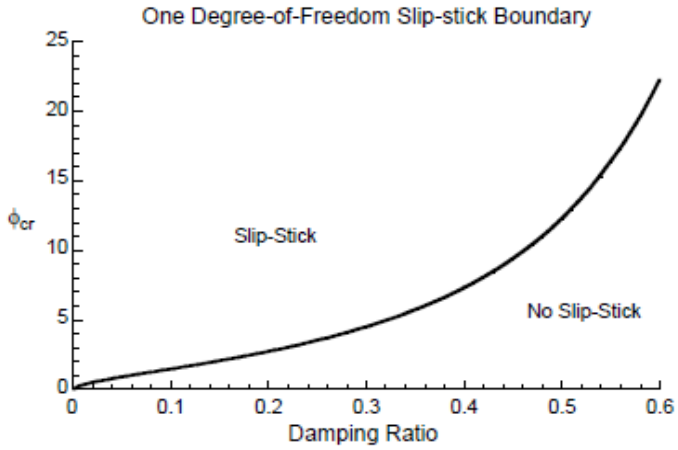

Fig. 2-16 Relationship between the non-dimensional number value of ϕ_{cr} and the damping ratio of the system (after Wensrich, 2006)

To investigate the powder properties relevant for slip-stick motion which is deemed to be the cause of silo quaking and silo music, Schulze (2003) carried out a series of tests to measure the shear stress and the shear velocity with a computer-controlled ring shear tester. In terms of influence of the shear velocity, both materials investigated, i.e., polyethylene powder and limestone powder, showed a sharp variation of shear stress

with a stepwise increase in the shear velocity, as schematically illustrated in Fig. 2-17. In turn, the so-called “slide-hold-slide” tests were conducted to investigate the influence of the duration of the stick period on the static friction which has to be overcome subsequently. At first the powder specimen was sheared until steady-state flow (shear stress) was attained. Then the motor was stopped and restarted after a defined holding time Δt. Subsequently, it was observed that the shear stress exhibited a maximum much higher than that measured at steady-state flow when the specimen was sheared again. Furthermore, the longer the holding time, the larger the maximum shear stress (see Fig. 2-18) would become. Therefore, Schulze stated that powder properties play an important role in slip-stick motion.

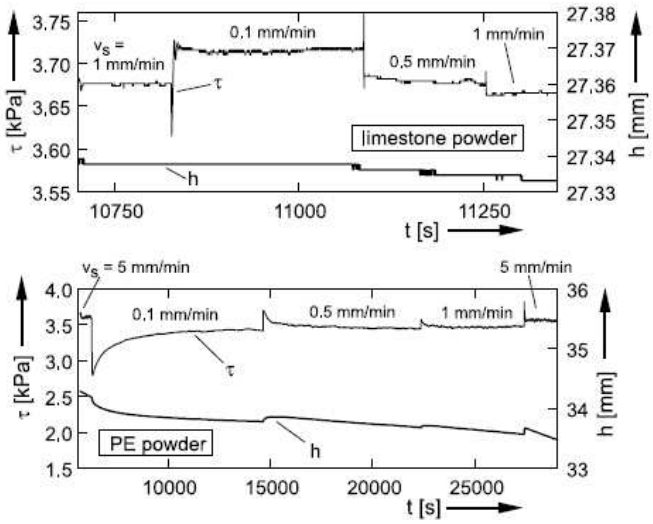

Fig. 2-17 Shear stress and specimen height as a function of time at stepwise varied shear velocity under a constant normal stress (after Schulze, 2003)

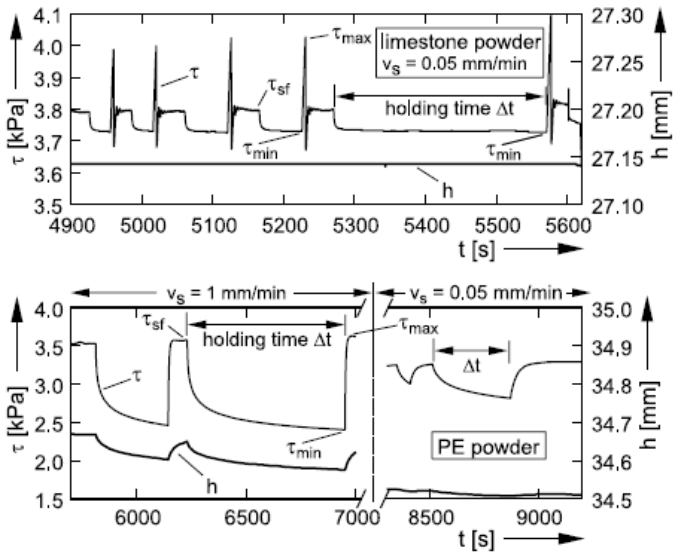

Fig. 2-18 Shear stress and specimen height vs. time during a slide-hold-slide test for limestone powder and PE powder (after Schulze, 2003)

Buick et al. (2005) carried out laboratory tests to investigate predominantly the probable source of silo quaking and silo music, i.e., the slip-stick motion between the stored solid and the walls and within the solid for different particle and wall materials. During the tests slip-stick motion was only observed for particles known to honk in a full-scale silo. A series of tests were conducted to investigate the effects of shearing rate, stress level, and period under load using polyethylene terephthalate (PET) and polypropylene (PP) pellets. Especially, the slip-stick motion was noted to be very much stress-level dependent, with considerably larger fluctuations at larger normal stress, and very little fluctuations at very low stress level (see Fig. 2-19). This observation is consistent with the fact that silo music does not occur when the fill level is below a certain level.

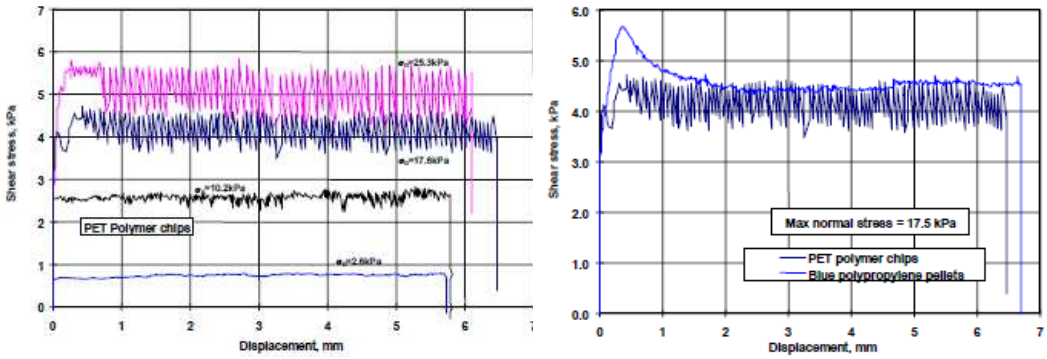

Fig. 2-19 Shearing response of PET and PP pellets on an aluminium wall (after Buick et al., 2005)

2.6 Concluding remarks

The failures and severe damage of silo structures occur mainly due to insufficient knowledge of silo pressure especially during discharge. In the last decades silo research in this field was mainly governed by experiments, analytical theories and numerical calculations which becomes promising with the help of substantial progress made in computational science. By overcoming the shortcomings of experiments and theories, numerical calculations, especially FE method, are capable of describing the complex bulk material behaviour in a qualitatively and quantitatively satisfying manner.

The current literature on dynamic phenomena in silos has been reviewed and it has been established that a more deep understanding of dynamic phenomena and a more thorough appreciation of the mechanism involved in these phenomena in silos. More detailed literature review on different aspects will be presented in introductions of the following chapters of this thesis. They include FE modelling of silo behaviour, FE prediction of dynamic pressure in silos, analytical model of stress wave propagation in granular

media, experimental investigation of silo behaviour and an advanced material model (non-coaxial model) used in FE simulation of silo behaviour.

Chapter 3

Numerical aspects of ALE modelling of granular flow in silos

3.1 Introduction

Numerous simulations have been performed using the finite element method to study various aspects of silo behaviour either during filling or during discharge, such as the pressure profile, the role of flow pattern, the influence of fluidity, the development of shear bands, the role of eccentricity, the influence of inserts in silos, and the dilatancy of granular solids (Vidal et al., 2006; Karlsson et al., 1998; Zhong et al., 2001; Ayuga et al., 2001; Ding et al., 2003; Goodey et al., 2006). In terms of computational methods in continuum mechanics, they can be categorized into the purely Lagrangian formulation, the purely Eulerian formulation, and the arbitrary Lagrangian-Eulerian formulation. In a purely Lagrangian formulation, each individual node of the computational mesh is permanently connected to the same material point during motion. Such formulation, however, becomes powerless to describe large deformation because the element mesh may be severely distorted due to the fact that elements deform with the material. In a purely Eulerian formulation, the computational mesh is fixed spatially (elements retain their original shape) and the continuum moves with respect to the grid. In such formulation, however, problems may arise when free surface condition, prescribed boundary condition or continuum deformation with history-dependent constitutive relations are considered since the element mesh is not connected to the material. To

overcome the shortcomings of both formulations and to combine their best features, the Arbitrary Lagrangian-Eulerian (ALE) formulation has been developed in which the mesh is neither connected to the material nor fixed spatially but can be prescribed in an arbitrary manner (Donea and Huerta, 2003), as shown in Fig. 3-1. Noh (1964) and Hirt, Amsden and Cook (1974) made the original developments by first proposing the ALE method in the context of fluid dynamics. The method was subsequently applied to nonlinear solid mechanics by Haber (1984); Liu et al. (1986); and Benson (1989). More recently, the method has been applied in various solid mechanics problems, including: the incompressible hyperelasticity (Yamada and Kikuchi, 1993), metal forming simulation (Ghosh et al., 1996; Gadal et al., 1998), transient dynamic analysis (Rodriguez-Ferran, et al., 1998), hyperelastoplasticity (Rodriguez-Ferran et al., 2002), finite strain plasticity (Armero and Love, 2003), and pressure-sensitive materials (Khoei et al., 2008). The application of ALE method has proved to be an effective measure to simulate the silo behaviour (Ding et al., 2003; Wojcik and Tejchman, 2009; Yang et al., 2011; Wang et al., 2011).

In order to achieve a satisfactory degree of accuracy in the finite element analysis using the ALE method in the present study, several numerical treatments must be made carefully. These treatments range from the ALE formulation, the ALE solution scheme and the ALE boundary definition, the initial state of stress prior to material flow and the interaction between the stored material and the silo walls. This chapter describes the initial exploration of these numerical issues as a precursory study to simulate the silo behaviour during filling and discharge. In the later sections of this chapter, the

simulation of a conical hopper discharge is undertaken as an example to indicate the advantage of ALE in solving mesh distortion due to the large deformation.

3.2 Uncoupled ALE solution

In the ALE description, three different configurations are considered: the material domain R_X , consisting of material particles X , the spatial domain R_x, made up of spatial points x, and the referential domain R_χ, composed of reference points χ, as shown in Fig. 3-2.

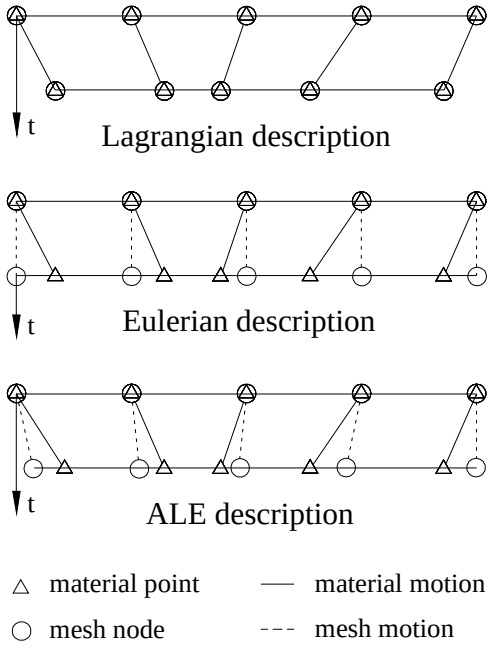

Fig. 3-1 One dimensional example of Lagrangian, Euerlian and ALE mesh and material particles motion (redrawn after Donea and Huerta, 2003)

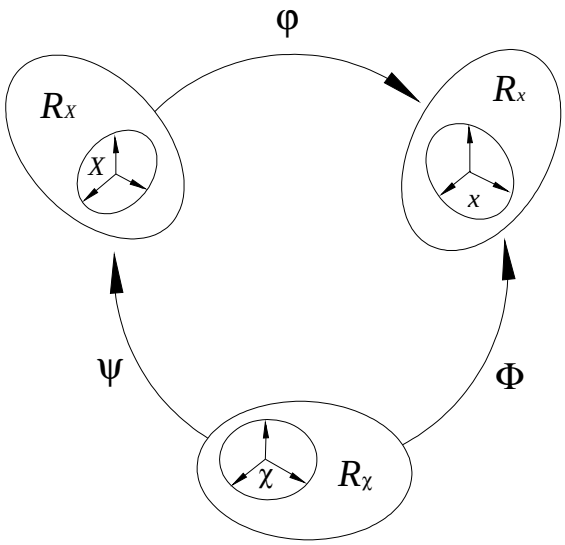

Fig. 3-2: The motion of ALE computational mesh is independent of the material motion (redrawn after Donea and Huerta, 2003)

'One-to-one' transformations between the three domains, denoted by φ, Φ, and Ψ respectively are shown in Fig. 3-2. The general relationship between material time derivatives and referential time derivatives of any scalar function (Donea and Huerta, 2003) can be expressed as

$$\left.\frac{\partial f}{\partial t}\right|_X = \left.\frac{\partial f}{\partial t}\right|_\chi + c_i \frac{\partial f}{\partial x_i} \tag{3-1}$$

where

$$c_i = u_i - \tilde{u}_i \tag{3-2}$$

is the convective velocity defined as the connection between material velocity u_i and mesh velocity $\tilde{u}_i$ in ALE kinematics.

In the ALE context, two different approaches are available for dealing with the governing equations in a dynamic analysis (Rodriguez-Ferran et al., 1998). One method

is to solve the fully coupled equations by firstly transforming the governing equations into matrix equations which contain convection terms for mass, momentum and stress, respectively, and then integrating them in time by means of an explicit predictor-corrector method. The other method is to treat material and convective effects separately in the Lagrangian phase and Eulerian phase combined with a smoothing procedure, respectively. In the present study, the latter one, the so-called uncoupled Arbitray Lagrangian-Eulerian formulation accessible in the program Abaqus/Explicit, was employed with the help of the operator splitting technique (SIMULIA 2008). The whole solution procedure is schematically illustrated in Fig. 3-3.

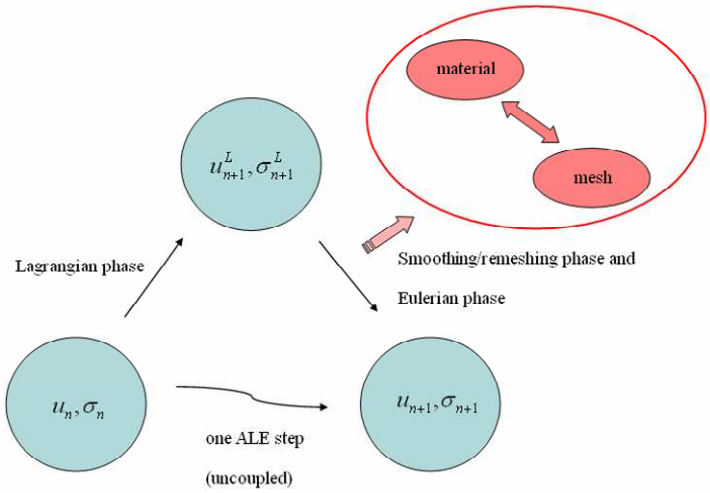

Fig. 3-3 Uncoupled ALE solution procedure: history-dependent variables (u_n, σ_n) in time step n+1

In the operator splitting technique, every time step Δt is subdivided into two phases: a material (or Lagrangian) phase, where convective terms in the governing equations are neglected, and a convection (or Eulerian) phase (Liu et al., 1986; Donea et al., 2004).

3.2.1 Lagrangian (or material) phase

In the Lagrangian phase, the convective terms are neglected, so the governing equations for compressible flow are identical to a time step in a standard Lagrangian analysis. Thus, the governing equations in the dynamic analysis can be written as

$$\left.\frac{\partial \rho}{\partial t}\right|_{\chi} = -\rho \frac{\partial u_j}{\partial x_j} \tag{3-3a}$$

$$\rho \left.\frac{\partial u_i}{\partial t}\right|_{\chi} = \frac{\partial \sigma_{ij}}{\partial x_j} + b_j \tag{3-3b}$$

$$\left.\frac{\partial \sigma}{\partial t}\right|_{\chi} = q \tag{3-3c}$$

which need to be integrated at each time step to update the stress from σ_n at time t_n to σ_{n+1}^L after the Lagrangian phase. The notation $\left|_{\chi}\right.$ means 'holding χ fixed', ρ is the density of material, b_j is the force per unit volume and q accounts for both the pure straining of the material and the rotational terms that counter the non-objectivity of the material stress rate (Huerta and Casadei, 1994). It implies that the grid points move attached to material particles as the convective terms are ignored. Therefore, the Lagrangian phase can be performed with the same stress update algorithm used in Lagrangian simulations, which deal with the constitutive equation at the Gauss point level.

3.2.2 Smoothing scheme

To reduce mesh distortion in the spatial domain, a remeshing, or smoothing procedure must be applied between the Lagrangian and Eulerian phase. In addition, due to the

independent motion of mesh from that of material, a specified mesh velocity $\tilde{v}$ is required for determining the convective velocity, c_i, considering the implementation of the governing equations. Therefore, a suitable remeshing scheme is needed.

There are various remeshing schemes proposed by researchers (Donea and Huerta, 2003; Benson, 1989; Ghosh et al., 1991). The most commonly used remeshing schemes are based on the Laplacian approach and mid-area averaging technique. The basic disciplines are: (1) mesh distortion is controlled by moving the inner nodes in an appropriate way; and (2) boundary nodes are forced to move with the material along the normal to the surface and relaxed along the tangent.

In the Laplacian approach, spatial position of the considered node X_n can be relocated by averaging the spatial positions of the nodes L_i, connected to X_n by element edges as (Khoei et al., 2008)

$$x_{n+1} = \frac{1}{N}\sum_{i=1}^{N} L_i \tag{3-4}$$

Where x_{n+1} presents the new spatial position of node X_{n+1}, and N is the number of edges of four-node element connecting to node X_n (typically, N =4).

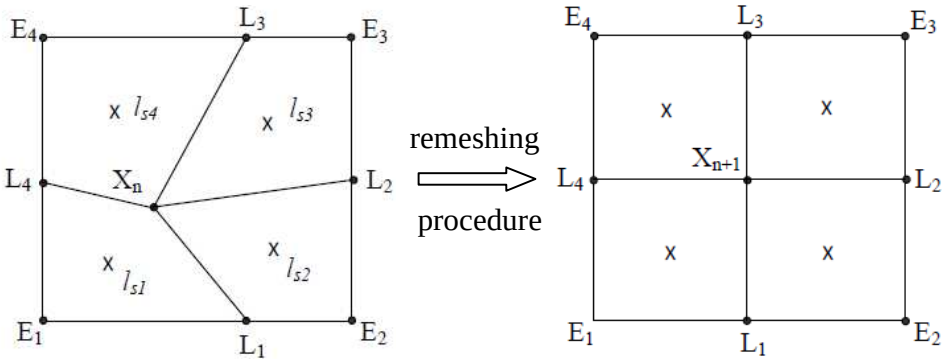

Fig. 3-4 Remeshing procedure in smoothing phase

Equipotential smoothing is a higher-order Laplacian method that relocates a node by calculating a higher-order, weighted average of the positions of the node's eight nearest neighbouring nodes in two dimensions (or its eighteen nearest neighbouring nodes in three dimensions). In Fig. 3-4 the new position of node X_{n+1} is based on the position of all the surrounding nodes, L_i and E_i.

The mid-area averaging approach can be considered as a modification of the Laplacian approach. In this approach, the new node X_{n+1} is in the centroid of all connected elements taking different element areas into account. Thus, the spatial position of smoothed node X_n can be obtained as

$$x_{n+1} = \frac{\sum_{i=1}^{N} A_i l_{Si}}{\sum_{i=1}^{N} A_i} \tag{3-5}$$

where l_{Si} is the location of the centroid of element E_i (see Fig. 3-4), A_i is the area of element E_i and N is the number of edges of four-node elements connecting to node X_n.

Laplacian smoothing is a low computational-cost algorithm and is commonly used for low to moderately distorted mesh domains. For domains with severely distorted mesh and boundaries of complex curvature, mid-area averaging smoothing generally results in a more balanced mesh but costs much more than Laplacian approach in computation. And equipotential smoothing is the most expensive algorithm in the three and is not employed in the present study where the combination of Laplacian and mid-area averaging approach of smoothing is employed by specifying the weighting factor for each method (SIMULIA 2008).

After smoothing the location of all nodal points x_{n+1} at time t_n, the convective velocity c_{n+1} can be determined using Equation (3-2) with the help of the material displacement d_{t+1} and mesh displacement $\tilde{d}_{t+1}$.

3.2.3 Eulerian (or convection) phase

The Eulerian phase in the final part of the operator splitting technique includes remapping the variables of the solution obtained by the Lagrangian phase onto the newly relocated mesh, which is developed through the mesh smoothing procedure.

In the Eulerian phase, the convective terms which were neglected during the Lagrangian phase are taken into account. Due to the fact that we are dealing with history-dependent materials and different material integration points have different histories, these quantities must be updated in order to compute the history-dependent variables in the following time step. Unfortunately, these variables are computed at discrete integration

points, which normally lie inside the element. This yields a discontinuous field and produces numerical problems, since the spatial gradient of these variables are required (Khoei et al, 2008). To overcome these difficulties, an algorithm that circumvents the computation of the stress gradient based on Godunov technique was employed in the present study (SIMULIA 2008). In this case, the constitutive equation (3-3c) can be written as

$$\left.\frac{\partial \delta}{\partial t}\right|_{\chi} + c_j \frac{\partial \delta}{\partial x_j} = 0 \tag{3-6}$$

Indeed, the internal variables commonly used in nonlinear mechanics must also be convected following Equation (3-6), so δ can be considered as any stress-related component (a component of the stress tensor or an internal variable, i.e., the bulk density ρ, the effective plastic strain $\bar{\varepsilon}^p$, and the stress σ). Equation (3-6) is required to be integrated at each time step to update the stress from δ_{n+1}^L to δ_{n+1} at time t_{n+1}. Here, when the Godunov-like technique is implemented, the stress-related component δ_{n+1}^L is transferred from the Lagrangian mesh to the relocated Eulerian mesh.

In the ALE formulation, besides the content discussed above, there exist more issues, such as explicit time step, solid-wall boundary conditions, and mesh dependence, which need to be explored. More discussions about these issues will be given in the following sections. In the ALE dynamic analysis, the numerical time integration of the momentum balance places a limit on the maximum time step Δt. This limitation is associated with

the stability of the explicit time integration scheme employed in the FE simulations, and will be discussed in detail in Section 3.3 of this chapter.

3.3 Explicit dynamic analysis

In the present study, the ALE formulation was accessible in the Abaqus/Explicit program (SIMULIA 2008). To simulate the silo discharge process which involves very large deformation, the uncoupled Arbitrary Lagrangian-Eulerian formulation with the adaptive meshing technique was employed using an explicit time integration scheme.

3.3.1 Numerical implementation

The explicit dynamic analysis procedure in Abaqus is based upon the implementation of an explicit time integration rule together with the use of diagonal ("lumped") element mass matrices. The equations of motion for the body are integrated using the explicit central-difference operator

$$u^N_{(i+1/2)} = u^N_{(i-1/2)} + \frac{\Delta t_{(i+1)} + \Delta t_{(i)}}{2} \dot{u}^N_{(i)} \tag{3-7}$$

$$d^N_{(i+1)} = d^N_{(i)} + \Delta t_{(i+1)} u^N_{(i+1/2)} \tag{3-8}$$

where d^N is a degree of freedom (a displacement or rotation component) of node N and the subscript i refers to the increment number in an explicit dynamic step. The central-difference integration operator is explicit in the sense that the kinematic state is advanced using known values of velocity $u^N_{(i-1/2)}$ and acceleration $\dot{u}^N_{(i)}$ from the previous increment. The acceleration at the beginning of an increment is computed by

$$\dot{u}_{(i)}^{N} = (M^{NV})^{-1}(F_{(i)}^{V} - I_{(i)}^{V}) \tag{3-9}$$

where M^{NV} is the mass matrix, F^{V} is the applied load vector, and I^{V} is the internal force vector. A lumped mass matrix is used because its inverse is simple to compute and because the vector multiplication of the mass inverse by the inertial force requires only *n* operations, where *n* is the number of degrees of freedom in the model. The explicit procedure requires no iterations and no tangent stiffness matrix. The internal force vector I^{V} is assembled from the contributions from each individual elements such that a global stiffness matrix need not be formed. The key to the computational efficiency of the explicit procedure is the use of the diagonal element mass matrices in the explicit dynamic analysis.

3.3.2 Nodal mass and inertia

The explicit integration scheme in Abaqus/Explicit requires nodal mass or inertia to exist at all activated degrees of freedom unless constraints are applied using boundary conditions. More precisely, a nonzero nodal mass must exist unless all activated translational degrees of freedom are constrained; and nonzero rotary inertia must exist unless all activated rotational degrees of freedom are constrained. Nodes that are part of a rigid body do not require mass, but the entire rigid body must possess mass and inertia unless constraints are used. When the degrees of freedom at a node are activated by elements with a nonzero mass density (e.g. solid, shell, beam) or mass and inertia elements, a nonzero nodal mass or inertia occurs naturally from the assemblage of lumped mass contributions.

3.3.3 Stability of numerical results

The explicit procedure integrates through time by using many small time increments. The central-difference operator is conditionally stable, and the stability limit for the operator (with no damping) is given in terms of the highest radian frequency ω_{max} of the system as

$$\Delta t \le \frac{2}{\omega_{\max}} \tag{3-10}$$

With damping, the stable time increment is given by

$$\Delta t \le \frac{2}{\omega_{\max}}(\sqrt{1+\xi_{\max}^2} - \xi_{\max}) \tag{3-11}$$

where $\xi_{\max}$ is the fraction of critical damping in the mode with the highest frequency. Contrary to our usual engineering intuition, introducing damping to the solution reduces the stable time increment. In Abaqus/Explicit a small amount of damping is introduced in the form of bulk viscosity to control high frequency oscillations. In the present study, the linear bulk viscosity pressure and quadratic bulk viscosity pressure were generated by setting two damping coefficients to be 0.06 and 1.2, respectively (SIMULIA 2008), which are not included in the material point stresses. A study of sensitivity of these two viscosity parameters to numerical solutions will be presented in later section of this chapter.

3.3.3.1 Estimating the stable time increment size

An approximation to the stability limit is often estimated as the smallest transit time of a dilatational wave across any of the elements in the mesh

$$\Delta t \approx \frac{L_{\min}}{c_d} \tag{3-12}$$

where $L_{\min}$ is the smallest element dimension in the mesh and c_d is the dilatational wave speed, which can be computed by density ρ and effective Lames constants $\tilde{\lambda}$, $\tilde{\mu}$, $c_d = \sqrt{\frac{\tilde{\lambda} + 2\tilde{\mu}}{\rho}}$.

This estimation for Δt is only approximate and in most cases is not a conservative estimation. In general, the actual stable time increment chosen by Abaqus/Explicit will be less than this estimation by a factor between $1/\sqrt{2}$ and 1 in a two-dimensional model and between $1/\sqrt{3}$ and 1 in a three-dimensional model. The time increment chosen by Abaqus/Explicit also accounts for any stiffness behaviour in a model associated with penalty contact. Besides, the stable time increment size is also estimated from the convective velocity c_i, the relative motion between the material and the mesh that occurs in ALE formulation (Rodriguez-Ferran et al., 1998).

The time increment used in an analysis must be smaller than the stability limit of the central-difference operator. Failure to use a small enough time increment will result in an unstable solution. When the solution becomes unstable, the time history response of solution variables, such as displacement, strain, stress etc, will usually oscillate with increasing amplitudes. The total energy balance will also change significantly.

To reduce the chance of a solution going unstable, the time increment can be adjusted by specifying a constant scaling factor in the program Abaqus/Explicit (SIMULIA 2008).

This factor can be used to scale the default global time estimate, the element-by-element estimate, or the fixed time increment based on the initial element-by-element estimate, which will be introduced in the following section; however it cannot be used to scale a fixed time increment specified directly by the user.

3.3.3.2 Automatic time increment estimation

The default estimation scheme for time stability limit of the explicit operator in Abaqus/Explicit is fully automatic and requires no user intervention. Two types of estimation are used to determine the stability limit: element by element and global. An analysis always starts by using the global estimation and may switch to the element-by-element or other ones under certain circumstances, as explained below.

(1) Element-by-element estimation

The element-by-element estimator determines the time stability limit using the current dilatational wave speed in each element. Since the element-by-element estimation algorithm determines the maximum frequency of elements, it is conservative and will give a smaller time increment than the true stability limit that is based upon the maximum frequency of the entire model. In general, constraints such as boundary conditions and kinematic contact have the effect of compressing the eigenvalue spectrum, and the element-by-element estimation do not take this into account.

The concept of the stable time increment as the time required to propagate a dilatational wave across the smallest element dimension is useful for interpreting how the explicit

procedure chooses the time increment when element-by-element stability estimation controls the time increment.

(2) Global estimation

In a dynamic analysis of Abaqus/Explicit, the explicit operator initially uses the global estimation to determine a stability limit based on the maximum frequency of the entire model using the current dilatational wave speed. And this stability limit estimation scheme will remain as the step proceeds unless the element-by-element estimation is employed, or a fixed time increment is specified. The use of global estimation will be prevented when any of the following capabilities are included in the model: thick shells (thickness to characteristic length ratio larger than 0.92), material damping, distortion control and adaptive meshing. The use of rigid bodies and elements that are part of a rigid body does not affect the global time increment. The global estimator will usually allow time increments that exceed the element-by-element values.

A fixed time increment scheme is available in the program using a user-specified time increment which will be kept constant through the whole analysis.

3.3.4 Comparison of the ALE in Abaqus/Explicit and Abaqus/Standard

Both the program Abaqus/Explicit (with an explicit scheme) and Abaqus/Standard (with an implicit scheme) support the ALE technique. The capability and function between them are different. To indicate one of the reasons for choosing Abaqus/Explicit rather than Abaqus/Standard to simulate the silo discharge process, a comparison of ALE

technique between them has been made. The ALE technique in Abaqus/Explicit is generally more robust and can provide better features for controlling the mesh than the ALE in Abaqus/Standard. The ALE technique in Abaqus/Explicit is able to create an entirely Eulerian model, to improve the quality of the mesh initially before deformation begins, and to define tracer particles which enable tracking and output of material-based solution quantities while the ALE technique in Abaqus/Standard provides limited functions mainly for structural acoustic analyses and the modelling of ablation processes, which are not relevant to the present study. A comparison of the capability and function of ALE in Abaqus/Explicit and Abaqus/Standard is made and summarised in Table 3-1 (SIMULIA 2008).

Table 3-1 Comparison of ALE between Explicit and Standard

Capability and function	Abaqus/Explicit	Abaqus/Standard
Large-deformation problem	Yes	No
Remeshing	Laplacian, Mid-area, Equipotential, or combined approach	Laplacian
Description of flow problem	Lagrangian and Eulerian formulation	Lagrangian formulation
Post processing	Tracking and output of material-based solution quantities	No tracking

It is clearly seen that Abaqus/Explicit is the better choice to simulate the dynamic phenomenon during silo discharge, which is the focus of this thesis.

3.4 Numerical implementation issues

3.4.1 Modelling the initial state

In the present study, each numerical computation consists of two steps. The first step is to simulate the end of filling condition (termed the initial state) and the second one is to model the discharge (termed flow state) in a silo. An accurate description of the filling pressure in a silo is a necessary precursor for the study of the discharge process. The 'layer-by-layer' progressive loading of gravity was used to simulate the filling process (Ai et al., 2010). For each layer, the gravitational load was applied in a smooth manner which will be presented later, in order to avoid sudden and jerky movement. To perform stress/displacement filling analysis, there are two options in Abaqus. One is the static stress analysis in Abaqus/Standard, which uses Newton's method to solve nonlinear equilibrium equations and it is an implicit procedure. The other one is the dynamic analysis in Abaqus/Explicit, which uses the central-difference operator and it is an explicit procedure. In the present study, the dynamic analysis in Abaqus/Explicit was used for the filling process. The main reason for choosing Abaqus/Explicit rather than Abaqus/Standard in modelling filling process is the numerical convergence difficulty that can arise when the 'IMPORT' technique is used.

The 'IMPORT' technique is used to connect the filling computation to the discharge computation by importing the deformed mesh and its associated material state from the static stress analysis in Abaqus/Standard to the dynamic stress analysis in Abaqus/Explicit. Due to the constraint of element type in the 'IMPORT' technique, the

reduced integration element to be used in the explicit dynamic analysis must be adopted in the static analysis, which may lead to numerical discontinuity because of large principal stresses at the early stage of material deformation (Zienkievicz, 1977, Bjorkman, 2007; Dodds, 1982). The numerical exercises performed have also shown that convergence difficulty was frequently encountered when the implicit scheme was employed in Abaqus/Standard. As a result, it was decided that the dynamic analysis with explicit scheme would be employed to simulate both the silo filling and the silo discharge simulations.

To secure an accurate result for the initial state in simulation, a comparison of the stress state after filling process was made between using the implicit scheme and the explicit scheme. Fig. 3-5 shows the time history of wall normal pressure at a typical point during one-layer filling in an example hopper. Also, a comparison of normal pressure distribution along the hopper walls is made and shown in Fig. 3-6. The filling pressure distribution predicted by the explicit scheme is almost identical to those by the implicit scheme, which validates the use of the explicit scheme in simulating the filling process or the initial state.

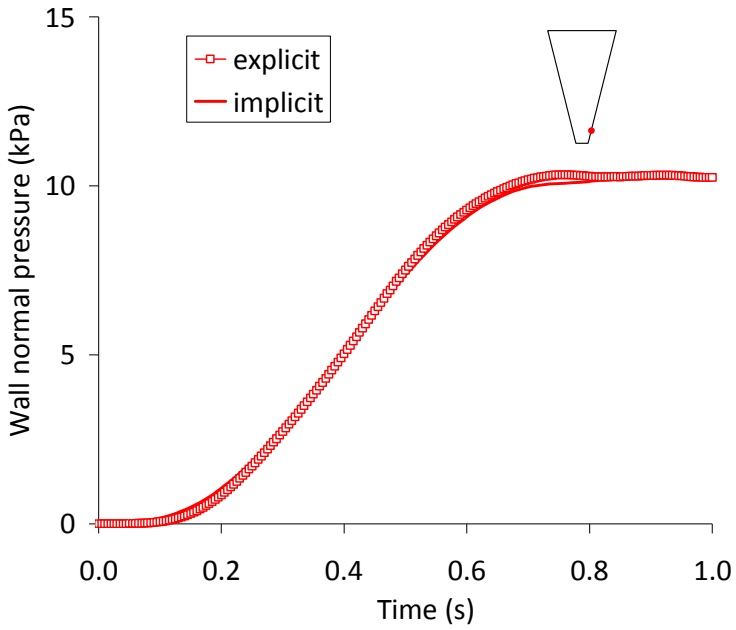

Fig. 3-5 Time histories of wall normal pressure at a typical point during filling using the explicit and implicit scheme

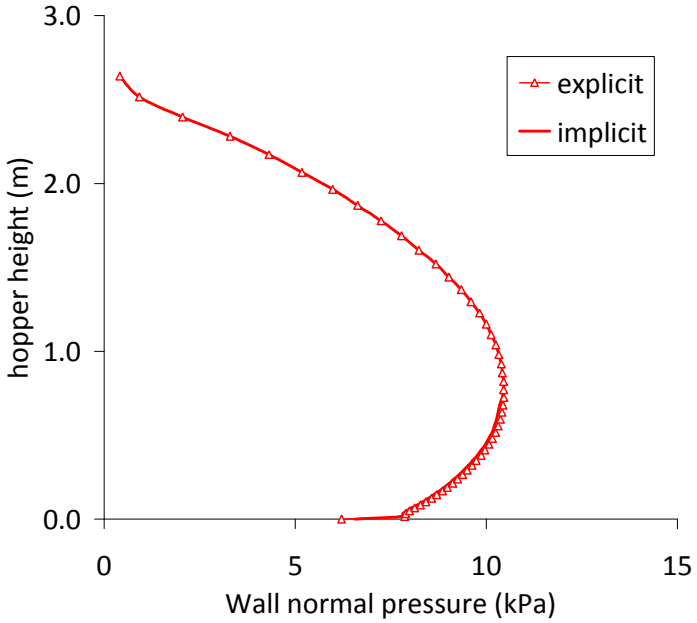

Fig. 3-6 Wall normal pressure distributions after filling process using the explicit and implicit schemes

3.4.2 Numerical convergence study

As discussed in Section 3.3, the element-by-element estimation algorithm was adopted to determine the time increment in simulations and a scale factor was used to scale the time step size in order to secure a satisfactory numerical convergence (SIMULIA 2008). The scale factor was set as 1.0 initially by default. Smaller values of the scale factor were used to compare and to obtain an accurate prediction of the pressures in a silo with the explicit scheme. Fig. 3-7 shows the normal pressure distributions along the hopper wall at a certain time point during discharge using various scale factors. Through this figure, the numerical results tended to be stable as the scale factor decreased.

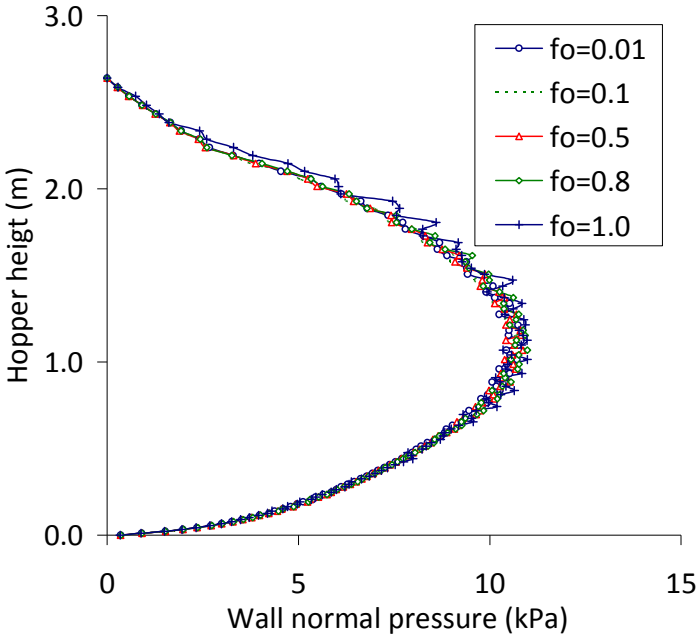

Fig. 3-7 Wall normal pressure distributions using various scale factors to control the time step size

A further exploration of convergence of the numerical solution was made by calculating the representative deviation as follow:

$$S_0 = \sqrt{\frac{1}{N}\sum_{i=1}^{N}\left(\frac{P_i - P_{i0}}{P_{i0}}\right)^2} \tag{3-13}$$

where P_i is the predicted wall normal pressure at point *i* at a certain time point during discharge with a specified scale factor, P_{i0} is the wall normal pressure at point *i* predicted with the scale factor of 0.01, assuming that it is the most accurate prediction. S_0 denotes the representative deviation, a estimator of variation of predicted pressure from the most accurate prediction. Calculated results are shown in Table 3-2. Fig. 3-8 shows the representative deviation of predicted pressure as a function of the scale factor. Therefore, it is proved that an excellent convergence of the numerical solution can be achieved by using a scale factor of 0.1 under a time saving scheme with explicit scheme, which will be applied to the FE modelling of hopper discharge in the remainder of this thesis.

Table 3-2 Calculated representative deviations with varying scale factors

Scale factor	0.01	0.1	0.3	0.5	0.8	1.0
Time increment (s)	1.0×10^{-7}	1.0×10^{-6}	4.0×10^{-6}	5.0×10^{-6}	8.0×10^{-6}	1.0×10^{-5}
Deviation, S_0	0	0.01	0.04	0.1	0.4	0.85

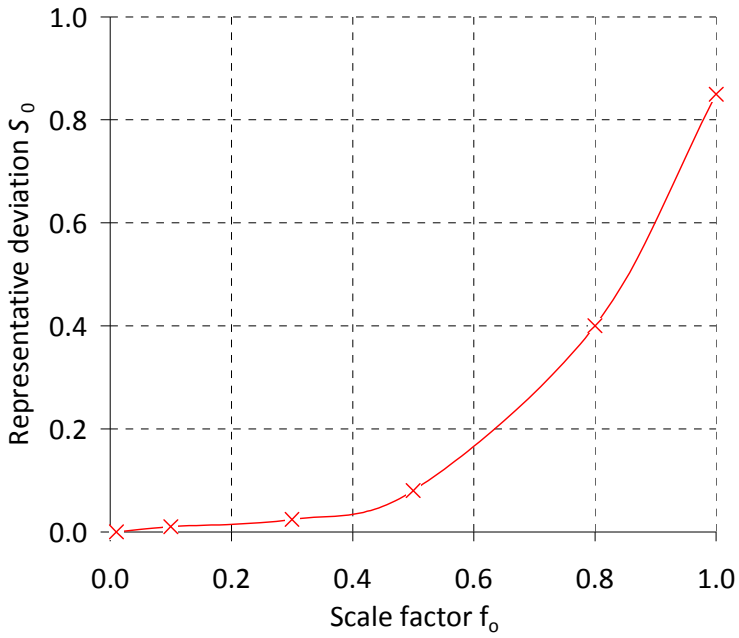

Fig. 3-8 Deviation of wall pressure using various scale factors

3.5 Boundary conditions

By using FE model based on the Arbitrary Lagrangian-Eulerian formulation in the present study, the silo discharge process was model as the material flowing out through the boundary at the outlet while the mesh remained stationary at the bottom boundary of the silo.

3.5.1 ALE boundaries

To simulate the discharge process, the explicit ALE analysis is employed with the adaptive meshing technique. In the ALE, both Lagrangian and Eulerian boundaries were used (SIMULIA 2008). Here, a hopper discharge is used as an example to introduce the ALE boundary definition. The sides of granular solid mass and its top are defined as

Lagrangian boundaries such that the granular solid mass can slide along the walls and the top mesh can flow together with the material during discharge. However the hopper outlet has an Eulerian boundary. The outlet nodes of the Eulerian boundary are constrained vertically so that the mesh cannot drop out of the hopper. The adaptive meshing technique is used to control mesh distortion and helps to maintain a high-quality mesh throughout the analysis even though large deformation or loss of material occurs. Within the ALE domain, it allows the mesh to move independently of the material. Fig. 3-9 shows the ALE boundary definition and an axisymmetric geometry used for the FE simulation.

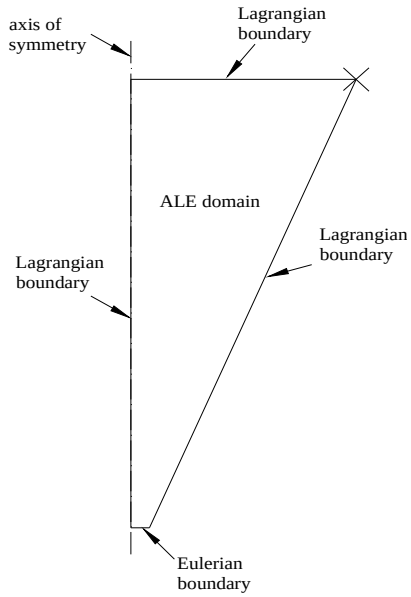

Fig. 3-9 ALE boundaries and an axisymmetric hopper

3.5.2 Outlet boundary condition

Through the outlet, the material stored in the hopper is emptied either freely due to the gravity (free flow) or in a controlled way (controlled flow). These flows are achieved

numerically by the action of a kinematic boundary condition. In the present study, the free flow is firstly modelled by setting the outlet boundary free instantaneously in the beginning of discharge. The evolution of velocity at the outlet with time was predicted and shown in Fig. 3-10. The start of discharge is at total time of 12.0s.

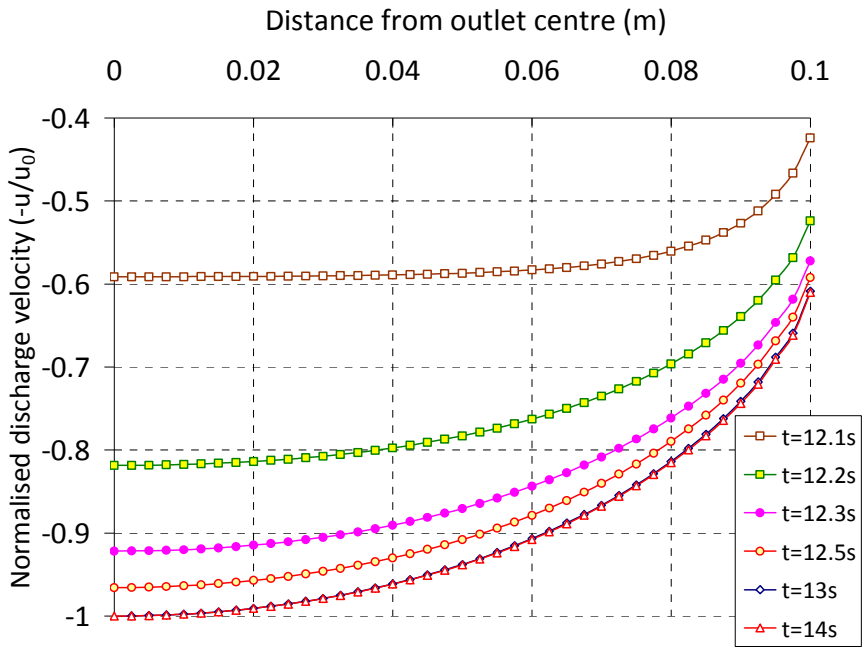

Fig. 3-10 Outflow velocity profile at various time points

To obtain a controlled flow, at the outlet a maximum outflow velocity was specified as a kinematic boundary condition, i.e. starting from zero, the maximum velocity is reached after an opening period of 2.0s. The form of this boundary condition is given in Equation (3-14), and shown in Fig. 3-11.

$$u(t) = \begin{cases} \dfrac{u_0}{2}\left(1 - \cos\dfrac{\pi t}{2}\right) & \text{for } t < 2.0s \\ u_0 & \text{for } t > 2.0s \end{cases} \tag{3-14}$$

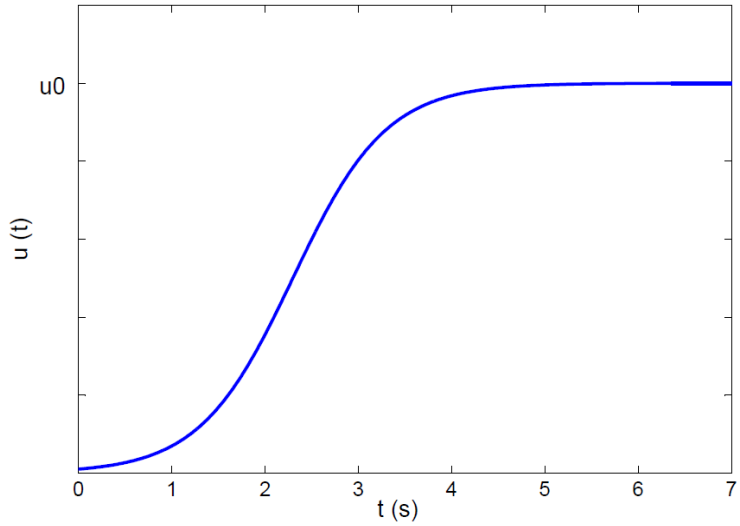

Fig. 3-11: A boundary condition applied to the outlet of hopper

The effect of these outlet boundary conditions on the numerical solution of silo wall pressure will be explored in Chapter 4.

3.6 Solid-wall interaction

An accurate characterization of the interaction between the granular solid and the silo walls is very important for modelling the granular flow and predicting the pressures acting on the walls. In terms of FE modelling, the definition of interaction between the solid and walls plays an important role in the accuracy of results using the explicit scheme. In our simulations contact pair surfaces based on the contact pair contact

algorithm available in Abaqus/Explicit were used to model the interaction between the solid and walls.

In the contact pair contact algorithm, the contact surface properties (including element-based/node-based surface, element type of surfaces), and the contact properties which govern the mechanical behaviour when two surfaces are in contact, such as frictional law and the contact formulation (including constraint enforcement method, master-slave algorithm, and the sliding formulation) have significant influence on the numerical results and must be paid due attention. An appropriate model can well describe the interaction between the solid and the silo wall, which influences the flow pattern, occurrence and location of shear zone within the material near the walls, and the wall pressure distribution during discharge. In the contact pair contact algorithm, the contact surfaces were defined at the beginning of the analysis. The wall side, considered as a non-deformed body, was set as the master surface and the side of granular solid mass was defined as the slave surface. The two surfaces interact with each other throughout the analysis. The contact behaviour at the walls was computed in the normal and tangential direction.

3.6.1 Tangential (frictional) contact behaviour

The contact behaviour in the tangential direction is modelled as the friction at the contact between the solid surface and the wall surface. When the pair surfaces are in contact they transmit shear as well as normal forces across their interface. There is generally a relationship between these two force components. The relationship, known

as the friction between the contacting surfaces, is usually expressed in terms of the stresses at the interface. In the present study, the Coulomb friction model available in Abaqus/Explicit was employed to model the frictional behaviour between the solid surface and the wall surface.

As the basic concept of the Coulomb friction model, the maximum allowable frictional (shear) stress across the interface is related to the normal pressure between the contacting surfaces. There are two states: the sticking and the slipping states as defined in Coulomb friction model, which is divided by a critical shear stress τ_{crit}. In the sticking state there is no relative motion between the contacting surfaces and the shear stress is smaller than the critical shear stress. When the shear stress reaches the critical value, the two contacting surfaces start to slide relative to one another; this state is called sliding. The critical shear stress can be expressed in the form:

$$\tau_{crit} = \mu\sigma_n \tag{3-15}$$

where σ_n is the normal contact pressure; and μ is known as the coefficient of friction. The basic friction model assumes that the coefficient of friction μ is identical in all directions which is known as the isotropic friction.

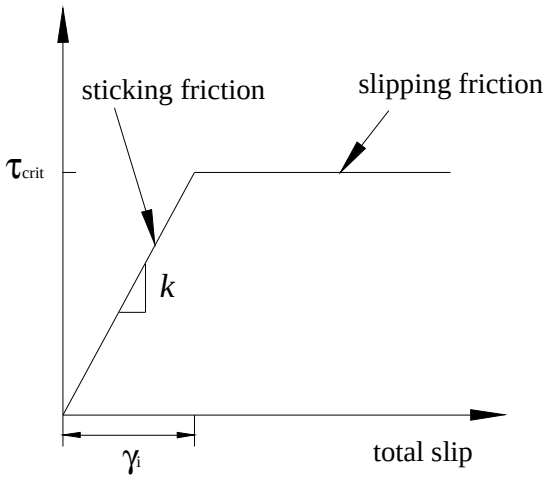

Fig. 3-12 Elastic slip versus shear traction relationship for sticking and slipping friction

In our simulations the so-called ‘penalty method’, based on the basic Coulomb friction model, was used to defined the frictional contact behaviour in Abaqus/Explicit (SIMULIA 2008). The penalty method allows that a small slip may occur even though the friction model determines that the current state is “sticking”. In other words, the slope of the shear stress versus total slip relationship may be finite (equal to *k*) while in the “sticking” state, as shown in Fig. 3-12. This slope is also called ‘friction stiffness’ when the penalty method is used for describing frictional contact behaviour. The friction stiffness is a very important parameter in the friction model with the penalty method, and its determination will be introduced in detail later.

The friction stiffness for frictional contact behaviour is usually determined automatically by the program Abaqus/Explicit and is the same as that used for normal contact behaviour, which will be presented in the following part. Nonetheless, the friction

stiffness can be examined by an allowable elastic slip γ_i as shown in Fig. 3-12. The allowable elastic slip is defined as:

$$\gamma_i = \delta_0 l_i \tag{3-16}$$

where δ_0 is a scale factor with the default value of 0.005 in Abaqus/Explict; l_i is characteristic length, which is closely related to the size of elements of the contacting surface.

Also, Abaqus/Explicit allows the user to specify a factor by which to scale the default friction stiffness. Here, a two-dimensional numerical model consisting of a rectangle sample (2.0m×1.0m) contacting with a base surface is used to investigate the frictional contact behaviour, as shown in Fig. 3-13. The sample was modelled as an elastic body and was broken into two first-order 4-node quadrilateral elements. The base surface was modelled using non-deformable 2-node rigid elements. A series of numerical tests were performed to investigate the effect of several parameters on the frictional contact behaviour when the penalty method in the contact pair contact algorithm was used to model the interaction between the sample and base surface with a constant coefficient of the Coulomb friction. A pressure of 2.0 kPa was applied downwards on the top of the sample. After that, a progressively increasing pressure was imposed on the left side to move the sample onto the rigid surface in the *x* direction. The red dot at the bottom of the sample was set as a reference point where the frictional traction due to the contact with the base surface and its displacement in the *x* direction was measured to investigate the relationship between the frictional traction and the shear displacement. In the

numerical model, the pressure on the top surface was first prescribed in a smooth manner by using the 3rd order built-in load amplitude function in Abaqus/Explicit (SIMULIA 2008) in order to avoid the sudden and jerky effect. Under these boundary and loading conditions, different coefficients of friction and different friction stiffness achieved by means of adjusting the scale factor were used to investigate the frictional contact behaviour in the numerical tests. Fully mobilised friction was reached in each case. The relationship between the frictional traction and shear displacement at the reference point is obtained and shown in Fig. 3-14. As discussed above, until the frictional traction at the reference point increases and overcomes the critical friction which can be obtained by Equation (3-16) with a coefficient of friction, the point starts to move under a constant frictional traction.

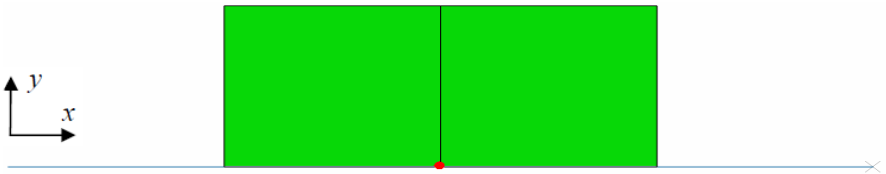

Fig. 3-13 FE mesh of the 2-D model for frictional contact and the reference point

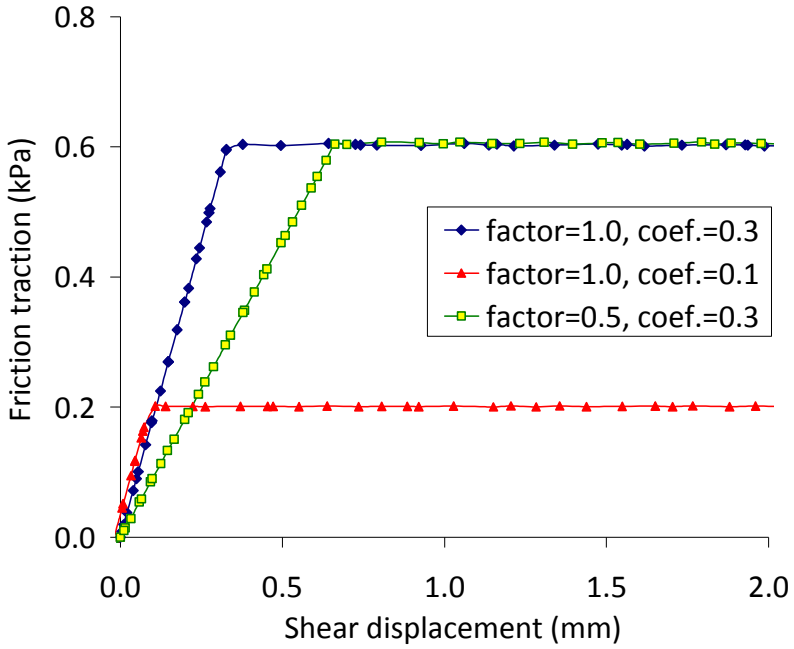

Fig. 3-14: Relationship between frictional pressure and displacement at the reference point with various scale factors of friction stiffness and coefficients of friction

3.6.2 Normal contact behaviour

The contact behaviour in the normal direction is modelled using a penalty function, which is used to constrain the penetration depth between the contacting surfaces (SIMULIA 2008). This penalty function relates the constraint normal force directly to the penetration distance between the contacting surfaces.

Abaqus/Explicit provides two algorithms to define the normal contact behaviour, i.e. kinematic or penalty function. In the numerical exercises, when the default kinematic function was imposed in the normal direction, the running of the programme was interrupted right at the beginning with many warnings issued "For contact pairs that are not tied, too large penetration distance leads to significant mesh distortion…". This is because no penetration is allowed within the kinematic algorithm. But this problem was overcome after replacing the kinematic function by the penalty function.

The use of penalty function results in less stringent normal contact constraints than the kinematic function. The penalty function allows for treatment of more general types of contact. By introducing a "spring" stiffness the penalty function relates the normal contact pressure directly to the penetration distance. The normal stiffness is determined automatically by the program Abaqus/Explicit, such that the effect on the time increment is minimal yet the allowed penetration is not significant in the analyses. Like the stiffness in frictional contact, Abaqus/Explicit allows the user to specify a factor by which to scale the default normal stiffness.

Once again, a simple two-dimensional numerical model consisting of cubic sample (2.0m×2.0m) contacting with a base surface is used to investigate the effect of normal stiffness on the normal contact behaviour as shown in Fig. 3-15. The sample was modelled as an elastic body and was partitioned into four first-order 4-node quadrilateral elements. The base surface was modelled using non-deformable 2-node rigid elements. Two lateral sides of the sample were fixed in the *x* direction but free in the *y* direction, thus, there was no transverse motion. The penalty function was used to describe the

normal contact behaviour between the sample and base surface. A progressively increasing pressure of 20.0 kPa was applied on the top of the sample in a smooth manner by using the 3rd order built-in load amplitude function in Abaqus/Explicit (SIMULIA 2008) in order to avoid the sudden and jerky effect. The red dot at the bottom of the sample was set as a reference point where the reaction pressure due to the contact with the base surface and the penetration distance were measured to investigate the normal stiffness. It has been observed that this reference point had the identical reaction pressure to that of the corresponding point of the base surface. The scale factor of 1.0 is the default normal stiffness used by Abaqus/Explicit. Through these numerical tests, the default normal stiffness was very close to a hundred times the value of elastic stiffness of the material used to describe the sample. The different scale factors for the default normal stiffness were adopted in the numerical simulations and gave a same eventual magnitude but different slopes of reaction pressure to the penetration distance at the reference point, as shown in Fig. 3-16. From this figure, it can be seen that the numerical solution of rarefaction pressure is not sensitive to the stiffness. The penetration distances are relatively small in these simulations and have negligible effect on the numerical solution. This will be further investigated using a hopper example in a later section of this chapter.

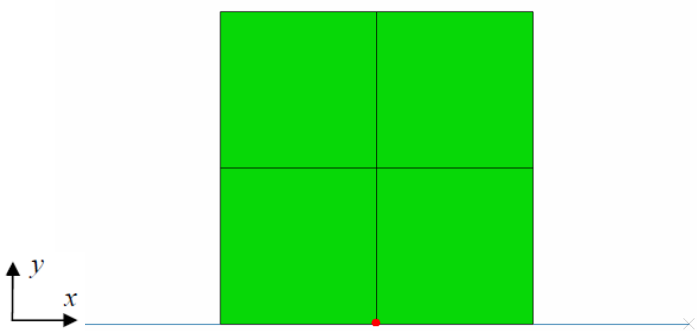

Fig. 3-15 FE mesh of the 2-D model for normal contact and reference point

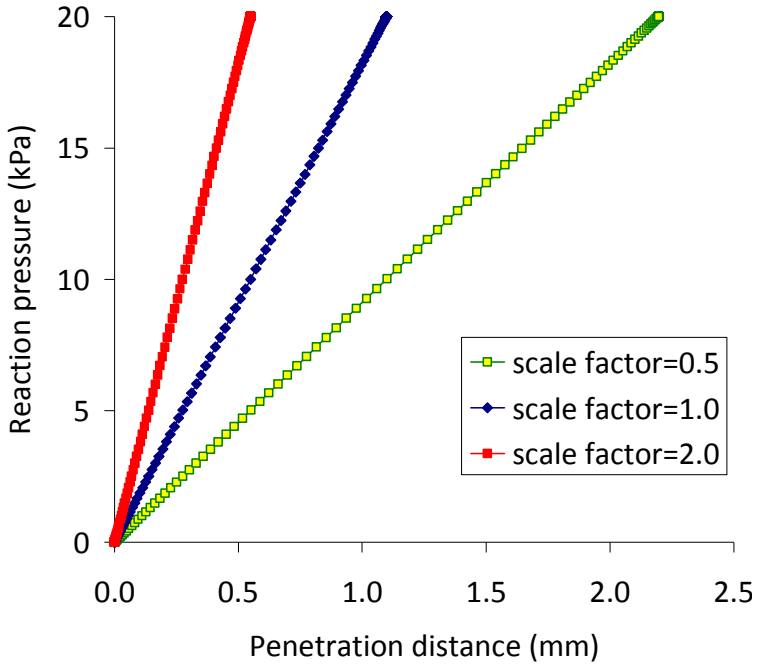

Fig. 3-16 Relationship between reaction pressure and penetration distance at the reference point with various scale factors for normal stiffness

3.6.3 Effect of stiffness on stable time increment

In both frictional and normal contact behaviour, an additional stiffness is introduced into the model when the penalty method is used. The stiffness can affect the stable time increment as the explicit time integration scheme was employed in FE simulations

(SIMULIA 2008). Abaqus/Explicit can automatically account for the effect of the stiffness under the automatic time increment estimation scheme. Usually, this effect is small to the whole numerical analysis.

Since achieving a numerically stable time increment under the explicit scheme is greatly related to the dilatational wave speed directly governed by the stiffness, the penalty method characterized by an additional stiffness will affect the time increment, and moreover, increase the time consumption in the computation. As far as the present numerical analysis of this thesis is concerned, a modification of the frictional stiffness behaviour by changing the allowable elastic slip, or a modification of the stiffness in normal contact behaviour by specifying a scale factor may change the stable time increment significantly. Table 3-3 summarises the relationship between the stiffness used in contact algorithm and the time increment in the explicit analysis.

Table 3-3 Effect of stiffness on time increment

Stiffness scale factor	Percentage of the time increment to that without contact
0.5	130%
1.0	96%
10.0	34%
100.0	13%
1000.0	4%

A larger friction coefficient also leads to a higher computational effort. This is because the program determines the friction stiffness by means of an allowable elastic slip, as

discussed in Section 3.6.1, which is fixed when the size of elements of the contacting surface is fixed. Thus, an increase in the friction coefficient results in an increase in the critical shear stress obeying the Coulomb law at the specified elastic slip limit, resulting in a greater frictional stiffness which may lead to a significant decrease in time increment (larger computational effort).

3.7 A numerical example of hopper

To verify the FE model using ALE formulation, a numerical example of hopper discharge was used in this section. An axisymmetric geometry with a height of 2.64 m and an outlet of 0.1 m in radius was employed (see Fig. 3-9). The granular solid stored was modelled as an elastic-perfectly plastic material with the well-known Drucker-Prager failure criterion. The interaction between the solid and walls was modelled using contact pair surfaces which implement a penalty function to constrain the penetration distance. Friction at the contact was modelled using the penalty method based on the Coulomb model with a constant coefficient of 0.3. The details about the contact surface have been presented in Section 3.6 of this chapter. The granular solids in the hopper were broken into a mesh consisting of 15 and 50 elements (first-order 4-node quadrilateral elements with reduced integrations) in radial and axial direction respectively; and the hopper wall was considered as rigid with 50 two-node rigid elements. A finer mesh was also presented in this example for comparison. The initial state for the filling process was modelled following the procedure presented in Section 3.4.1. The sides of granular solid mass and its top were defined as Lagrangian boundaries and the hopper outlet had an Eulerian boundary. The outlet nodes of the

Eulerian boundary were constrained vertically. The free flow was applied in this example by setting the outlet boundary free instantaneously in the beginning of discharge. The details about the boundary conditions can be found in Section 3.5.

3.7.1 Optimal ALE mesh

As the ALE approach is applied in modelling of hopper discharge, mesh result shows a significant progress in solving mesh distortion problem when large deformation occurs.

The resulting deformed meshes at different stages of hopper discharge computation are shown in Fig. 3-17. Two quantities were measured: one is the vertical falling distance of the central point of solid top surface d_t, the other is the aspect ratio of the critical element which is located at the centre of hopper bottom. The aspect ratio of the critical element is determined by dividing its vertical size by its horizontal size at each deformation stage.

A qualitative assessment of the mesh quality can be made by investigating the evolution of element configuration near the outlet during the hopper discharge. For the filling process, there was no difference observed in the element deformation between the traditional analysis with Lagrangian formulation (without ALE) and the analysis with ALE formulation. For the discharge computation, severe distortion in elements was found near the outlet even at very early stage of discharge when using the Lagrangian formulation, while the elements remain regular with a high-quality mesh when the analysis with ALE formulation was used even after a long period of discharge. The results of analysis with the coarse and fine mesh using the Lagrangian and ALE formulation are respectively shown in Fig. 3-17.

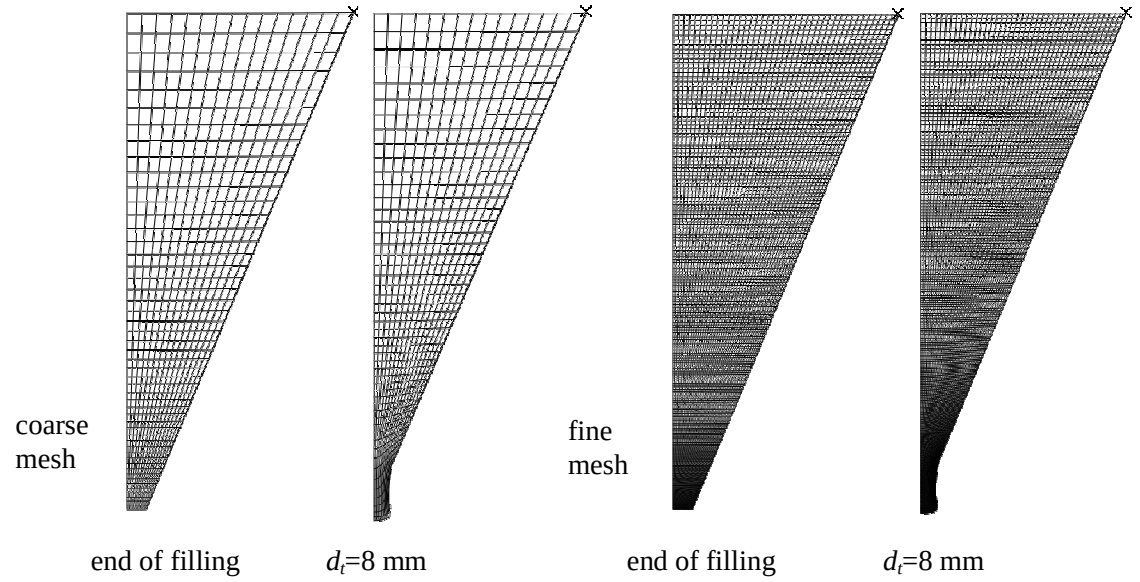

(a)

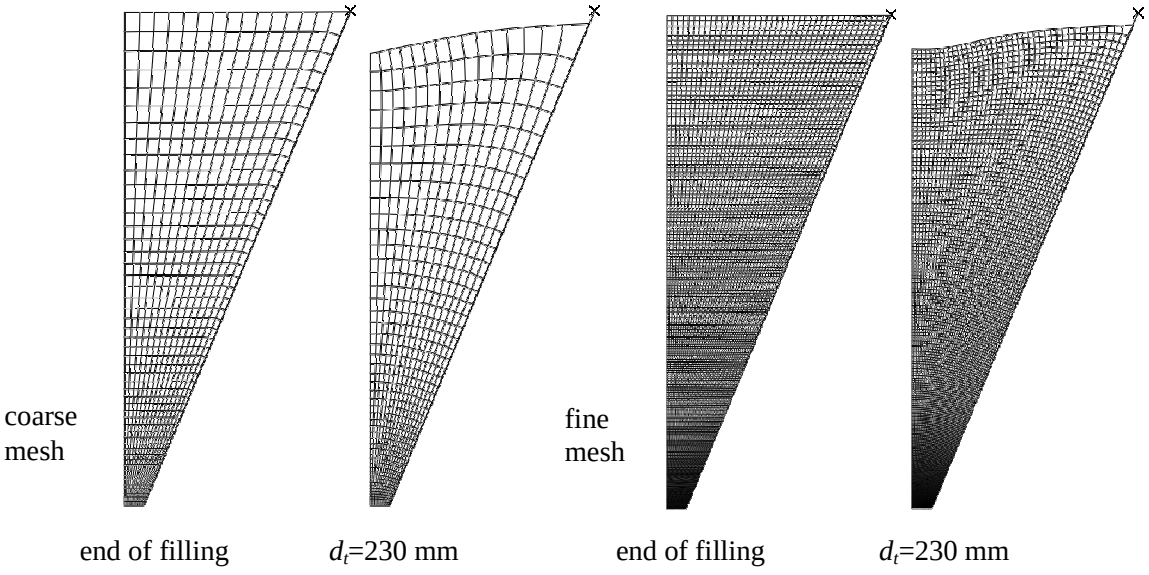

(b)

Fig. 3-17 Evolution of deformed mesh versus top-surface vertical displacement with and without ALE adaptive mesh technique: (a) without ALE; (b) with ALE

A quantitative comparison of mesh quality in the analyses with and without the ALE formulation is shown in Fig. 3-18, which shows the evolution of aspect ratio of the critical element as a function of the falling distance of the central point of solid top surface d_t during discharge. From Fig. 3-18, it is seen that for the Lagrangian formulation, the critical element rapidly became severely distorted with an aspect ratio reaching 7 resulting in the numerical computation being suspended at a falling distance of about 25 mm at the top surface. This problem was not solved even in the computation with a fine mesh. In contrast, the computation with the ALE formulation was performed normally with a high-quality mesh such that almost the entire discharge process can be simulated. The aspect ratio of the critical element remained constant during the discharge analysis and there was no significant difference between the coarse mesh and the fine mesh.

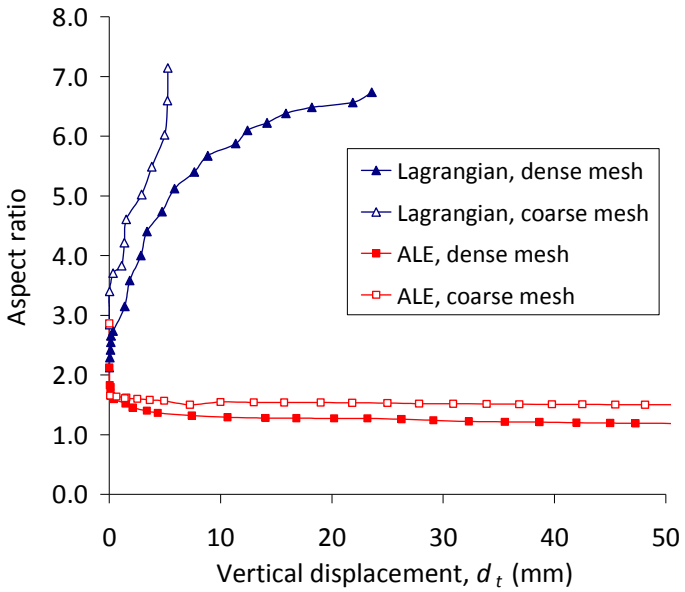

Fig. 3-18 Aspect ratio of the critical element versus top-surface vertical displacement

3.7.2 Sensitivity of bulk viscosity

In this numerical example, the linear bulk viscosity pressure and quadratic bulk viscosity pressure were generated by setting two damping coefficients to be 0.06 and 1.2, respectively, as a reference case (SIMULIA 2008), which are not included in the material point stresses and used to control high frequency oscillations. Two different values of those damping coefficients were also adopted to compare with the reference case. Fig. 3-19 shows wall normal pressure distributions along the hopper walls using different bulk viscosity parameters. Through this figure, it can be seen that the solution is not sensitive to the bulk viscosity parameters for both filling and discharge pressures.

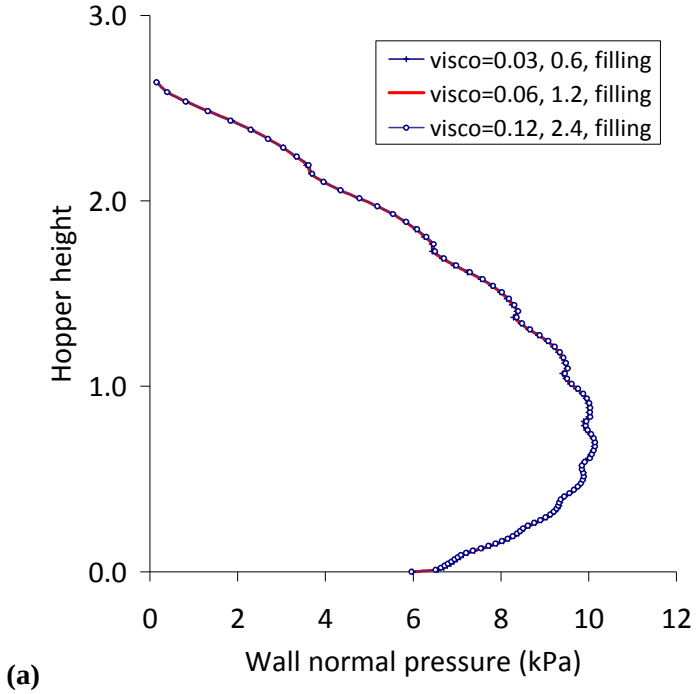

(a)

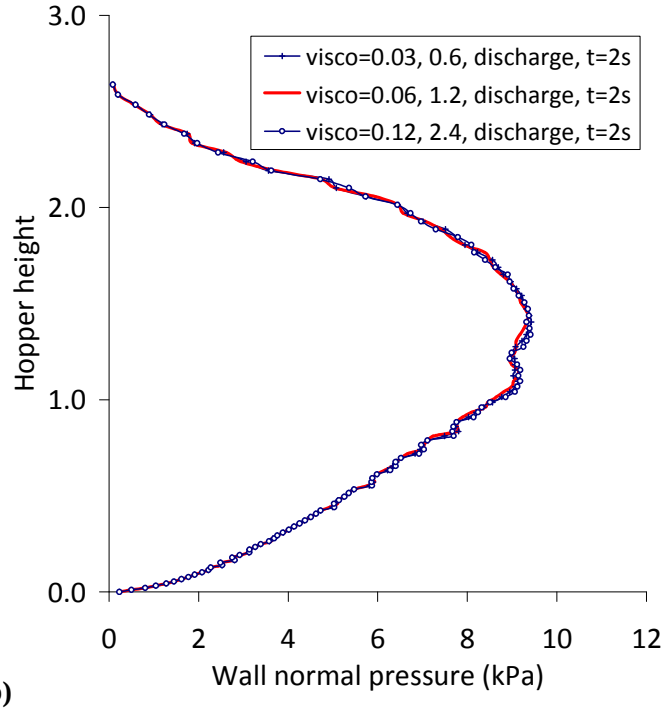

(b)

Fig. 3-19 Wall normal pressure using different damping coefficients: (a) end of filling; (b) discharge at t=2s

3.7.3 Sensitivity of normal stiffness

As described in Section 3.6.3, the penetration has an inverse relationship with the normal stiffness when the penalty function was used to model normal contact behaviour. To investigate its sensitivity to the numerical solution, different scale factors for the normal stiffness were adopted in this example. Fig. 3-20 shows the wall normal pressures using different scale factors for normal stiffness in penalty function. It shows that there is no difference in the wall pressure between these normal stiffnesses. It implies that the numerical solution is not sensitive to the penetration between the solid and hopper walls in the present FE model.

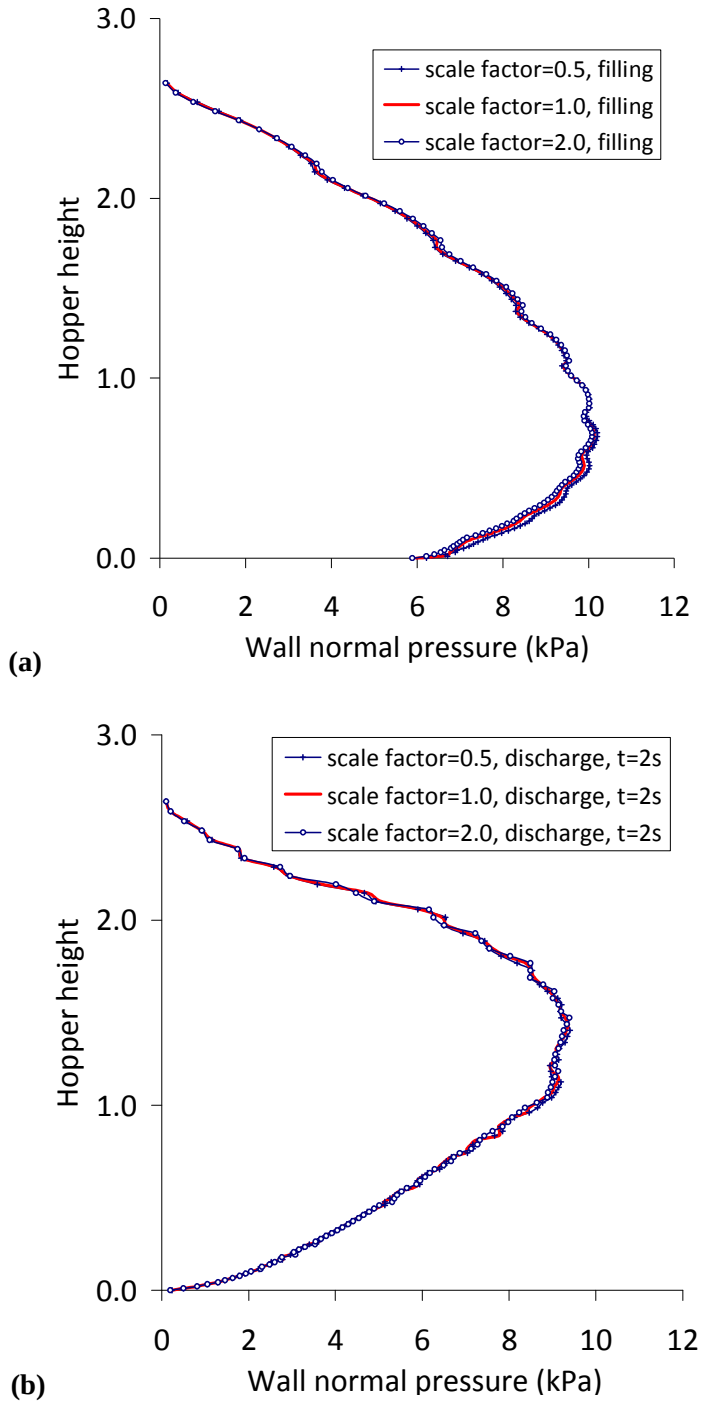

Fig. 3-20 Wall normal pressure using different scale factors for normal stiffness in penalty function: (a) end of filling; (b) discharge at t=2s

3.8 Concluding remarks

In this chapter, much effort has been made to explore and optimise the use of the Arbitrary Lagrangian-Eulerian formulation in Abaqus to model silo discharge.

In order to overcome the shortcomings of the purely Lagrangian formulation and the purely Eulerian one, the Arbitrary Lagrangian-Eulerian formulation has been developed to model continuum mechanic problems involving large deformation. The ALE technique was applied by performing a splitting operator to separate the Lagrangian phase from the Eulerian phase bridging by a smooth phase. The ALE governing equation was obtained by substituting the relationship between the material time derivative and the grid time derivative into the governing equations of continuum mechanics. The analysis was carried out according to the Lagrangian phase at each time step until the required convergence is achieved. The smoothing phase was then applied to keep the mesh configuration regular. In Eulerian phase, the variables of the solution obtained by the Lagrangian phase onto the newly relocated mesh are remapped. Special care has been taken with respect to fundamental mathematical background to the ALE formulation, including kinematics, dynamic analysis, smoothing scheme and stress update. These efforts can help understand the finite element analysis on silo discharge using the ALE method in the present study.

The dynamic analysis in Abaqus/Explicit has proved to be able to model the initial filling state in a silo, instead of using the static stress analysis in Abaqus/Standard. This dynamic analysis uses the central-difference operator and is an explicit procedure. To

avoid sudden and jerky movements, the load of gravity was applied in a smooth manner by using the 3rd order built-in load amplitude function in the Abaqus programme. To ensure the accuracy of the calculation, the kinetic energy, internal energy, final displacements and stress distributions at the end of the analysis were investigated. These indicated a stable converged numerical solution was obtained.

Two outlet boundary conditions were used to model the silo discharge. One is the boundary condition for a gravitationally free flow, which was firstly simulated by setting the outlet boundary free instantaneously in the beginning of discharge. The other one is the boundary condition for a controlled flow, which was achieved by accelerating the boundary downwards until it reached a specified velocity profile. Both of them will be explored further in the FE simulations in the next chapter.

The interaction between the stored solid and the silo walls was modelled using contact surfaces which implement a penalty function to constrain the penetration depth. This penalty function relates the constraint normal pressure directly to the penetration distance. Friction at the contact was modelled using the Coulomb frictional model with a constant coefficient of friction.

Finally, the advantage of the ALE technique was demonstrated through a numerical example of hopper discharge which was compared with those of the more traditional FE method.

Chapter 4

Numerical calculations of dynamic pressure during hopper discharge using the ALE formulation

4.1 Introduction

Silos are widely used for the storage of bulk solid in industry. In the design of silos, the pressure acting on the silo walls during filling and discharge are the main loads that need to be determined for design. Silo pressure during filling and storing are generally accepted to be well represented by Janssen type pressure equation (Janssen, 1895). However during discharge, the silo pressure tends to exhibit time and space variations and more work is needed to define the discharge pressure more accurately. With the general lack of understanding and information with regard to discharge pressure, most national standards have defined discharge pressure for symmetrical silos simply using a multiplication factor applied to the filling pressure based on Janssen's theory and its improvement in different ways by other authors (Rotter, 2001). There is strong evidence in silo experiments (Hartlen et al., 1984; Ooi et al, 1990; Brown et al., 1996; Robert, 1996; Ramirez et al., 2010) that silo pressure during discharge can be quite different from pressure during filling, so more work is needed in this area.

Whilst FE predictions (Ooi and Rotter, 1990; Goodey et al, 2003; Goodey, 2006; Chen et al., 2010) of wall pressures at the end of filling stage are in good agreement with both

theoretical results and experimental results, the FE modelling of the wall pressures during discharge are relatively rare and requires more fundamental research. Rombach and Eibl (1998) performed a dynamic finite element analysis and presented dynamic pressures profiles dependent on space and time just at the beginning of the emptying stage. In other studies, either remesh-rezoning technique or assumed failure boundary was used to describe large deformation occurring during the discharge stage in order to avoid mesh distortions (Martinez et al., 2002; Vidal et al., 2005).

The present study describes results of a finite element (FE) simulation for a conical hopper discharge, which was carried out using an Arbitrary Lagrangian-Eulerian (ALE, in short) formulation with an explicit time integration scheme. The method is able to simulate almost the entire silo discharge process without mesh distortion problem which are often encountered in the modelling of granular flow involving very large deformation such as silo discharge (Tejchman and Gudehus, 1993; Martinez et al., 2002). The dynamic events predicted by the present FE simulation were studied to provide further insight into the fluctuating pressure patterns often observed in silo discharge experiments. Temporally averaged discharge pressures are compared with analytical solutions. The oscillating discharge pressures were found to be dominated by two major frequencies at about 5 Hz and at less than 1 Hz, respectively, for the particular case under consideration. The causes for these events have been investigated which lead to the conclusion that the stress wave and moving shear zone phenomena are responsible for these effects.

4.2 FE modelling implementation

4.2.1 Geometry and contents

A conical hopper with an axisymmetrical geometry is considered in the present FE simulation (see Fig. 4-1). The height of the hopper h_0 is 2.64 m, radius at the top 1.2 m, radius at the bottom 0.1 m and apex half angle $\alpha = 22^o$.

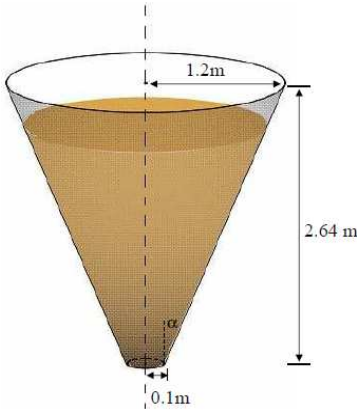

Fig. 4-1 Geometry of the model hopper

In the FE simulations, the stored granular solid was modelled with a linear elastic-perfectly plastic stress-strain relationship using a linear Drucker-Prager failure criterion (SIMULIA 2008). The stored material within the hopper was broken into a fine mesh of 8000 first-order 4-node quadrilateral elements with reduced integrations (see Fig. 4-2). The walls were modelled using 100 non-deformable 2-node rigid elements, and their interactions with granular solids were modelled using Mohr-Coulomb type contact with a constant coefficient of wall friction.

In the present FE simulation, material properties were chosen so that they represent a material that is widely used in FE modelling of silo discharge by other researchers (Ayuga et al., 2001; Martinez et al., 2002; Wang et al., 2012). Typical material parameters used are presented in Table 4-1.

Table 4-1 Material parameters

Bulk density (ρ_b)	1000 kg/m3
Young's modulus (E)	5.5e5 Pa
Poisson's ratio (ν)	0.3
Internal angle of friction (ϕ_i)	30º
Dilation angle (ψ)	10º
Coefficient of solid-wall friction	0.267

To avoid mesh distortion during initialisation and flow, the FE simulations were performed based on the so-called uncoupled Arbitrary Lagrangian-Eulerian (ALE) formulation (Donea and Huerta, 2003) using the adaptive meshing technique in the program Abaqus/Explict (SIMULIA 2008). A non-linear dynamic analysis was performed using an explicit time integration scheme. To obtain a stable solution, the time increment was of order 1×10^{-6}. The geometric non-linearity was taken into account. In order to limit numerical oscillations, linear bulk viscosity and quadratic bulk viscosity coefficients were set as 0.06 and 1.2, respectively, which were not included in the material point stress (SIMULIA 2008). In the ALE, both Lagrangian and Eulerian boundaries were used. The sides and top surface of the material were defined as Lagrangian boundaries while the base (outlet) was set to be an Eulerian boundary (see

Fig. 4-2). An adaptive meshing technique was used to control mesh distortion and helps to maintain a high-quality mesh throughout the analyses even though large deformation occurs. This same methodology has previously been successfully applied to the numerical analysis of silo behaviour (Yang et al., 2011; Wojcik and Tejchman, 2009; Wang et al., 2012).

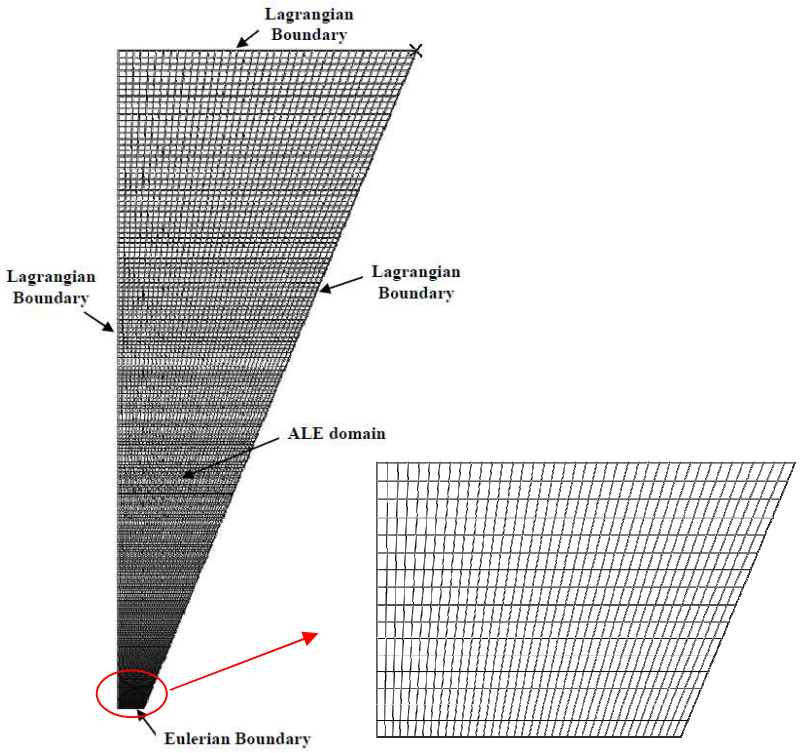

Fig. 4-2 Discretization grid and ALE boundaries

4.2.2 Flowing boundary at the outlet

The end of filling state in the hopper was modelled by discretizing the final geometry of the solid fill into ten layers and then activating each layer sequentially in the FE analysis starting from the bottom layer. The numerical process involved achieving equilibrium for each activated layer under gravitational loading before the next layer was laid on

with a “stress free” state, thereby simulating the progressive filling process (Ai et al., 2011). It was assumed that the top surface of the solid is at the top of the hopper.

To simulate the discharge process, a gravitational free flow was firstly considered by removing the constraints at the hopper outlet instantaneously. The numerical outcome displayed in Fig. 4-3 shows that the discharge velocity u_{dis} increased rapidly and then reached a constant level u_0 at $t=t_f$. For the purpose of comparison, discharge under a controlled flow was also simulated. This was numerically achieved by accelerating the boundary downwards until it reached a specified velocity which was then kept constant after $t=t_0$. t_0 was usually set to a longer value than t_f in the free flow, here, $t_0=2t_f$. A series of constant velocities ($u_{dis}=u_0$, $1/2u_0$, $1/4u_0$, $1/10u_0$, $1/100u_0$) for the controlled flow were taken into account in the present FE simulations, as shown in Fig. 4-3.

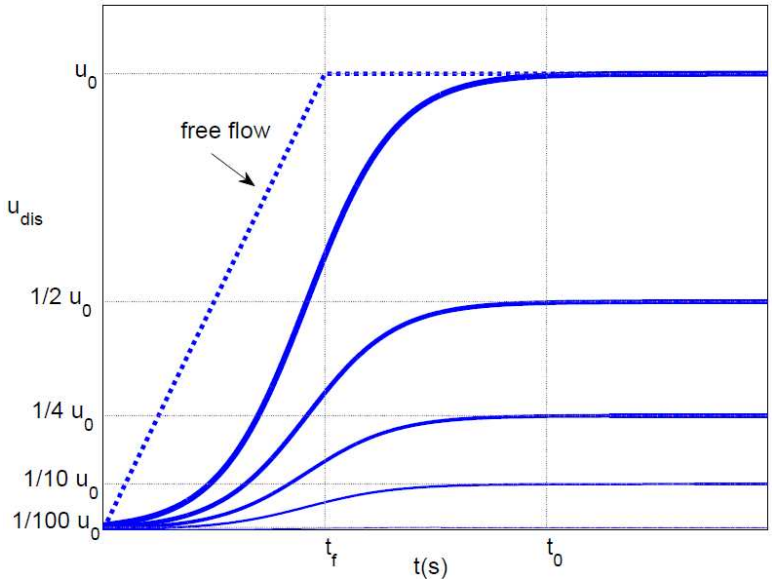

Fig. 4-3 Time history of discharge velocity at the central node

4.3 Introduction to existing theories

4.3.1 Classical hopper pressure theories

The determination of pressure acting on the silo wall is a well-known problem that has long been studied since Janssen (1895) first proposed the analytical solution of the differential equation corresponding to the vertical equilibrium in a horizontal solid slice in a cylindrical silo. Due to its simplicity, Janssen's method has been adopted as a theoretical basis in most national standards. As far as discharge is considered, Eurocode 1 (EN 1991-4: 2006) evaluates the discharge pressures by applying equations based on the Walker's theory (1966). The Walker's (1966) and McLean's (1985) methods are appropriate to use to compare with the present FE simulations for a conical hopper discharge.

Walker improved Janssen's analysis to determine silo pressure in the cylindrical part by considering in greater detail the actual stress distribution in the wall region, and extended it to the case of conical hoppers. Using the slice element method, Walker gave the solution to the pressure acting on the wall as:

$$p_{nw} = (\sigma_{hh})_w \frac{1+\sin\phi\cos(\omega+\phi_w)}{1-\sin\phi\cos(\omega+\phi_w+2\alpha)} \tag{4-1}$$

in which

$$(\sigma_{hh})_w = \frac{\gamma h'}{m-1}[1-(\frac{h'}{h_a})^{m-1}] + Q_0(\frac{h'}{h_a})^m \tag{4-2}$$

$$m = \frac{2\sin\phi\sin(\omega+\kappa\phi_w+2\kappa\alpha)}{\tan\alpha\{1-\kappa\sin\phi\cos(\omega+\kappa\phi_w+2\kappa\alpha)\}} \tag{4-3}$$

where Q_0 is the uniform surcharge acting on the top surface of the stored solid; in the case under consideration there is no applied stress on the top surface of the fill and so $(\sigma_{hh}) = Q_0 = 0$; p_{nw} is the wall normal pressure; h' is the height of material measured vertically from the apex of hopper; h_a is the maximum of h' in the hopper. ϕ is the effective angle of internal friction of the bulk solid, ϕ_w is the hopper wall friction angle, and γ is specific weight of the stored solid. κ is a constant and $\kappa = -1$ is for filling and storing case, and $\kappa = 1$ for discharge case (Nedderman, 1992).

Based on the Jenike and Johanson's (1968) radial stress field solution, McLean (1985) recommended that a value of the parameter m in Equation (4-3) should be deduced as

$$m = \frac{2\mu_w}{\tan\alpha} \tag{4-4}$$

where μ_w is the coefficient of wall friction.

4.3.2 Empirical equation of flow rate

There exists a great deal of prediction methods of mass flow rate for silo discharge. Now we can say that the mass flow rate depends on material bulk density ρ_b, particle size of material d, acceleration due to gravity g, orifice diameter of the container D_0, and coefficient of wall friction μ_w, as follows

$$W = f(\rho_b, g, D_0, \mu_w, d) \tag{4-5}$$

Beverloo et al. (1961) plotted their experimental results in the form $W^{2/5}$ *vs* D_0 and proposed a prediction formula, as follows

$$W = C\rho_b\sqrt{g}(D_0 - \lambda d)^{5/2} \tag{4-6}$$

where C is deemed to be slightly dependent on μ_w and takes a value close to 0.58. A large value of 0.64 should be given to exceptionally smooth particles such as spherical glass beads. The parameter λ is about 1.5 for spherical particles but takes somewhat larger values for angular particles (Nedderman, 1992). Particle size d takes the value of zero in the present numerical simulation.

Beverloo's prediction is applicable only for cylindrical bunkers and funnel flow hoppers. In mass flow conical hopper, the effect of the apex half-angle α becomes important.

Nedderman (1992) extended Beverloo's formula by incorporating the statement given by Rose and Tanaka (1956) for mass flow conical hopper

$$W = W_B F(\alpha, \phi_d) \tag{4-7}$$

where W_B is the mass flow rate predicted from the Beverloo's formula as given in Equation (4-6), ϕ_d is the angle between the stagnant zone boundary and the horizontal, and $F(\alpha, \phi_d)$ is given by

$$F(\alpha, \phi_d) = (\tan\alpha \tan\phi_d)^{-0.35} \quad \text{for } \alpha < 90^0 - \phi_d$$

$$F = 1 \quad \text{for } \alpha > 90^0 - \phi_d \tag{4-8}$$

4.4 FE results

4.4.1 Transient phenomena in the beginning of discharge

The present FE analysis simulated a total time of 72s for the granular solid handling process. The period for filling was from 0s to 10s, and a storage period of 2s was set prior to the start of the discharge process. The discharge process was simulated from t=12s to t=72s with a period of 60s.

In the beginning of discharge, there exists an initial stage (Ostendorf et al., 2003) when the transient phenomenon occurs. As the outlet of the hopper was opened, granular flow developed. The developing discharge velocity over time is as shown in Fig. 4-4. A stable

discharge velocity profile (u_0≈1.0 m/s) tended to be reached at t=14s, about 2s after the start of discharge.

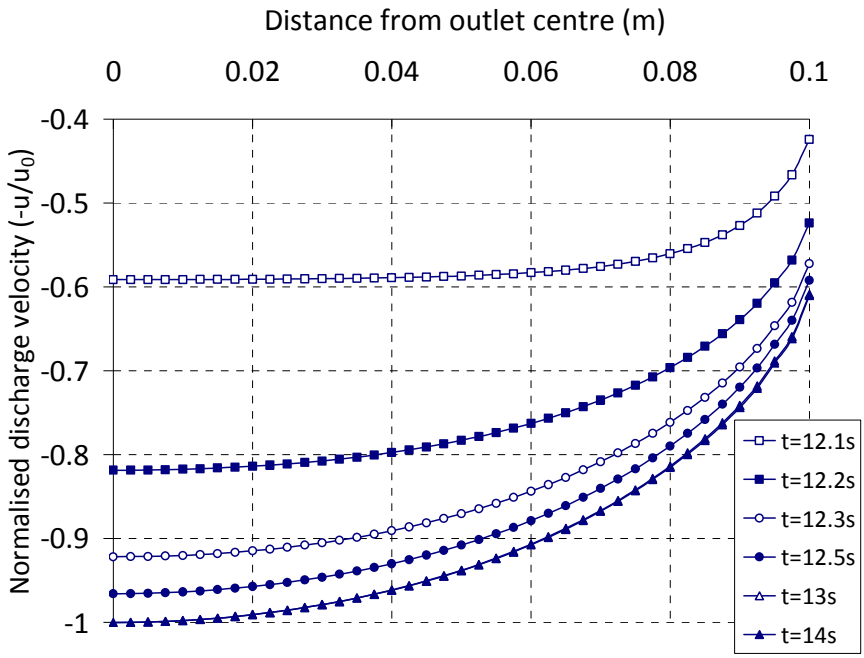

Fig. 4-4 Discharge velocity profiles along the hopper outlet at different time points

In addition, the stress field within the granular solid experienced a switch from an active (the major principal stresses are vertically oriented) to a passive state (the major principal stresses are horizontally oriented) (Nedderman, 1992). The calculated principal stress orientations at the selected six time instances after filling are shown in Fig. 4-5. Furthermore, the switch of the stress state propagated from the bottom to the top of the hopper and brought passive stress state to the whole flowing zone. As such, an "arched" stress field (Ooi and Rotter, 1991) was formed in much of the hopper. A similar switch of stress field, which was used to identify the flow pattern (either mass or funnel flow), was reported in the FE modelling of silo discharge by Karlsson et al. (1998).

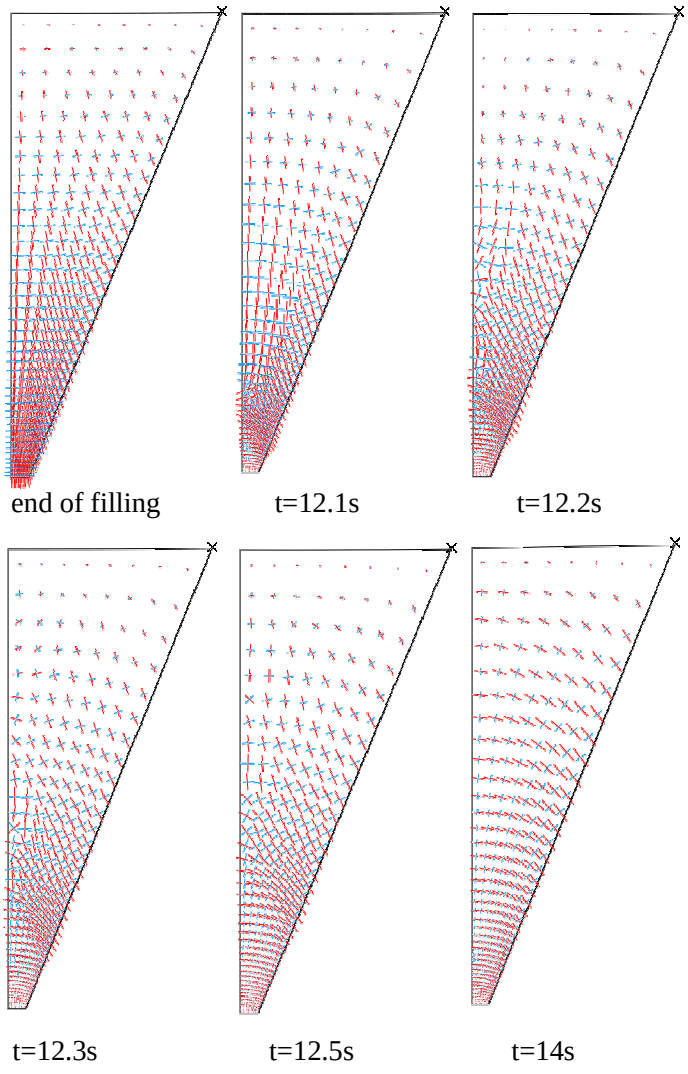

Fig. 4-5 Principal stress orientations at different discharge time instances; red lines representing major principal stress and blue one for minor principal stress

Fig. 4-6 shows the evolution of the calculated wall pressure distribution at various time points. The vertical height is normalised by the total height h_0 measured from the outlet of the hopper. The mean pressures are obtained by temporally averaging over the first two seconds after discharge started. From this figure, it is clearly seen that the peaks of normal pressure and shear stress propagated from the low height level to the higher

level, which can be associated with the switch of stress field. As the hopper bottom was removed and the solid began to move downward, the stress level at the bottom decreased significantly. Subsequently, the normal pressures p_{wn} and shear pressures p_{ws} on the wall tended to increase higher up in order to fulfil the equilibrium of forces. Fig. 4-7 shows the time series of the normal wall pressure at different points of the hopper at incipient discharge. Point *f* shows a very similar wall pressure history and is not shown in this figure. It is clearly seen that the peak pressures occurred just after discharge started, which can be associated with the peaks progressing upwards rapidly as shown in Fig. 4-6. A similar observation was reported in the experimental investigation carried out by Ostendorf et al. (2003). The difference is that the pressures in the lower part dropped quickly after the peak occurred due to the relatively high discharge velocity in the present FE simulation.

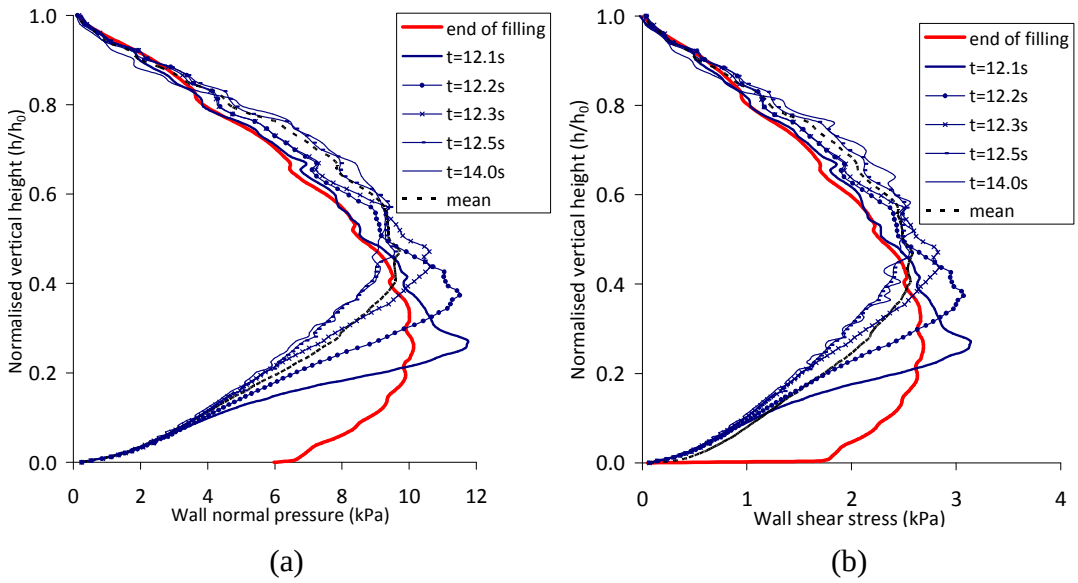

Fig. 4-6 Wall pressure distributions at various time points: (a) wall normal pressure; (b) wall shear pressure. The mean pressures are obtained by temporally averaged over the first two seconds period after discharge started.

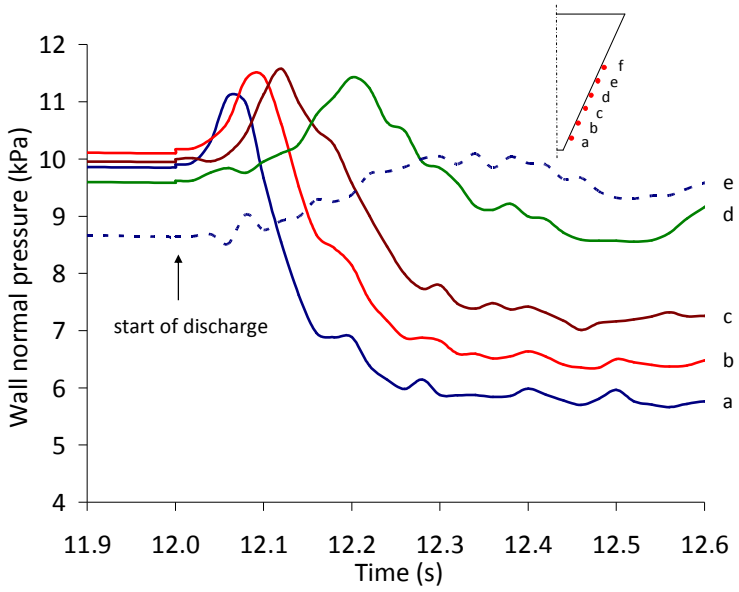

Fig. 4-7 Time histories of wall normal pressure at different points of the hopper at the incipient discharge

4.4.2 Comparison with existing theories and equations

The calculated wall normal pressure distributions along the hopper wall during filling and discharge were compared with those predicted by the theoretical solutions, as shown in Fig. 4-8. Since the height is normalised by the total height h_0 measured from the outlet of the truncated hopper, the theoretical solution shows a negative height below the hopper outlet. The wall pressures calculated by the present FE simulation were temporally averaged over the fist 10 seconds period after the start of discharge. Doing so has two purposes: one is to avoid the transient effects on wall pressures at the beginning of discharge (the transient effects are studied separately); the other is to ensure that the hopper is effectively still fully filled with granular solid in a short period of discharge. The averaged pressure is determined by the following equation:

$$p_{wn} = \frac{1}{N}\sum_{i=1}^{N} p_{wn(i)} \tag{4-9}$$

where $p_{wn(i)}$ represents the normal pressure at a specified wall point at the i th time point and p_{wn} is the average normal pressure at the corresponding wall point from the N time points within the period of 10s.

From Fig. 4-8, a good degree of agreement can be seen between the numerical and theoretical predictions of wall pressure at the end of the filling process. Since a truncated conical hopper was used in numerical modelling, there is blank pressure at the lower part for the numerical prediction; whilst the theoretical solutions show a continuous pressure distribution ending at the apex of the hopper. For the discharge pressure, it is clearly seen that the calculated pressure pattern also follows the theoretical solutions well.

Namely, the pressure peaks moved from the low part to the higher part of the hopper due to the movement of stress field switch. The discrepancy of discharge pressure distribution between the numerical and theoretical predictions is not surprising since Walker's and McLean's solutions for the passive state are complying with the static equilibrium in the conical hopper.

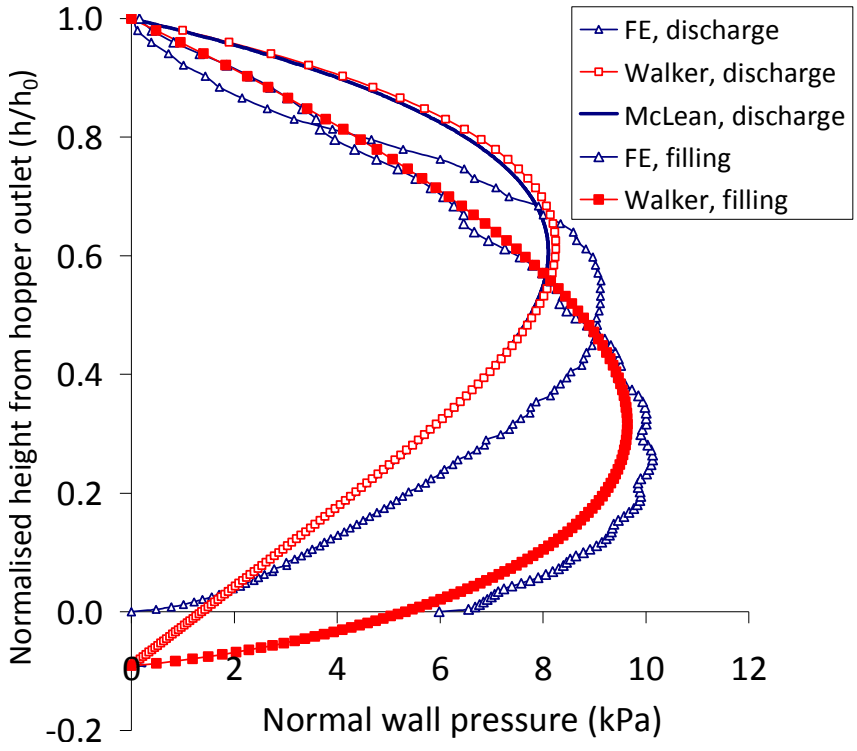

Fig. 4-8 Wall normal pressure distributions along the hopper wall at the end of filling and discharge period

A comparison of mass flow rate prediction between the numerical and the Beverloo equation (1961) was performed to further verify the present FE model. The relevant parameters for the Beverloo's equation are summarised in Table 4-2. The mass flow rate from the numerical simulation was computed from the product of the granular solid

density, the area of the hopper outlet and the velocity relative to the outlet. Whilst Beverloo's equation gives a constant mass flow rate, a progressively increase flow rate is predicted by the present FE simulation until a steady discharge velocity was achieved about 2 s after discharge started. From Fig. 4-9, it is clearly seen that the fully developed flow rate from the FE computation matches the Beverloo's empirical equation very well.

Table 4-2 Parameters used in Beverloo's equation

C	D_0 (m)	λ	d	α^o	ϕ_d^o	ρ_b (kg/m^3)
0.58	0.2	1.5	0	22.6	67.4	1000

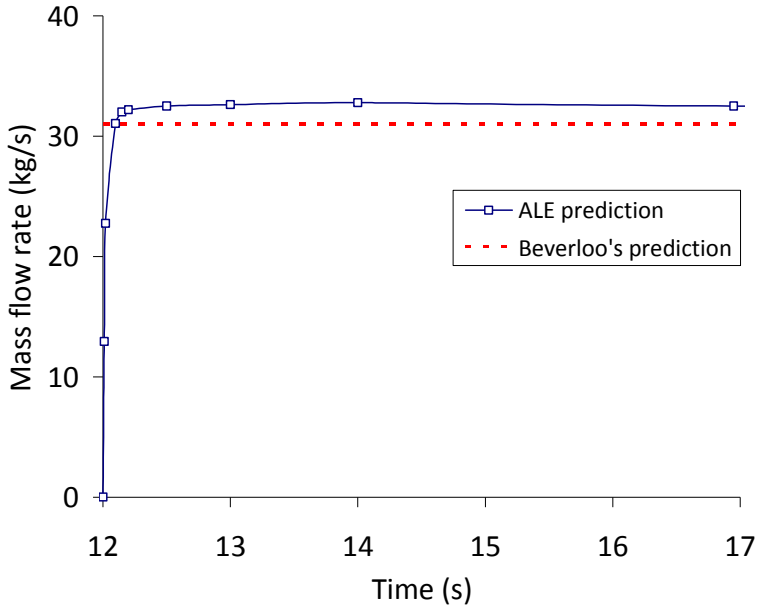

Fig. 4-9 Mass flow rate prediction

4.4.3 Pressure fluctuations during discharge

4.4.3.1 Wall pressures

When the steady state flow is reached, the pressure and discharge velocity do not change as much as beginning of discharge. The statement is valid for time averaged data. When looking at the instantaneous flow, pressures exhibit the oscillatory characteristics (Ostendorf et al., 2003; Nielsen et al., 1998; Bohrnsen et al., 2004). However, the measurement of the pressure may not be meaningful because experimental measurements can be affected by local auto-induced phenomena created by local pressure cells (Artoni et al., 2009; Artoni et al., 2011).

Fig. 4-10 (a) shows the time histories of calculated wall normal pressures at three different positions (*a*, *e* and *f*) at the hopper wall during the discharge process. These pressures exhibit fluctuating patterns. Similar fluctuation of discharge pressures has been reported in experimental observations by Ostendorf et al. (2003), as shown in Fig. 4-10 (b). By using Fourrier transformation, the frequency spectrum analysis was performed for the whole time history of discharge pressure at the typical point *e* in the present FE simulation. The results are shown in Fig. 4-11 which indicates two dominant frequencies, one at less than 1 Hz and the other at about 5 Hz.

A further investigation was conducted by dividing the whole time history of pressures at the point *e* into six continuous time series and analyzing their frequency spectrums separately, as shown in Fig. 4-12. It can be seen that the frequency of 5 Hz existed in all six time intervals; whilst the pressure in earlier periods had a varying frequency around 1 Hz when those of following time series have a frequency of less than 1 Hz.

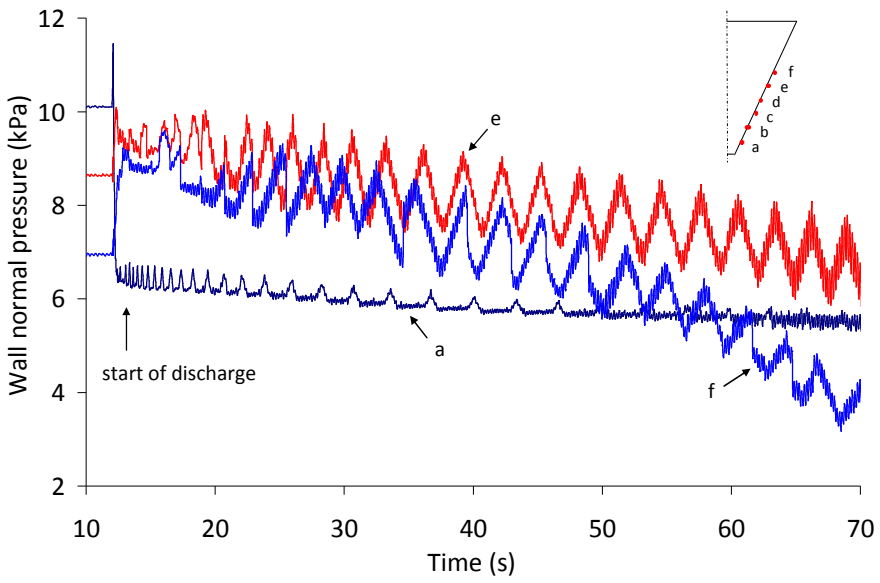

(a)

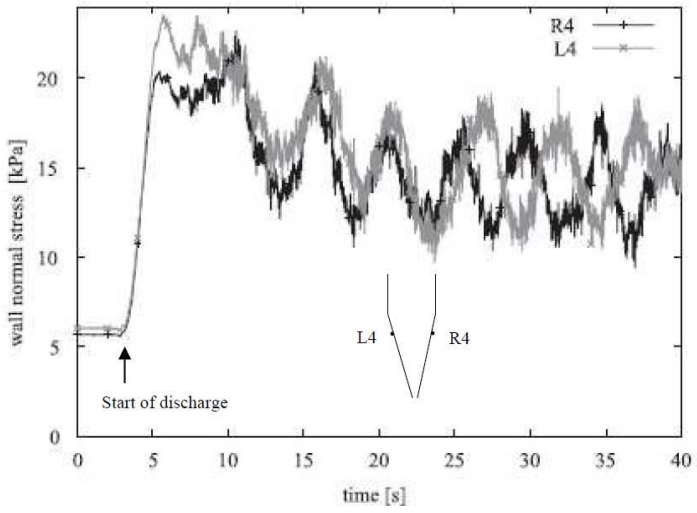

(b)

Fig. 4-10 Time histories of normal wall pressure at various points of the hopper during discharge: (a) FE simulation, (b) Experimental measurements. (after Ostendorf et al., 2003)

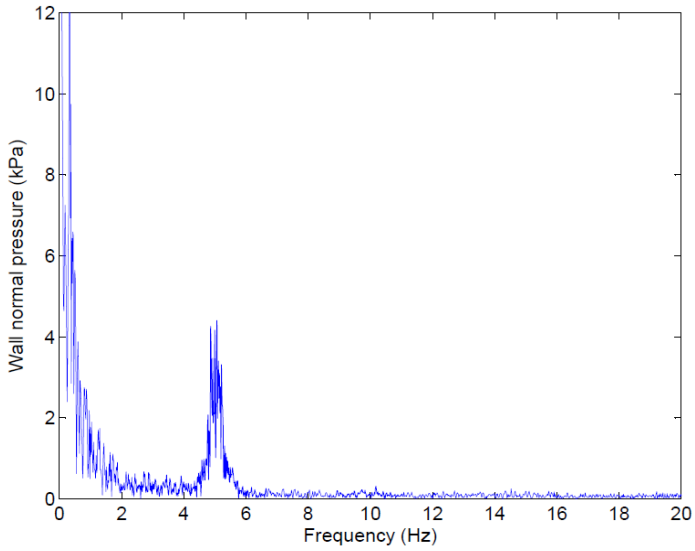

Fig. 4-11 Frequency spectrum of the calculated wall pressure at point *e* for the whole process of discharge, t=12~72s

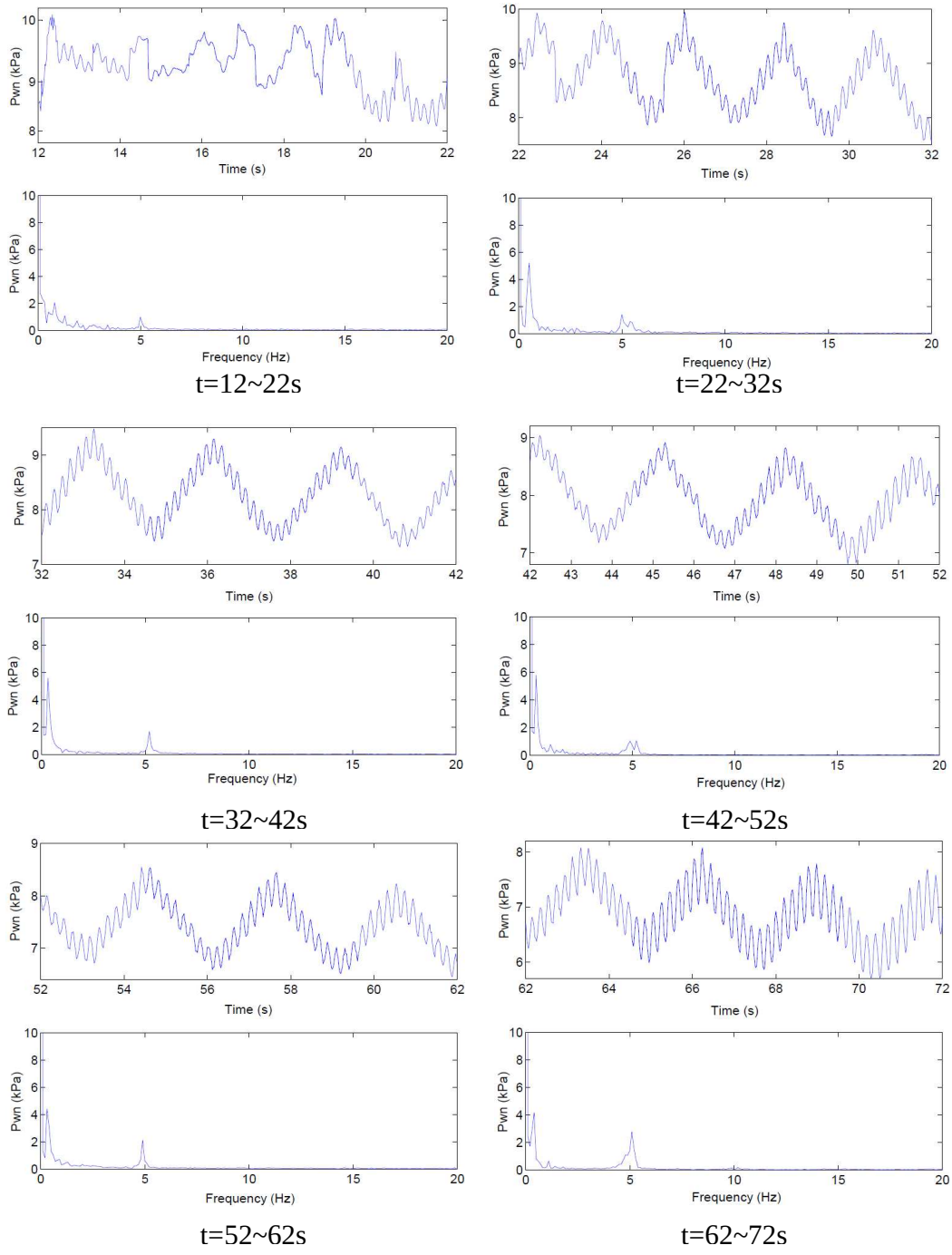

Fig. 4-12 Time histories of normal wall pressures at point *e* and the frequency spectrum

In addition, the wall shear stress was also investigated through the present FE simulations. The shear stress at the typical point *e* on the hopper wall is compared with the normal pressure in Fig. 4-13. From this figure, it is seen that the shear stress at point *e* has the same fluctuating pattern as the normal pressure.

Further, the mobilised friction ratio of the shear stress to the normal pressure at the wall was explored and it can be calculated at a single point of the wall, as follows

$$\mu_0 = \frac{p_{ws}}{p_{wn}} \tag{4-10}$$

where p_{ws} is the wall shear stress, and p_{wn} is the wall normal pressure. In the present FE simulation, the coefficient of wall friction under Coulomb friction law is set as 0.267 (ϕ_w=15º). Fig. 4-14 shows the mobilised ratio μ_o at point *e*. The mobilised ratio appears to fluctuate between 0.266 and 0.268 with the average value at the input value of 0.267.

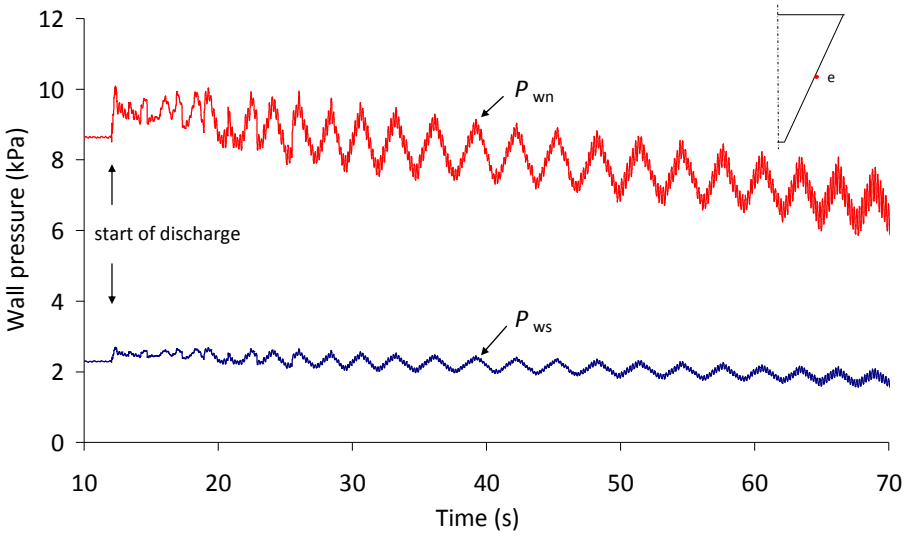

Fig. 4-13 Time histories of wall normal pressure and shear stress at point *e*

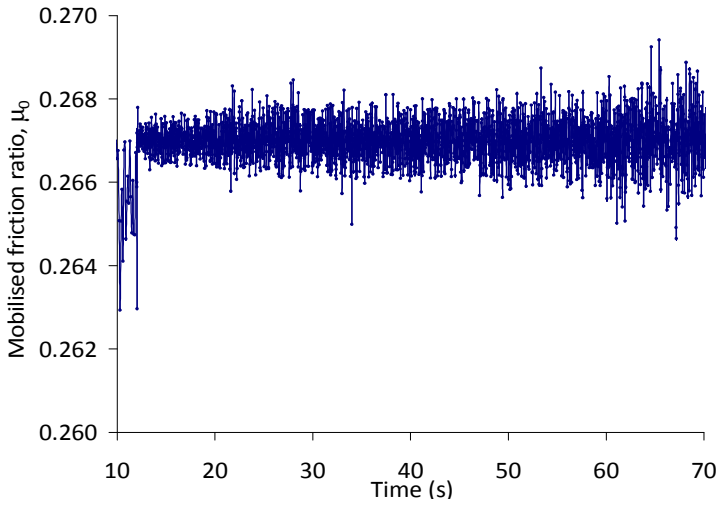

Fig. 4-14 Time history of the mobilised ratio of the shear to the normal pressure μ_0 at point *e* with an input coefficient of friction of 0.267

4.4.3.2 Internal stress within granular solid

Like the wall pressure, the internal stress within the granular solid strongly oscillated with fluctuating peaks solid. The location of sections and points investigated in the

present FE simulation is shown in Fig. 4-15. Fig. 4-16 shows the time history of the radial stress at various points within the solid during hopper discharge. The radial stress at point *e*1, which is located very close to the wall, has similar pattern to the wall normal pressure at point *e*. That is, large fluctuation has the frequency of less than 1 Hz and small fluctuation has the frequency of 5 Hz. Along the same horizontal line, the stresses at points *e*2 and *e*3 away from the wall are characterized by small fluctuations at frequency of about 5 Hz and less than 1 Hz, as shown in Fig. 4-16 (a). In the vertical generator direction, the radial stress apparently exhibited oscillatory characteristics all through the hopper. The only difference is that the magnitude of the stress fluctuations are larger higher up in the hopper, as shown in Fig. 4-16 (b).

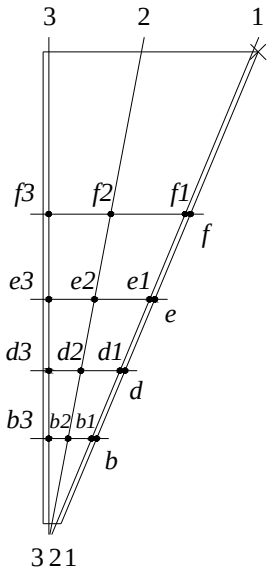

Fig. 4-15 Locations of investigated points and sections

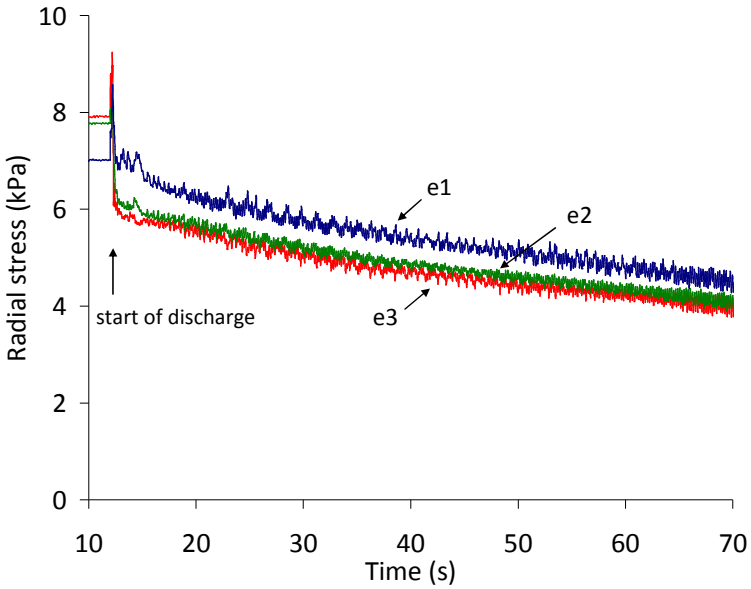

(a)

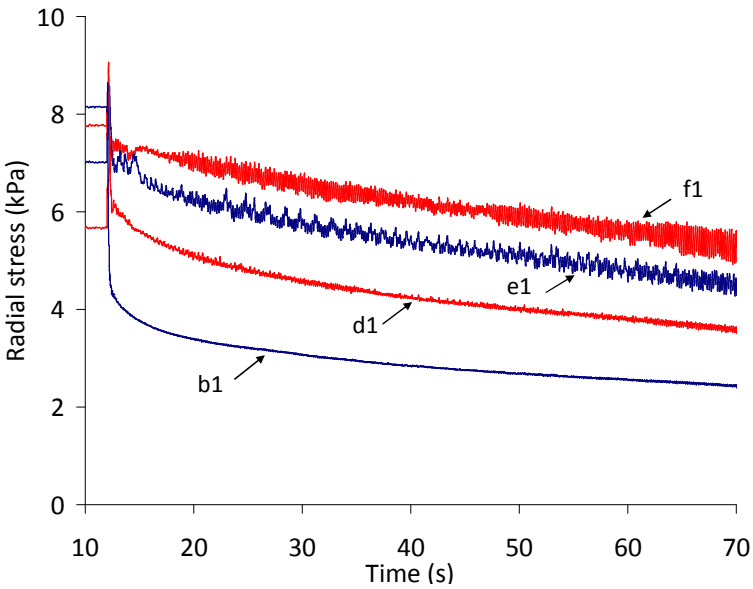

(b)

Fig. 4-16 Time histories of radial stress at various points: (a) along a horizontal direction; (b) along a vertical generator direction

In turn, the distributions of the vertical stress along section *e-e* and section *b-b* are shown in Fig. 4-17. These stresses were plotted by the instantaneous values at a certain time point. From this figure, it can be seen that non-uniform stresses along these horizontal sections evolved during hopper discharge with the vertical stress decreasing progressively as the granular solid was withdrawn.

The distributions of radial stresses in three vertical sections, i.e., section 1-1, section 2-2 and section 3-3 are plotted and shown in Fig. 4-18. The oscillations of stress became stronger in vicinity of the central axis of the hopper. In general, the magnitudes of radial stress decreased as the granular solid was discharged.

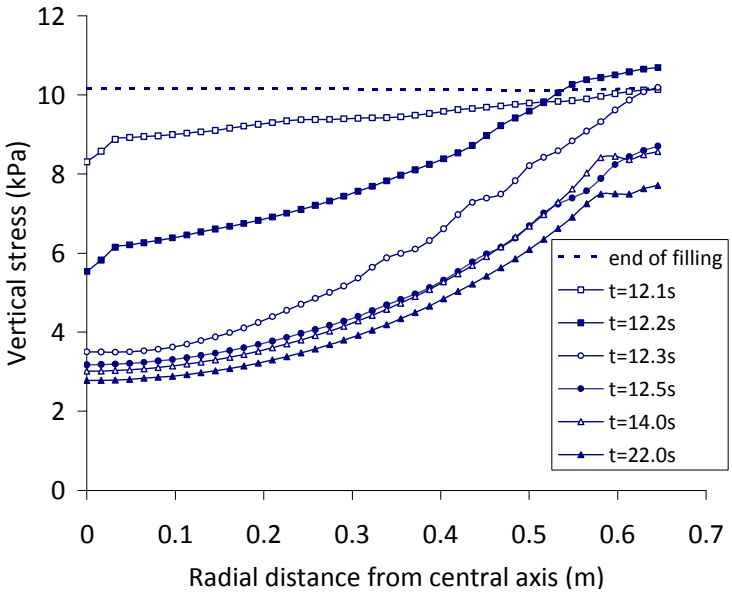

(a)

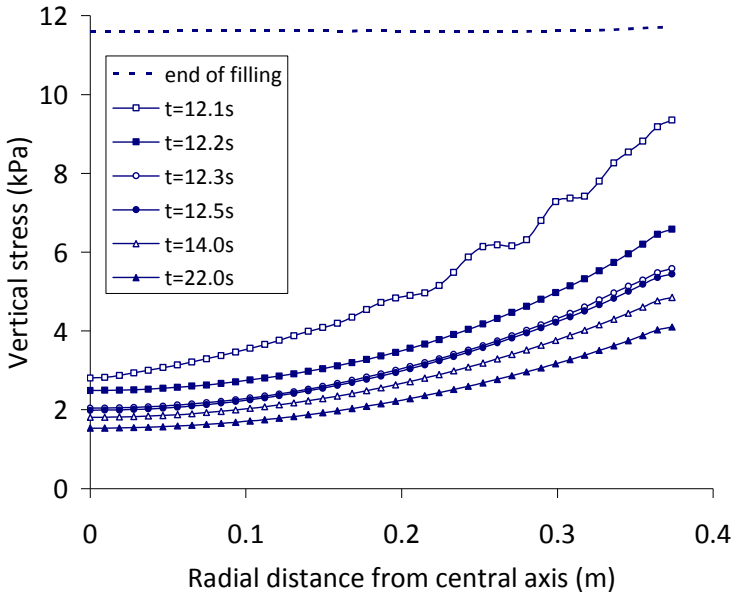

(b)

Fig. 4-17 Distribution of vertical stress at various time points: (a) along section e-e; (b) along section b-b

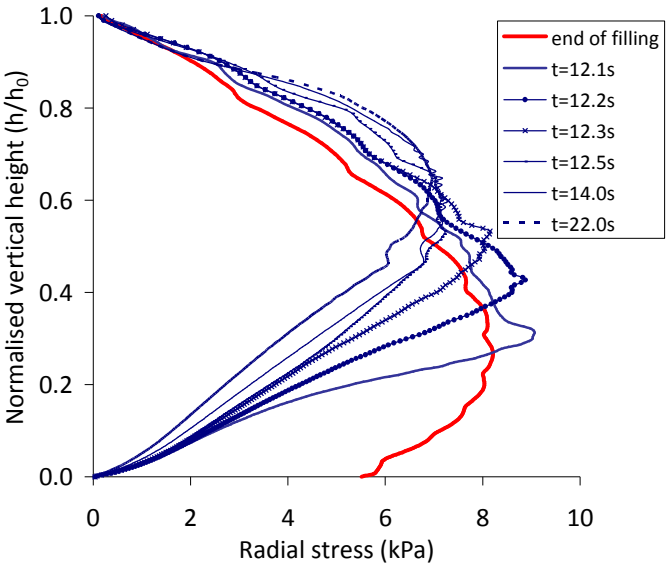
1.0
0.8
0.6
0.4
0.2
0.0
Normalised vertical height (h/h0)
0
2
4
6
8
10
Radial stress (kPa)
end of filling
t=12.1s
t=12.2s
t=12.3s
t=12.5s
t=14.0s
t=22.0s

(a)

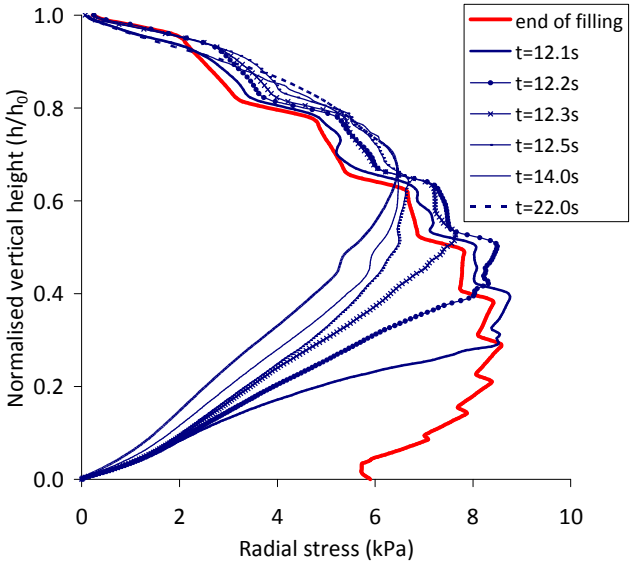
1.0
0.8
0.6
0.4
0.2
0.0
Normalised vertical height (h/h0)
0
2
4
6
8
10
Radial stress (kPa)
end of filling
t=12.1s
t=12.2s
t=12.3s
t=12.5s
t=14.0s
t=22.0s

(b)

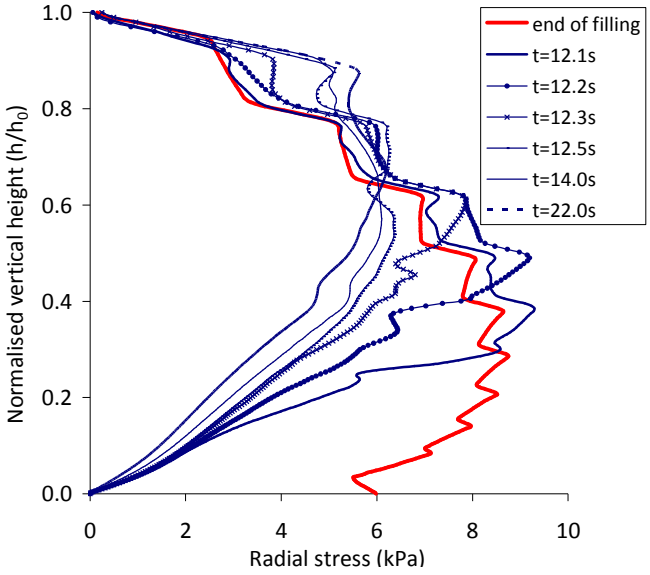

(c)

Fig. 4-18 Distribution of radial stress at three vertical sections at various time points: (a) section 1-1; (b) section 2-2; and (c) section 3-3

4.5 Discussion on dynamic pressure

For the pressure fluctuation at much larger amplitudes with frequencies of less than 1 Hz, a probable explanation can be found by studying the evolution of shear zone and slip-stick wall motion during discharge. The occurrence of shear zones within granular solid during silo discharge has been reported in experimental observation by Blair-Fish and Bransby (1973). The shear zones are presented by high shear stress zone in the present FE simulation. A shear failure zone is evaluated by the ratio μ of the second invariance of the stress deviator q to hydrostatic pressure p within the solid when the

Drucker-Prager failure criteria is used in programme Abaqus (SIMULIA 2008), as follows

$$\mu = q / p \tag{4-11}$$

The input angle of internal friction of 30º for stored material in the present FE simulation gives a limit value of 0.5773 for the stress ratio. An examination of the propagation of the shear failure zones during discharge is shown in Fig. 4-19. The failure zone is characterized by the light yellow colour in the contour figure. Fig. 4-19 reveals an intermittent shear failure arching zone located in the upper half of the hopper. The corresponding states for the simulation with a slower controlled outlet flow (Fig. 4-19b: $u=1/2u_0$) are compared with those for free flow (Fig. 4-19a). Associated with these intermittent arching shear zones in the solid, the displacement of the solid adjacent to the wall showed a slip-stick motion as indicated in Fig. 4-20. Each slip was found to correspond to a reduced stress ratio in the arching shear zone identified. The pressure shock related to slip-stick motion has been reported in experimental observations (Blair-Fish and Bransby, 1973; Michalowski, 1990; Roberts, 1996). The frequency of the slip-stick motion and intermittent shear zone are all less than 1 Hz which provides a plausible explanation for these larger pressure fluctuations.

As far as the minor pressure fluctuation with a frequency of about 5 Hz is concerned, it is probably caused by the longitudinal wave propagation within the granular solid stored in the hopper. The frequency of any longitudinal wave travelling within the granular solid in the hopper can be estimated from the wave equation for an elastic bar of hopper height with free ends (Prakash, 1981).

$$f_n = \sqrt{\frac{E(1-v)}{\rho_b(1+v)(1-2v)}} / 2h_f \tag{4-12}$$

$$= \sqrt{\frac{550000(1-0.3)}{1000(1+0.3)(1-2\times 0.3)}} / 2\times 2.64 \cong 5.2Hz$$

where E denotes the Young's modulus, v is the Poisson's ratio, ρ_b is the bulk density of the granular solid and h_f is the height of the fill in the hopper. This confirms that the 5 Hz fluctuation at small amplitudes in the predicted pressure is caused by the longitudinal wave propagation.

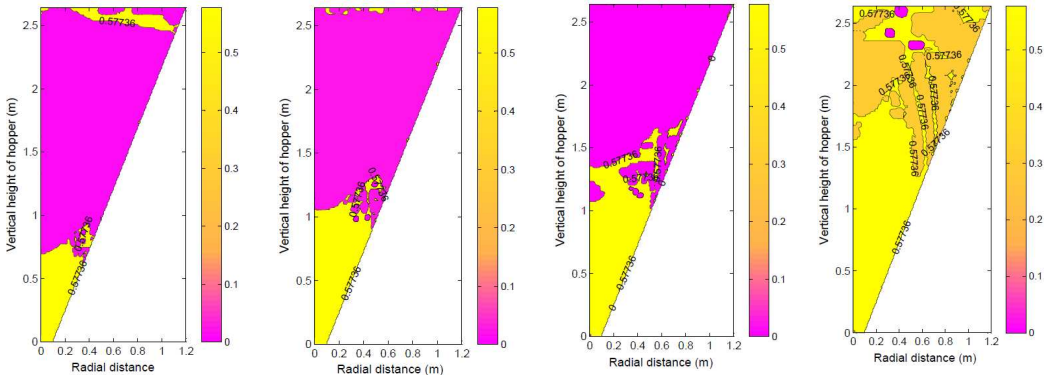

t=12.1s t=12.2s t=12.3s t=12.5s

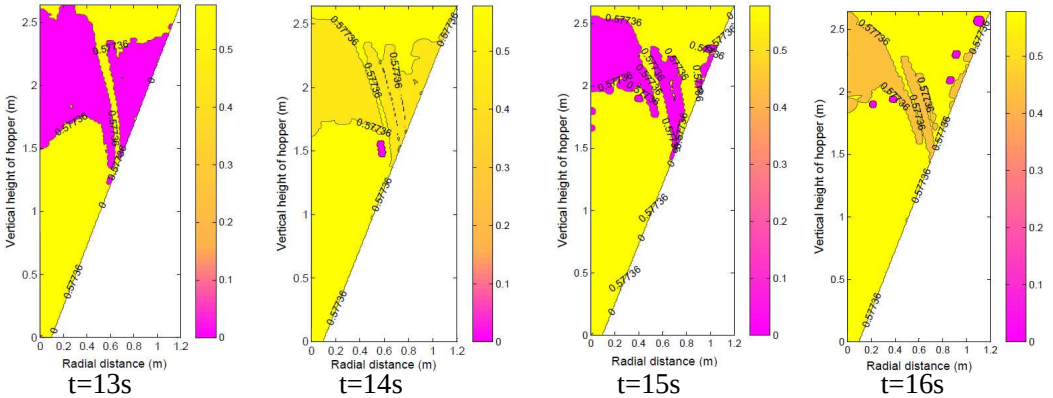

t=13s t=14s t=15s t=16s

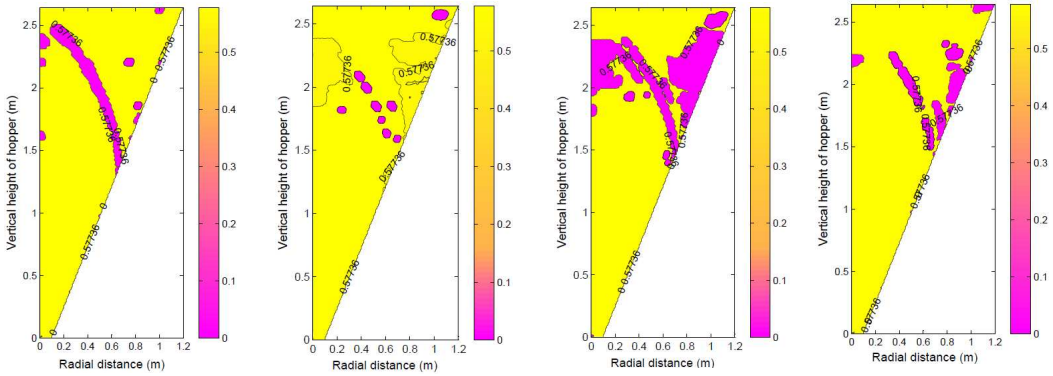

t=23s t=24s t=25s t=26s

(a)

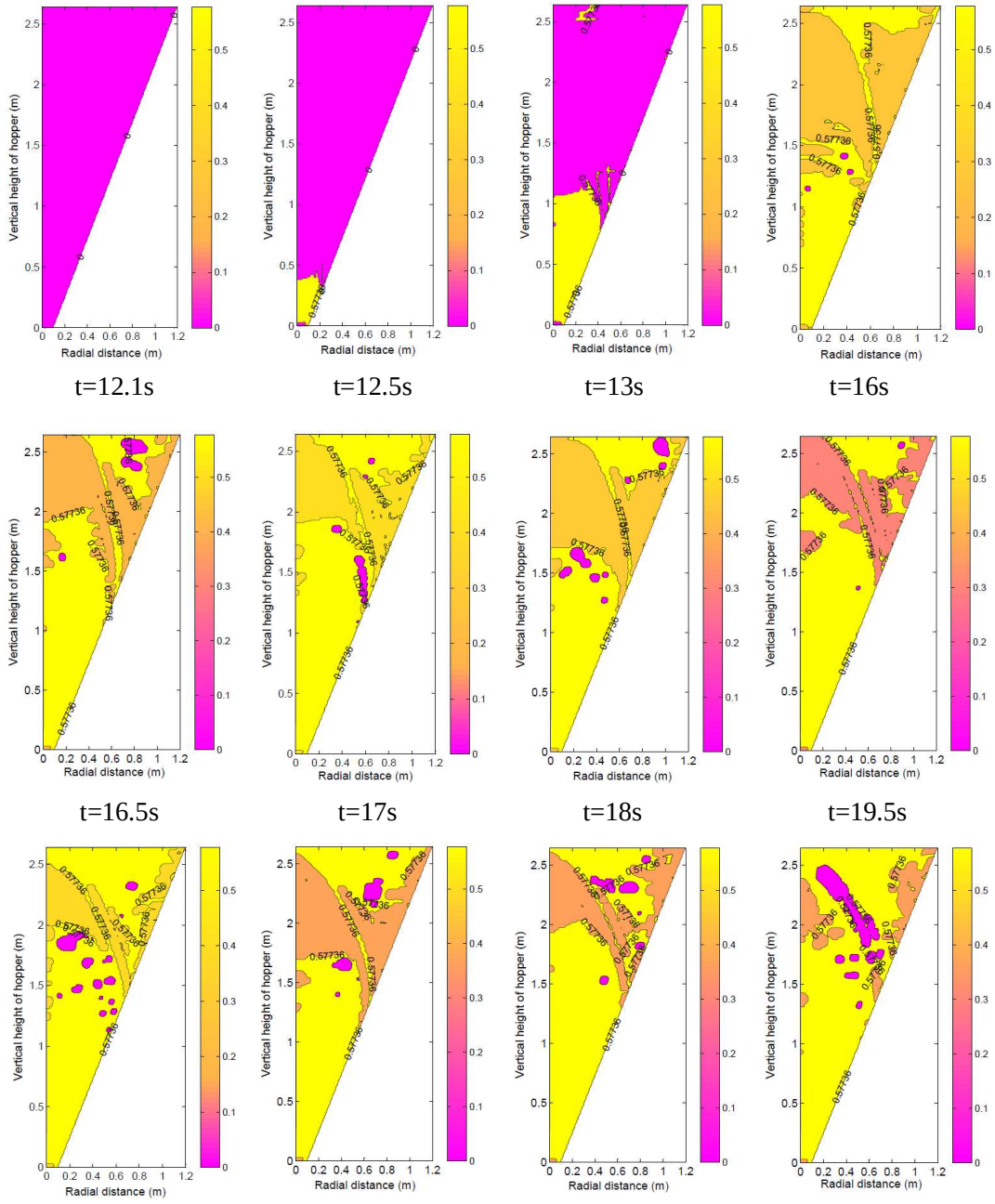

(b)

Fig. 4-19 Contours of stress ratio (q/p) at various discharge time points: (a) free flow; (b) controlled flow ($u=1/2u_0$)

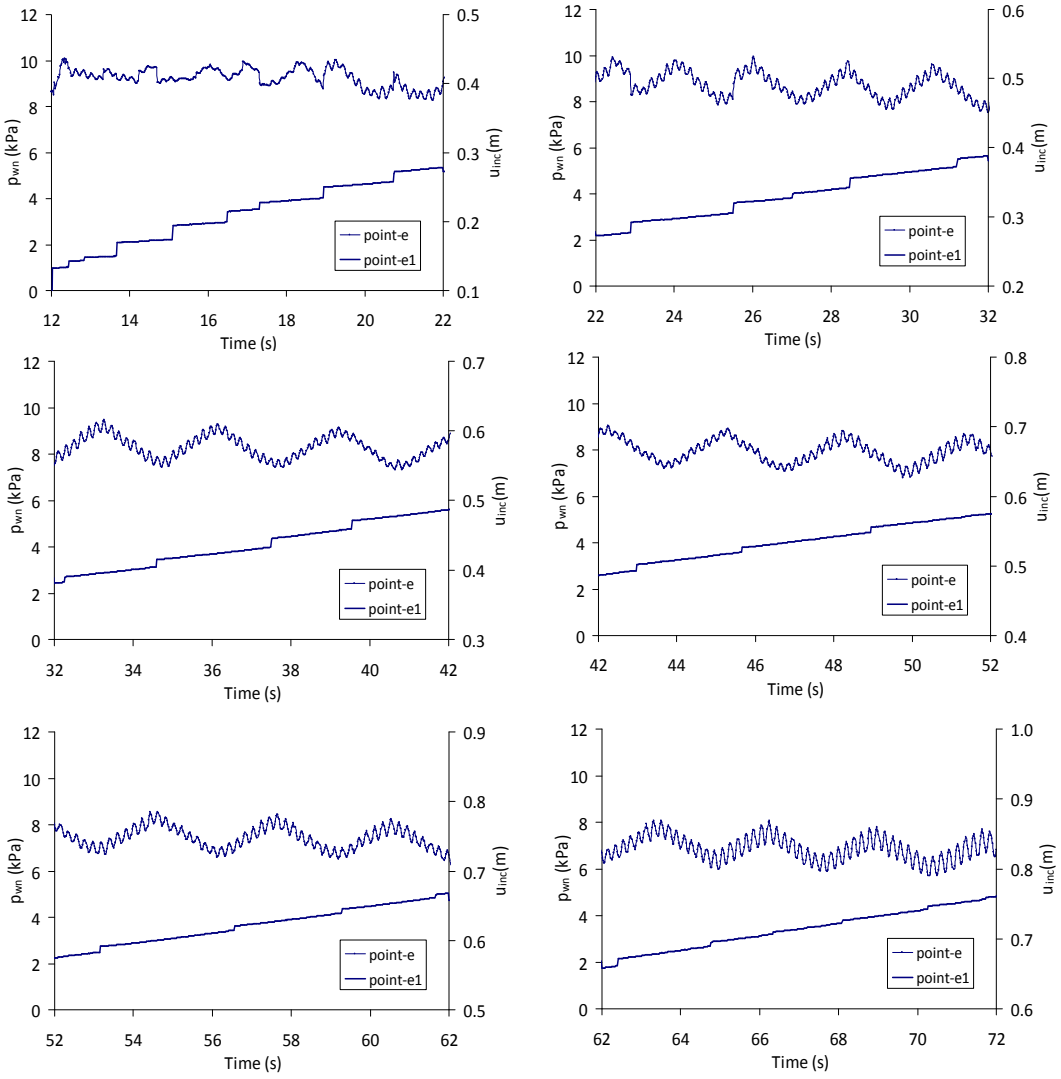

(a)

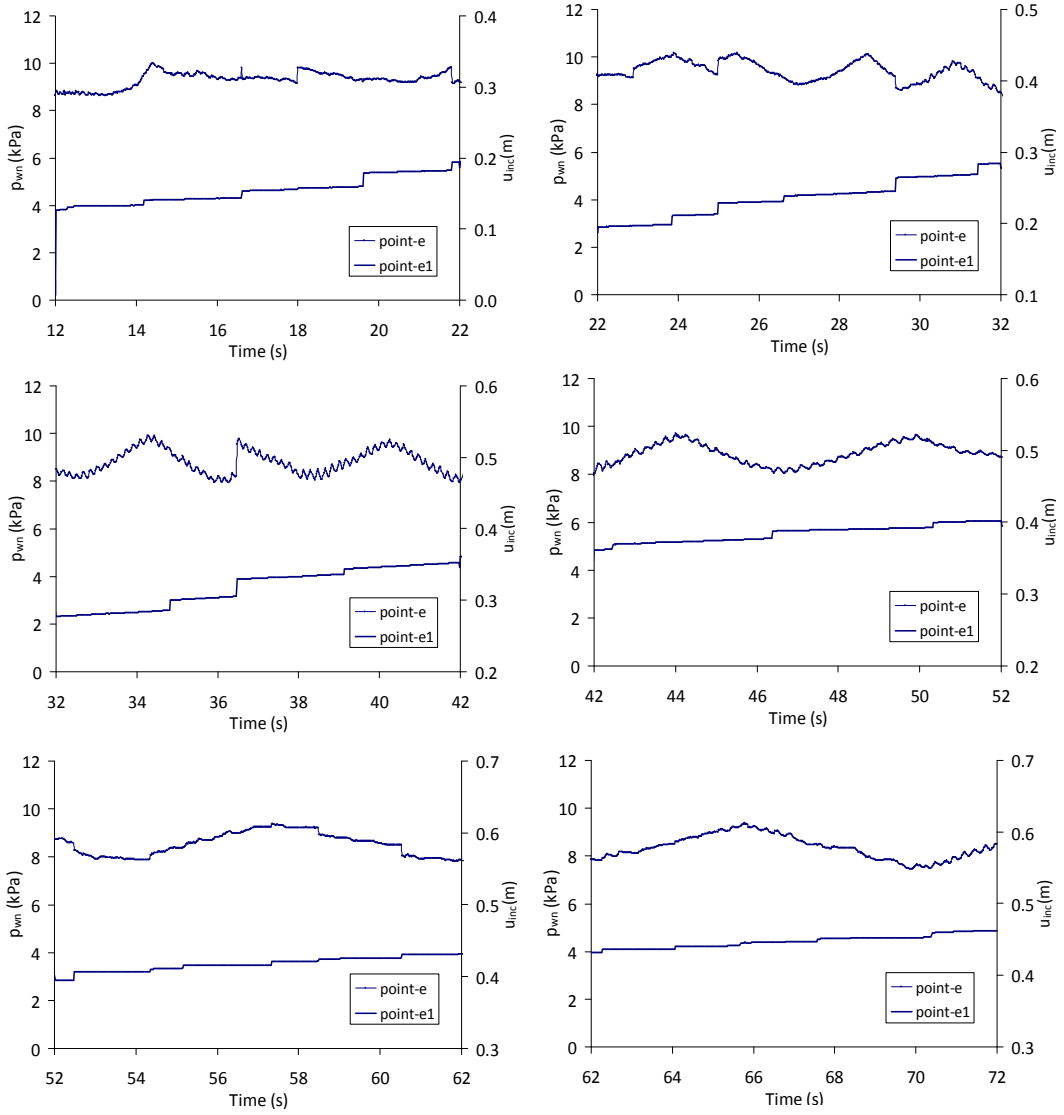

(b)

Fig. 4-20 Wall normal pressure (p_{wn}) at point-*e* and slip displacement (u_{inc}) at point-e1 at the hopper wall: (a) free flow; (b) controlled flow ($u=1/2u_0$)

4.6 Influence of key parameters on numerical outcomes

4.6.1 Effect of Young's modulus

Fig. 4-21 shows the time histories of normal wall pressure at point-*e* on the hopper wall (see Fig. 4-13) calculated by the FE simulations using elastic modulus E=5.5e5 Pa and E=5.5e6 Pa. Fig. 4-22 shows the frequency spectrum of the calculated normal wall pressure at point-*e* for the E=5.5e6 Pa case. The dominant frequency for the large amplitude fluctuations remained less than 1 Hz, whilst the dominant frequencies for the smaller amplitude fluctuations were in the range of 11~16 Hz which is about 3 times that of the reference case using Young's modulus of 5.5e5 Pa. According to Equation (4-12) for determining the fundamental frequency of the longitudinal vibration in an elastic bar, it is easy to explain why the frequency of small fluctuations, which is associated with the longitudinal wave, increases when a larger Young's modulus was used in the FE simulation. The frequency depicted in Fig. 4-22 is thus in accordance with the theoretical formula. Once again, this provides us with some confidence for the explanation of the cause of the small pressure fluctuations predicted by the FE model during hopper discharge.

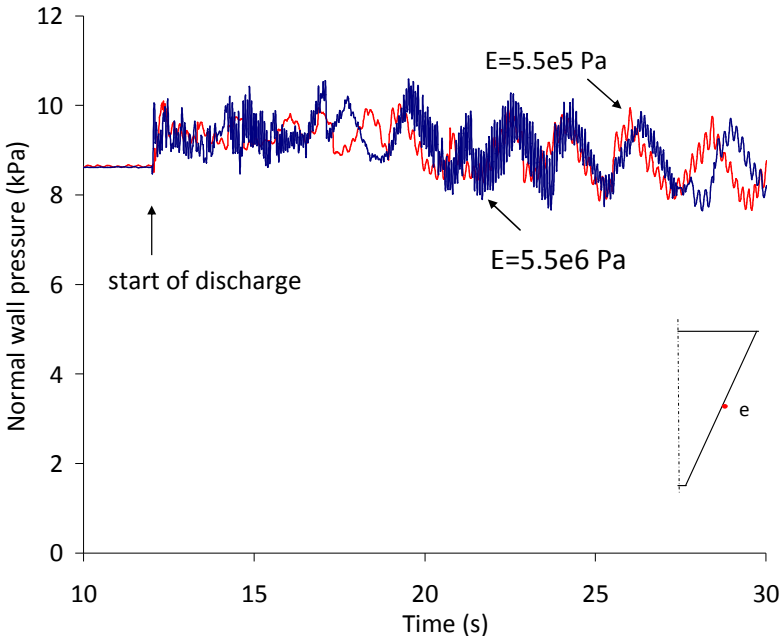

Fig. 4-21 Normal wall pressure for two solid elastic moduli

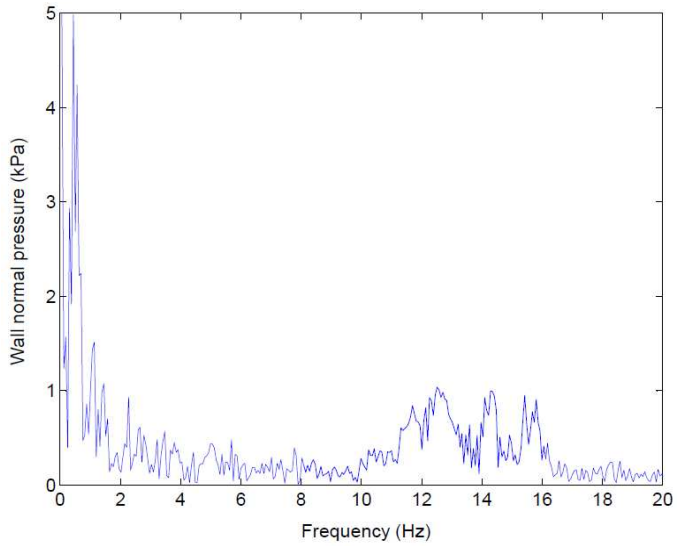

Fig. 4-22 Frequency spectrum of calculated normal wall pressure at point-*e* using Young's modulus of 5.5e6 Pa

4.6.2 Effect of discharge velocity

The time histories for the computed normal wall pressures at three different positions on the hopper wall for different controlled discharge flow rates are shown in Fig. 4-23. The large amplitude pressure fluctuations can be seen to reduce both in the amplitude and the frequency when smaller discharge velocities were adopted in the FE simulations. It can be foundt that the predicted dominant frequency of large amplitude fluctuations at the typical point *e* on the hopper wall decreases as the discharge velocity reduces. A similar effect has been observed in silo experiments by other researchers (Roterts, 1996; Wensrich, 2002).

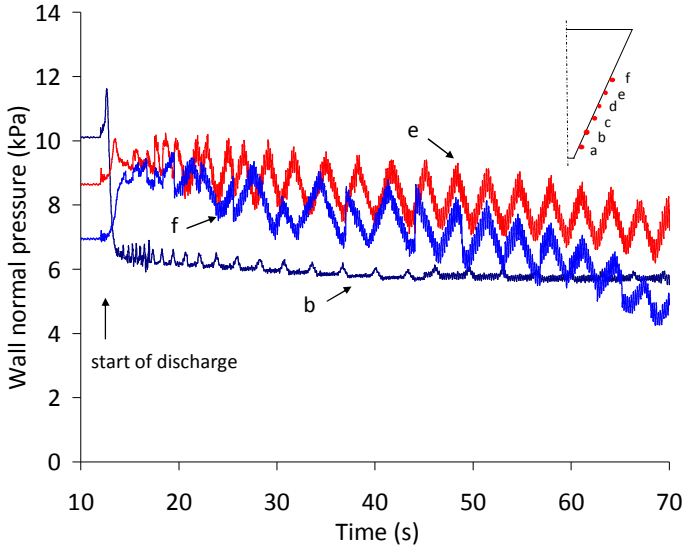

(a) $u=u_0$

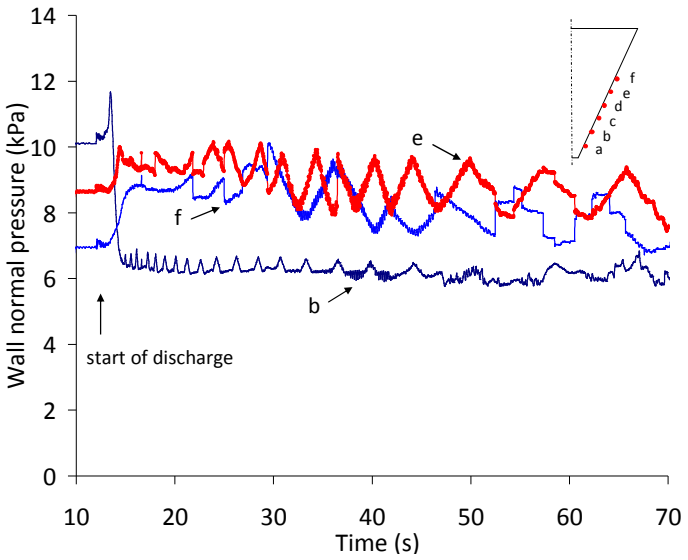

(b) u=1/2u$_0$

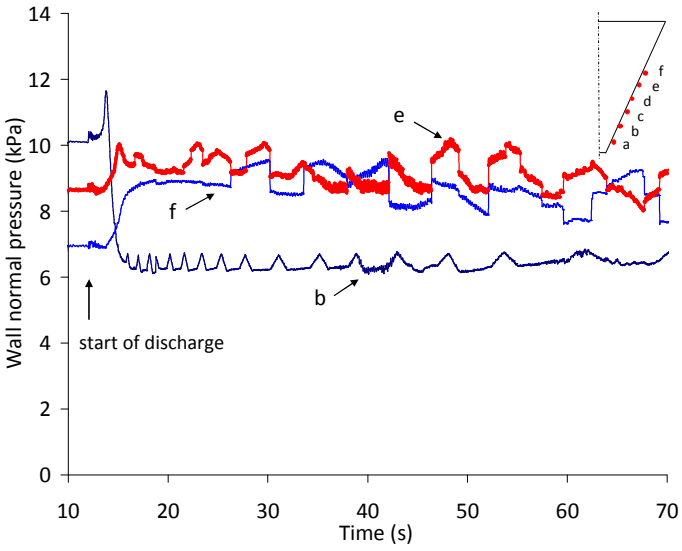

(c) u=1/4u$_0$

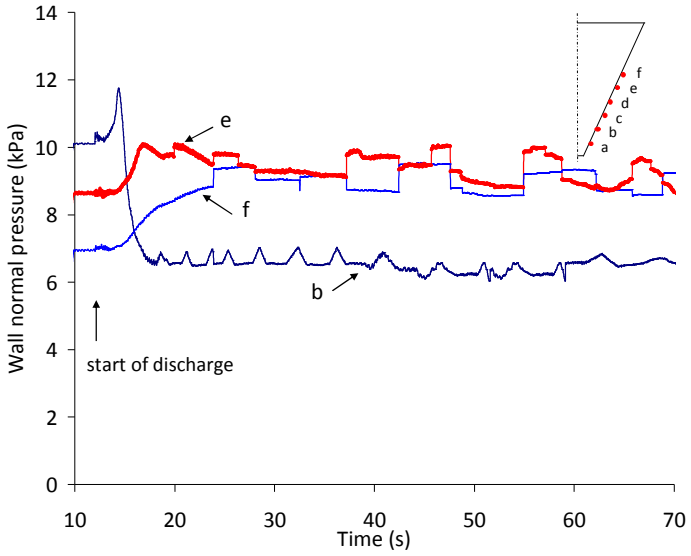

(d) u=1/10u$_0$

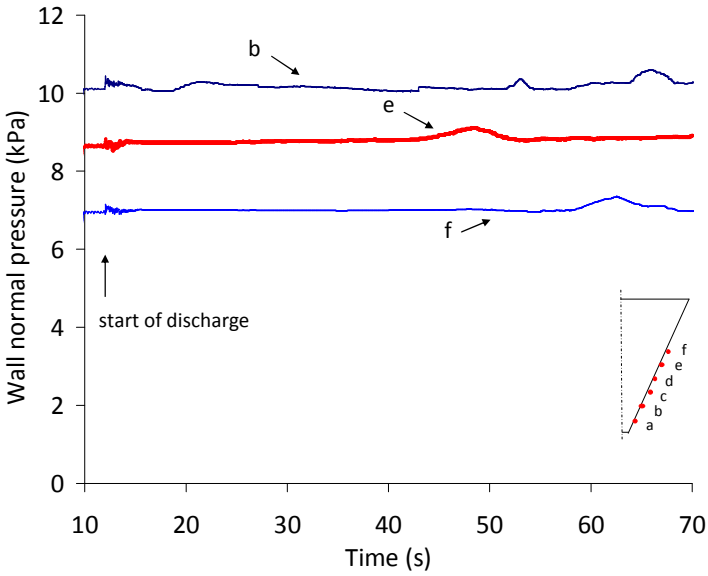

(e) u=1/100u$_0$

Fig. 4-23 Normal wall pressure at various wall points with varying discharge velocity under controlled discharge

4.6.3 Effect of wall roughness

The FE simulations with smooth hopper walls where the coefficient of wall friction was set to 0.01 were also performed and these were compared to the reference case with rough hopper walls where the coefficient of wall friction was set to 0.267 (see Fig. 4-24). In the figure, contours are shown of the tracers used to track the motion of solid particles at various discharge time points in the FE simulations. These contours indicate that mass flow was obtained during hopper discharge for both cases. Without wall friction, material moved at a faster discharge rate out of the hopper and with a uniform velocity and stress profile across horizontal sections. From the pressure-time plots in Fig. 4-25, comparison of these two types of walls indicates that the wall pressures for the rough walls fluctuated more strongly than those with smooth walls. The fluctuations of wall pressure with smooth walls was caused only by the longitudinal wave propagation in the granular solid whereas the presence of wall roughness has induced an intermittent shear failure zone within the solid, giving rise to another dominant pressure fluctuation with a much larger amplitude but smaller frequency as discussed above.

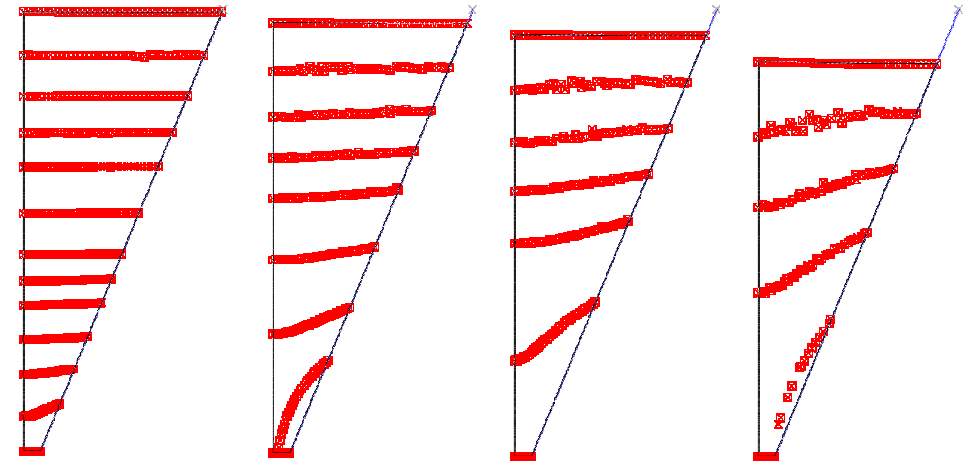

t=12.5s **t=16s** **t=23s** **t=32s**

(a)

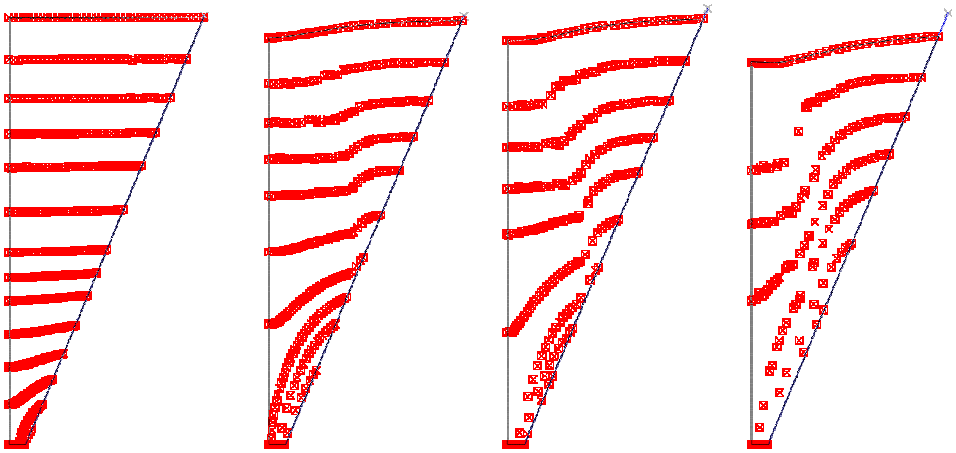

t=12.5s **t=16s** **t=23s** **t=32s**

(b)

Fig. 4-24 Contours of flow pattern at various discharge time points: (a) smooth walls; (b) rough walls

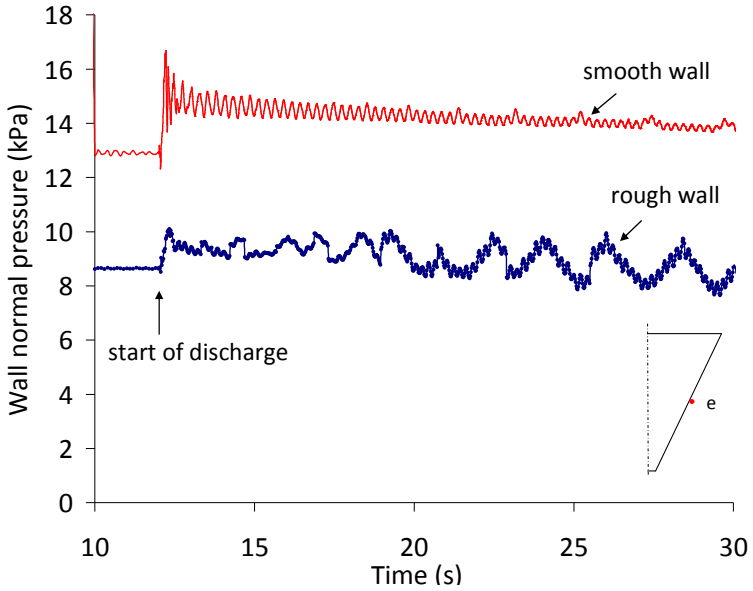

Fig. 4-25 Time histories of normal wall pressure at point-*e* with smooth walls and rough walls

4.7 Concluding remarks

It has been shown that the FE model based on the ALE formulation is an effective technique to simulate the silo discharge process by overcoming the mesh distortion problem caused by large deformation. By defining an adaptive mesh for the granular solid and suitable boundary conditions for the mesh region, a good degree of success has been obtained. The discharge pressures and mass flow rate predicted by the present FE model are in close agreement with the theoretical solutions. The transient dynamic phenomena induced by the silo discharge have been analyzed in significant detail. In particular, the dynamic fluctuations of pressure have been investigated thoroughly. The predicted fluctuations exhibited two primary frequencies. By analyzing the wave effects and the development histories of the shear zones within the solid, the governing

mechanisms have been found that the relatively high frequency event was attributable to the stress wave propagation within the granular solid, while the event with relatively low frequency and much larger amplitude was associated with the moving shear zones within the flowing material and the associated slip-stick motion between the granular solid and the walls.

Further exploration of the FE modelling of the discharge process was performed to investigate the effect of Young's modulus, discharge velocity and wall roughness. The frequency of fluctuations in normal wall pressure due to the longitudinal wave propagation can be dominated by the Young's modulus. Both the frequency and the amplitude of the large fluctuations in wall pressure can be reduced as the discharge velocity decreases. The presence of wall roughness has induced an intermittent shear failure zone within the store solid, giving rise to the dominant wall pressure fluctuation with large amplitude but small frequency.

The FE calculated wall pressure and flow rate in silos are very sensitive to changes of the wall friction angle. Thus, an improved description of the interaction behaviour between the granular solid and the wall is a crucial issue for predicting the wall pressure. To obtain an accurate prediction for shear failure within the granular solid during silo discharge, advanced material constitutive models which are able to capture the characteristics of micro-structure, such as the changes of void ratio, are quite required.

Chapter 5

Rarefaction wave propagation in tapered granular columns

5.1 Introduction

The transmission of stress waves within granular medium is a complicated issue because of the heterogeneity and nonlinearity inherent in these systems. In the last decades, propagation of stress waves in granular media has been extensively studied and reported in the literature. These treatments range from analytical methods (Gregor and Rumpf, 1975; Ocone and Astarita, 1995; Weir, 2001), to experimental investigation (Liu and Nagel, 1992; Ben-Dor et al, 1997; Hardin and Richart, 1963; Musmarra et al., 1995; Tournat et al., 2004) to more recent studies using numerical simulation (Melin, 1994; Berezin et al., 2001; Hostler and Brennen, 2005; Oveisy et al., 2009; Mouraille et al., 2009).

The study of stress waves in granular medium is of general interest in many industrial applications. An understanding of the propagation of stress waves in granular medium is required for the study of the dynamic aspects of industrial handling of bulk materials. For example, the discharge of granular materials from silos is often characterized by vibrations or pulsations known as ‘silo quaking’ (Roberts and Wensrich, 2002). Wensrich (2002) proposed that these pulsations or vibrations are due to compression and

rarefaction waves in the granular materials, which are caused by slip-stick motion between the granular material and the silo walls.

Borzsonyi and Kovacs (2011) reported experimental observation of sound waves in a granular material during a resonant test-scale silo discharge. The grain motion was tracked by high-speed imaging while the resonance of the silo was detected by piezoelectric accelerometers and acoustic method. Their major observation was that the wave velocity was not constant throughout the silo but increased considerably toward the transition zone in the lower end of the silo. In this region, the strong stress oscillations were observed. Moreover, the amplitude of the oscillations increased with height and led to slip-stick motion in the upper part of the silo. This conclusion supports the viewpoint of Roberts and Wensrich (2002) and Wensrich (2002).

Propagation of pressure fluctuations such as these were first studied analytically by Boutreux et al. (1997), who proposed a dynamic version of the Janssen model in a column of linear elastic material in the absence of gravity. This contribution studied the role of wall friction on the behaviour of pressure steps in the system (analogous to the water hammer problem). Friction was mobilised in a direction opposite to the direction of propagation, and it was shown that in this situation, a compression front decayed exponentially.

Using a similar dynamic version of Janssen's silo model, Wensrich (2002) later showed that the action of wall friction also has an important role in the growth of rarefaction waves. In the model, it was assumed that friction was fully mobilised in the upward

direction (akin to Janssen's original model) and the action of a rarefaction wave was to overcome friction and motivate the flow of initially stationary material. Using this model it was shown analytically that a rarefaction wave starting at the base of the silo, initially of magnitude σ_0^+, grows with the following form:

$$\sigma^+(x,t) = \sigma_0^+ e^{\frac{x}{2X_0}} \tag{5-1}$$

in which x is the distance travelled by the wave (in the upward direction), σ is the principal stress in the axial (x) direction, $X_0 = D/4\mu k$ is the Janssen characteristic depth of the column, D is the diameter of the column, μ is the coefficient of friction between the material and the column walls, and k is the coefficient of lateral pressure.

In this chapter, we will extend the work of Wensrich (2002) to the study of tapered column of granular material. In particular, we will examine the geometry effect on the rate of growth of rarefaction waves. Propagation of elastic waves in a solid body with variable cross section has been extensively studied and reported in the literature (Brillhart and Dally, 1968; Yang and Hassett, 1972; Rogge, 1971; Kenner and Goldsmith, 1968). Kenner and Goldsmith (1968) and Lewis, Goldsmith and Cunningham (1969) experimentally studied the response of conical bars to impact loads. Suh (1972) determined the stress pulse amplification ratio in truncated cones for various cones angles. Rogge (1971) developed, by perturbation analysis, an equation for elastic wave propagation in an arbitrary solid of revolution.

The present approach will adopt the analytical technique presented by Wensrich (2002). In addition to developing a new description for tapered columns with frictional boundaries, we will also present the results of a finite element (FE) study of the same phenomenon using the uncoupled Arbitrary Lagrangian-Eulerian formulation (ALE). The numerical results will serve to verify the predictions of the analytical models and provide a method to examine the limits of the validity of the modelling assumptions. The FE model continues to provide an effective means of studying wave propagation in hoppers with much larger half angles.

5.2 Convergent and divergent columns

5.2.1 Physical system and modelling assumptions

To study the geometry effect on wave propagation in granular solid, the present study will develop two models: a converging axisymmetric column (conical with apex downwards; see Fig. 5-1); and a diverging axisymmetric column (apex upwards). To facilitate analytical solutions, we make the assumption that the half angle of the cone is small in each case. Principally for this reason, we will refer to these systems as converging/diverging columns, rather than using the term “hopper” for the converging case. The base of the column consists of a boundary that moves as a function of time in order to disturb the system-creating waves that travel up through the material.

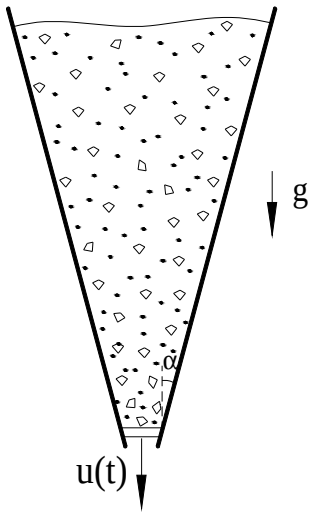

Fig. 5-1 A cone of granular material

In each case, we assume that the cone of material is acted upon by frictional forces that originate from the interaction of the material with the walls of the container as is typical in the analysis of a conical hopper (Nedderman, 1992). We assume that Coulomb friction at the wall interface is fully mobilised in the upward direction with a coefficient of friction of μ. Friction is a difficult phenomenon to model analytically due to its incremental non-linearity. For this reason we restrict our analysis to the case where the disturbance creates rarefaction waves in the material and friction is maintained at its maximum limiting value.

The assumption that the cone angle is small allows us to assume the material moves in one direction only, and that the velocity profile is approximately constant across the diameter with the exception of a small boundary layer. We will also make the assumption that the disturbances are small and the density does not vary significantly, and that the transverse stress is in a constant ratio to the axial stress σ_x.

From this perspective, we can restrict the number of unknown state variables in this system to two: the velocity and the principal stress in the radial direction emanating from the apex of the cone. Both of these variables are functions of both time and position.

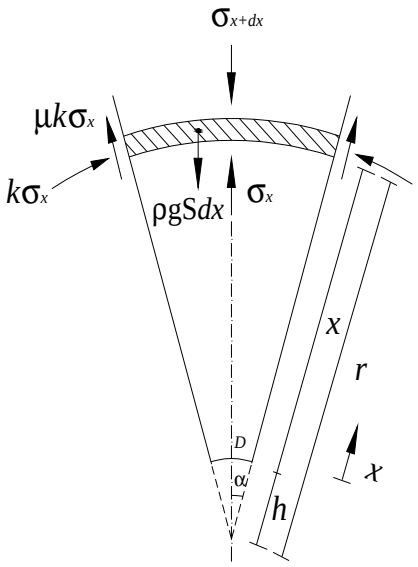

Fig. 5-2 Forces acting on a differential element of material in the converging column

5.2.2 Converging column model

Consider a converging column of half-angle α as shown in Fig. 5-2. To compare this model directly to the previous work by Wensrich (2003), we consider the case where the conical column is truncated at the base with outlet diameter D and the coordinate x measured from the base. The two coordinates are related by

$$x = r - h, or, = r - \frac{D}{2\sin\alpha} \tag{5-2}$$

The forces acting on a differential element of thickness dx and surface area S are the forces due to gravity, wall boundary stresses and the internal stresses as shown in Fig. 5-2. Summing the forces in the vertical direction, the equation of motion for this thin shell is given by

$$\frac{\partial u}{\partial t} = -g - \frac{\sin^2 \alpha}{2\rho(1-\cos\alpha)} \frac{\partial \sigma_x}{\partial x} + \frac{k \sin\alpha(\sin\alpha + \mu\cos\alpha)}{\rho(x+h)(1-\cos\alpha)} \sigma_x \tag{5-3}$$

Following on from the assumption of small disturbances only, we consider the stress to be of the following form:

$$\sigma = \hat{\sigma} + \sigma^+(x,t) \tag{5-4}$$

where $\hat{\sigma}$ is the background stress state, and σ^+ is the small disturbance in stress which varies with both position and time. We also assume the material approximately has an elastic response. If the tangential stiffness at the current stress state of the material is given by Θ, we can describe the constitutive response of the material by the following:

$$\frac{\partial \sigma^+}{\partial t} = -\Theta \frac{\partial u}{\partial x} \tag{5-5}$$

By differentiating Equation (5-3) with respect to x, and Equation (5-5) with respect to t, we can combine these two equations to provide a dynamic model of the system:

$$\frac{\partial^2 \sigma^+}{\partial t^2} - A^2 \frac{\Theta}{\rho} \frac{\partial^2 \sigma^+}{\partial x^2} + B \frac{\Theta}{\rho} \left(\frac{1}{(x+h)} \frac{\partial \sigma^+}{\partial x} - \frac{1}{(x+h)^2} \sigma^+ \right) = 0 \tag{5-6}$$

where

$$A = \sqrt{\frac{\sin^2 \alpha}{2(1-\cos\alpha)}}, \text{ and } B = \frac{k \sin\alpha(\sin\alpha + \mu\cos\alpha)}{(1-\cos\alpha)}$$

Note that the acceleration due to gravity is not present in this equation. This implies that gravity does not play a role in the propagation of small waves. Similar to the models developed by Boutreux et al. (1997) and Wensrich (2002) (with $\alpha = 0$), Equation (5-6) is of the general form of the well known Telegraph equation. Compared to the earlier work, we see that the coefficients in Equation (5-6) are substantially different from the case of $\alpha = 0$ and are no longer constant.

The first two terms form the one-dimensional wave equation with an elastic wave speed of

$$c_{el} = A\sqrt{\frac{\Theta}{\rho}} \tag{5-7}$$

The constant A is very close to 1 for small values of α, however it should be noted that this wave speed is undefined at $\alpha = 0$. This is a direct consequence of the degeneration of the coordinate transformation (Equation (2)) at $\alpha = 0$, and does not reflect any kind of physical reality. In the limit, as α tends to zero, the wave speed approaches the values defined by Boutreux et al. (1997) and Wensrich (2002).

In order to proceed, we can look for solutions of the form (Chester, 1971):

$$\sigma^{+}(x,t) = w(x)v(x,t) \tag{5-8}$$

Substituting this expression into our governing equation provides the following (note that prime denotes differentiation with respect to x, and $c^2 = \Theta/\rho$):

$$w\frac{\partial^2 v}{\partial t^2} - c^2 A^2 w\frac{\partial^2 v}{\partial x^2} + c^2\left(\frac{B}{x+h}w - 2A^2 w'\right)\frac{\partial v}{\partial x} - c^2\left(\frac{B}{(x+h)^2}w - \frac{B}{x+h}w' + A^2 w''\right)v = 0 \quad (5\text{-}9)$$

By careful selection of the function $w(x)$, we can manipulate the terms of this differential equation. In particular, selection of $w(x)$ so that

$$w' - \frac{B}{2A^2}\frac{1}{(x+h)}w = 0 \quad (5\text{-}10)$$

provides us with a version of the Telegraph equation (in v) with no first order derivatives with respect to x. This version is known as the standard "conservative" form (Fleishman, 1963), and represents a system that shows no dissipation (only dispersion).

Equation (5-10) can be solved using the integration factor:

$$I(x) = (x+h)^{-\frac{B}{2A^2}} \quad (5\text{-}11)$$

Multiplying by this factor, the solution to Equation (5-10) can be written as

$$w(x) = \Gamma(x+h)^{\frac{B}{2A^2}} \quad (5\text{-}12)$$

where Γ is a constant of integration. Substituting expressions for A and B, we can express solutions to Equation (5-6) in the following form:

$$\sigma^+(x,t) = (x+h)^{k(1+\frac{\mu}{\tan\alpha})} v(x,t) \quad (5\text{-}13)$$

where the function $v(x,t)$ satisfies a conservative form of the Telegraph equation. This equation describes the rate of growth of disturbances in our system. If we introduce a small disturbance of magnitude σ_0^+, Equation (5-13) predicts that the magnitude of this disturbance will grow with the following form:

$$\frac{\sigma^+}{\sigma_0^+} = (1 + \frac{2x\sin\alpha}{D})^{k(1+\frac{\mu}{\tan\alpha})} \quad (\alpha \neq 0) \tag{5-14}$$

5.2.3 Diverging column model

In a similar fashion, we can consider the behaviour of small disturbances in a diverging column of material subject to the same conditions and assumptions (see Fig. 5-3). In this case, we define our coordinate system in the opposite direction and the coordinate transformation remains the same (given in Equation (5-2)). The significant changes amount to changes in sign of the terms associated with gravity (which is irrelevant) and friction. Following through a similar analysis, it is possible to show that the rate of growth in this case is defined by

$$\frac{\sigma^+}{\sigma_0^+} = (1 - \frac{2x\sin\alpha}{D})^{k(1-\frac{\mu}{\tan\alpha})} \quad (\alpha \neq 0) \tag{5-15}$$

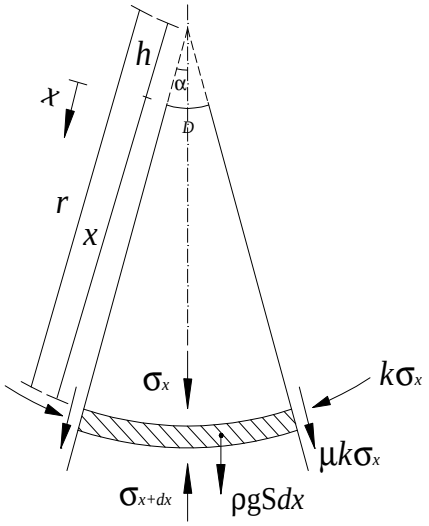

Fig. 5-3 Forces acting on a differential element of material in the diverging column

It should be noted that Equation (5-15) is written with respect to a coordinate system that is positive downward. If we consider disturbances travelling up the material column, the sign of the coordinate variable x is negative.

5.2.4 Comparison to parallel columns

On first examination Equation (5-14) and (5-15) appear remarkably different from the case of a parallel column (Equation (5-1)). This seems odd until it is observed that the coordinate system that Equation (5-14) and (5-15) are based on breaks down at $\alpha = 0$. While the forms appear quite different, numerically they are remarkably similar. Fig. 5-4 shows the growth of a disturbance (of unit magnitude) based on Equation (5-1), (5-14) and (5-15) for a single system over a range of half angles. It is clear from Fig. 5-4 that these three functions show a smooth transition around $\alpha = 0$. Indeed, it is possible to show that Equation (5-14) and (5-15) tend towards Equation (5-1) in the limit as α tends to zero. By taking the natural logarithm of Equation (5-14), and letting α tend toward zero, we obtain the following:

$$\begin{aligned}\lim_{\alpha\to 0}\left(\ln\frac{\sigma^+}{\sigma_0^+}\right) &= \lim_{\alpha\to 0}\left(k\left(1+\frac{\mu}{\tan\alpha}\right)\ln\left(1+\frac{2x\sin\alpha}{D}\right)\right)\\ &= \lim_{\alpha\to 0}\left(k\left(1+\frac{\mu}{\tan\alpha}\right)\frac{2x\sin\alpha}{D}\right)\\ &= \frac{2\mu kx}{D}\end{aligned} \tag{5-16}$$

which is perfectly consistent with Equation (5-1).

The analytical solutions predict that when a column is slightly diverging, the rarefaction wave grows significantly faster (than a parallel column) as the wave propagates up the column. The reverse is true for a converging column.

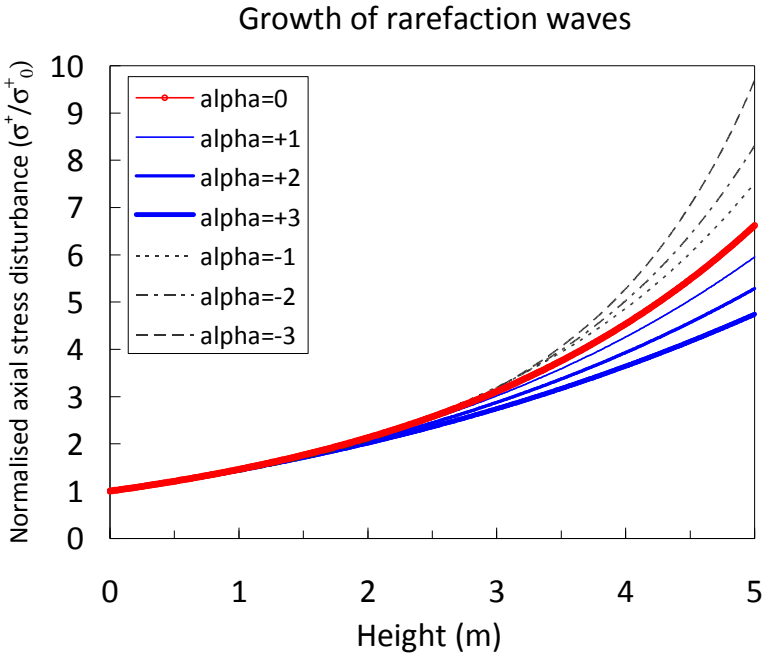

Fig. 5-4 Growth of a unit disturbance over various half angles for convergent, parallel and divergent columns (D =1m, μ =0.3, k =0.55)

5.3 Finite element modeling

Finite element modelling was carried out in order to evaluate the accuracy of the analytical models, and in particular, test the durability of the assumptions made. The simulations focused on a series of axisymmetric columns with a height of 5 m. The apex half-angle of the columns were varied over both positive (converging columns) and

negative (diverging columns) values. In all but one simulation, the diameter of the base of the column was set to 1 m.

To avoid mesh distortion during initialisation and flow, the FE simulations were performed based on the so-called uncoupled Arbitrary Lagrangian-Eulerian (ALE, in short) formulation with the adaptive meshing technique in the programme Abaqus/Explict (SIMULIA 2008). A non-linear dynamic analysis was performed using an explicit time integration scheme. To obtain a stable solution, the time increment was of order 1×10^{-6} s. As the viscosity of granular material is not known, the default linear bulk viscosity in Abaqus was used (SIMULIA 2008). In the ALE, both Lagrangian and Eulerian boundaries were used, with the sides and top surface of the material as Lagrangian boundaries while the base (outlet) was set to be an Eulerian boundary. The adaptive meshing technique was used to control mesh distortion and helps to maintain a high-quality mesh throughout the analyses even though large deformation occurs. This same methodology has previously been successfully applied to numerical analysis of silo behaviour (Wojcik and Tejchman, 2009; Yang et al., 2011; Wang et al., 2011).

In the simulations, the granular material was modelled as an elasto-plastic medium with a Drucker-Prager failure criterion (Drucker and Prager, 1952). The contact behaviour at the walls was modelled using contact surfaces which implement a penalty function to constrain the penetration depth (SIMULIA 2008). This penalty function relates the constraint normal pressure directly to the penetration distance. Friction at the contact was modelled using the Coulomb friction model with a constant coefficient. In each case, the material within the columns was broken into a fine mesh of first-order 4-node

quadrilateral elements with reduced integrations (10 mm in size). The walls were modelled using non-deformable 2-node rigid elements (20 mm in size).

Material properties representing a cohesionless dry sand were used. Typical material properties are shown in Table 5-1 and several of these values were varied in order to examine the sensitivity of the results.

Table 5-1 Material parameters

Bulk density (ρ_b)	1500 kg/m^3
Young's modulus (E)	2.0 MPa
Poisson's ratio (ν)	0.3
Internal angle of friction (ϕ_i)	30º
Dilatancy angle (ψ)	10º
Coefficient of solid-wall friction	0.3

5.3.1 Modelling the initial state

The initial state in the column was modelled by discretising the final geometry of the solid column into ten layers and then activating each layer sequentially in the FE analysis starting from the bottom layer. The numerical process involved achieving equilibrium for each activated layer under gravitational loading before the next layer was laid on with a "stress free" state, thereby simulating the progressive filling process (Ai et al., 2011).

A suitable surcharge pressure was also applied to the top surface of each model to create an approximately constant pressure profile in the initial state. This condition allowed

rarefaction waves which were created at the base to travel as far as possible through material in a constant state of stress before they interact with the top surface. Since the analytical solutions essentially describe a semi-infinite column, this technique provided the longest time over which we could directly compare the solutions.

5.3.2 Generation of rarefaction waves

Once properly initialised, rarefaction waves of various sizes were generated at the base of the column by the action of a kinematic boundary condition. In practice this was achieved by accelerating the boundary downwards until it reached a specified velocity which represents the initial size of the disturbance. The form of this boundary disturbance is given in Equation (5-17), and shown in Fig. 5-5:

$$u(t) = \begin{cases} \frac{u_0}{2}\left(1-\cos\frac{\pi t}{0.005}\right) & \text{for } t < 0.005s \\ u_0 & \text{for } t > 0.005s \end{cases} \tag{5-17}$$

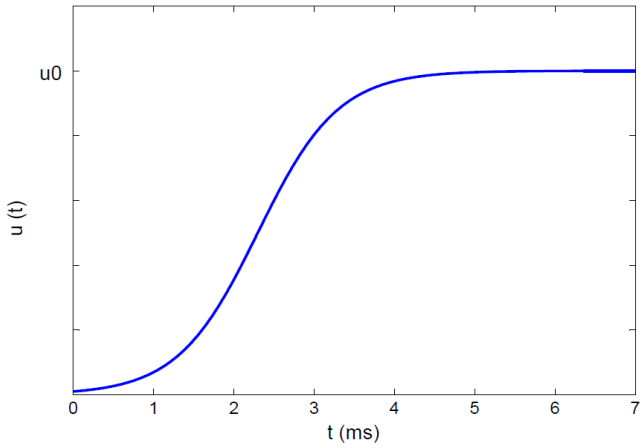

Fig. 5-5 Boundary condition applied to the base of the column to produce a rarefaction wave

The wave generated by this disturbance then travels upward through the material until it reaches the top surface. During this time we can examine the behaviour of the wave in terms of the velocity and stress profile of column.

5.4 Simulation results

5.4.1 Parallel column (α=0)

All of the rarefaction waves generated in the parallel column appeared to grow exponentially as predicted by the analytical model. Fig. 5-6 shows some typical results for a 1 m diameter column with a coefficient of friction of μ=0.3, an initial density of 1500 kg/m^3, and subject to the boundary condition shown in Fig. 5-5 with discharge velocity u_0=0.05 m/s.

In Fig. 5-6, the movement and growth of the rarefaction wave can be clearly seen. Also shown in Fig. 5-6 is the predicted magnitude from Equation (5-1). It is immediately apparent from that the rate of growth matches reasonably well with the predicted behaviour from the analytical model. In this case of a parallel column ($\alpha = 0$), the analytical model has been validated experimentally (Roberts, 1996; Wensrich, 2002; Roberts and Wensrich, 2002). Furthermore, we explored the time history of pressure at typical wall points (A, B, C and D) of different heights (h_1=1.5 m, h_2=2.5 m, h_3=3.5 m and h_4=4.5 m) in the column (see Fig. 5-7). It is clearly seen that the peak of normal pressure is growing as the wave travels upwards, and then it seems to shrink when

reflected by top surface of the material. This provides us with some confidence over the accuracy of the FE model.

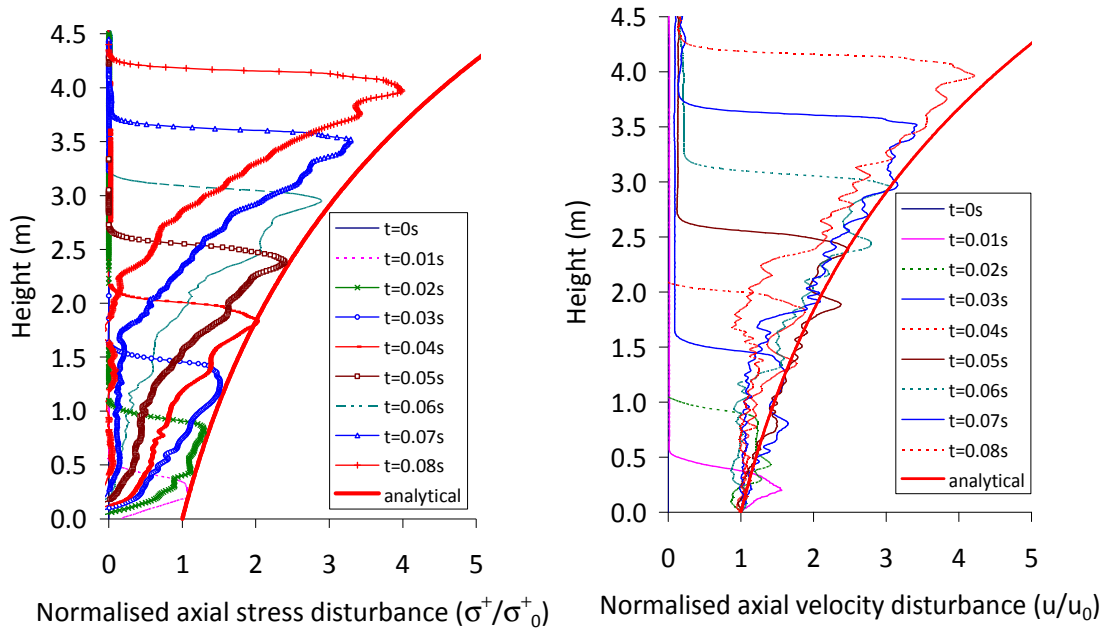

(a) **(b)**

Fig. 5-6 Propagation of a rarefaction wave up the material column. The numerical solution shows an exponential growth of the magnitude of the disturbance with column height: (a) shows the disturbance in terms of axial stress; (b) shows the disturbance in terms of velocity. In both cases, the magnitude of the disturbance is normalised by the initial magnitude generated by the boundary condition

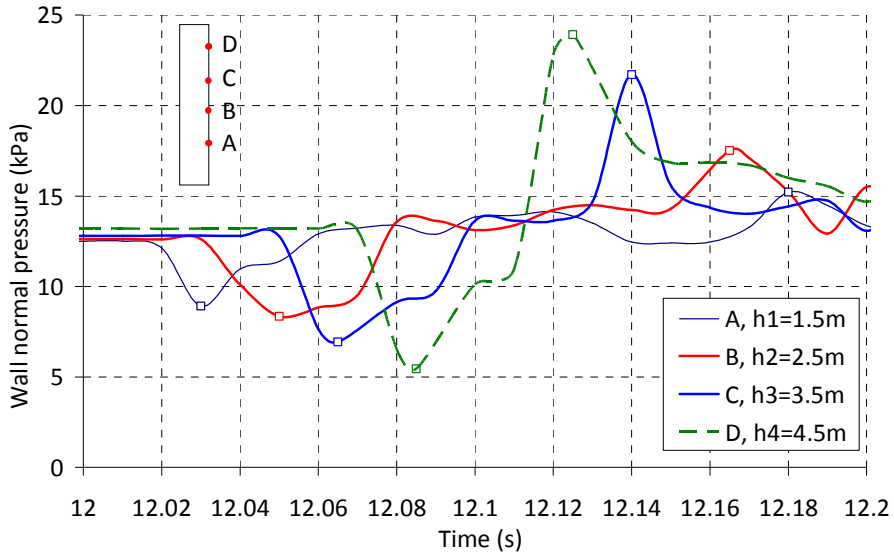

Fig. 5-7 Time history of wall normal pressures at typical wall points of different heights in the parallel column

Fig. 5-8 (a) shows the cross-diameter velocity profiles at four different heights (h_1=1.5 m, h_2=2.5 m, h_3=3.5 m and h_4=4.5 m) of the parallel column at the moment when the rarefaction wave reaches. From Fig. 5-8, it is seen that the axial velocity profile is approximately constant across the diameter. Fig. 5-8 (b) shows the cross-diameter radial stress profiles at the same heights and at the same time points, respectively, as those for the velocity profiles. Similarly, uniform stress profiles exist across the diameter within the parallel column of material.

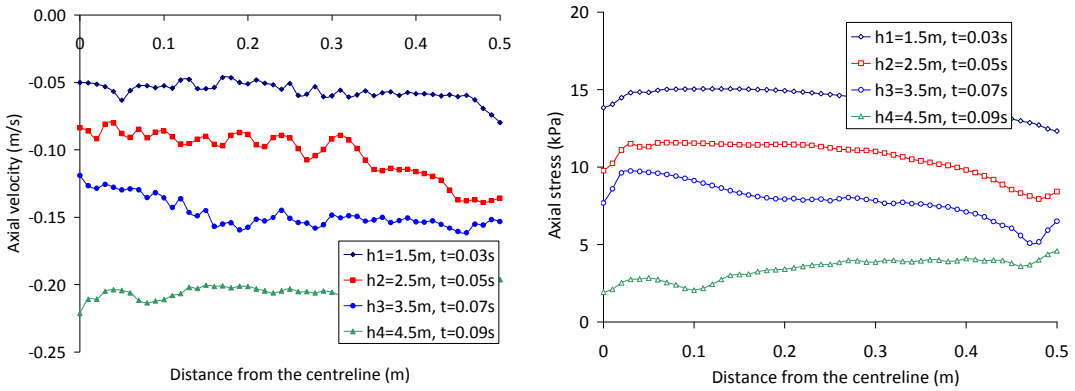

(a) **(b)**

Fig. 5-8 Profiles of characteristics across the diameter at different heights in the parallel column (α=0°): (a) shows the axial velocity profile; (b) shows the axial stress profile

To develop this further, a range of simulations were carried out over a range of parameter values. In each case, we can directly compare the rate of exponential growth in the numerical simulation to the analytical model. A similar comparison between the analytical model and experimental measurements has been made by Wensrich (2003).

Table 5-2 summarises the 5 different simulations that were carried out. In each case, Table 2 provides the model parameters, a calculated value of Janssen's characteristic depth X_o, and an exponent of the rate of exponential growth predicted by each FE simulation. The Poisson's ratio ν assumed in each simulation has been varied to give rise to different values of lateral pressure ratio k so that the influence of k can be explored. In each case, the value of k has been evaluated as the ratio of the transverse to the axial stress in each numerical simulation after the initial state of stress has been established (see Section 5.3.1). Fig. 5-9 compares the predicted rates of exponential growth as a function of the Janssen characteristic depth X_0 for this set of simulations are

compared with the exponent given by from Equation (5-1). A good degree of agreement is observed.

Table 5-2 A summary of FE results

No.	*D* (m)	μ	k	X_0 (m)	u_0 (m/s)	Exponent
FE-1	1	0.3	0.55	1.51	0.05	0.3
FE-2	1	0.5	0.7	0.71	0.05	0.53
FE-3	1	0.3	0.32	2.61	0.05	0.16
FE-4	1	0.3	0.4	2.08	0.05	0.22
FE-5	0.5	0.3	0.65	0.64	0.02	0.7

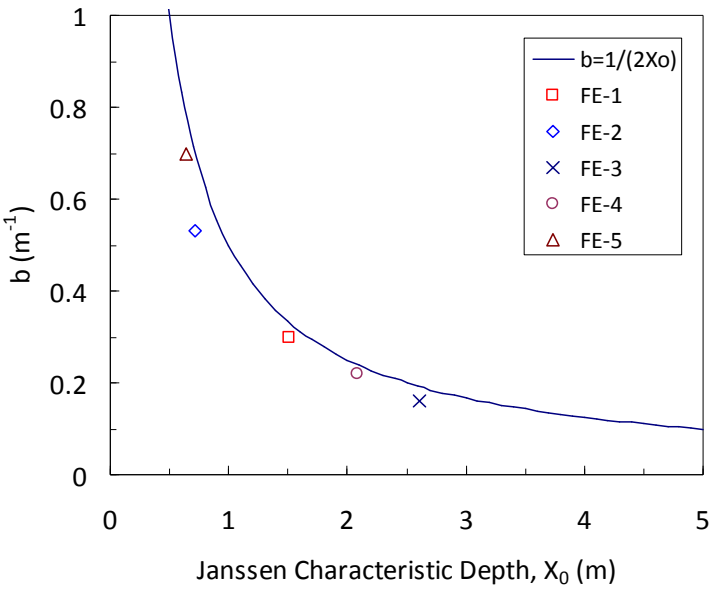

Fig. 5-9 Predicted exponential growth constant as a function of Janssen characteristic depth

5.4.2 Converging/diverging columns

With some confidence in the ability of the numerical model, we now turn our attention to the case of convergent/divergent columns. A number of simulations were carried out over a range of cone half-angles from $\alpha = -10^0$ (diverging) to 10^0 (converging). The properties in Table 5-1 were used for all these simulations.

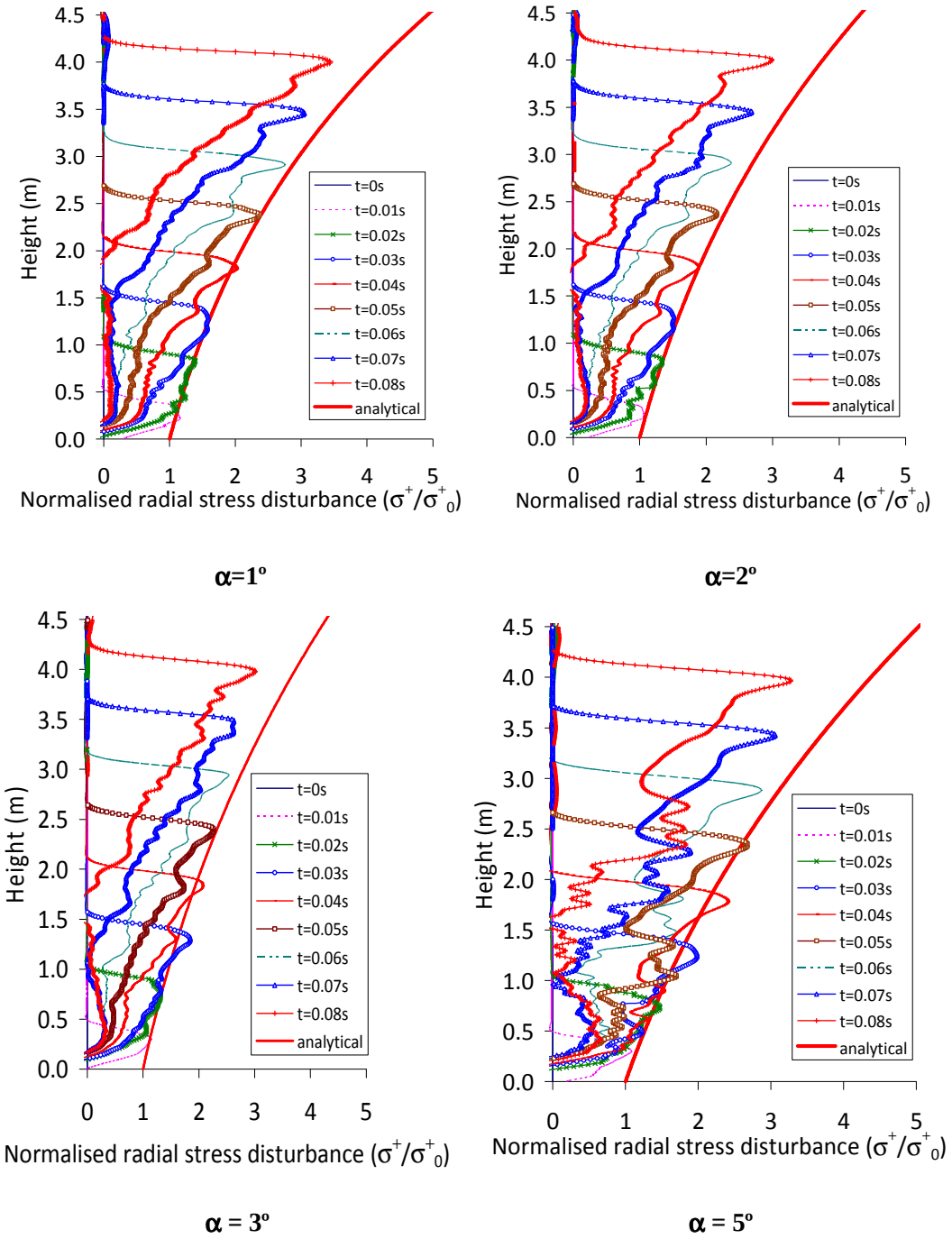

Fig. 5-10 Propagation of a rarefaction wave up the converging column with various half angles. The numerical solution shows an exponential growth with vertical height.

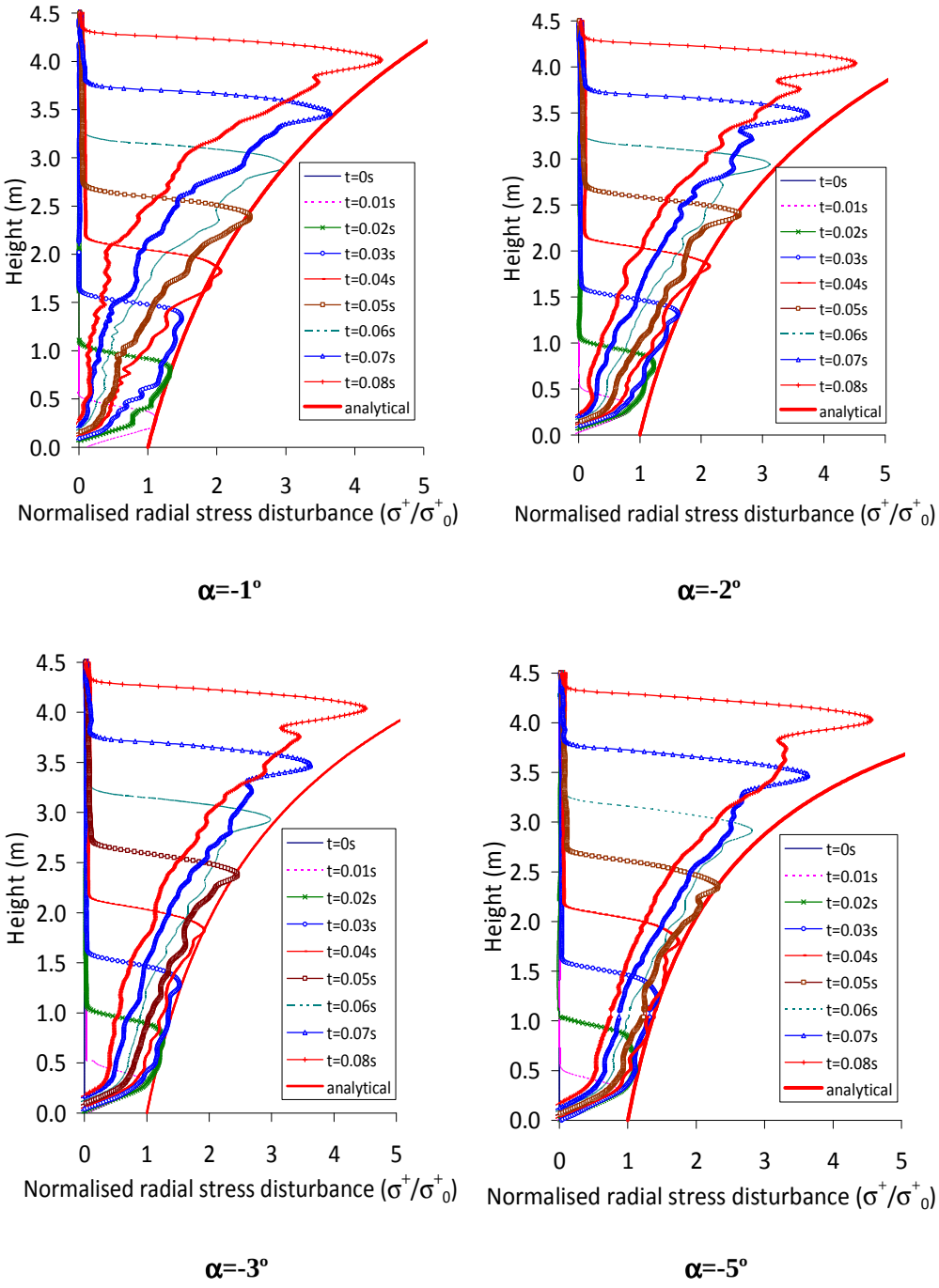

Fig. 5-11 Propagation of a rarefaction wave up the diverging column with various half angles. The numerical solution shows an exponential growth with vertical height.

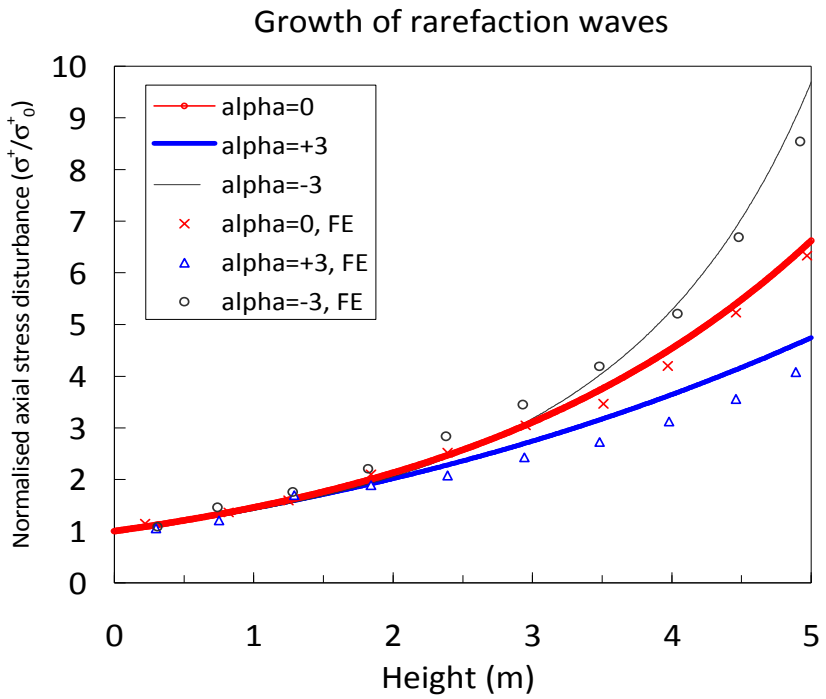

Fig. 5-12 Growth of rarefaction waves with distance travelled for varying half angles of cone

Fig. 5-10 and Fig. 5-11 show the results of a series of simulations for various half angles. The movement and growth of the rarefaction wave can be clearly seen. In particular, it is also clear that the rate of growth for the divergent case is noticeably more that than that of the convergent column. Also shown in Fig. 5-10 and Fig. 5-11 are the predictions from the analytical models. We note that the FE predicted growth of the wave for both cases match the analytical solutions fairly well.

This data is shown again in Fig. 5-12 in the form of the peak values reached by the waves at different heights. These values are directly compared to the analytical solutions for the parallel, convergent and divergent columns. It is evident that the analytical models describe the behaviour of the FE simulations well within the range ($-3^o < \alpha < 3^o$).

When we stray further from this range the quality of the prediction begins to suffer. We can measure the quality of the prediction by calculating a representative deviation between the FE and the analytical solutions. From the FE solution we can obtain the position of the peak of the wave $x_{\max}$ and the corresponding magnitude of the disturbance $\sigma^{+}_{\max}$ at a series of representative time steps t_i. Using these values, we can calculate a representative deviation from the equation:

$$S_0 = \sqrt{\frac{1}{N}\sum_{i=1}^{N}\left(\frac{\sigma^{+}_{\max}(t_i) - \sigma^{+}_{p}(x_{\max})}{\sigma^{+}_{0}}\right)^2} \tag{5-18}$$

where σ^{+}_{p} is the predicted magnitude of the disturbance given by Equation (5-1), (5-14) or (5-15) as appropriate.

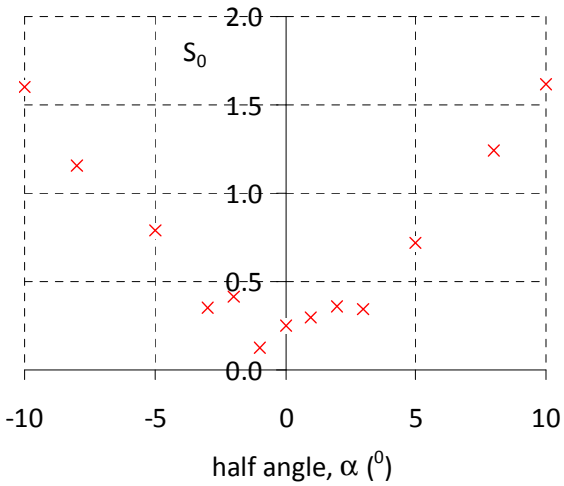

Fig. 5-13 Deviation of stress disturbance between analytical and numerical predictions

Fig. 5-13 shows the results of this calculation as a function of the cone half-angle α. The discrepancy between the analytical predictions and the numerical results is relatively stable over the range of -3° < α < 3°. Outside of this region the prediction

rapidly begins to deteriorate. It is most likely that this is due to the violation of our assumption that the system can be treated as being one-dimensional. In other words, the magnitude of the variation in the velocity profile across the differential slice is no longer insignificant.

5.4.3 A hopper with a large half angle

Fig. 5-14 shows the normalised radial stress disturbance (σ^+/σ^+_0) at different time points in hoppers with an apex half angle of 22º. As shown in Fig. 5-14, the movement of the rarefaction waves can be seen. However, the waves are not growing but, shrinking with the distance they travelled. It is apparent that the predictions using the one-dimensional analytical model deteriorate and does not match those in numerical simulations at all.

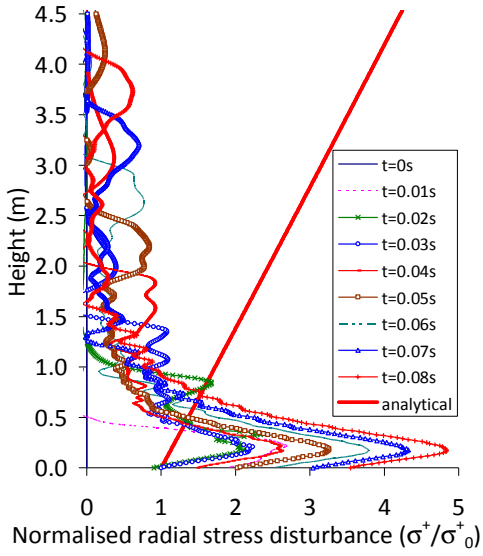

Fig. 5-14 Propagation of a rarefaction wave up the material in hoppers with a large half angle of 22º

Fig. 5-15 (a) shows the cross-diameter velocity profiles at four different heights in the hopper at the moment when the rarefaction wave reached. Unlike constant velocity

profile in parallel column (α=0°), noticeably non-uniform velocity profile is created in the hoppers column with large half angles. Fig. 5-15 (b) shows the cross-diameter radial stress profiles at the same heights and at the same time points, respectively, as those for the velocity profiles. These unsteady states across the diameter in the hoppers lead to the invalidity of the analytical model with the assumptions that the material moves in one direction only, and that the velocity profile is constant across the diameter.

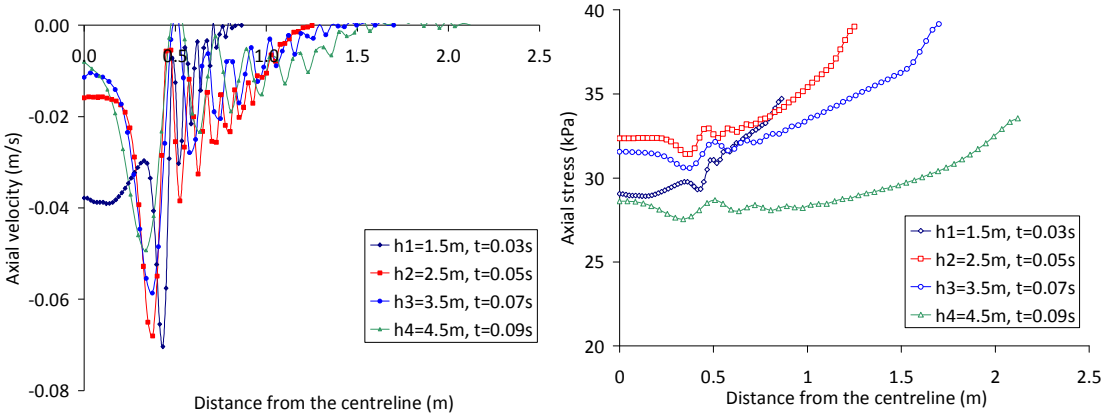

(a) **(b)**

Fig. 5-15 Profiles of characteristics across the diameter at different heights in a hopper with a large half angle (α=22°): (a) shows the axial velocity profile; (b) shows the axial stress profile

5.5 Concluding remarks

The propagation of one-dimensional longitudinal pressure waves in granular material has a significant influence on industrial handling of granular material. Following on from the cylindrical model of Wensrich (2002), the effect of slightly diverging and slightly converging boundaries on the behaviour of rarefaction waves in granular columns has been examined. This work has demonstrated that the exponential growth of

rarefaction waves reported elsewhere in the literature can be enhanced or reduced by altering the geometry of the column.

The effect has been successfully demonstrated using a simple one dimensional analytical model together with FE modelling of axisymmetric tapered columns. These two approaches show a good deal of consistency over a range of small cone half-angles ($|\alpha| <$ 3º). At larger angles the analytical model begins to break down. This is thought to be due to the inadequacies of the one-dimensional approach for half-angles outside this region. A more complex two-dimensional version of the dynamic model is required for half-angles greater than 3º. The FE model does not make the one dimensional assumption, and should continue to provide an effective means of studying wave propagation in hoppers and silos with much larger half angles.

The findings above can be extended to the effects on the silo structure. The numerical and analytical solutions have predicted an exponential growth of any rarefaction disturbance propagating up the silo height. It thus provides a possible explanation that during silo discharge, a relatively small stress impulse set off by the incipient discharge at the silo outlet may propagate into a significantly large stress disturbance higher up in the silo which may induce significant dynamics leading to silo quaking phenomenon. Whilst experimental validation of the numerical and analytical predictions of the present study is beyond the scope of this paper, our work supports the hypothesis that a slightly diverging silo (tapering inwards towards the top) would experience a much greater growth of a stress disturbance induced at the silo outlet than a parallel walled silo.

Chapter 6

An investigation of wall pressure and flow in a flat-bottomed silo

6.1 Introduction

Prior to Janssen's theory (1895), experimental investigations into the pressures acting on silo walls have been undertaken by Roberts (1882, 1884). Since then a huge number of tests have been conducted and contributed to the development in the field of silo pressures and flow pattern. A full review is well beyond the scope of this thesis. During silo discharge phenomena pressure fluctuations occur, causing silo quaking which may affect the silo structure. Up to now, many of the problems have not been understood completely. This review will highlight several experimental investigations on dynamic pressures during discharge and associated flow pattern development in full-scale or test-scale silos.

A series of silo model tests with sand was carried out by the researchers at the Technical University of Denmark (Munch-Andersen et al., 1992). These tests were conducted with different test conditions, such as smooth or rough walls, centric stream filling or distributed filling and flat bottom or hopper bottom. These conditions were known to have a great influence on the pressures and the flow pattern. The filling pressure distributions along the silo wall were observed to scatter slightly with respect to the

Janssen profile. By contrast, the discharge pressures were difficult to grasp and they showed significant fluctuations with a mean overpressure of about 1 kPa comparing to the filling pressure. In addition, the flow patterns were investigated and deduced from the shape of the top surfaces and the pressure observations.

Ostendorf et al. (2003) conducted an experimental investigation into dynamic pressures in a large model silo. Adjustable discharge rates between 0.3 kg/s and 10 kg/s were adopted in the discharge process. In this experiment, it was noted that the transient pressure jump occurred at the beginning of discharge. Meanwhile, the pressure fluctuations at the transition between cylindrical section and hopper section were recorded with a frequency of about 0.2 Hz for the discharge rate of 5 kg/s. Furthermore, they drew a conclusion that the frequency of pressure fluctuations increased linearly with the discharge rate. However, presentation of pressure fluctuations at a limit number of positions makes the results unconvincing.

Ding (2005) measured frictional traction and normal pressures in a 9 m tall circular silo. He conducted an investigation into not only the pressure distribution along the generator in the hopper and barrel section but also the hoop distribution by means of placing four equally spaced pressure cells around the transition circumference. It was observed that the pressure had a sudden change in value at the commencement of discharge through the pressure evolution. Furthermore, considerable pressure variations around the circumference just below the transition were recorded.

Ramirez et al. (2010) carried out tests to measure the pressure using plate-type normal pressure cells mounted along a vertical line of the walls of a full-scale silo. Agricultural materials, i.e., wheat and maize, were used in these tests. The experimental results obtained showed that the filling pressure distributions deviated somewhat from the load distribution obtained applying the Janssen's theory. On the other hand, the representative discharge pressure pattern for wheat fitted well with what was expected in a mass flow silo. Meanwhile, a high peak pressure was produced during the discharge of maize near the junction ('effective transition') 1m above the transition between the hopper and the cylindrical part. This observation showed that the 'effective transition' was taking place at that level and indicated a semi-mass flow regime has developed during discharge. Finally, they stated that the interpretation of phenomena studied by means of silo test using pressure distribution obtained by the actual pressure cells during filling and discharge should be carefully carried out and relative values of pressure should be more preferable than absolute ones.

Two key flow patterns may be identified during the discharge of granular material from silos: mass flow and funnel flow (Rotter, 2001). In mass flow all particles are in motion. Funnel flow is generally defined as any flow pattern which is not mass flow, and can be subdivided into internal (or pipe) flow and semi-mass (or mixed) flow. In the semi-mass flow some granular solids are stationary and there is a flow channel boundary separating the flowing and stationary solids. Semi-mass flow is characterised by mass flow in the upper part of the silo whilst converging internal flow takes over nearer the outlet where

stagnant zones of stationary solids appears. The flow boundary intersects with the silo wall at the level called the effective transition.

The study of silo flow is a challenging task and many experimental and analytical approaches have been attempted to investigate the silo flow (Litwiniszyn, 1963; Mullins, 1972; Tuzun and Nedderman, 1979; Zhong et al., 2001; Sielamowicz, 2006; Hartl, 2008). The silo flow has been extensively studied using different numerical methods. They include the pure kinematic approach (Watson and Rotter, 1996), the boundary element method (Wu, 1992), meshless method (Wieckowski, 2000; Beuth et al., 2007), the discrete element method (DEM) (Ketterhagen et al., 2009), and the finite element (FE) method. Compared with other methods, the FE method has difficulties in the simulation of dynamic flowing processes. To simulate silo flow, different FE approaches have been attempted, such as the Lagrangian method with remeshing and rezoning (Martinez et al., 2002), the Lagrangian method with a priori of flow channel boundaries (Vidal et al., 2005), the Eulerian method (Karlsson et al., 1998), the explicit arbitrary Lagrangian-Eulerian (ALE) analysis (Yang et al., 2011), etc.

This chapter presents the results of laboratory tests in a flat-bottomed silo which was carried out by Rotter et al. at University of Edinburgh in 2004. All the resource adopted in the present study has been presented in this thesis. In the laboratory tests, most attention is paid to the pressures exerted on the walls. The dynamic pressures occurred during the discharge process, which have been observed in the silo experiments. The numerical simulation for the material handling in the flat-bottomed silo has been carried out using the FE model based on the uncoupled Arbitrary Lagrangian-Eulerian

formulation. Additionally, the FE prediction of the flow pattern is also presented. The flow channel boundaries are chosen by the position where the vertical velocity at a given height falls below a give proportion of the centreline velocity at that height.

6.2 Methodology

Tests were carried out with dry sand in a flat-bottomed silo located at the University of Edinburgh (Rotter et al., 2004). Normal pressures cells were mounted in the silo wall. Filling and discharge pressure measurements were compared with the FE prediction. Dynamic phenomena mainly in the measured pressure, which occurred during discharge process, were discussed. The flow pattern observed in the silo experiment was also compared with that predicted by the FE simulation.

6.2.1 Test set-up

The model silo was transported to Edinburgh after dismantling at the Technical University of Demark in 2003. The silo walls are made of epoxy and the thickness is 20 mm. A picture of the test rig including filling and storage facilities is shown in
Fig. 6-1. The silo with flat bottom is cylindrical with a diameter of 0.7 m and a height of 4 m. The outlet at the bottom is circular with a diameter of 0.04m (see Fig. 6-2). In the silo wall was installed a total of 56 normal pressure measuring cells at eight levels: seven cells were mounted at a single level and spaced 45º apart around the circumference (see Fig. 6-2). The pressure cells were mounted flat on the inside of the silo wall and were covered with an epoxy adhesive mixed with sand. In this way the

cells did not introduce any imperfections on the silo walls, or cause any change in wall friction. Seven pressure cells, distributed along a vertical line (labelled 5 at Generatrix 225º) (see Fig. 6-2) were selected in the study of this chapter and normal pressure distributions along this vertical line can be obtained. For these selected cells in the present study, A5, B5, C5, D5, F5, G5 and H5 was located at the height of 0.35 m, 0.7 m, 1.05 m, 1.4 m, 2.1 m, 2.8 m and 3.5 m, respectively, above the bottom. Cell E5 was reported to be not working properly and removed in the present study.

Fig. 6-1 Picture of silo facility used for the experiment

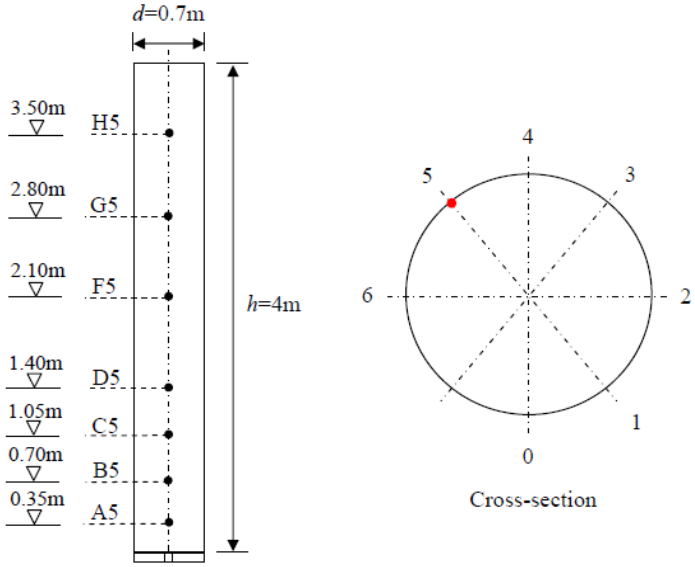

Fig. 6-2 Main dimensions of the silo and pressure cell layout

The normal pressure cells were calibrated and evaluated prior to the tests. Each silo test was conducted in the following way: The filling and discharge processes were approximately 30 min and about 40 min respectively. Between these processes there was a storage period of 26 min. The silo facility was designed for distributed filling which was established by feeding the dry sand such that the surface was kept approximately horizontal. The concentric discharge was operated by opening the outlet at the bottom and the sand was withdrawn under gravity. All the channels were sampled every 6 seconds for obtaining readings from the pressure cells. Analogue signals (mV) from the pressure cells were sampled using a 'MicroLink' data logger connected to a PC. The readings were converted to normal pressure (kPa) by means of the calibration curve, obtained as described in the internal report (Rotter et al., 2004).

6.2.2 Finite element modelling

A FE model based on the ALE formulation was developed to simulate the mechanical behaviour of the granular system during filling, storage and discharge. The model silo was modelled as an axisymmetric system. The dimensions were consistent with those of the flat-bottomed silo model. A concentric circular outlet was set with a diameter of 0.04 m as in the experiment. To achieve accurate results, a fine mesh was employed for the FE model as a result of a mesh sensitivity test. The stored dry sand was modelled using 14000 first-order 4-node quadrilateral elements with reduced integration and the walls were modelled using 200 2-node rigid elements, as shown in Fig. 6-3. The interaction between the walls and sand was modelled using contact surfaces which implement a penalty function to constrain the penetration depth (SIMULIA 2008). This penalty function relates the constraint normal pressure directly to the penetration distance between the wall surface and solid surface. A detailed introduction on the contact surfaces and the penalty function can be found in Chapter 3. The friction at the contact was modelled using the Coulomb friction model with a constant coefficient of friction.

In the FE model, the stored dry sand was described using an elastic-perfectly plastic stress-strain response under a linear Drucker-Prager (DP) failure criterion (SIMULIA 2008).

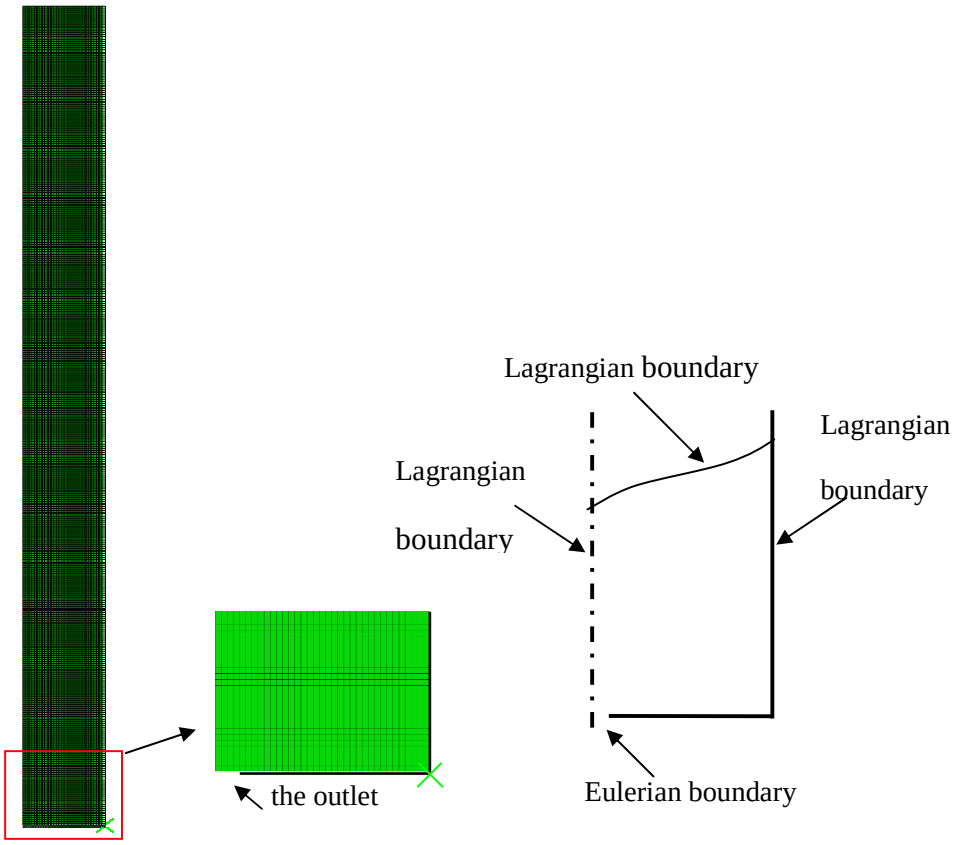

Fig. 6-3 FE mesh and boundaries

Table 6-1 summarises the physical parameters for the dry sand which were collected from the laboratory tests (Zhong et al., 2004; Wojcik et al., 2007; Ding, 2004) and they were used in the present FE model. The elastic modulus of the sand was chosen as 2.0 MPa, which was estimated from the confined compression tests (Ai, 2010).

Table 6-1 Material properties used in the FE model

Physical parameters	value
Average unit weight γ (kN/m^3)	14.27
DP friction angle ϕ_i (º)	35
DP dilation angle ψ (º)	10
DP cohesion c (Pa)	1
Young's Modulus (MPa)	2.0
Coefficient of wall friction	0.63

To avoid mesh distortion due to large deformation during the discharge in the silo, the uncoupled Arbitrary Lagraing-Eulerian technique was employed in the program Abaqus/Explicit (SIMULIA 2008). Similarly, the ALE boundaries were defined as those for the hoppers in previous chapters. The sides and top surface of the material were defined as Lagrangian boundaries while the outlet was set to be an Eulerian boundary, as shown in Fig. 6-3.

6.3 Test results and discussion

Fig. 6-4 shows the averaged normal pressures observed at different heights above the bottom of the silo from three tests. The pressure increased progressively until the end of the filling period and stayed almost constant during storage until the start of discharge. The discharge part exhibited the characteristic profile of dynamic pressures during silo discharge. From the curves of B5, C5, D5, F5 and G5, an overpressure can be observed during the early period of discharge. It shows that the overpressure can rise up to 2 kPa

at pressure cell D5 and F5, corresponding to the height of 1.4 m and 2.1 m above the bottom, respectively.

It can be seen that there is no well-defined level at which the discharge pressure started to fluctuate. The fluctuations showed an increase in amplitude with increasing height above the bottom. The pressure started to oscillate strongly with big amplitudes above 1.4 m which were recorded by cells D5, F5, G5 and H5.

A possible explanation can be given to that behaviour from the flow pattern. A semi-mass flow where the boundary of the flowing solid intersected the vertical walls of the silo at a point, leading to local high pressures at this location, was likely to occur in the flat-bottomed silo (see Fig. 6-6). No clearly intersection point could be observed between the flowing zone and non-flowing zone at the walls. The actual shape of the semi-mass flow was quite uncertain, but the top surface indicated that there existed a plug flow zone in the upper part during most of discharge.

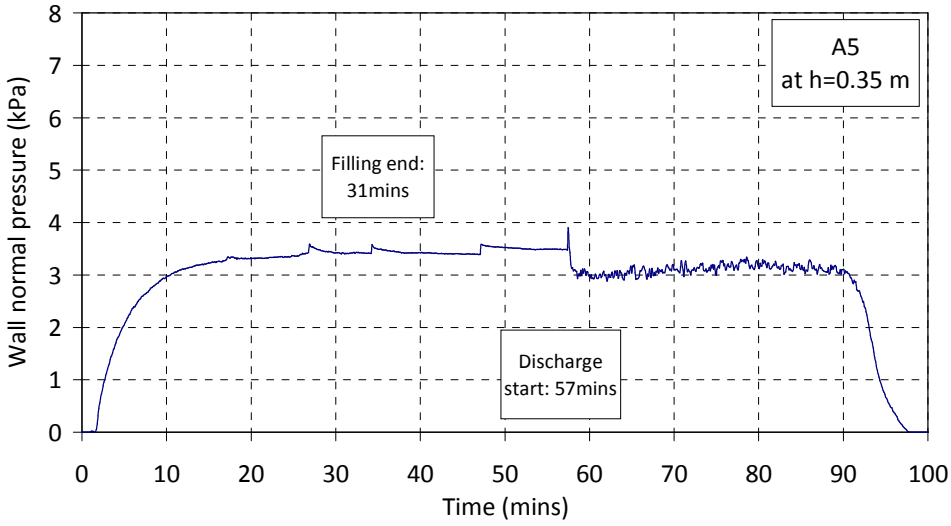
A5
at h=0.35 m
Filling end:
31mins
Discharge
start: 57mins
Wall normal pressure (kPa)
Time (mins)
0
1
2
3
4
5
6
7
8
0
10
20
30
40
50
60
70
80
90
100

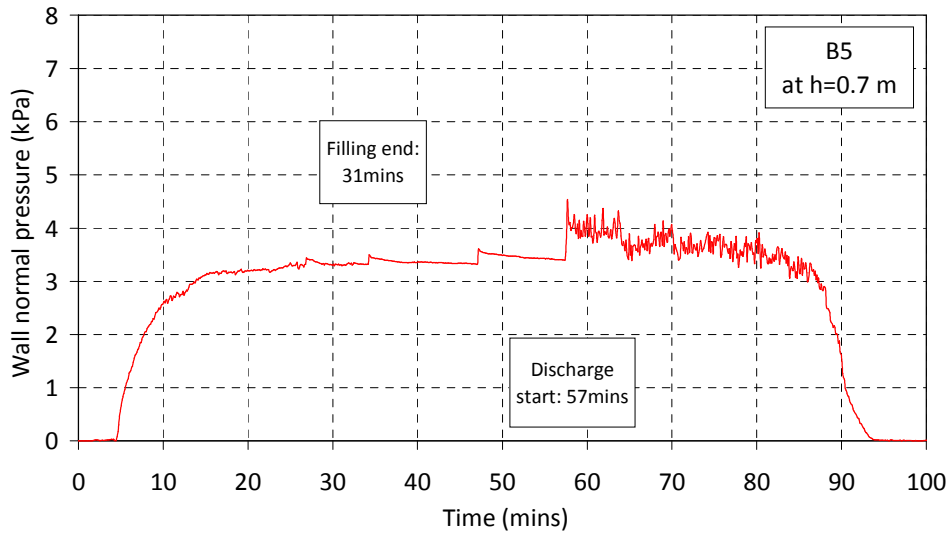
B5
at h=0.7 m
Filling end:
31mins
Discharge
start: 57mins
Wall normal pressure (kPa)
Time (mins)
0
1
2
3
4
5
6
7
8
0
10
20
30
40
50
60
70
80
90
100

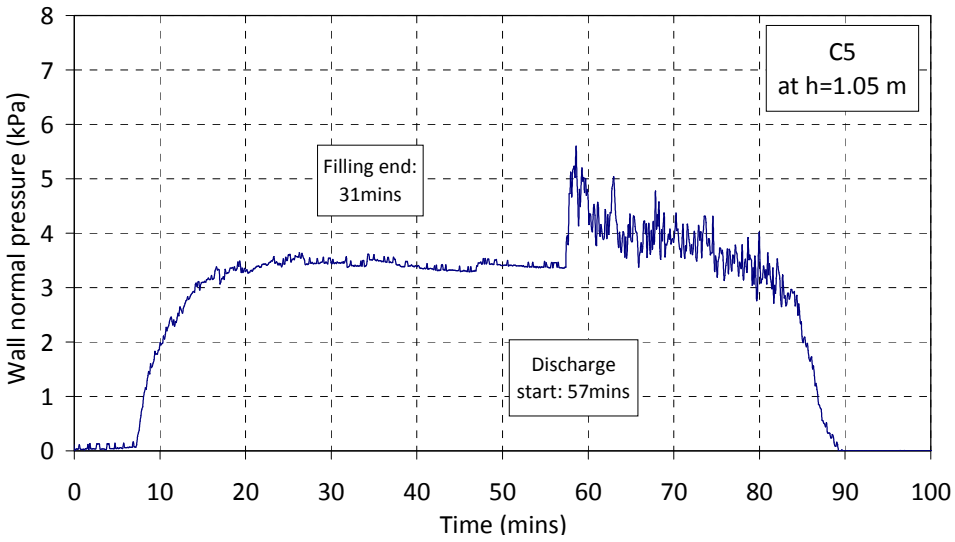
C5
at h=1.05 m
Filling end:
31mins
Discharge
start: 57mins
Wall normal pressure (kPa)
Time (mins)
0
1
2
3
4
5
6
7
8
0
10
20
30
40
50
60
70
80
90
100

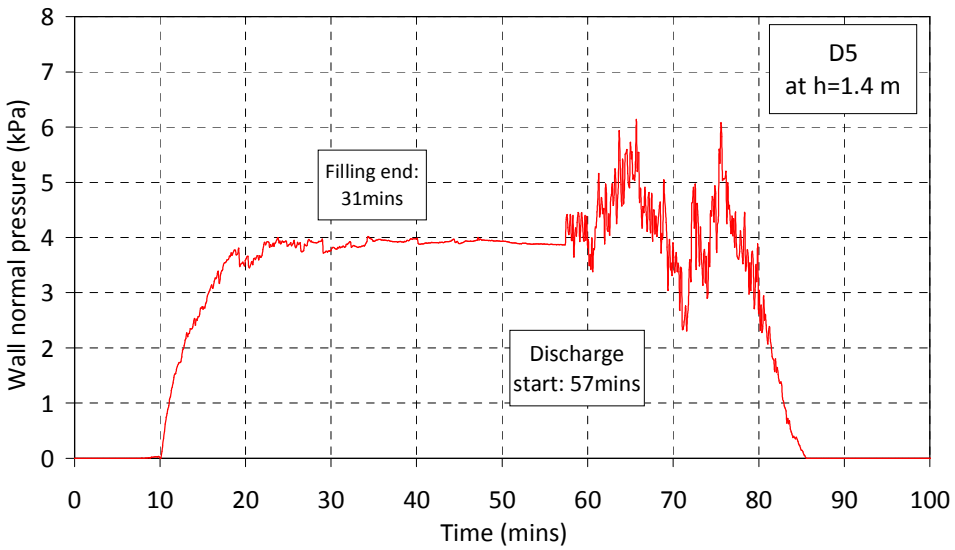
D5
at h=1.4 m
Filling end:
31mins
Discharge
start: 57mins
Wall normal pressure (kPa)
Time (mins)
0
1
2
3
4
5
6
7
8
0
10
20
30
40
50
60
70
80
90
100

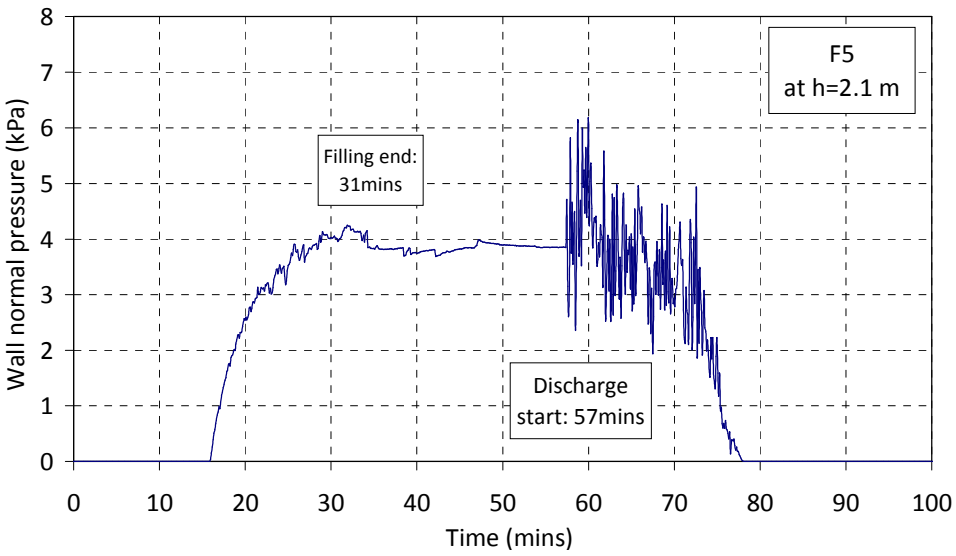
F5
at h=2.1 m
Filling end:
31mins
Discharge
start: 57mins
Wall normal pressure (kPa)
Time (mins)
0
1
2
3
4
5
6
7
8
0
10
20
30
40
50
60
70
80
90
100

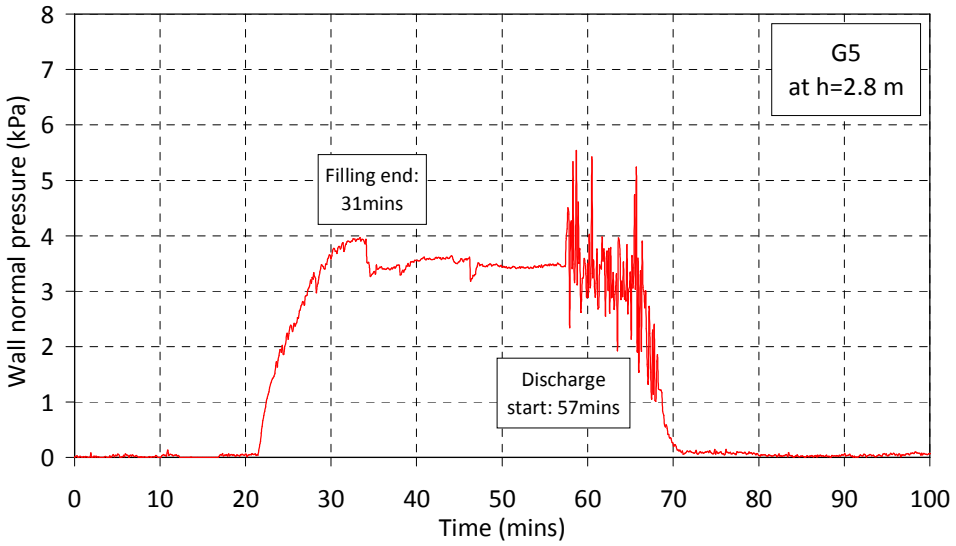
G5
at h=2.8 m
Filling end:
31mins
Discharge
start: 57mins
Wall normal pressure (kPa)
Time (mins)
0
1
2
3
4
5
6
7
8
0
10
20
30
40
50
60
70
80
90
100

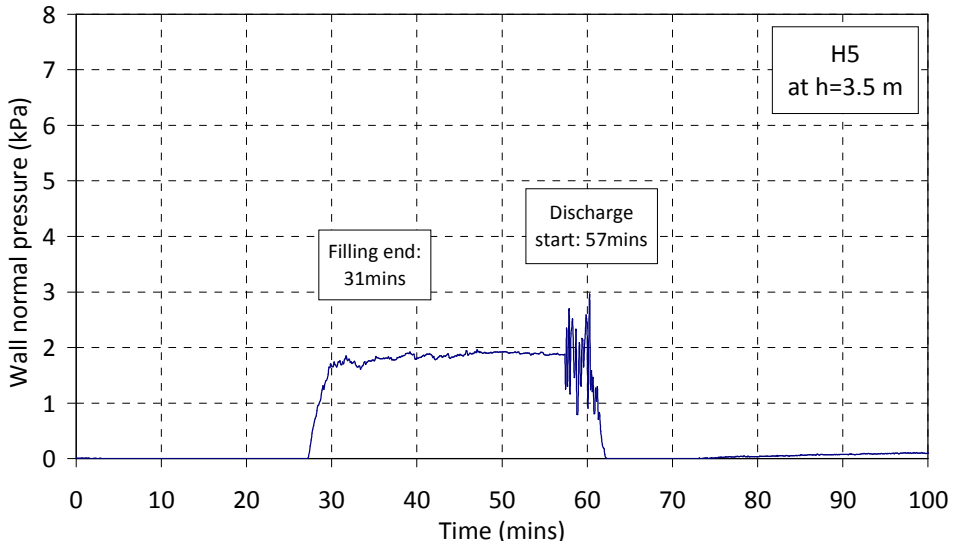

Fig. 6-4 Wall normal pressure measurements for seven pressure cells at different levels along the vertical line (Generatrix 225º)

6.4 FE results

The numerically calculated pressure distribution along the silo walls is compared with the results of the experiments in this section.

6.4.1 Filling pressures

Fig. 6-5 shows the predicted filling pressure distribution in comparison with those obtained by the experiment and classic theory. The experimental results were obtained from the pressures averaged over 10 min after the end of filling. The averaged pressures are determined by the following equation:

$$\overline{p}_{wn} = \frac{1}{N}\sum_{i=1}^{N} p_{wn(i)} \tag{6-1}$$

where $p_{wn(i)}$ represents the normal pressure at a specified wall point at the i th time point and $\overline{p}_{wn}$ is the averaged normal pressure at the corresponding wall point from the N time points within the period of interest.

The numerical predictions were selected at the end of filling analysis. Filling pressures were also calculated using Janssen's formula (1895) with lateral pressure ratio *k* of 0.38 as suggested by Jenike et al. (1973). A good agreement between numerical prediction, the experiments and theoretical solution can be seen in the pressure distribution.

6.4.2 Discharge pressures

To recognize different stages of discharge and directly make a comparison between the experiment and numerical simulation, a volume percentage is introduced to evaluate the emptying level of material. The volume percentage can be determined by following equation:

$$V_{dis} = \frac{V_0 - V'}{V_0} \times 100\% \qquad (6\text{-}2)$$

where *V'* is the transient volume of material left in the silo during discharge, and V_0 is the volume of stored material prior to discharge. The flow was observed to reach the steady state when the volume percentage is about 10% both during the laboratory tests and numerical simulation.

Fig. 6-5 shows the discharge pressure distribution in the early stage of discharge. Due to the strong oscillation of pressure, an averaging process is required. The experimentally

measured pressures were temporally averaged over the first 4 minutes after the start of discharge. And the mean numerically calculated pressures were obtained by averaging over the first 100 seconds after discharge (with a volume percentage of 10%), at which the silo is considered to have the same emptying level of material volume to that in the experiment.

Fig. 6-5 shows that the pressures predicted by the FE model are consistent with those measured in the experiments through the height of this silo. From end of filling to initial discharge, the pressure increased in a zone from about 1 to 3 m above, and decreased rapidly in the bottom zone up to the level of about 1 m. This meant that the mass balance was being fulfilled. The highest values of pressure during the experiment were found in the earliest moments of the discharge and at the effective transitional level (about 1 m above the bottom) where the flow boundary might have intersected the silo wall. It is well accepted that at this transition, high pressures are present when semi-mass flow is taking place as in the experiments. However, this transition may vary in time and space. Therefore, in order to prevent structural failures, it was necessary to understand the development of flow pattern in this type of silo, which will be explored in the flowing section.

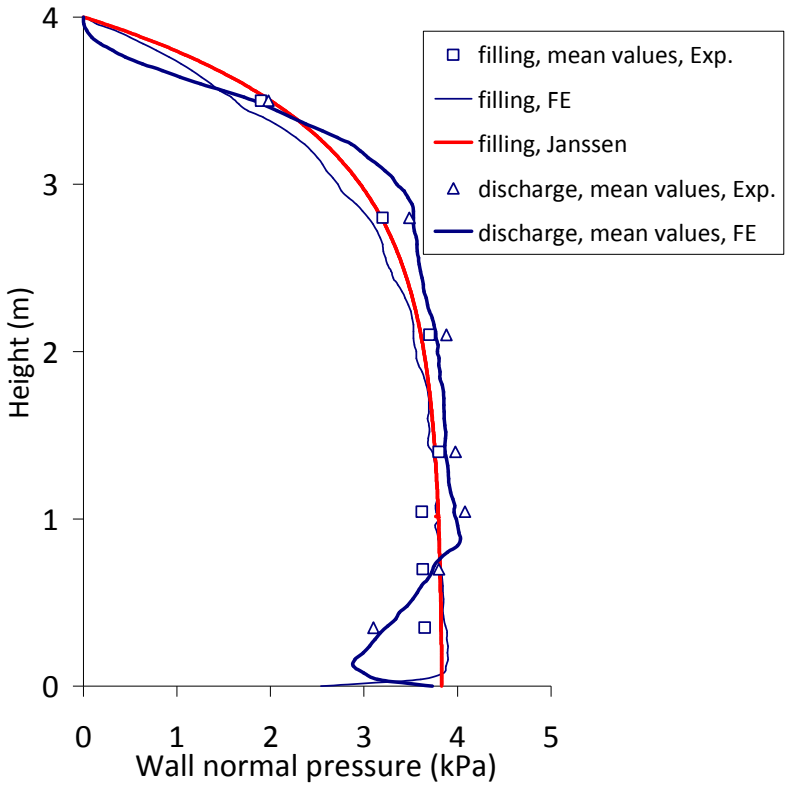

Fig. 6-5 Wall pressure distribution at different stages in the flat-bottomed silo

6.4.3 Flow pattern

The experiments in the flat-bottomed silo have a discharge rate of about 0.1 m height drop per minute. The effective transition height of 0.7 m was observed through the semi-transparent silo wall at about 2 minutes after the start of discharge. It appeared to move upwards for a total of 18 minutes discharging time and stopped at 1 m high, as shown in Fig. 6-6. These observations were based on the observations during the experiments with dry sand.

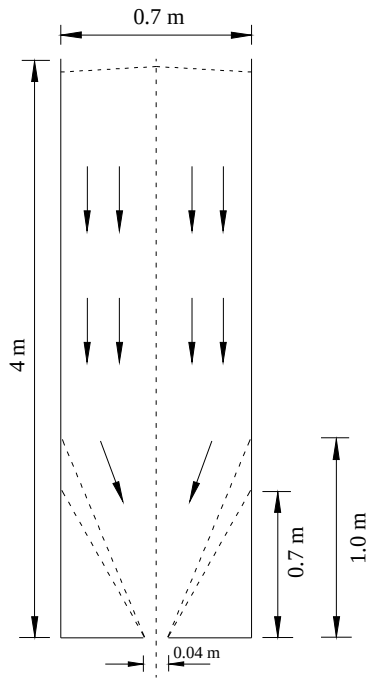

Fig. 6-6 Geometry and observed flow channel boundary of the flat-bottomed silo (redraw after Rotter et al., 2004)

The flow pattern that developed during silo discharge was also evaluated from the FE simulation. To qualitatively present the development of flow pattern, tracers were defined in the referential mesh in the FE model. Using adaptive meshing technique in the ALE method, the movement and deformation of the mesh by definition no longer represent the material movement. The red tracers can be seeded at each node to monitor the material movement. Here, to display the material movement clearly at a reasonable computational cost, a limited number of nodes along several partition lines were seeded with tracers, as shown in Fig. 6-7. The tracer movements at various stages of discharge are displayed in Fig. 6-7. The tracers toward the central axis moved faster than those closer to the silo walls, while the tracers situated at the bottom right-hand side corner did

not move since discharge started. On the whole, the tracer movement indicates that semi-mass flow was predicted.

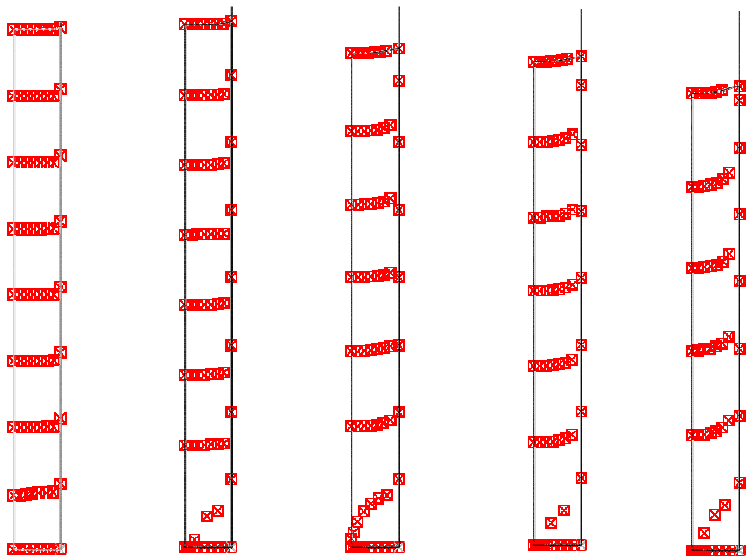

V_{dis}=0.1% **V_{dis}=3%** **V_{dis}=6%** **V_{dis}=10%** **V_{dis}=20%**

Fig. 6-7 Tracer movements versus volume percentage (V_{dis}) at different stages of discharge in the flat-bottomed silo

In addition, the flow channel of the semi-mass flow can be evaluated using the vertical velocity profile of the material. The vertical velocity profiles at various heights for the steady state flow, where the velocity field does not change any more during discharge, are shown in Fig. 6-8. All the vertical velocities have been normalised by dividing them by the modulus of the vertical velocity at the outlet centreline. This produced a minimum normalised value of vertical velocity in the entire domain of -1. It is clearly seen that the flow took place some distance away from the wall, and the flowing zone became wider higher up the height. Above the height of 0.7 m, the uniform velocity profile across the cross-section proves that there existed a plug flow zone in the upper

part of the silo. Below this height, the velocity profile was no longer uniform but started to converge due to the stagnant zone of stationary solid existing at bottom right-hand side corner of the silo. Thus, the flow pattern is typified as semi-mass flow.

A flow channel boundary can be found and defined as the interface between flowing and stationary solid. In the current continuum method, a continuous velocity field throughout the silo can be obtained, which makes it feasible that the flow channel boundary (FCB) is predicted (Watson and Rotter, 1996). First, we postulate a criterion which defines where the flow channel boundary is. In the present study, this was chosen as the position where the vertical velocity at a given height falls below a given proportion of the centreline velocity at that height.

Taking the case of steady-state flow (V_{dis}=10%), Fig. 6-9 shows contours of points at which the vertical velocity has fallen to a given proportion of the centreline velocity at the same height. These contours are deemed to provide a useful criterion from which the flow channel boundary may be drawn (Watson and Rotter, 1996). In Fig. 6-9, it can be seen that the FCB found using a criterion of this kind is not a conical surface (which would be given by a linear relationship between radial coordinate and height) but that it is curved and becomes steeper away from the outlet. As a wide range of conceivable FCB definitions is shown in Fig. 6-9, the insensitivity of the criterion to the adopted proportion is indicated with the flow boundary having the curved geometry. It is likely that we can judge that the solid moving at 0.001 would have indiscernible movement within the timescales and variabilities involved here. Thus, the FCB was chosen somewhat arbitrary to be defined by the criterion at which the vertical velocity is equal

to 0.001 of the centreline vertical velocity at the same height. This is consistent with the experimental observations (0.7 m ~ 1.0 m high for the effective transition).

Next, the development of vertical velocity profile during the discharge process was evaluated from the FE simulation. Fig. 6-10 shows the velocity profile at three instants using the value of 0.001 as the criterion to define the FCB. The evolving FCB at different flow states (represented by discharge volume percentage) is shown in Fig. 6-11. These results match qualitatively well the experimental results (Kvapil, 1959; Lenczner, 1963; Bransby et al., 1973). The contours of vertical velocity obtained from the FE simulation at various discharge stages are shown in Fig. 6-12. It is clearly seen that the flowing zone, which was created at the outlet, rapidly extended upwards to the free surface and then swelled laterally.

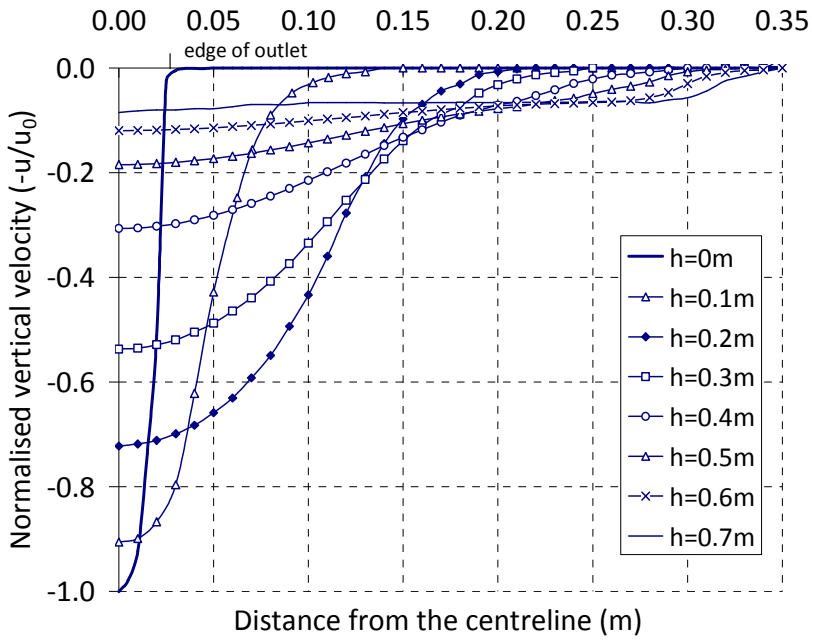

Fig. 6-8 Horizontal profiles of vertical velocity at various heights (steady state flow at the stage of t_{dis}=4 min, V_{dis}=10%)

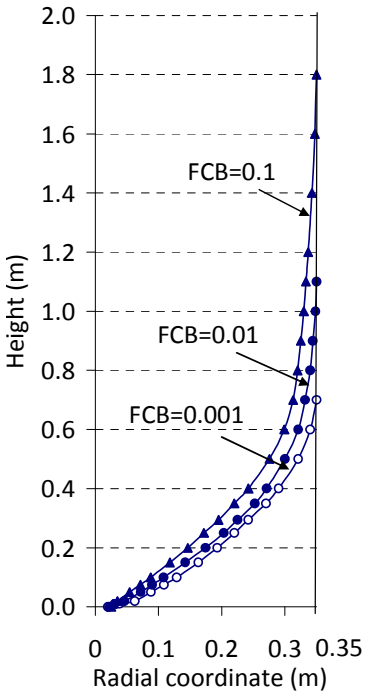

Fig. 6-9 Variation of the flow channel boundary (FCB) with the chosen criterion

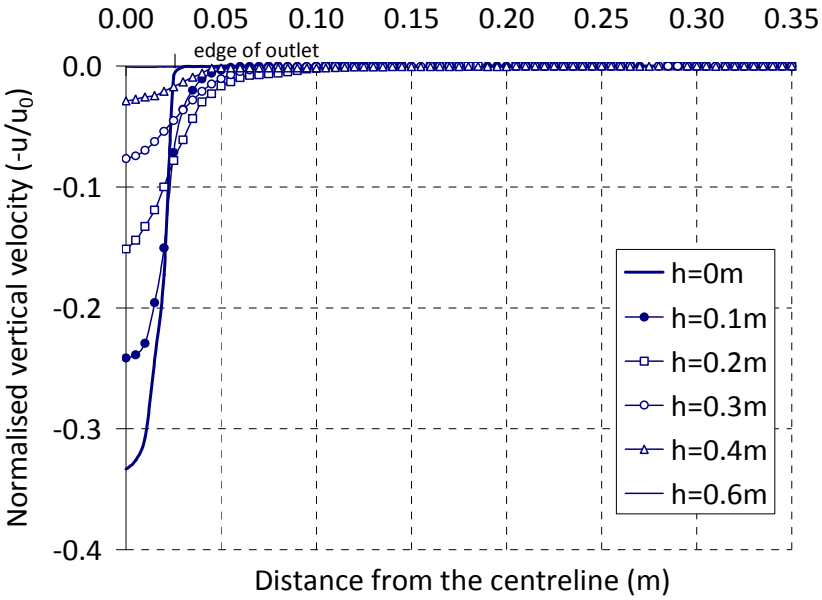

at the stage of t_{dis}=10s, V_{dis}=0.1%

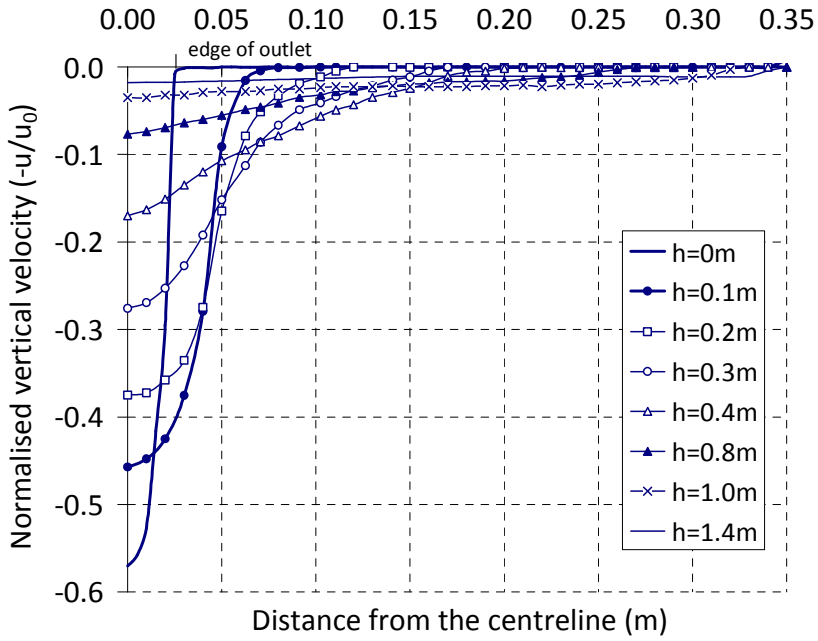

at the stage of t_{dis}=1min, V_{dis}=3%

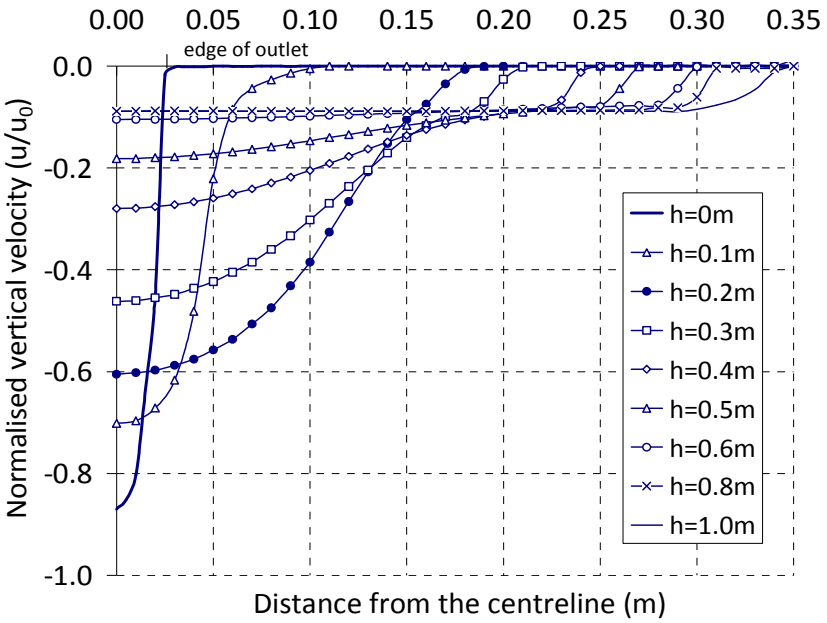

at the stage of t_{dis}=2min, V_{dis}=6%

Fig. 6-10 Horizontal profiles of vertical velocity at various heights at various discharge stages

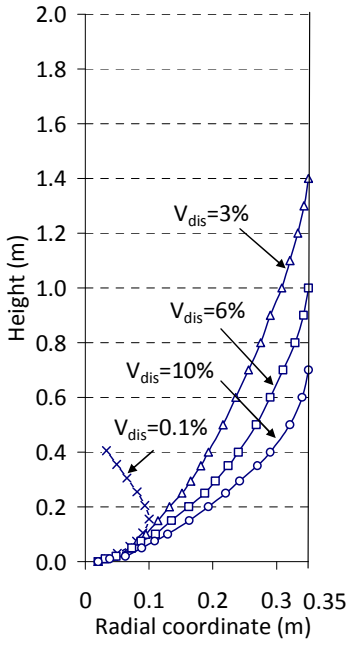

Fig. 6-11 Variation of the flow channel boundary (FCB) at various discharge stages

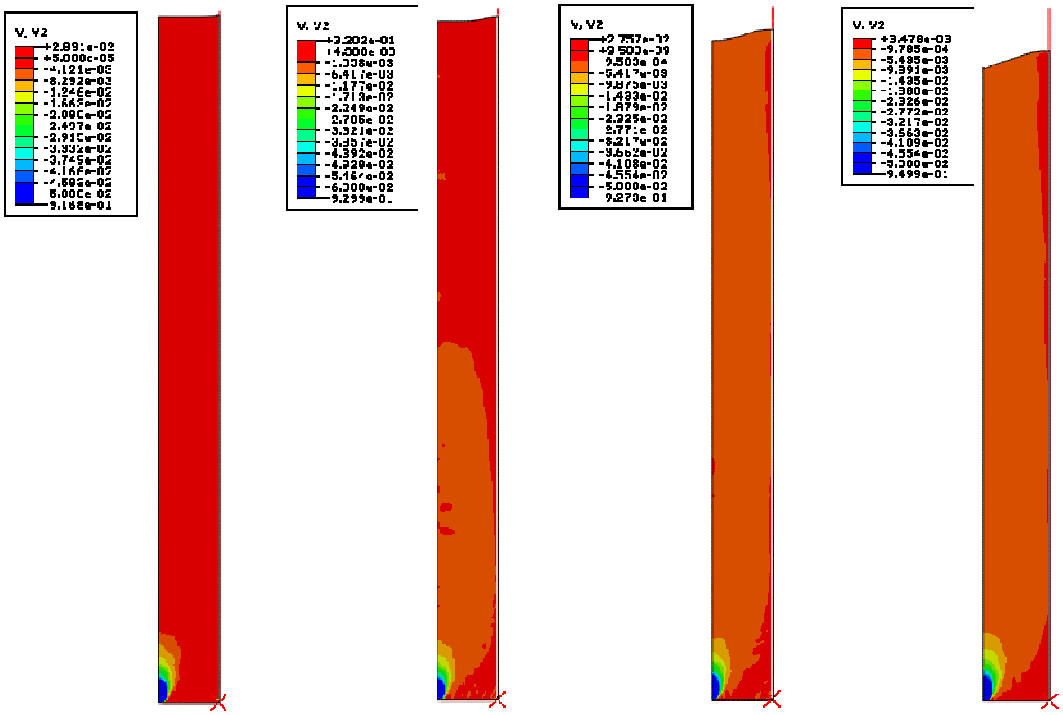

(a) (b) (c) (d)

Fig. 6-12 Contours of vertical velocity at various discharge stages: (a) at t_{dis}=10s, V_{dis}=0.1%; (b) at t_{dis}=1min, V_{dis}=3%; (c) at t_{dis}=2min, V_{dis}=6%; (d) at t_{dis}=4min, V_{dis}=10%

6.5 Concluding remarks

Pressure measurements in a flat-bottomed silo with dry sand have shown that the filling pressure increased progressively as the material was fed into the silo and the pressure stayed almost constant during storage; and the discharge pressure fluctuated with certain amplitudes. The varying extent of pressure fluctuations at the cells can be related to the flowing zone in the semi-mass flow where the fluctuations increased their amplitude with the height above the bottom. The averaged pressure distribution along the vertical line on the silo wall computed by the FE model matched those measured in the

experiment both at the end of filling and during discharge process. Additionally, the flow pattern predicted by the FE simulation has been shown to be semi-mass flow in this silo. The good agreement with experimental results validates the applicability of the FE model based on the uncouple Arbitrary Lagrangian-Eulerian formulation. With the help of particular strength of the ALE method in avoiding mesh distortion and tracking the movement of material, it has produced satisfactory predictions of semi-mass flow and the transient development of flow channel boundary in the flat-bottomed silo.

Chapter 7

Wall pressures in a cylindrical bin with a conical hopper

7.1 Introduction

Silos consisting of a cylindrical bin and a conical hopper (S-CC) are a kind of commonly-used containers for bulk handling in a wide variety of industries. The pressures exerting on the walls during processing are very important parameters concerning the design and safe operation of the silos; however, there is still a lack of clear descriptions of the pressures in this kind of silos, especially during discharge. Simple analytical models published in the past seem to be insufficient to describe the complex behaviour of granular material in silos of such geometry. More sophisticated numerical simulations that take into account aspects such as the silo geometry, interaction between granular solid and the silo walls, as well as emptying process, could provide much greater capacity for investigating into such complex response phenomena.

The last two decades have seen many attempts at developing finite element (FE) models to represent the behaviour of granular materials during silo discharge (Rombach and Eibl, 1998; Ayuga et al, 2001; Guaita et al, 2003; Wojcik et al, 2009; Wojcik and Tejchman, 2009). However, apart from the difficulty with mesh distortion caused by large deformations as discussed in previous chapters, it has been evident that the continuum FE method has other limitations in simulating granular flow in such silos. For

instance, it is difficult to handle an abrupt change of direction at the transition from the vertical section to the converging section (Ooi, 1990; Ding et al., 2003). The numerical difficulty with the singularity at the transition has not been addressed fully in the literature. Existing continuum approaches often circumvent the problem by using a conical hopper and flat-bottomed silo to examine the silo flow (Wojcik and Tejchaman, 2009; Yang et al, 2011).

Another aspect that is of particular importance to the simulation of the wall-pressure distribution in S-CC, as well as in other types of silos, is the interaction between the silo structure and the stored material. According to Janssen's law, the saturated level of wall pressures strongly depends on coefficient of wall friction μ_w. Traditionally, wall friction behaviour can be described by the Coulomb friction model, relating tangential and normal pressures on the walls through a constant friction coefficient. Such a simplified approach is sufficient to describe the frictional behaviour for silo filling and storage, but it is not when comes to silo discharge during which the coefficient of wall friction may markedly vary due to relatively rapid sliding velocity of solid particles against the walls (Moore, 1975; Tejchman, 2001; Artoni et al., 2009). A modification factor may be adopted to represent the variability of the coefficient of wall friction, in accordance with a normal wall pressure distribution (Rotter, 2001), and the maximum and minimum values of the coefficient of wall friction may be calculated by multiplying and dividing the mean value by the modification factor (Vidal et al., 2005). However, an investigation of the actual dependence of the wall pressures upon a varying friction condition is still lacking. In order to predict wall pressures in silos during discharge, an appropriate

model which is capable of describing the effect of wall conditions as a function of the flow properties is required in FE analysis (Wojcik and Tejchman, 2009).

This chapter presents the simulation of discharge pressures using the FE model with Arbitrary Lagrangian-Eulerian formulation, particularly for S-CC silos. For verification, a model S-CC silo tested by the researchers at the Technical University of Demark (Munch-Andersen et al., 1992) is chosen for the simulation, and the FE results are compared with the experimental observations. The key aspects in the numerical modelling include dealing with the complex geometry of the silo and the wall boundary condition between the granular solid and the silo walls. The predicted dynamic pressures are studied in detail, and some interpretations of the fluctuating pressure patterns, which were also observed in the experiments, are provided in relation to the study presented earlier in Chapter 4.

7.2 Overview of the silo model test

The silo model tests (herein called “Danish test”), which are used to compare with present FE simulations, were carried out by the researchers at the Technical University of Demark. The model silo has been used for tests with different materials (Munch-Andersen et al., 1992). The present study is focused on the tests with dry sand.

The silo model is 5 m high and has an internal diameter of 0.70m. It is made of epoxy and the wall thickness is 20 mm. A sketch of this silo is shown in Fig. 7-1. The silo is flat bottomed, but can be equipped with a hopper bottom placed on the flat bottom. The

hopper is made of mild steel and it has an apex half-angle α of 20º. A series of tests were carried out with different test conditions, such as smooth or rough walls, flat bottom and hopper bottom. These conditions are known to have a significant influence on the pressures (Munch-Andersen et al., 1992). For the present numerical study, the tests with smooth walls and a hopper bottom are considered.

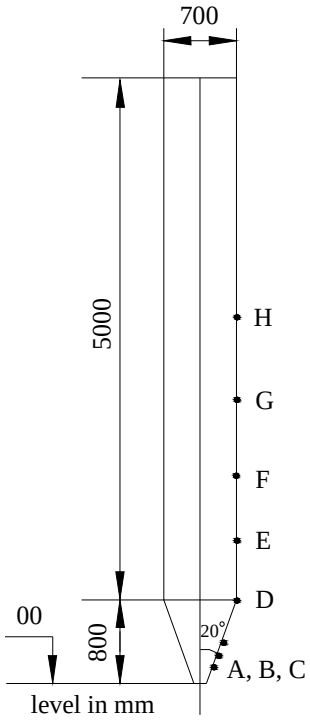

Fig. 7-1: Configuration of the silo model: a cylindrical bin with a conical hopper

7.3 FE modelling

As described in previous chapters, in the present study the FE analysis of granular material behaviour during silo filling and discharge is performed using the uncoupled Arbitrary Lagrangian-Eulerian formulation. By comparing the numerical results with the

observations from the silo model tests involving a hopper bottom, the soundness and accuracy of using ALE modelling to simulate the complex processes involved will be further evaluated.

Similar to the analysis presented in Chapter 4, the granular material is simulated as elastic-plastic body with a Drucker-Prager failure criterion. The contact behaviour at the walls is modelled using a surface contact algorithm which implements a penalty function to constrain the penetration depth (SIMULIA 2008). This penalty function relates the constraint normal pressure directly to the penetration distance. Friction at the contact is modelled using the Coulomb friction model with a constant coefficient. Other general modelling considerations, including the uncoupled ALE formulation with an explicit time integration scheme can be found in Chapter 4.

In the current FE simulations of the Danish tests involving the model silo with a conical hopper and dry sands, the material within the silo is descretised into a fine mesh of first-order 4-node quadrilateral elements with reduced integrations, and the silo walls are modelled using non-deformable 2-node rigid elements.

Material properties representing a cohesionless dry sand are used. Except the Young's modulus and Poisson's ratio, which are defined in accordance with some other dry sand simulations (Ding, 2003), all other properties are obtained from the silo model tests. The mean unit weight γ is estimated from the reported total weight of sand and the filling surface level at rest in the tests. The wall friction coefficient is calculated as the asymptotic Janssen shear stress, $p_w^{\infty}\,(=\frac{1}{2}\gamma R)$, divided by the estimated horizontal

pressure p_h^{∞}. For smooth wall, the lateral pressure ratio is calculated as the asymptotic horizontal pressure divided by the mean measured bottom load. According to the record of the Danish test, the internal friction angle of sand is determined as 40º for the present FE analysis. Typical material properties and corresponding parameters of Drucker-Prager failure criterion are summarised in Table 7-1.

Table 7-1 Material parameters in ALE model

Unit weight (γ)	15.0 kN/m^3
Young's modulus (E)	2.0 MPa
Poisson's ratio (ν)	0.3
DP internal friction angle (ϕ_i)	40º
DP dilatancy angle (ψ)	10º
DP cohesion (c_0)	1 Pa
Coefficient of wall friction	0.67

7.3.1 Treatment of transition

The transition between the vertical section and converging section is a critical point of the silo structure in the FE analysis of silos with a hopper bottom (Ooi, 1990; Keiter and Rombach, 2001) as it may give rise to numerical difficulties. Since the granular solid is treated as a continuum in a classical FE analysis, an abrupt transition on the silo wall is likely to induce a serious singularity problem as material just above it must slide vertically, whilst that below it must slide in an inclined direction. Moreover, an abrupt transition may also generate very high pressure peaks in the FE analysis, as reported by Ooi (1990), Keiter and Rombach (2001). To solve such problems, an artificial geometric

transition termed a knuckle was proposed by Ooi (1990) in which the transition is described by a curved trajectory with a continuous function, and the influence of the knuckle geometries was investigated with polynomials of different orders using cubic element mesh. In the work of Keiter and Rombach (2001), a smoothing of the transition with slope and curve compatibilities of the elements was adopted for handling the singularity problem. Although such treatments have been effective in overcoming the numerical difficulty and reducing spurious pressure peaks dramatically, they do not tend to predict realistically the wall pressure distribution around the transition (Ding et al., 2003). The effect of these treatments on the wall pressure predictions has been discussed in the literature for the silo filling phase; however, little is known about the potential effect for silo discharge.

The finite-sliding formulation in Abaqus/Explicit for contact between two surfaces, as adopted in the present study, allows for arbitrary separation and sliding of the surfaces (SIMULIA 2008). In this formulation, a solid point D' at the transition is constrained to slide along the wall surface, irrespective of the orientation of this surface. This behaviour is possible because the solver tracks the position of the solid point D' relative to the wall surface as the bodies deform. The program uses a global contact searching algorithm to track the motion of the surfaces during the analysis. In this approach it computes the distance from a given slave node to all of the master surface facets and searches only the nearest facet to the slave node. Fig. 7-2 shows the possible evolution of the contact between the solid point D' and wall surface. Solid point D' is in contact with the wall element facet with end point D_1 and D at time t_1. The load transfer at this

time occurs between the solid point D' and wall point D_1 and point D only. Later on, at time t_2, the solid point D' will find itself in contact with next nearest element facet with end point D and D_2 due to the gravity of the material. Then the solid point D' can move along this element face. In the process, the numerical difficulty caused by the abrupt transition is resolved by using the finite-sliding formulation in the program Abaqus/Explicit.

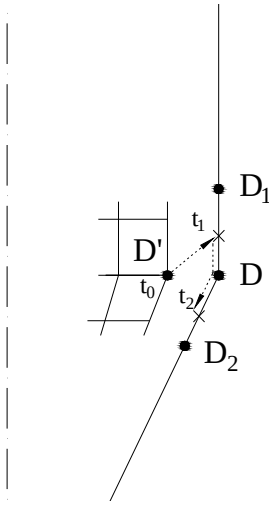

Fig. 7-2 Trajectory of solid point D' in finite-sliding contact

In the present study, the above "abrupt" transition scheme is employed, along with a so-called 'filleting' technique, to examine the effect of transition treatment on the analysis of the S-CC silos during the discharge phase. In the "filleting" technique considered, the vertical section at the top end and the converging section at the bottom are connected by a circular blend of a specified radius in order to smooth the solid and wall edges contacting around the transition, as shown in Fig. 7-3). This technique has been applied successfully by Ding et al. (2003) in which an investigation of geometric effect on the

wall pressures was performed by varying the filleting radius. The finite-sliding formulation was not adopted in the FE model of Ding et al. (2003) when an earlier version of Abaqus was used.

For the comparison herein the silo transition is curved into a smoothed curvature with varying radii of 0.2 m, 1.0 m and 3.0 m, respectively. The transition with a filleting radius of 0.2 m is actually very close to that with an abrupt corner. After each change of the transition geometry, the mesh grid is redesigned as schematically shown in Fig. 7-3.

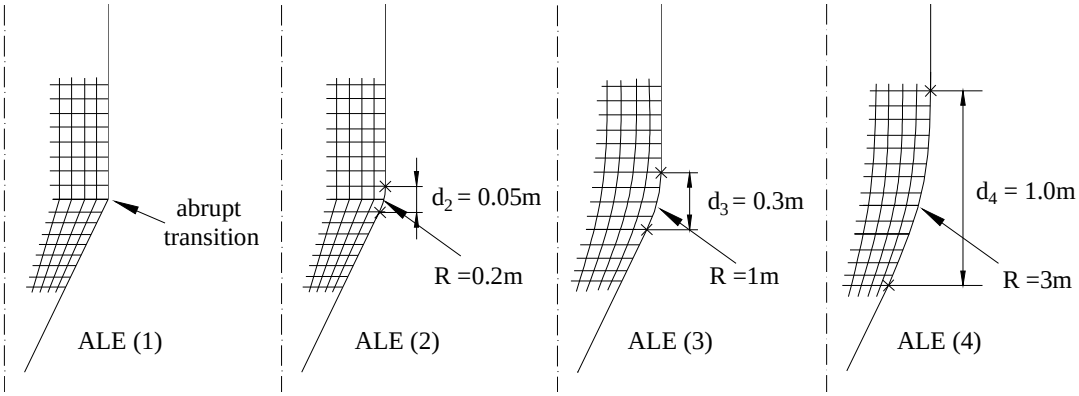

Fig. 7-3 Transition corner: ALE (1) –abrupt transition (no fillet); ALE (2) –filleting radius of 0.2m; ALE (3) –filleting radius of 1m; ALE (4) –filleting radius of 3m

7.3.2 Dynamic friction coefficient

It is generally known that the coefficient of friction that resists the initiation of slipping from a sticking condition is different from the coefficient of friction that opposes ongoing slipping. The former is typically referred to as the static coefficient of friction μ_s, and the latter is referred to as the kinetic coefficient of friction μ_k. Typically, the static coefficient of friction is higher than the kinetic coefficient of friction (Rabinowicz,

1951; Rabinowicz, 1965). The interpretation given by early researchers for this difference was that the strength of the contact junctions could increase with time in stationary contact. It is still a subject of debate about the reasons underlying the difference between static and kinetic coefficients of friction (herein called dynamic friction coefficient).

For the purpose of the present study concerning the influence of dynamic friction coefficient on silo wall pressures is investigated, the static coefficient of friction is considered to correspond to the value given at zero sliding velocity, while the kinetic coefficient of friction corresponds to the value given at the highest sliding velocity. The transition between static and kinetic friction is defined by a series of values specified at intermediate sliding velocities. Such a treatment is supported by a number of experimental observations and empirical formulas, which indicate that the coefficients of friction can be functions of sliding velocity between two surfaces in contact with each other (Kragelskii, 1965; Moore, 1975). Similarly, several empirical expressions have been proposed for quantitative treatments of the stationary contacting time effect on the coefficient of friction (Howe et al., 1955; Derjagin et al., 1957; Rabinowicz, 1965; Brockley and Davis, 1968). For example, Kato and Matsubayashi (1970) proposed that the coefficient of friction can be expressed with a simple exponential formula by the stationary contacting time.

For comparison, two methods are employed to simulate the frictional behaviour at the contact between the solid content and silo walls. One is to model the frictional behaviour using the Coulomb friction model with a constant coefficient which is independent of

the sliding velocity between two surfaces. The other is to describe the frictional behaviour by a model involving a static and a kinetic coefficient of friction directly, where the coefficient of friction is assumed to decay exponentially from the static value to the kinetic value according to the following formula:

$$\mu_d = \mu_k + (\mu_s - \mu_k)e^{-\varpi\dot{\gamma}} \tag{7-1}$$

where μ_k is the kinetic coefficient of friction, μ_s is the static coefficient of friction, ϖ is the decay coefficient which indicates an extent of the sliding velocity effect on dynamic friction coefficient, and $\dot{\gamma}$ is the siding velocity (Oden and Martins, 1985). A schematic illustration of the above relationship is shown in Fig. 7-4.

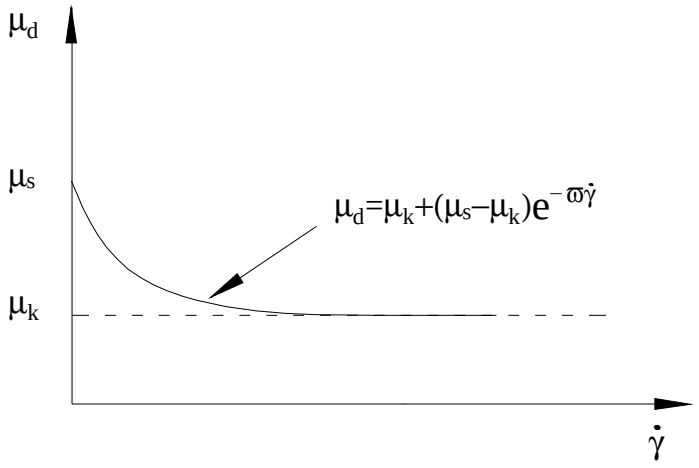

Fig. 7-4 Exponential decay friction model

7.4 Results and discussions

The filling condition is normally used by silo designers and researchers as the reference state against which discharge pressures during flow are assessed and predicted, therefore

a full clear description of filling pressure is vital even for studies of discharge (Rotter, 2002). In this section, the FE analysis results are presented and discussed starting with the filling pressure. It is noted that the filling pressures for the Danish test were obtained by the mean value of 3 cells at each level (Munch-Andersen et al., 1992). The discharge pressures shown for the Danish test are temporally averaged over the initial period of discharge. For the FE prediction, the filling pressures were presented at the end of filling analysis; whilst the discharge pressures were temporally averaged over the initial period of discharge, in line with the Danish test.

7.4.1 Effect of internal friction angle on filling pressure

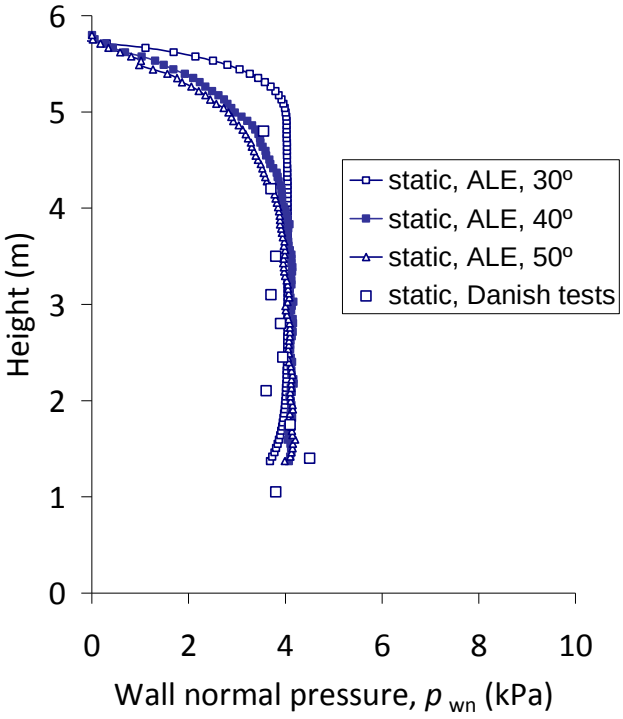

Fig. 7-5 Wall normal pressure at end of filling

According to the record of Danish test, the internal friction angle of sand was determined as 40º. For the present FE analysis, two referential values of 30º and 50º for γ=15 kNm^{-3} in accordance with Eurocode 1 (EN 1991-4: 2006) are used for comparison. Fig. 7-5 shows the wall normal pressures predicted at the end of filling, using the three different friction angles respectively, as compared with the experimental observations. It is indicated that the internal friction angle governs the lateral pressure ratio, which determines how rapid the pressure can achieve the asymptotic Janssen pressure, but has a less effect on the magnitude of the pressure. From Fig. 7-5 it is seen that the FE analysis with an equivalent internal friction angle of 40º matches the

experimental results quite well in the vertical section at the end of filling. Hence, the internal friction angle of 40° is appropriate for the sand in the Danish test and will be adopted in following analyses in this chapter.

7.4.2 Effect of transition corner

Fig. 7-6 shows the wall normal pressures for filling and discharge. In the figure the predictions from the present FE simulation for different modifications of the transition corner are compared with the observations from the Danish test and theoretical solutions.

The filling pressures on vertical walls are calculated using Janssen's formula (1895), and with a value for *k* of 0.38 as suggested by Jenike et al. (1973). The filling pressures on the hopper walls are determined using Eurocode based on Walker's theory (1966), with a wall pressure ratio for active state, $F_f = \frac{1+0.8\mu\cot\alpha}{1+\mu\cot\alpha}$, which was taken from the experimental data of Motzkus (1974). As for the discharge pressures, in vertical section the same method as that for filling pressures is used, while in the converging section these are determined by Walker's theory (1966) with a wall pressure ratio for passive state, $F_e = \frac{1+\sin\phi\cos\varepsilon}{1-\sin\phi\cos(2\alpha+\varepsilon)}$, where $\varepsilon = \phi_w + \sin^{-1}(\frac{\sin\phi_w}{\sin\phi})$, which is considered as a satisfactory estimate under mass flow discharge (Rotter, 2001). When using this method, at the top of the converging section a surcharge load should be given in the present case to represent the vertical load at the bottom of the vertical section, and this was obtained by Janssen's solution.

It can be seen from Fig. 7-6 that the present FE predictions match the experimental measurements quite well in the upper vertical section at the end of filling. For discharge, the pressures predicted along the vertical wall are almost identical to those established at the end of filling, whereas a pressure increase of about 1kPa was observed in the Danish test. Such a difference may be attributable to the use of a constant wall friction coefficient in the numerical simulation. The effect of using a variable coefficient of wall friction (called dynamic friction coefficient) will be explored in detail in the next section of this chapter. In the converging section, no comparison is made here due to a lack of measured data in the Danish test.

From the close-up view in Fig. 7-6, the pressure pattern predicted without filleting shows a significant peak at the transition, which, however, is not as high as seen in previous FE predictions (Ooi, 1990; Keiter and Rombach, 2001; Ding, 2003), and tends to be close to the theoretical results with Walker's solutions for static and flow state. As can be expected, the FE analysis with a very small filleting radius of 0.2 m produces almost an identical peak pressure as that with an abrupt transition. This also serves as a confirmation of the capability of the improved algorithm of contact for arbitrary surfaces in Abaqus program, as described earlier. The pressure patterns predicted with filleting radius of 1 m and 3 m show small peaks but the modification involves a significant 'man-made' section over a range of d_3 and d_4 above and below the transition, respectively, as shown in Fig. 7-6.

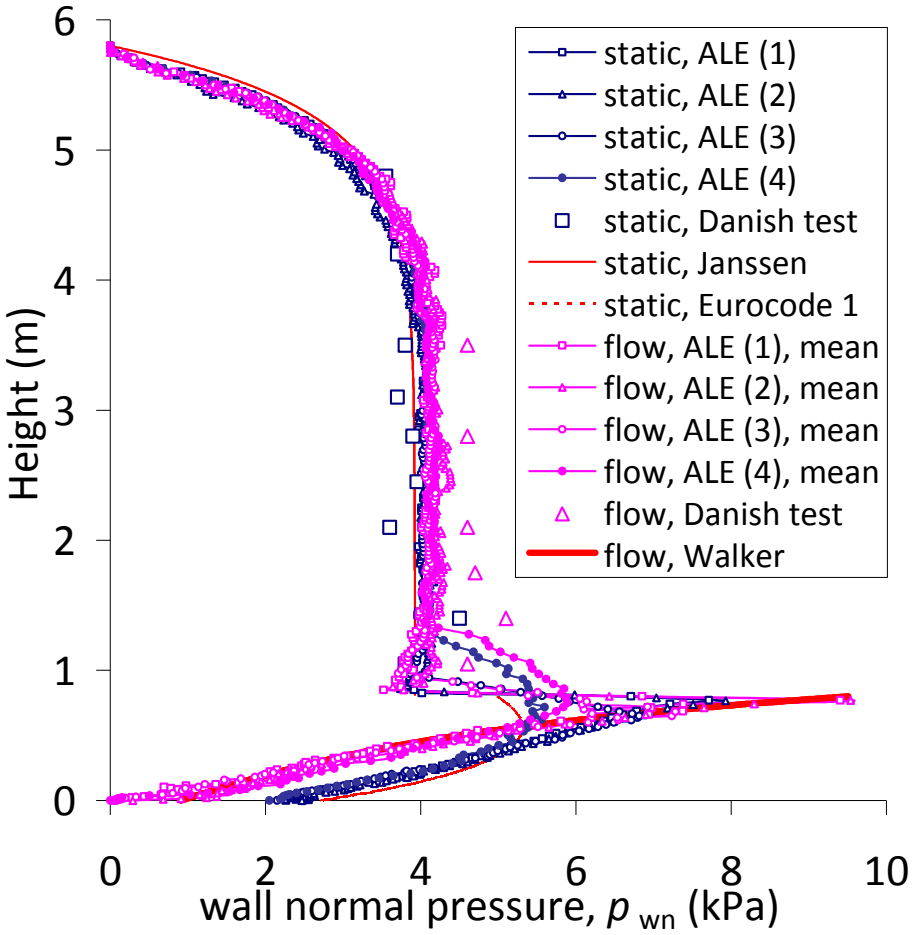
Height (m)
wall normal pressure, p_{wn} (kPa)
0
1
2
3
4
5
6
0
2
4
6
8
10
static, ALE (1)
static, ALE (2)
static, ALE (3)
static, ALE (4)
static, Danish test
static, Janssen
static, Eurocode 1
flow, ALE (1), mean
flow, ALE (2), mean
flow, ALE (3), mean
flow, ALE (4), mean
flow, Danish test
flow, Walker

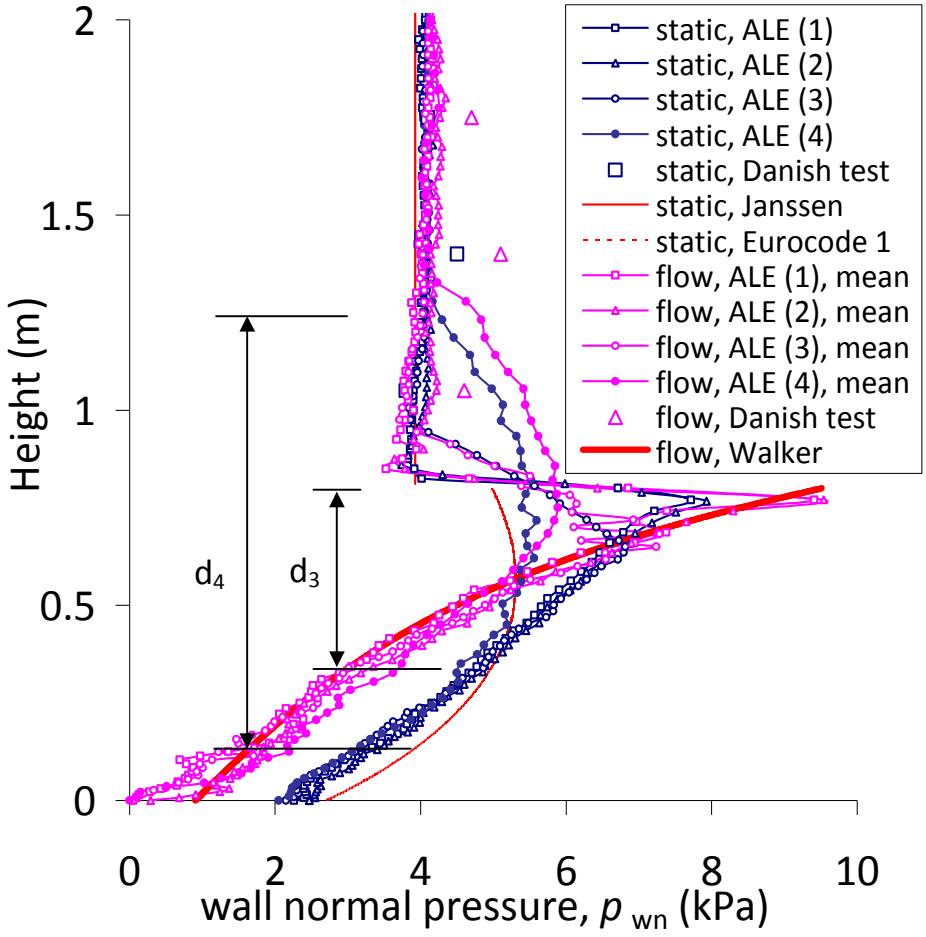

Close-up view

Fig. 7-6 Wall normal pressure distributions: ALE(1) –abrupt transition (no fillet), ALE(2) –filleting radius of 0.2m, ALE(3) –filleting radius of 1.0m, ALE(4) –filleting radius of 3.0m

To further improve the prediction with the abrupt transition (no filleting), especially concerning the pressures around the transition, a finer mesh was used throughout the whole geometry, as shown in Fig. 7-7. Fig. 7-8 (a) compares the predicted wall normal pressure distributions using different element sizes. The values at the transition are plotted against the minimum element size in the whole mesh in the close-up view in Fig. 7-8 (b), and the results show good convergences (see Fig. 7-8 c). The minimum element

size was therefore chosen to be $r/35$ for the present numerical calculations. r is the silo radius of 0.35 m at the transition. The FE mesh for the reference case in the silo with an abrupt transition is shown in Fig. 7-7.

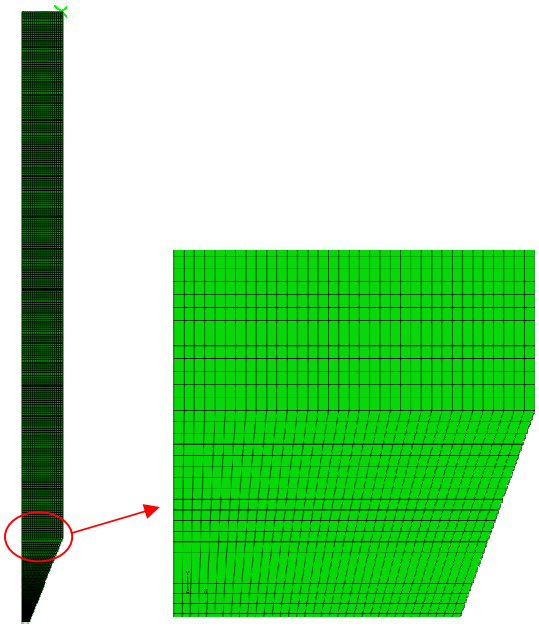

Fig. 7-7 FE mesh: the silo with an abrupt transition (no filleting)

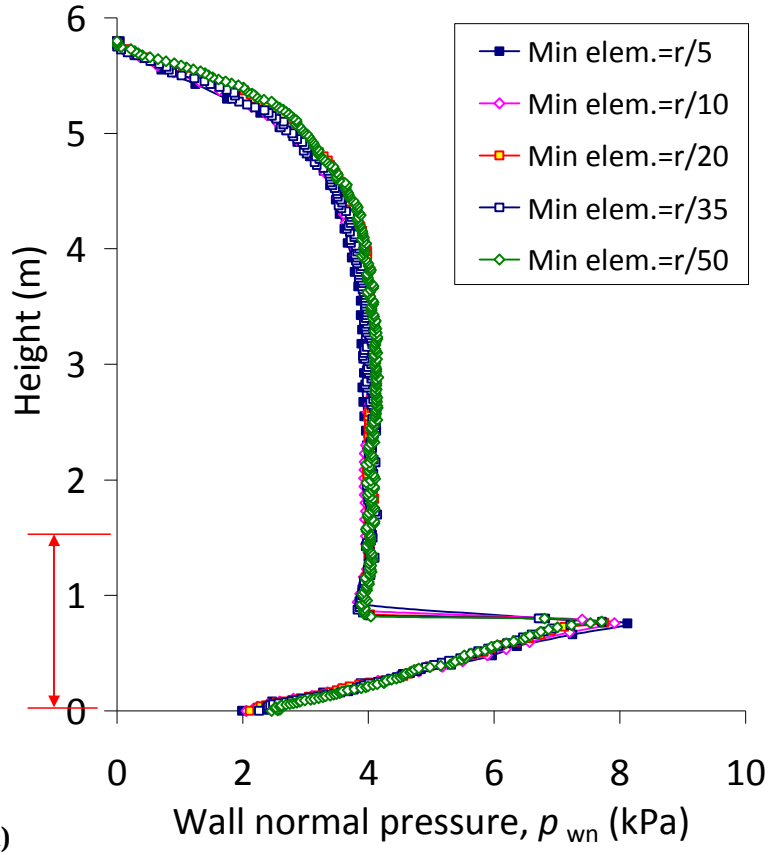
Min elem.=r/5
Min elem.=r/10
Min elem.=r/20
Min elem.=r/35
Min elem.=r/50
Height (m)
0
1
2
3
4
5
6
0
2
4
6
8
10
Wall normal pressure, p_{wn} (kPa)

(a)

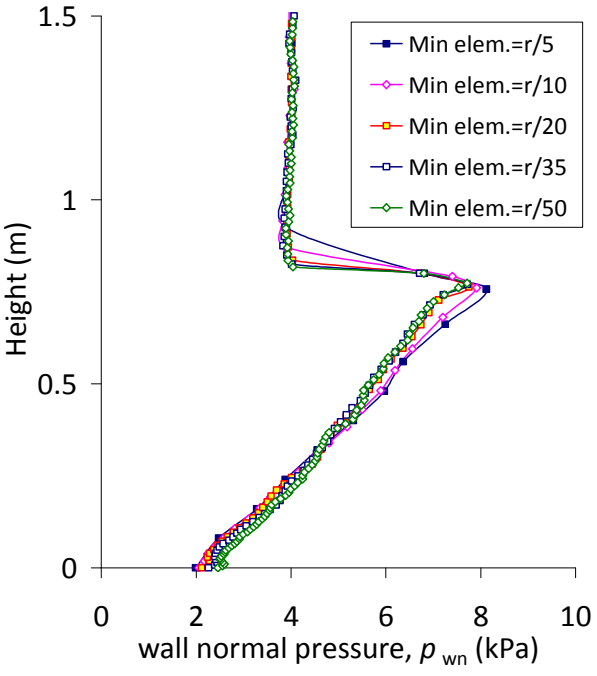
Min elem.=r/5
Min elem.=r/10
Min elem.=r/20
Min elem.=r/35
Min elem.=r/50
Height (m)
0
0.5
1
1.5
0
2
4
6
8
10
wall normal pressure, p_{wn} (kPa)

(b)

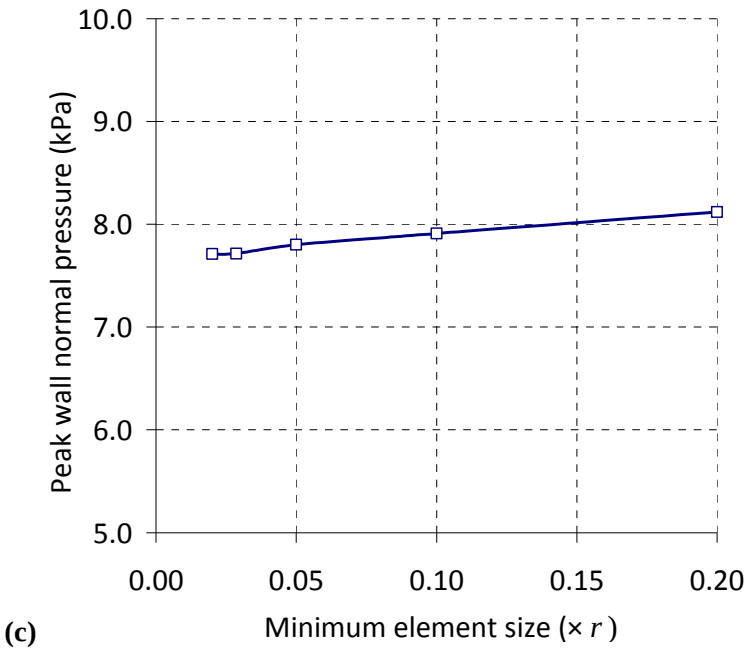

(c)

Fig. 7-8 Mesh convergence test without filleting: (a) normal wall pressure distribution; (b) close-up view for the height (0-1.5m); (c) detail of peak wall normal pressure at the transition (*r* is the silo radius of 0.35m at the transition)

7.4.3 Dynamic effect of wall pressure

Having verified the ability of the numerical model in dealing with abrupt transition in S-CC silos, in this section the results from the simulations with an abrupt transition are examined to evaluate the dynamic effect of wall pressures during discharge in the model silo.

Fig. 7-9 (a) shows the time histories of wall pressure at three points A, D, H of the silo wall during discharge. For each point, it is seen that there exists a varying degree of fluctuations during discharge, and this is qualitatively in agreement with the experiment as similar fluctuations were also recorded in the Danish test (Munch-Andersen et al.,

1992). Fig. 7-9 (b) shows time histories of wall normal pressure at the points (D_1 and D_2) neighbouring the point D at the transition (see Fig. 7-2). Similar pressure patterns to that at point D can be observed during discharge.

To further investigate the cause of the dynamic effect during discharge in the silo with abrupt transition, the frequency spectra of the normal pressures at the above-mentioned points are analysed with Fourier transformation, and the results are demonstrated in Fig. 7-10.

At point A, the pressure fluctuations with small amplitudes actually contain two distinctive frequencies, namely less than 1 Hz and around 13 Hz, as can be seen from Fig. 7-10 (a). The fluctuations with frequency of less than 1 Hz may be attributed to the evolution of shear zone and slip-stick wall motion within the converging section during discharge, as discussed in Chapter 4. On the other hand, a theoretical estimation of the frequency of the longitudinal wave travelling within the granular solid in the converging section yields a value of 14 Hz. This suggests that the about 13 Hz fluctuations in the computed pressure at point A is caused by the wave propagation.

At point D and H, the pressures also exhibit fluctuations with frequencies of less than 1 Hz, as shown in Fig. 7-10 (b) and (c), respectively. The fluctuations at point D have very large amplitudes. Such fluctuations may be attributed to the change of orientation of the major principal stress from vertical to converging. It is suspected that the fluctuations at point H occur due to the slip-stick wall motion in the higher part of the silo. This will be

verified by varying the coefficient of wall friction which will be discussed in Section 7.4.4.

From the simulation results, the coefficient of the "numerical" wall friction can be calculated at each time point for every point on the wall as

$$\mu_w = \frac{p_{ws}}{p_{wn}} \tag{7-2}$$

where p_{ws} is the predicted wall shear pressure; and p_{wn} is the predicted wall normal pressure. A slide occurs between the solid and silo walls if the coefficient of wall friction reaches its critical value of 0.67, as defined via the Coulomb friction model. The time histories of the so-calculated coefficient of wall friction at a series of points on the silo wall are shown in Fig. 7-11. It can be seen that the slip-stick motion, which is indicated by the fluctuations of the coefficient of friction, travels upwards along the silo walls at a certain speed.

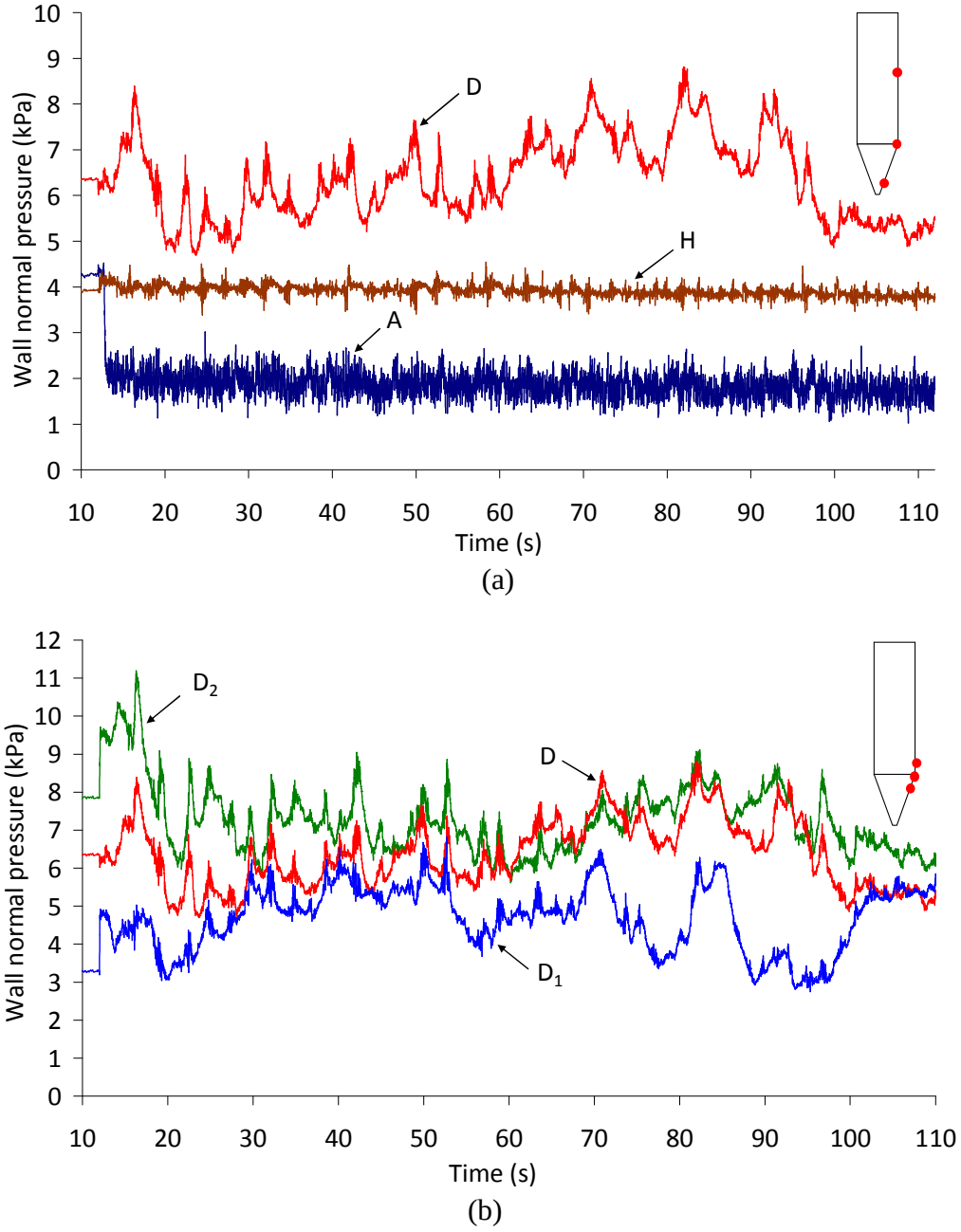

Fig. 7-9 Time histories of wall pressures at different levels of the silo with abrupt transition (no fillet): (a) at three points A, D, H; (b) at points neighbouring point D

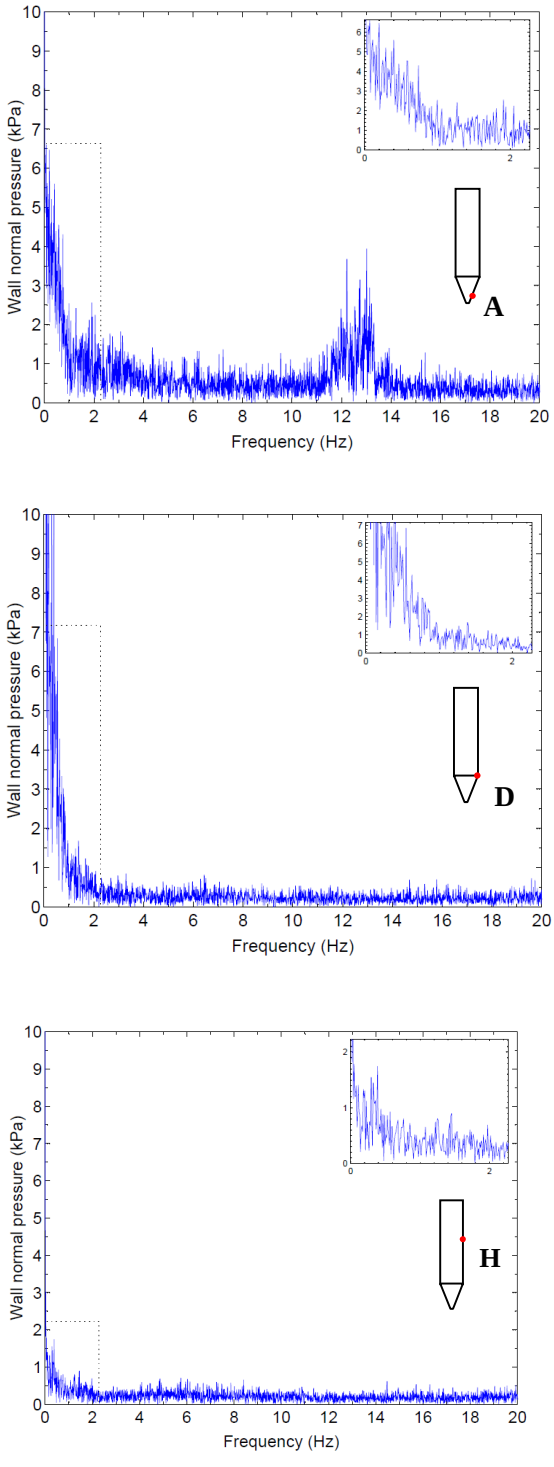

Fig. 7-10 Frequency spectrum of the predicted wall pressure at three points (A, D, H) of the silo with abrupt transition (no filleting)

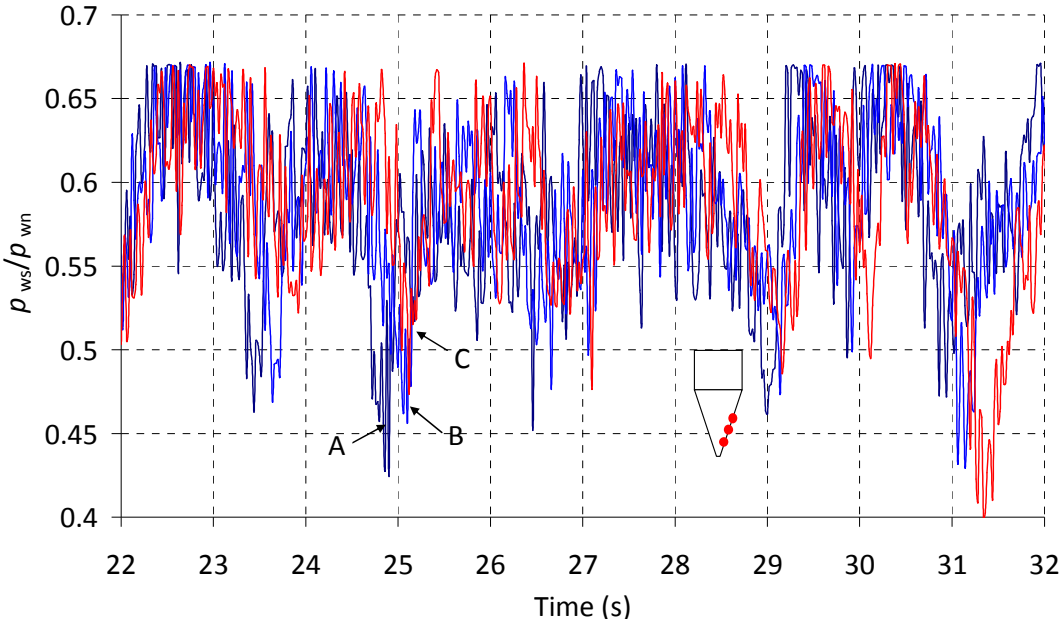

(a)

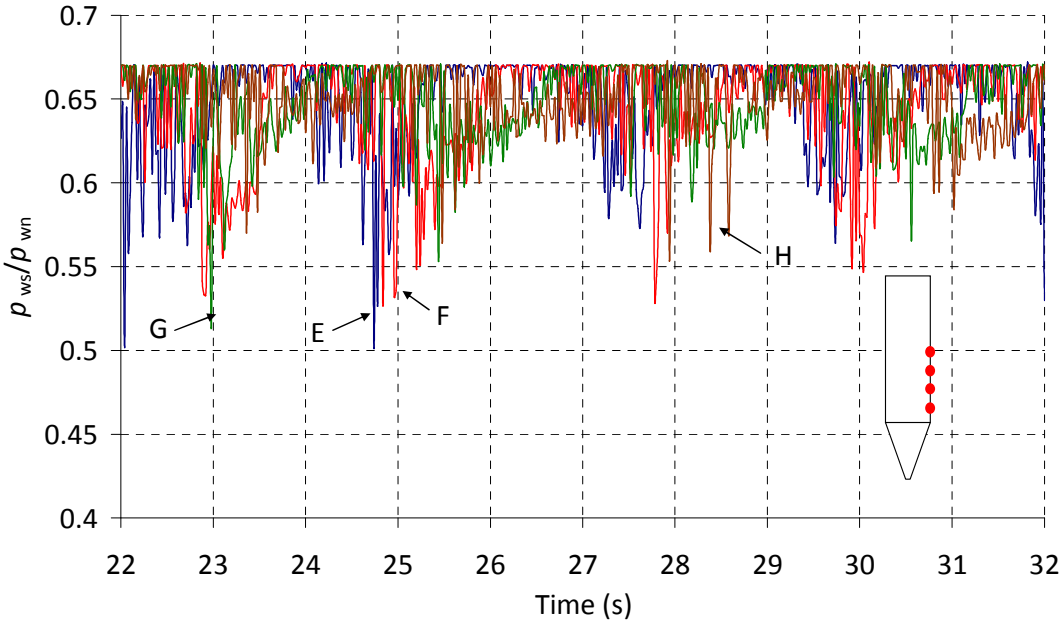

(b)

Fig. 7-11 Time histories of ratio of wall shear pressure to wall normal pressure at a series of points of the silo wall

7.4.4 Effect of wall friction conditions

The dynamic friction coefficient, as mentioned earlier, is adopted herein and it is assumed to have an exponential decay with respect to the sliding velocity between the solid and the walls. The static coefficient of friction μ_s, which applies to the onset of sliding, is set as 0.67 which is identical to the constant coefficient used in the previous simulations in this chapter. The kinetic coefficient of friction μ_k, which applies during the sliding motion, should be smaller than static friction coefficient and is set as 0.3 herein. It should be noted that usually both static and kinetic coefficients of friction depend on the condition of the surfaces in contact, and their determination requires physical measurements and cannot be obtained through modelling calculations (Oden and Martins, 1984). The decay coefficient ϖ is the parameter which controls how fast the level of kinetic coefficient of friction is reached with respect to the sliding velocity, and it is set as 2.

Fig. 7-12 shows the predicted wall normal pressures and those obtained from the Danish test and classical theories at the end of silo filling and during discharge. As noted before, the discharge pressures both for experimental tests and numerical simulation are temporally averaged over the initial period of discharge. From Fig. 7-12, slight difference can be found for wall pressure distribution at the end of filling when the dynamic wall friction coefficient is used as compared with that when a constant coefficient is adopted. This is quite expected because the effect of dynamic coefficient is not significant when the solid displaces only slowly relative to the wall during the filling process. Conversely, the dynamic friction effect becomes much more pronounced during

silo discharge due to increased sliding. Consequently, higher pressures are obtained from the analysis with the dynamic friction coefficient than those with the constant friction coefficient. The largest difference is observed to be about 1kPa and it occurs in the most part of the vertical section. Such increases of the wall pressure during silo discharge are in agreement with those observed in the Danish test. Clearly, as the dynamic wall friction decreases (exponentially in the FE model) with increase of the sliding velocity between the solid and the silo walls, it is expected according to Janssen law that the wall normal pressures will increase.

The achieved "numerical" dynamic wall friction coefficient can be calculated at every point on the wall as

$$\mu_d = \frac{p_{ws}}{p_{wn}} \tag{7-3}$$

where p_{ws} is the predicted wall shear pressure; and p_{wn} is the predicted wall normal pressure. For discharge (called 'flow' state), the mean dynamic wall friction coefficient was determined by the mean wall shear pressure and normal pressure over an initial period of discharge. It is different that for filling (herein called 'static' state), the wall pressure is extracted at the wall point at the end of filling analysis. The distributions of the dynamic friction coefficient μ_d and the coefficient of friction μ_w calculated by Equations (7-2) and (7-3), respectively, throughout the whole silo wall are shown in Fig. 7-13.

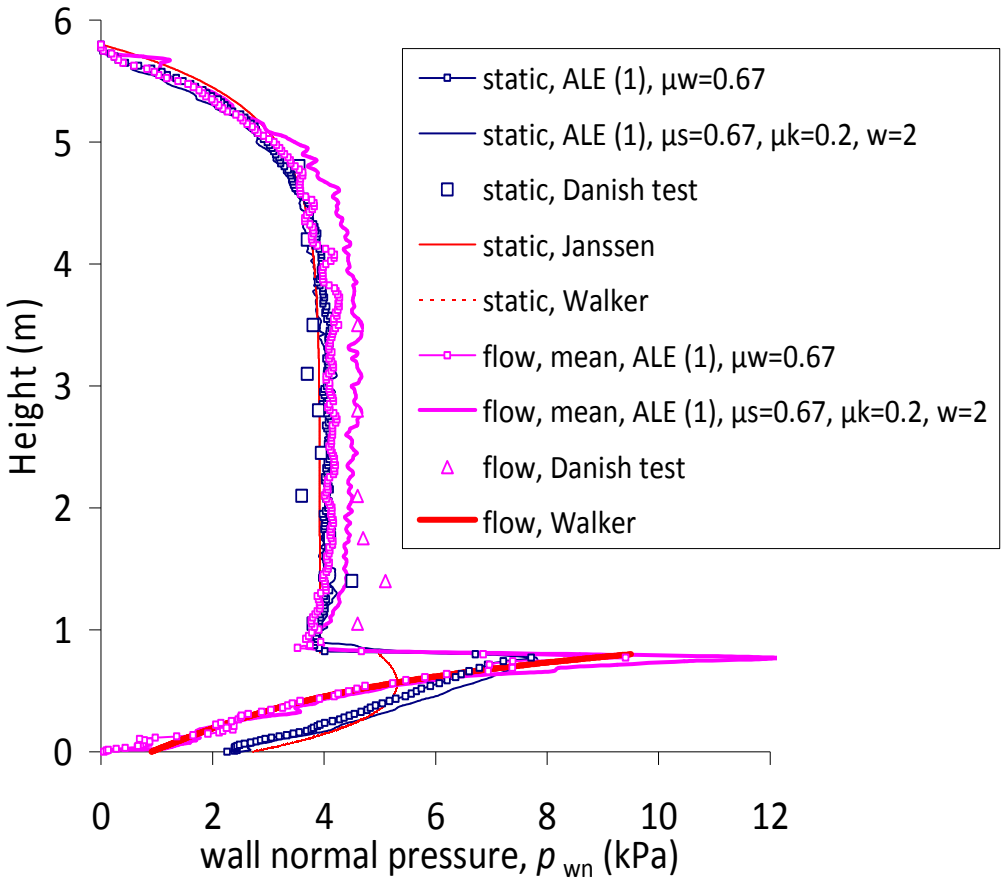

Fig. 7-12 Wall normal pressure distribution: ALE(1) –abrupt transition (no fillet), ALE(1), μ_d –abrupt transition with dynamic wall friction coefficient

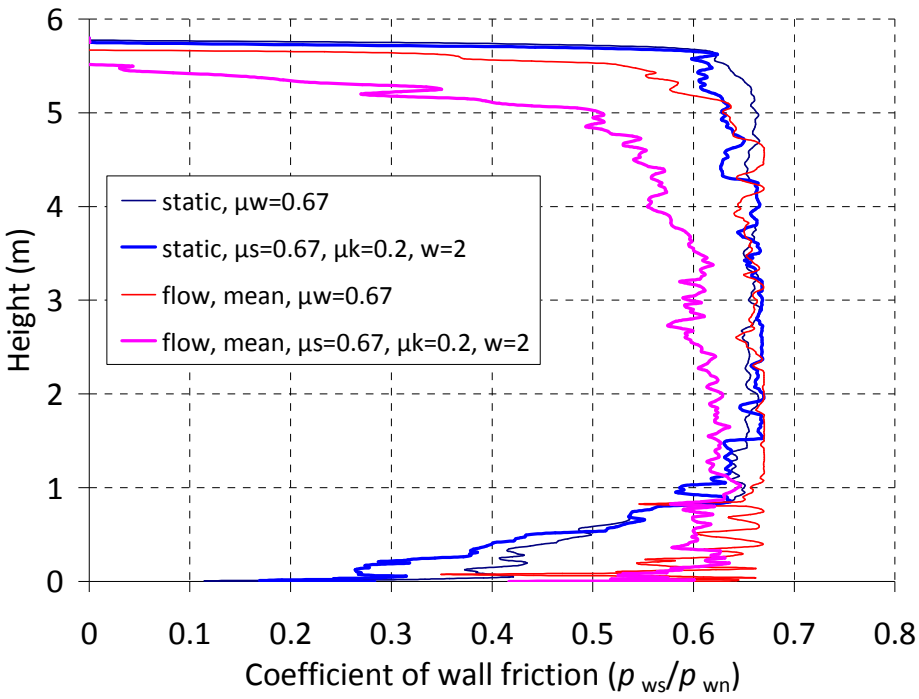

Fig. 7-13 Distributions of coefficient of wall friction at end of filling and during discharge

Different kinetic coefficient of friction μ_k and decay coefficient ϖ are also employed to investigate the effect of dynamic wall friction coefficient, and typical results are shown in Fig. 7-14. Comparing with Coulomb friction law with a constant friction coefficient, there is no difference in the predicted wall normal pressure at the end of filling when the dynamic friction coefficients are used, due to very small sliding velocity between the solid and the walls. In contrast, decreasing the kinetic coefficient of friction μ_k causes the wall normal pressures to increase throughout the whole silo walls, with more significant increase occurring in the vertical section. As expected according to Equation (7-1), a large decay coefficient of 4 gives a small dynamic coefficient of friction, consequently high wall normal pressures are obtained from the corresponding simulation.

The predicted wall shear stresses with varying kinetic coefficient of friction and decay coefficient are also temporally averaged and shown in Fig. 7-15. Approximately, the wall shear pressures do not vary so much as wall normal pressures through the whole silo when dynamic friction coefficients are used.

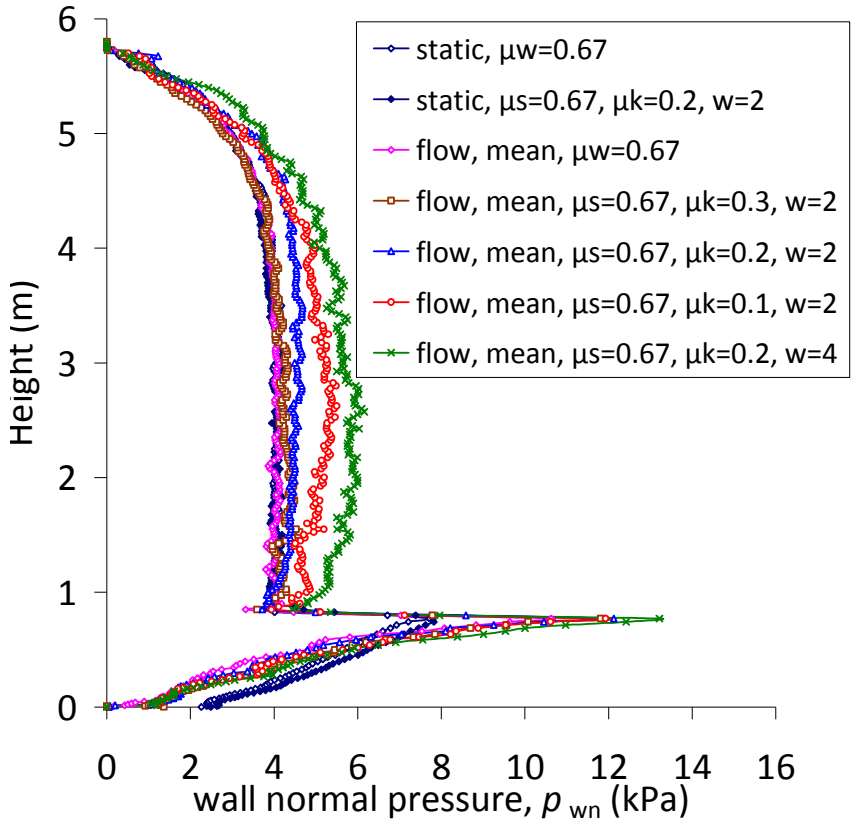

Fig. 7-14 Wall normal pressure distribution with varying kinetic friction coefficient and decay coefficient

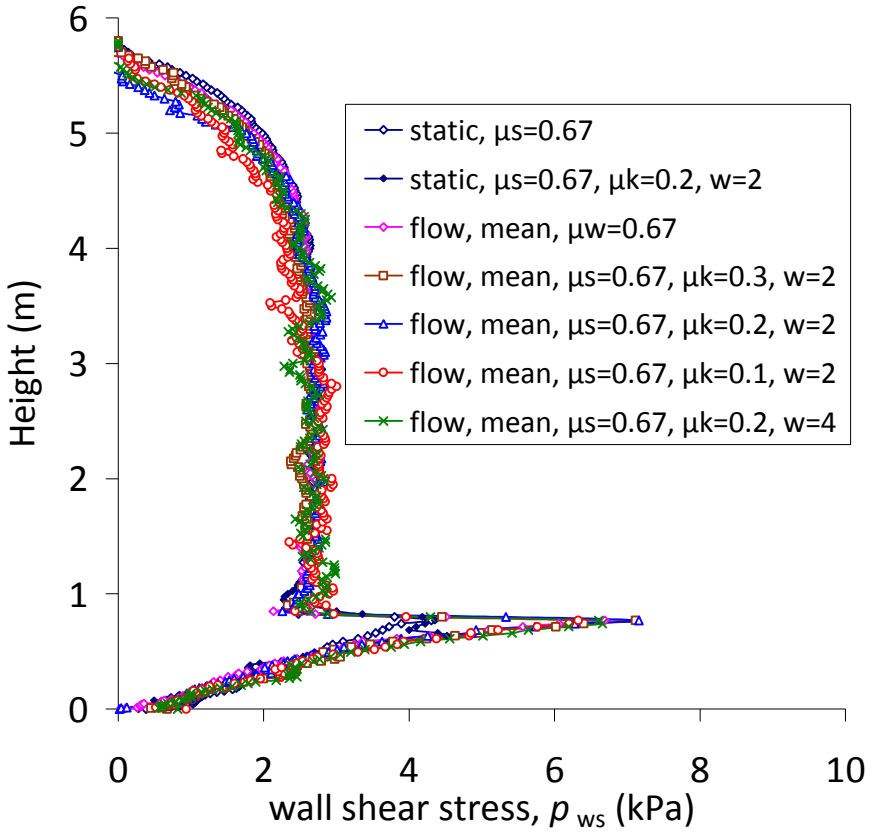

Fig. 7-15 Wall shear stress distribution with varying kinetic friction coefficient and decay coefficient

The coefficients of wall friction achieved at the walls corresponding to each case are calculated and shown in Fig. 7-16. Clearly, it indicates a converse trend to wall normal pressures in these cases. As expected from Janssen's law, wall normal pressures increase while the coefficient of wall friction decreases in the vertical section. The peak pressure at the transition between the vertical section and converging section is observed to also increase as the coefficient of wall friction decreases. In addition, the siding velocity of the solid against the walls are temporally averaged and shown along the vertical walls in Fig. 7-17.

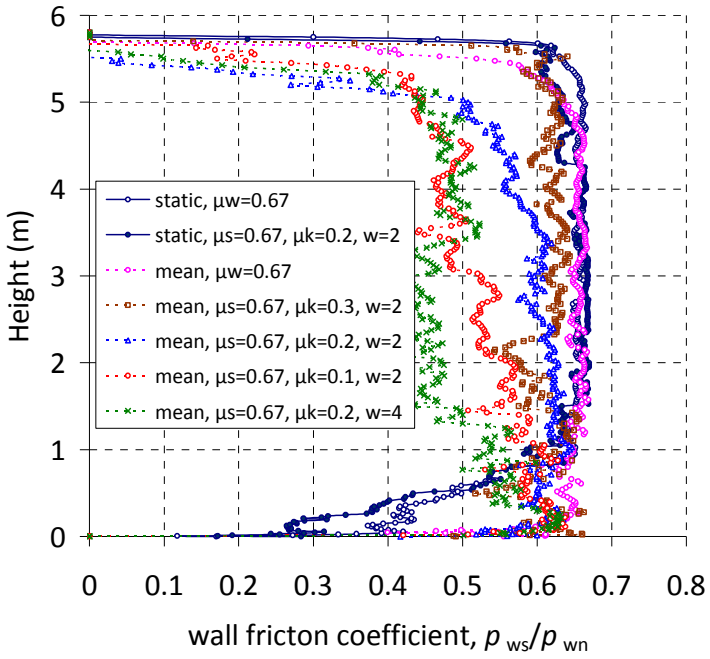

Fig. 7-16 Distributions of wall friction coefficient with varying kinetic friction coefficient and decay coefficient at end of filling and during discharge

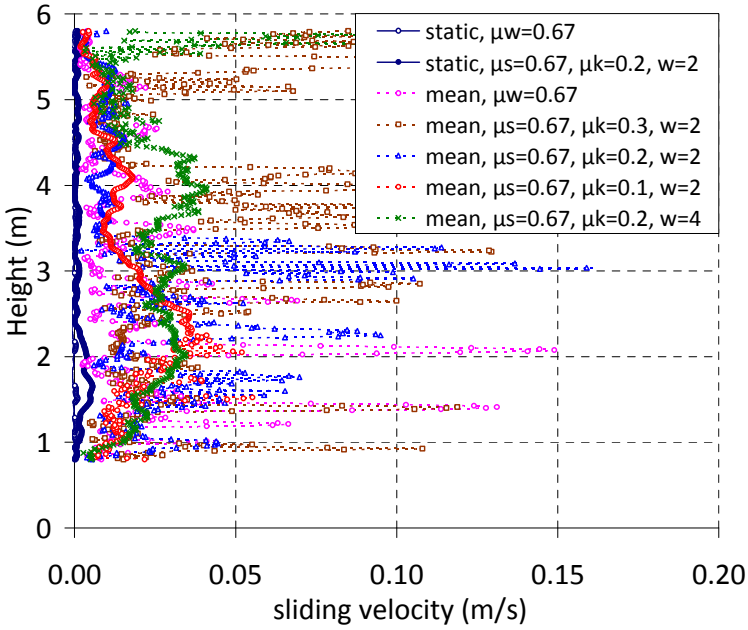

Fig. 7-17 Distribution of sliding velocity of the solid against the silo wall with varying kinetic friction coefficient and decay coefficient

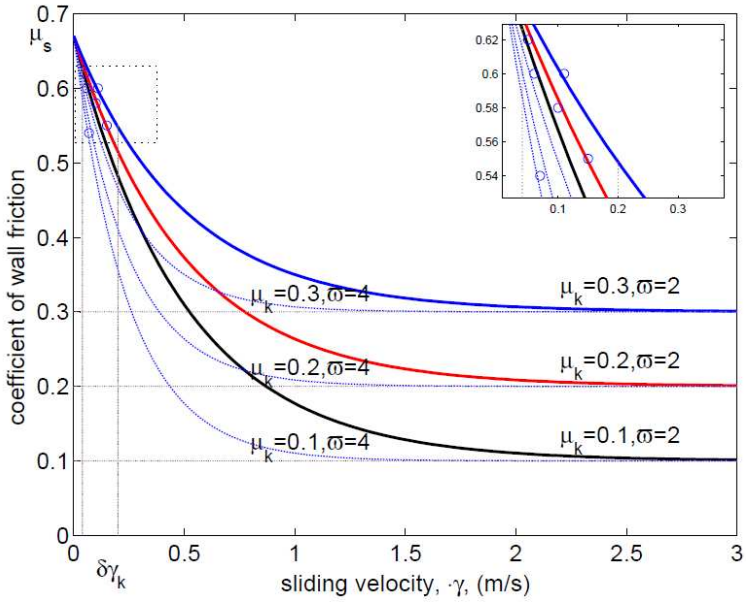

Fig. 7-18 Dynamic coefficient of friction as a function of sliding velocity of the solid against the silo wall

Fig. 7-18 shows the relationship between the coefficient of wall friction and sliding velocity of solid against the silo walls. From this figure, it is seen that the dynamic wall friction coefficient varies from 0.62 to 0.54 for the sliding velocity lying between 0.08 and 0.2 m/s. A similar change of coefficient of friction over the investigated range of sliding velocity can be found in experimental observations (Chowdhury et al., 2008). As a result of such change of wall friction coefficient the wall pressures varied dramatically as evidenced in Fig. 7-14. It should be mentioned that in the present study, due to the relatively low sliding velocity of the solid against the silo wall, the exponential relationship does not fully exhibit, and a linear trend seems to be clear as can be seen from the upper left corner in the chart (see Fig. 7-18). It can be envisaged that the whole exponential relationship can be obtained in a combination of a high sliding velocity and

a big decay coefficient ϖ. But in such a case the numerical convergence would be difficult to reach due to the solution for surface contact in programme Abaqus.

All the cases in the analyses presented so far in this chapter have been performed using a controlled exit discharge velocity of u_0. Now a double discharge velocity of $2u_0$ is considered in order to investigate the effect of velocity on the wall pressures when the dynamic wall friction coefficient is used. The time histories of the prescribed discharge velocity at the central point of the hopper outlet are shown in Fig. 7-19. Because of the sensitivity of the dynamic wall friction coefficient to the velocity, as expected higher wall pressures are produced under the double discharge velocity than under the original discharge velocity u_0. The distributions of the coefficient of wall friction along the silo walls with varying discharge velocity are temporally averaged and shown in Fig. 7-21. Distributions of sliding velocity against the silo walls are temporally averaged and shown in Fig. 7-22.

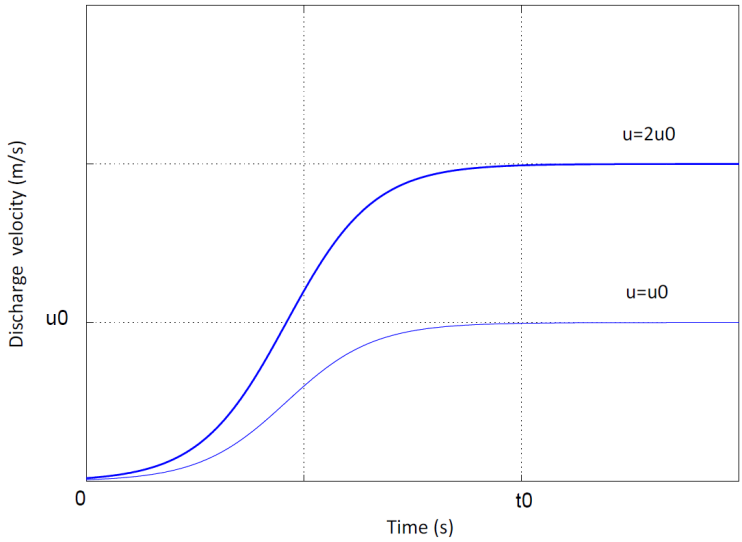

Fig. 7-19 Time evolutions of discharge velocity at the central point of hopper outlet

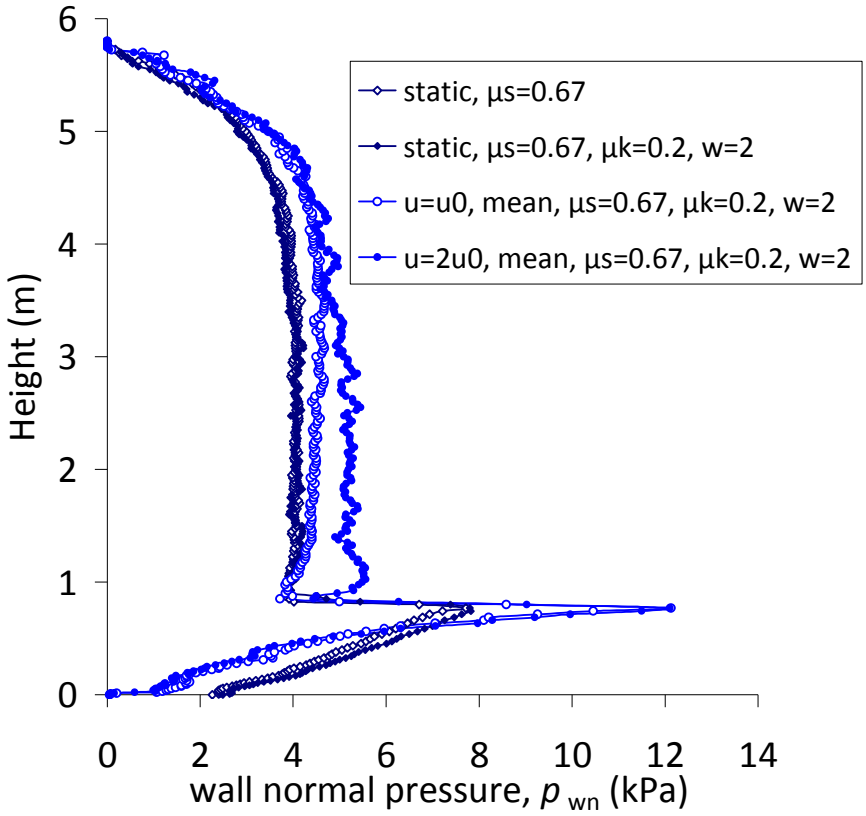

Fig. 7-20 Wall normal pressure distribution with varying discharge velocity

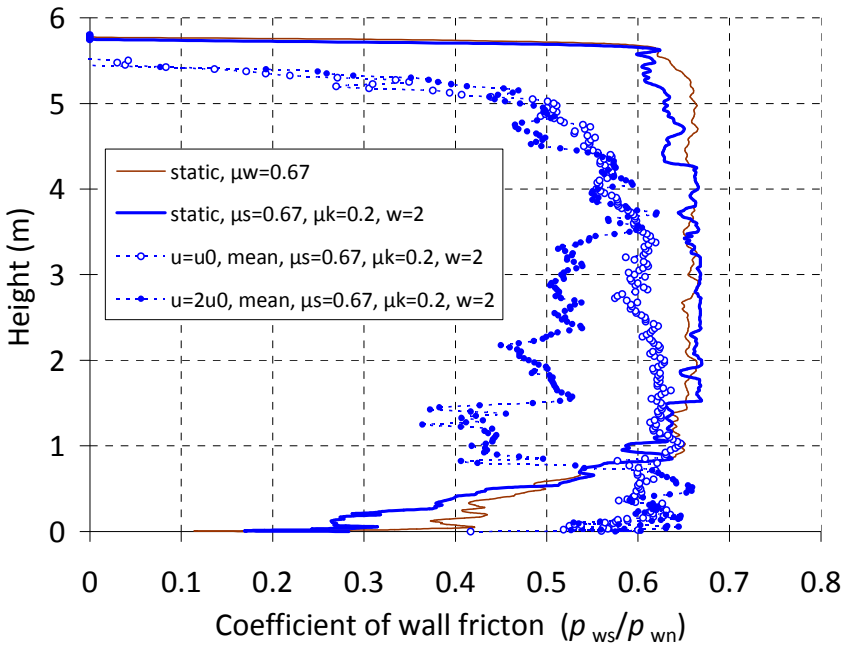

Fig. 7-21 Distributions of wall friction coefficient with varying discharge velocity

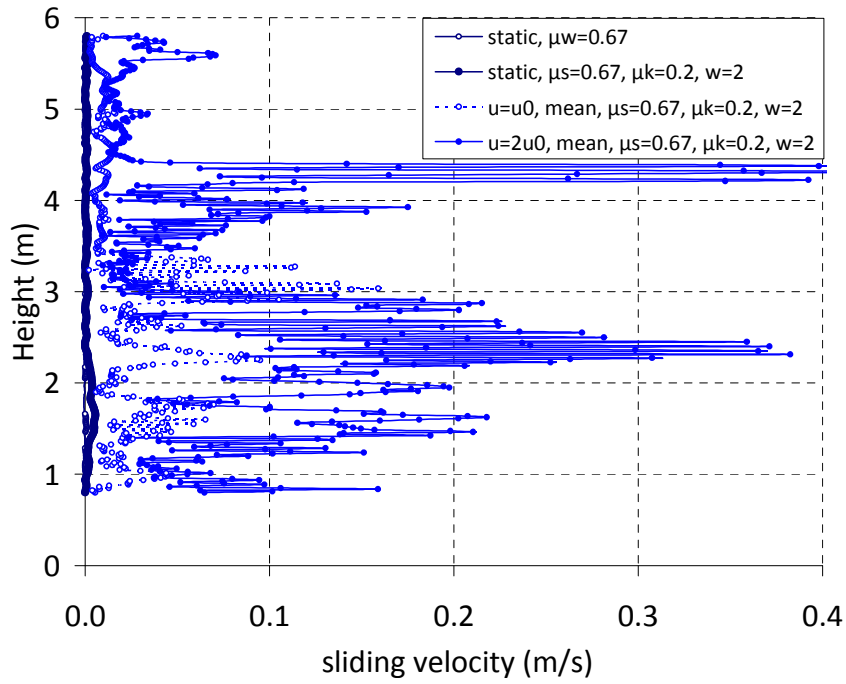

Fig. 7-22 Distribution of sliding velocity of the solid against the silo wall with varying discharge velocity

7.5 Concluding remarks

The wall pressures measured in Danish tests with smooth walls and a hopper bottom are used to compare and verify the predictions by the finite element analysis. It is demonstrated that the finite element analysis using the uncoupled ALE formulation performs satisfactorily in simulating filling and discharge for this type of silos with a hopper bottom. By comparing with the observations from the Danish test, the effect of internal friction angle of the solid has been investigated and results show that the internal friction angle is a governing factor on the lateral pressure ratio, which in turn determines how rapid the pressure can achieve the asymptotic Janssen pressure while the magnitude is less affected. By comparing the FE analysis with the experimental observations, the equivalent internal friction angle in the Danish test with dry sand was found to be about 40º.

With the aid of the finite-sliding formulation for contact between two arbitrary surfaces, more accurate predictions on the wall pressures at the abrupt transition between the vertical section and converging section can be achieved without any significant numerical treatment on the transition, such as filleting techniques employed by other researchers. Such treatments usually would cause alteration of pressures around the transition. The predicted wall pressures throughout the whole silo geometry by the present FE simulation are consistent with those obtained by the Danish test and classical theories.

As observed in the Danish test, significant pressure fluctuations are also found in the present FE simulations. The fluctuations exhibit different features in different sections of the silo. In the converging section, the pressure fluctuations with small amplitudes are found to contain two distinctive frequencies, on at less than 1 Hz and another around 13 Hz. These frequencies can be attributed to the evolution of the shear zone combined with the slip-stick wall motion, and the propagation of the longitudinal waves, respectively. The fluctuations at the transition between the vertical and converging sections have very large amplitudes. Such fluctuations can be attributed to the change of orientation of the major principal stress from vertical to the converging direction. In the vertical section, the fluctuations appear to occur due to the slip-stick wall motion. The fluctuations in the upper part are dominated by frequencies of less than 1 Hz.

The dynamic friction model, where the coefficient of wall friction is determined by an exponential relationship with respect to the sliding velocity between two contact surfaces, has been used to describe the frictional behaviour by specifying the static and kinetic coefficients. Such a wall boundary condition results in a reasonable prediction for silo wall pressures, especially in cases where the coefficient of wall friction is sensitive to the sliding velocity of the solid against the walls during discharge. With appropriate setting of parameters for the dynamic friction model, a discharge overpressure of about 1.0 kPa has been predicted in the numerical simulation, which is consistent with that observed in the Danish test.

Chapter 8

Non-coaxial model and its application

8.1 Introduction

Vast numerical simulations have been performed using the finite element method to predict silo discharge. To ensure realistic results, various aspects are required to be taken into account, the most important of which is the constitutive models for the granular materials. Flowing granular materials exhibit distinct characteristics. To describe these characteristics, a general constitutive law for granular flow remains an important open problem (Kamrin, 2010).

In spite of the use of various models, the non-coaxiality has not been appropriately taken into account (Yang et al., 2011). The non-coaxiality is the non-coincidence between principal stresses and principal plastic strain rates, and it is mainly attributed to the principal stress rotation in granular material (Roscoe et al., 1967; Symes et al., 1984). The non-coaxiality has been extensively studied in geomechanics and geotechnical engineering communities. Various models have been developed in geomechanics to simulate the principal stress rotation induced non-coaxiality (Hashiguchi and Tsutsumi, 2001; Li and Dafalias, 2004; Yu and Yuan, 2006; Yang and Yu, 2006).

In this chapter, the non-coaxial constitutive model is introduced to investigate the effects that have been well recognized in granular flow during silo discharge. The non-coaxial model, which was developed based on the Drucker-Prager failure criterion (Drucker and Prager, 1952), is first employed to investigate the effects of the non-coaxiality on stress-strain behaviour of granular solids subjected to simple shearing under various initial conditions. FE simulations are then performed using the non-coaxial model on a steep hopper and a flat-bottomed silo to investigate the influence on predictions of wall pressure.

8.2 Non-coaxial model

Due to principal stress rotations the principal axes of strain rates and stress are not coincident during the early stage of the shear deformation of granular solids. Of a particular note, the principal stress rotation in silo-discharge granular flow is larger than in geotechnical engineering, reaching even 90º in the converging section,. This section is aimed to introduce a well-established non-coaxial model based on the Drucker-Prager failure criterion. In the elasto-plastic theory, a brief description of the non-coaxial model will be given in this section.

8.2.1 Yield vertex non-coaxial model

In the elastoplasticity theory, the total strain rate can be decomposed into an elastic component $\dot{\varepsilon}^{e}$ and a plastic component $\dot{\varepsilon}^{p}$. According to the non-coaxial plasticity, $\dot{\varepsilon}^{p}$ is composed of a conventional coaxial part $\dot{\varepsilon}^{pc}$ normal to the yield surface and a non-

coaxial part $\dot{\varepsilon}^{pn}$ tangential to the yield surface. In summary, the total strain rate can be written as

$$\dot{\varepsilon}_{ij} = \dot{\varepsilon}_{ij}^{e} + \dot{\varepsilon}_{ij}^{pc} + \dot{\varepsilon}_{ij}^{pn} \tag{8-1}$$

The $\dot{\varepsilon}^{e}$ is related to stress rate $\dot{\sigma}$ as

$$\dot{\sigma}_{ij} = E_{ijkl}\dot{\varepsilon}_{kl}^{e} \tag{8-2}$$

$$E_{ijkl} = K\delta_{ij}\delta_{kl} + G(\delta_{ik}\delta_{jl} + \delta_{il}\delta_{jk} - \frac{2}{3}\delta_{ij}\delta_{kl}) \tag{8-3}$$

where E_{ijkl} is the elastic compliance tensor. K and G denote the elastic bulk and shear moduli, respectively. δ_{ij} denotes the Kronecher delta.

For the coaxial component $\dot{\varepsilon}^{pc}$, it can be determined based on conventional plasticity theory.

$$\dot{\varepsilon}_{ij}^{pc} = \dot{\lambda}\mathrm{I}_{ij} \tag{8-4}$$

$$\mathrm{I}_{ij} = \frac{\partial g}{\partial \sigma_{ij}} \tag{8-5}$$

$$\dot{k} = \dot{\lambda}\chi \tag{8-6}$$

where I denotes the coaxial plastic flow direction and g denotes the plastic potential function. $\dot{k}$ is the rate of hardening parameter and assumed to be a scalar for simplicity. χ is the quantity related to the evolution of the hardening parameter. The loading parameter $\dot{\lambda}$ is defined as

$$\dot{\lambda} = \frac{1}{K_p}(\omega_{ij}\dot{\sigma}_{ij}) \tag{8-7}$$

$$\omega_{ij} = \frac{\partial f}{\partial \sigma_{ij}} \tag{8-8}$$

where K_p denotes the coaxial plastic modulus and can be determined from a hardening rule; f denotes the yield function and ω represents the normal to the yield surface.

The non-coaxial component $\dot{\varepsilon}^{pn}$ in yield vertex theory (Rudnicki and Rice, 1975) is assumed to be linearly dependent on the non-coaxial stress rate as follows

$$\dot{\varepsilon}_{ij}^{pn} = \frac{1}{H_{nc}} \dot{s}_{ij}^{n} \tag{8-9}$$

$$\dot{s}_{ij}^{n} = \dot{s}_{ij} - \frac{s_{ij} s_{kl}}{s_{mn} s_{mn}} \dot{s}_{kl} \tag{8-10}$$

where s represents the deviatoric stress tensor, H_{nc} denotes the non-coaxial plastic modulus governing the response to the stress rate tangential to the yield surface. As a result, Equation (8-9) describes the non-coaxial deformation in the deviatoric stress space, as illustrated in Fig. 8-1. The formulations for $\dot{\varepsilon}^{pn}$ in Equation (8-9) and (8-10) can be further written as

$$\dot{\varepsilon}_{ij}^{pn} = \frac{1}{H_{nc}} T_{ijkl} \dot{\sigma}_{kl} = \frac{2G}{H_{nc} + 2G} T_{ijkl} \dot{\varepsilon}_{kl} \tag{8-11}$$

$$T_{ijkl} = \frac{1}{2}(\delta_{ik}\delta_{jl} + \delta_{il}\delta_{jk} - \frac{2}{3}\delta_{ij}\delta_{kl} - \frac{2\delta_{ij}\delta_{kl}}{s_{mn}s_{mn}}) \tag{8-12}$$

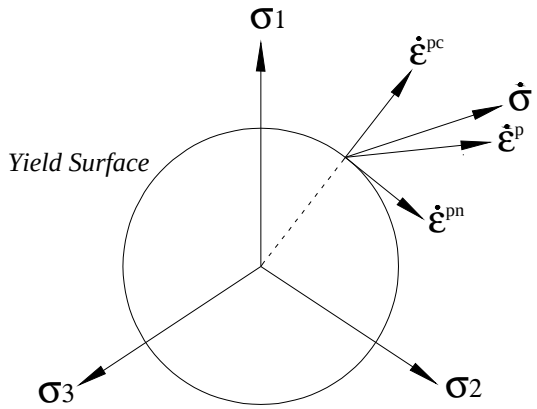

Fig. 8-1 Schematics of definition of the plastic strain rates normal and tangential to the yield surface in deviatoric stress space

Substituting the expressions for $\dot{\varepsilon}^{pc}$ and $\dot{\varepsilon}^{pn}$ into Equation (8-11) and (8-12), one can obtain the relationship between stress rate and strain rate, given as

$$\dot{\sigma}_{ij} = D^{ep}_{ijkl}\dot{\varepsilon}_{kl} = \left[E_{ijkl} - \frac{(E_{ijab}\mathrm{I}_{ab})(E_{klcd}\omega_{cd})}{K_P + \omega_{mn}E_{mnst}\mathrm{I}_{st}} - \frac{4G^2}{H_{nc} + 2G}T_{ijkl} \right]\dot{\varepsilon}_{kl} \qquad (8\text{-}13)$$

where D^{ep}_{ijkl} is the tangent stiffness which relates the strain rate with the stress rate. In the equation above, the first and second on the right hand side represent the contributions from the elastic strain rate and coaxial plastic strain rate, respectively. The third term represents the contribution from the non-coaxial plastic strain. This equation represents a general stress-strain relationship for the non-coaxial model.

In this chapter, the extended elasto-perfectly plastic Drucker-Prager yield criterion is employed to reflect the influence of the non-coaxial component. Without consideration of strain hardening, the non-coaxial influences can be embodied more clearly in the simple shear behaviour and in silo discharge.

8.3 Simple shear behaviour and simulations

To capture the key features of non-coaxiality, the simple shear test of a single element (Potts et al., 1987) was first simulated with the coaxial and non-coaxial models. A constant vertical pressure is applied at the top of the element, with its bottom fixed. The two sides of the element tilt with respect to the bottom corners. The element is free to expand during shearing. In all cases, an 8-noded biquadratic element with reduced integration is employed, and all the sides remain linear and parallel to their original ones throughout the loading, shown in Fig. 8-2. The vertical pressure σ_y is set as100 kPa. A prescribed shear strain γ_{xy} is applied. As a consequence of these prescribed boundary and loading conditions, the sample is subjected to a shear stress τ_{xy}, a change of stress in the *x* direction $\Delta\sigma_x$, and a direct strain ε_y in *y* direction. Since the plane strain condition in z direction and the full constraint on the movement in *x* direction were applied, we had σ_z equal to σ_x throughout the shearing.

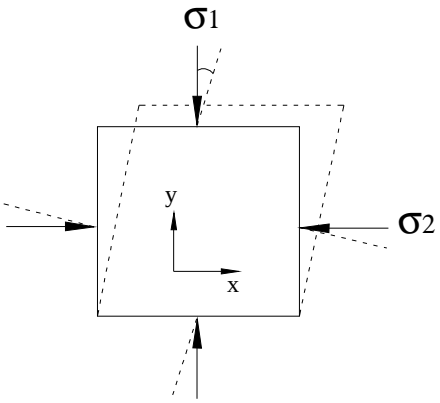

Fig. 8-2: The behaviour of a sample before and after shearing

A series of numerical simulations were performed to facilitate the investigations of the effect of plastic flow rule, Young's modulus and initial static lateral pressure ratio k . All the cases performed by varying material parameters in these investigations are listed in Table 8-1. Other material parameters are summarized in Table 8-2. The stress-strain relationship was described by the perfectly plastic model with a constant and low value of shear strength c_0.

Table 8-1 Cases of simulations

No.	ϕ (º)	ψ (º)	E (kPa)	k
1	30	0	10×10^4	0.4
2	30	30	10×10^4	0.4
3	30	0	0.4×10^4	0.4
4	30	0	2×10^4	0.4
5	30	0	50e4	0.4
6	30	0	10×10^4	2.0
7	30	0	10×10^4	1.0
8	30	0	10×10^4	0.8

Table 8-2 Material properties

Bulk density (kg/m^3) E	Shear Modulus (kPa) G	Perfectly plasticity (Pa) c_0	Non-coaxial plastic modulus (kPa) H
1.5×10^3	3.8×10^4	1.0	1.0×10^4

The sample first undergoes an elastic deformation and σ_x remains constant until the stress state reaches the yield surface. Subsequently, the plastic flow starts, and the stress state moves on the yield surface until all the stress stabilized at some certain values determined by the flow rule and the shear strength. As a result of the movement of the stress state, the principal stresses rotate. Thus, the rotation of principal stresses leads to non-coaxial effect.

8.3.1 Effect of plastic flow rule

Fig. 8-3 shows the predictions with *k* equal to 0.4 using zero plastic volumetric change (non-associated flow rule) and the associated flow rule. The evolutions of shear stress ratio τ_{xy}/σ_y, and angles of the major principal stress and plastic strain rate, are shown in Fig. 8-3 (a) and (b), with respect to the shear strain in percentage. A difference of the shear stress ratio was evaluated by subtracting shear stress ratio for coaxial model by that for non-coaxial model at each shearing stage. The differences of the shear stress ratio between coaxial and non-coaxial model using these two flow rules are also shown in Fig. 8-3 (c). The peak of difference of shear stress ratio for associated flow is higher than that for non-associated flow, and is close to 0.4. Fig. 8-3 (b) shows the coincidence

of the orientations of major principal stress and plastic strain rate as expected when coaxial model was used. However, when the non-coaxial model was employed, the direction of major principal strain rate departs and ahead of that for the major principal stress because the total plastic strain rate is increased in *xy* direction and decreased in *x* and *y* directions in the non-coaxial model. A detailed interpretation about the discrepancy of directions of major principal stress and major plastic strain rate can be found in Yang et al., 2006. Fig. 8-3 (b) shows that with the shear strain increasing, the orientations of the major principal stress and plastic strain rate evolve into coincidence. The fact that the principal strain rate direction is ahead of principal stress direction during the early stage of shearing and they tend to coincide during the later stage of shearing were also observed in experimental results for sand (Roscoe, 1970). As the inclusion of non-coaxial plastic strain increases the total plastic strain in *xy* direction, the shear stress ratio exhibits a soft response to the total shear strain as shown in Fig. 8-3 (a) when the directions of the major principal stress and plastic strain rare do not coincide.

The ultimate stress state depends on the shear strength and the flow rule used, rather than the initial conditions according to Potts et al. (1987). In the case of using zero plastic volumetric change, the ultimate σ_x and τ_{xy} are equal to σ_y and $0.5\,\sigma_y$, respectively. When the associated flow rule is employed, the ultimate σ_x and τ_{xy} are equal to $1.8\sigma_y$ and $0.6\,\sigma_y$, respectively. This results in different amount of principal stress rotation in these two cases. As shown in Fig. 8-3 (b) for zero plastic volumetric change, the angle of the major principal stress rotates 15^o and reaches 50^o at the end of shearing. In the case of using the associated flow rule, the rotation of the major principal

stress is about 30º. Because of the positive dependence of the predicted non-coaxial plastic strains on rotation of the principal stresses, the overall soft response of shear stress ratio is more significant when using associated flow rule. Fig. 8-3 (c) shows different peak of shear stress ratios at 0.28 and 0.36, respectively, for the non-associated and associated flow rule.

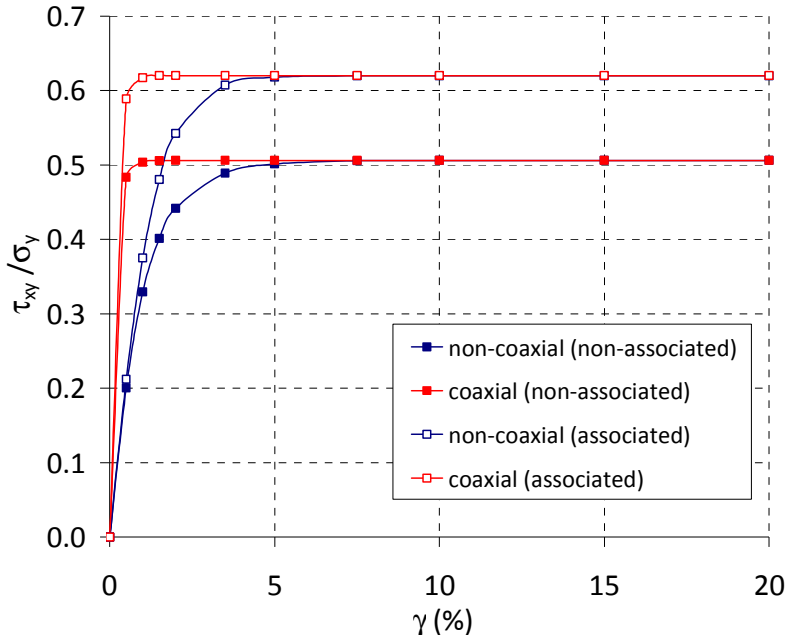
0.7
0.6
0.5
0.4
0.3
0.2
0.1
0.0
τxy /σy
0
5
10
15
20
γ (%)
non-coaxial (non-associated)
coaxial (non-associated)
non-coaxial (associated)
coaxial (associated)

(a)

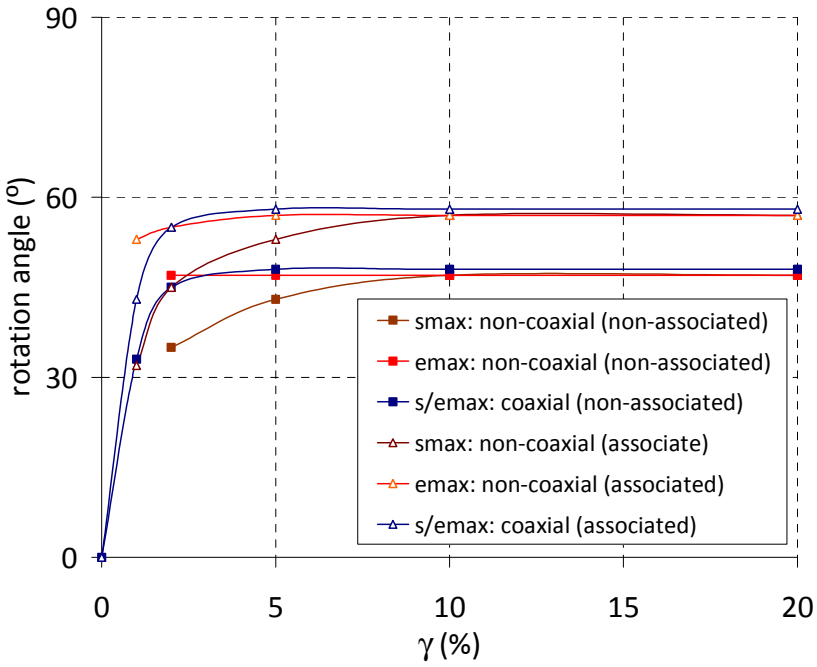
90
60
30
0
rotation angle (°)
0
5
10
15
20
γ (%)
smax: non-coaxial (non-associated)
emax: non-coaxial (non-associated)
s/emax: coaxial (non-associated)
smax: non-coaxial (associate)
emax: non-coaxial (associated)
s/emax: coaxial (associated)

(b)

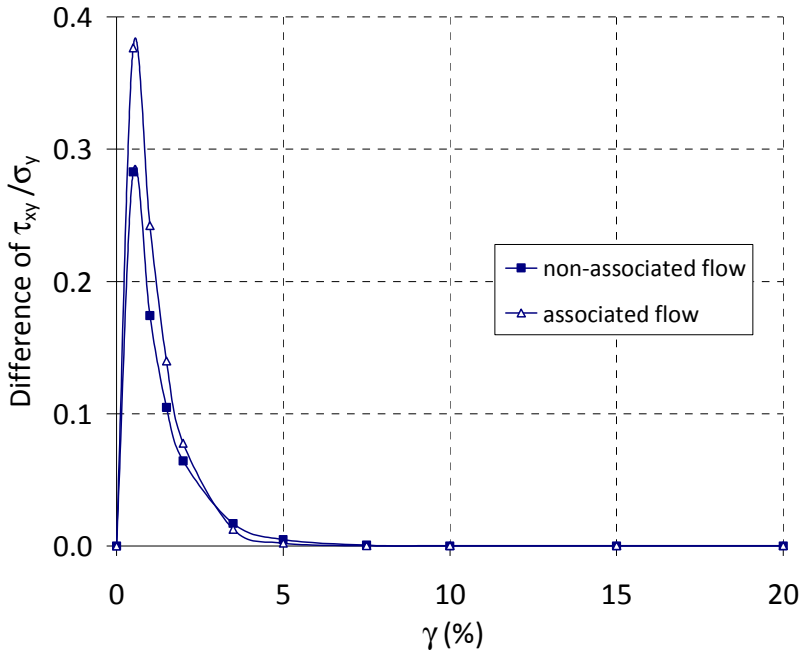

(c)

Fig. 8-3 Characteristic variables predicted by the coaxial and non-coaxial models, using the non-associated and associated flow rule, k=0.4, and E=10e4 kPa: (a) evolution of shear stress ratio (τ_{xy}/σ_y); (b) evolution of rotation angle of major principal stress (smax) and plastic strain rate (emax); (c) the differences of the shear stress ratio between coaxial and non-coaxial model at each shearing stage

8.3.2 Effect of Young's modulus

Fig. 8-4 shows the evolution of the shear stress ratio and rotation angles of major principal stress and plastic strain rate with respect to shear strain for various Young's moduli. The difference of shear stress ratio τ_{xy}/σ_y between the coaxial and non-coaxial model increases as the Young's modulus increases. In addition, the peak difference in shear stress ratio is considered as a function of Young's modulus, as shown in Fig. 8-5.

This peak of difference has a low level when Young's modulus is small and becomes high as Young's modulus increases.

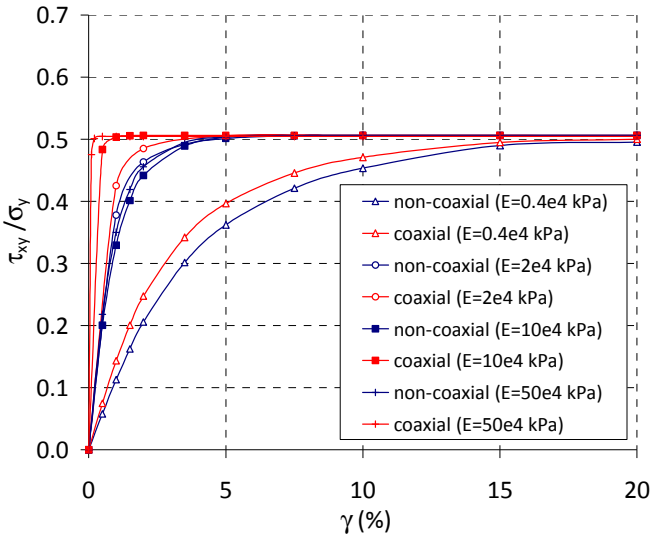

(a)

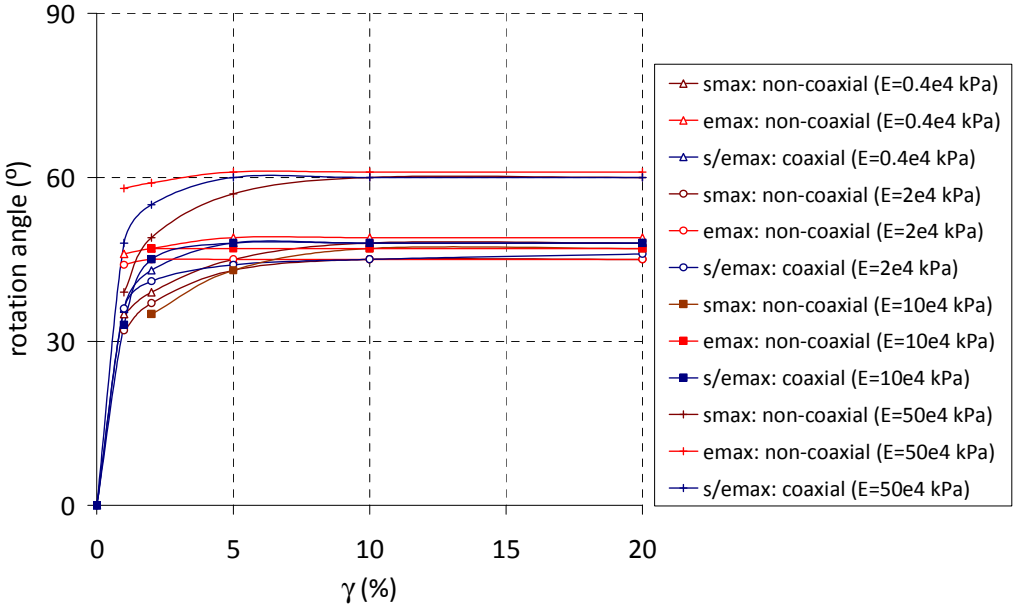

(b)

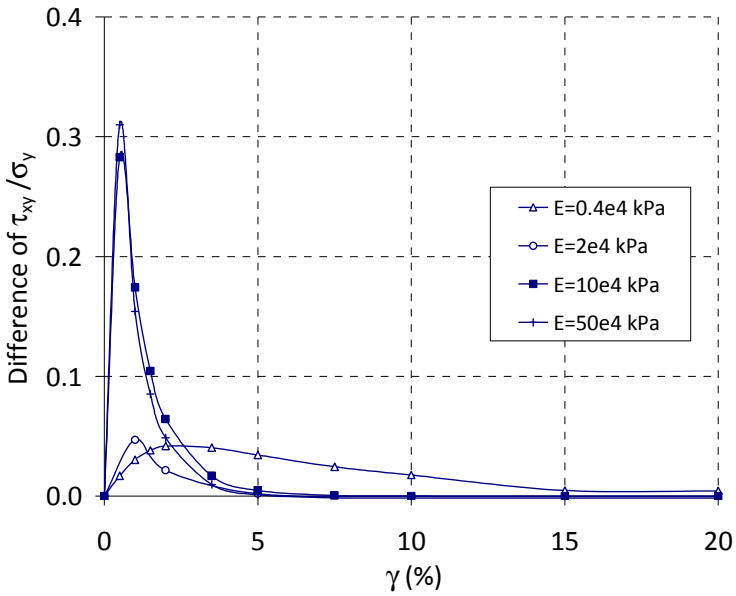

(c)

Fig. 8-4 Characteristic variables predicted by the coaxial and non-coaxial model with various Young's moduli, k=0.4, non-associated flow rule, and $\varepsilon_v^p = 0$: (a) evolution of shear stress ratio (τ_{xy}/σ_y); (b) evolution of rotation angle of major principal stress (smax) and plastic strain rate (emax); (c) the difference of the shear stress ratio between coaxial and non-coaxial model at each shearing stage

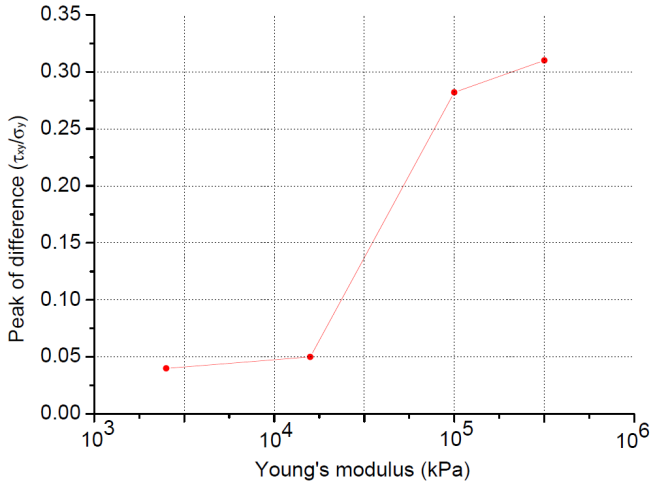

Fig. 8-5 Peak of difference between coaxial and non-coaxial model as a function of Young's modulus

8.3.3 Effect of lateral pressure ratio

Fig. 8-6 shows the predictions with various lateral pressure ratios using the zero plastic volumetric change. Similar to the prediction with k equal to 0.4, the shear stress ratios predicted by the non-coaxial and coaxial model converge with increase in the shear strain. For k=2.0, the major principal stress evolves faster than the major principal strain rate in terms of their directions. In addition, softening of the shear stress ratio occurs, as shown in Fig. 8-6 (a) and Fig. 8-6 (b). Due to the same direction of plastic strain in *xy* direction and opposite direction of plastic strain in *x* and *y* directions, the orientation of major principal stress surpasses that for major principal strain rate. Since a large σ_x can bear a larger shear stress during the early stage of shearing than a smaller one during the later stage of shearing with certain shear strength in the general stress space, the softening of shear stress ratio occurs when the initial σ_x ($2\sigma_y$) is larger than its ultimate value (σ_y). The use of non-coaxial model decreases the softening tendency of shear stress ratio in the case when k is equal to 2.0. Similarly, it decreases the hardening tendency when k equal to 0.4, shown in Fig. 8-6. A detailed interpretation about the discrepancy of directions of major principal stress and major plastic strain rate can be found in Yang et al., 2006.

To investigated the influence of initial static lateral pressure ratio k, the evolutions of shear stress ratio and rotation angles for k=0.8 and 1.0 with zero plastic volumetric change are also plotted with respect to shear strain in Fig. 8-6. Comparing the predicted results for these cases, it is revealed that the greater the lateral pressure ratio k, the smaller the differences of shear stress ratio between coaxial and non-coaxial model,

before the difference disappears at $k=1.0$. For $k>1.0$, the differences begin to increase as the lateral pressure ratio increases. The stress ratio using non-axial model exceeds that using coaxial model and softening of shear stress occurs. The peak difference of shear stress ratios for each case is considered as a function of lateral pressure ratio, as shown in Fig. 8-7.

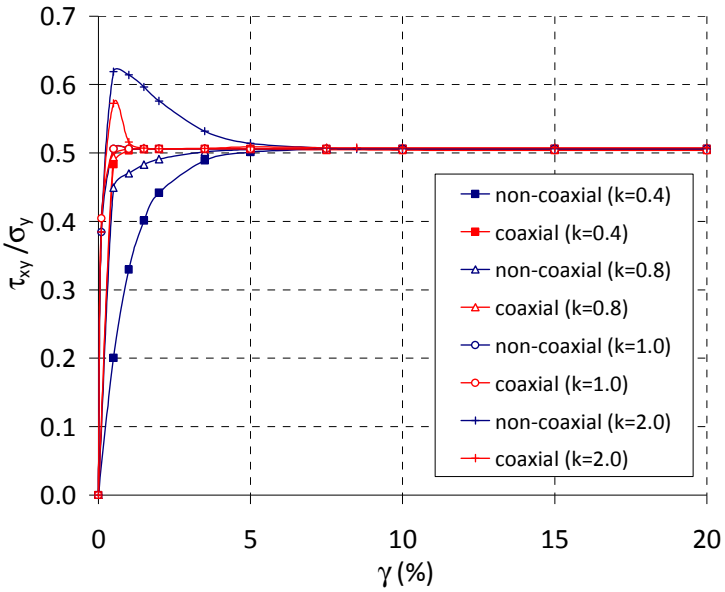
0.7
0.6
0.5
0.4
0.3
0.2
0.1
0.0
τxy /σy
0
5
10
15
20
γ (%)
non-coaxial (k=0.4)
coaxial (k=0.4)
non-coaxial (k=0.8)
coaxial (k=0.8)
non-coaxial (k=1.0)
coaxial (k=1.0)
non-coaxial (k=2.0)
coaxial (k=2.0)

(a)

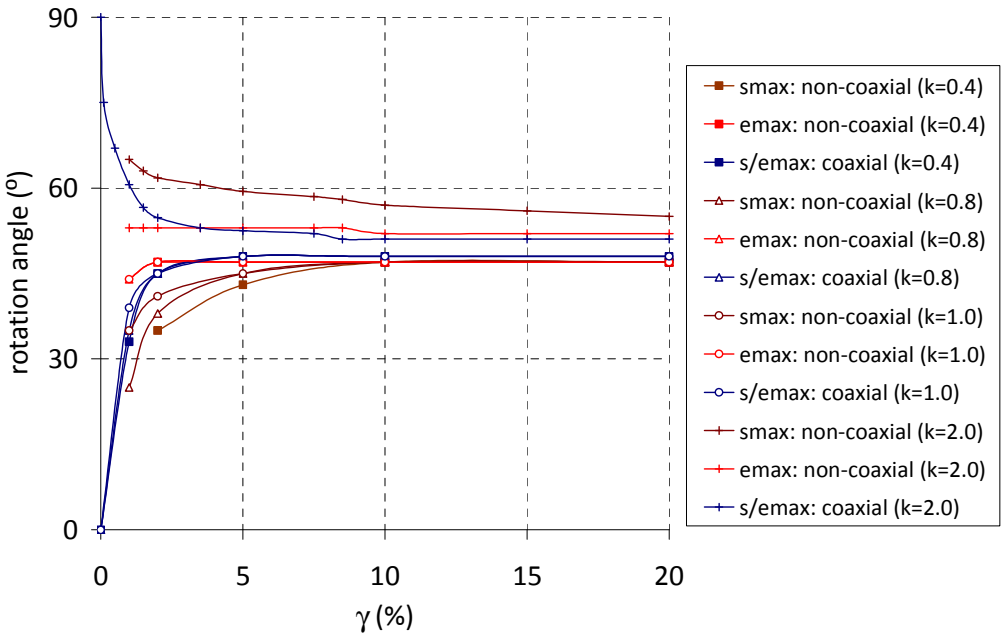
90
60
30
0
rotation angle (°)
0
5
10
15
20
γ (%)
smax: non-coaxial (k=0.4)
emax: non-coaxial (k=0.4)
s/emax: coaxial (k=0.4)
smax: non-coaxial (k=0.8)
emax: non-coaxial (k=0.8)
s/emax: coaxial (k=0.8)
smax: non-coaxial (k=1.0)
emax: non-coaxial (k=1.0)
s/emax: coaxial (k=1.0)
smax: non-coaxial (k=2.0)
emax: non-coaxial (k=2.0)
s/emax: coaxial (k=2.0)

(b)

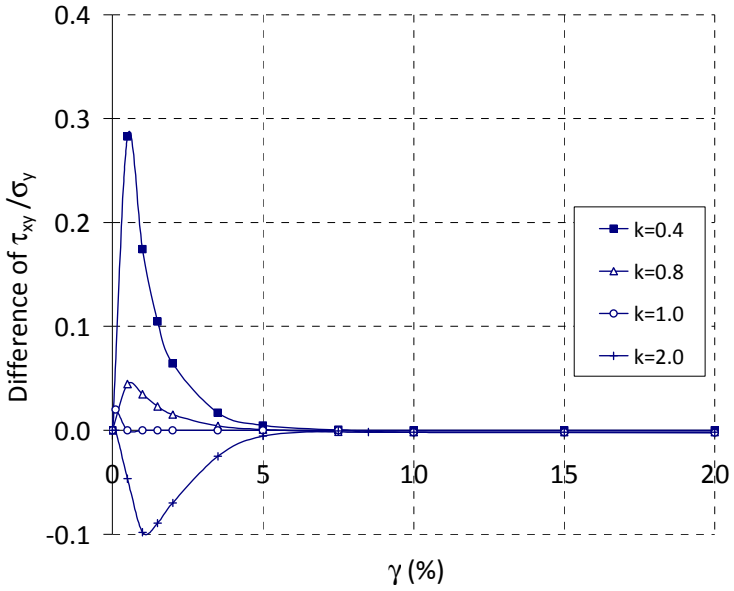

(c)

Fig. 8-6 Characteristic variables predicted by the coaxial and non-coaxial model with various lateral pressure ratios k, non-associated flow rule, and $\varepsilon_v^p = 0$: (a) evolution of shear stress ratio (τ_{xy}/σ_y); (b) evolution of rotation angle of major principal stress (smax) and plastic strain rate (emax); (c) the difference of the shear stress ratio between coaxial and non-coaxial model at each shearing stage

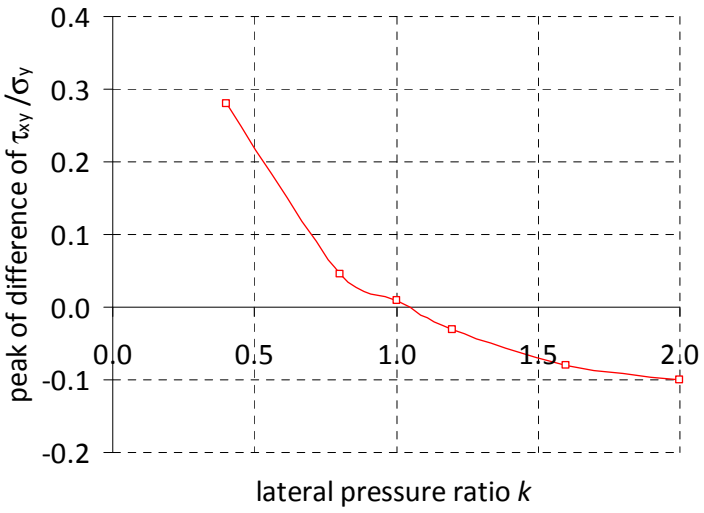

Fig. 8-7 Peak of difference between coaxial and non-coaxial model as a function of lateral pressure ratio *k*

8.4 Silo discharge simulation with non-coaxial model

The non-coaxial model has been successfully applied to numerical analysis of granular flow in a steep hopper and a flat-bottomed silo (Yang et al., 2011). The numerical results for the steep hopper are presented as the author's main contribution to the work of Yang et al. (2011). The results for the flat-bottomed silo are not shown but will be discussed in this section. The geometries and boundary conditions of these silos are shown in Fig. 8-8. The dynamic analysis in Abaqus/Explicit was employed using the central-difference operator (SIUMULIA 2008). The whole analysis was carefully defined and performed by two computational steps: the first step to model the filling achieved by applying the gravity load of the material in a smooth manner as described in Section 3.4 of Chapter 3; the second one is to simulate the discharge process by setting the outlet boundary free instantaneously. To avoid element distortion problem, the numerical analysis was performed with the Arbitrary Lagrangian-Eulerian technique.

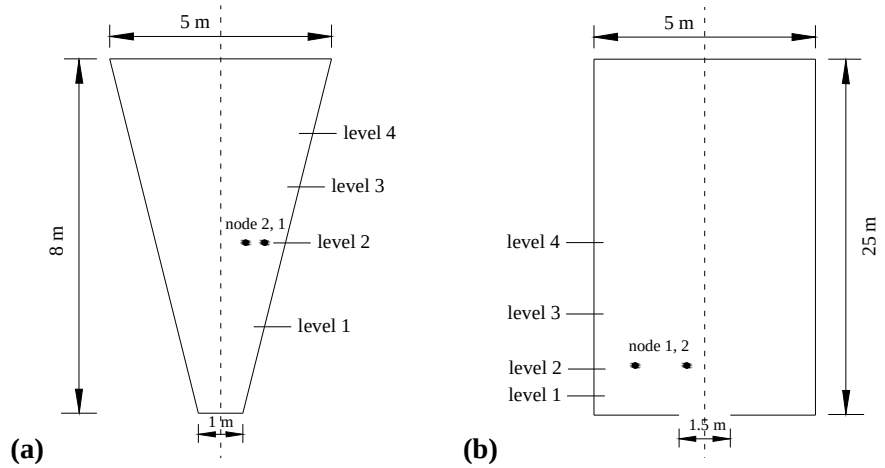

Fig. 8-8 Geometries and boundary conditions of the steep hopper and flat-bottomed silos: (a) steep hopper and (b) flat-bottomed silo

1200 and 2000 first-order 4-node quadrilateral elements with reduced integrations were used for simulation of the steep hopper and the flat-bottomed silo flow, respectively. Silo walls were modelled as rigid bodies and their interactions with granular solids by contact surfaces. A penalty function was used to constrain the penetration depth and the Coulomb friction model was employed with a constant coefficient.

A comparison between the predicted wall normal pressure distributions with and without non-coaxiality at the end of filling in the steep hopper was made and it was indicated that the non-coaxiality does not influence the filling wall pressures (see Fig. 8-9). This can be attributed to the small area where the plastic non-coaxial strain rate is created.

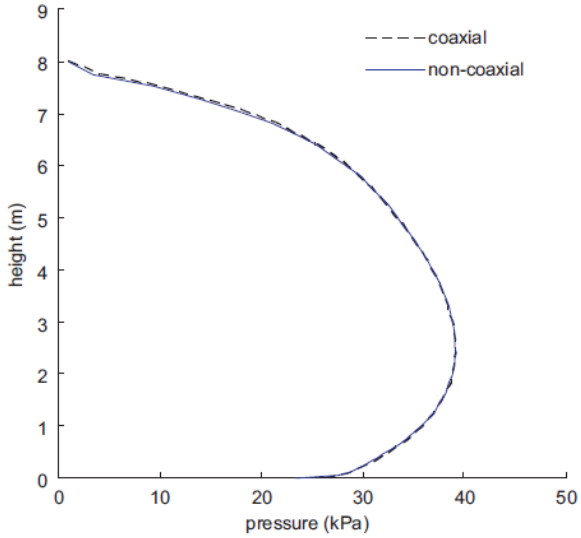

Fig. 8-9 Predicted wall normal pressure distributions at the end of filling in the steep hopper with and without considering the non-coaxiality (after Yang et al., 2011)

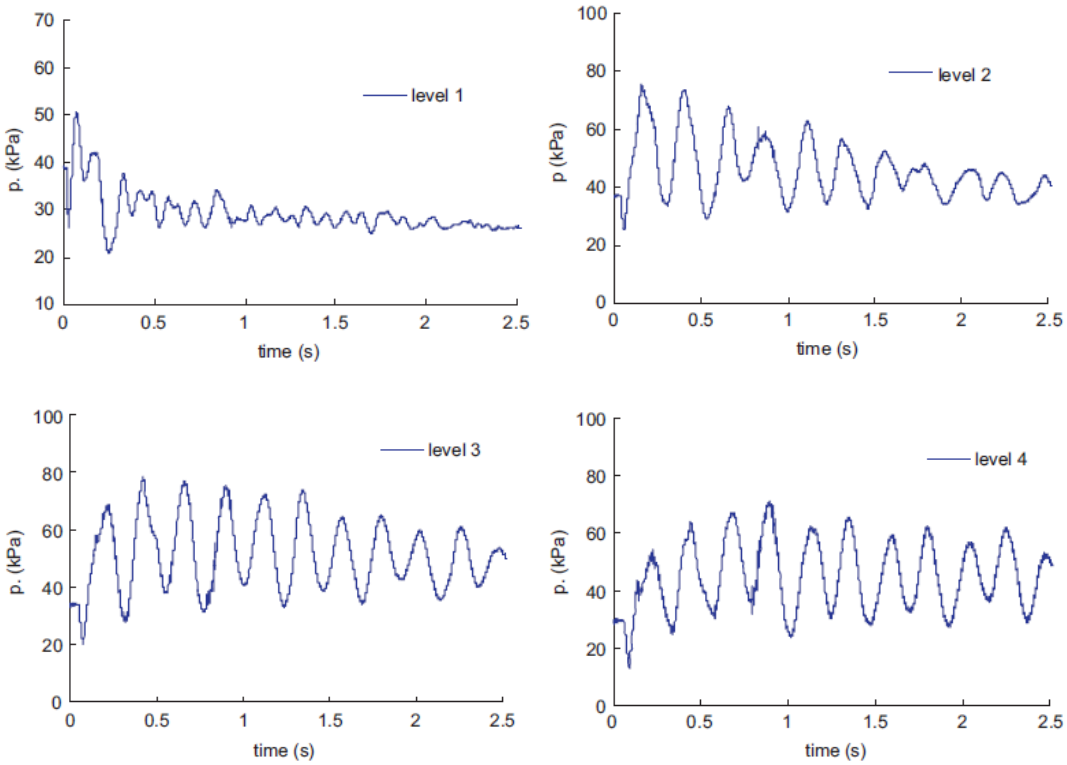

Fig. 8-10 Evolutions of wall normal pressures versus discharge time at different levels of the steep hopper without considering the non-coaxiality (after Yang et al., 2011)

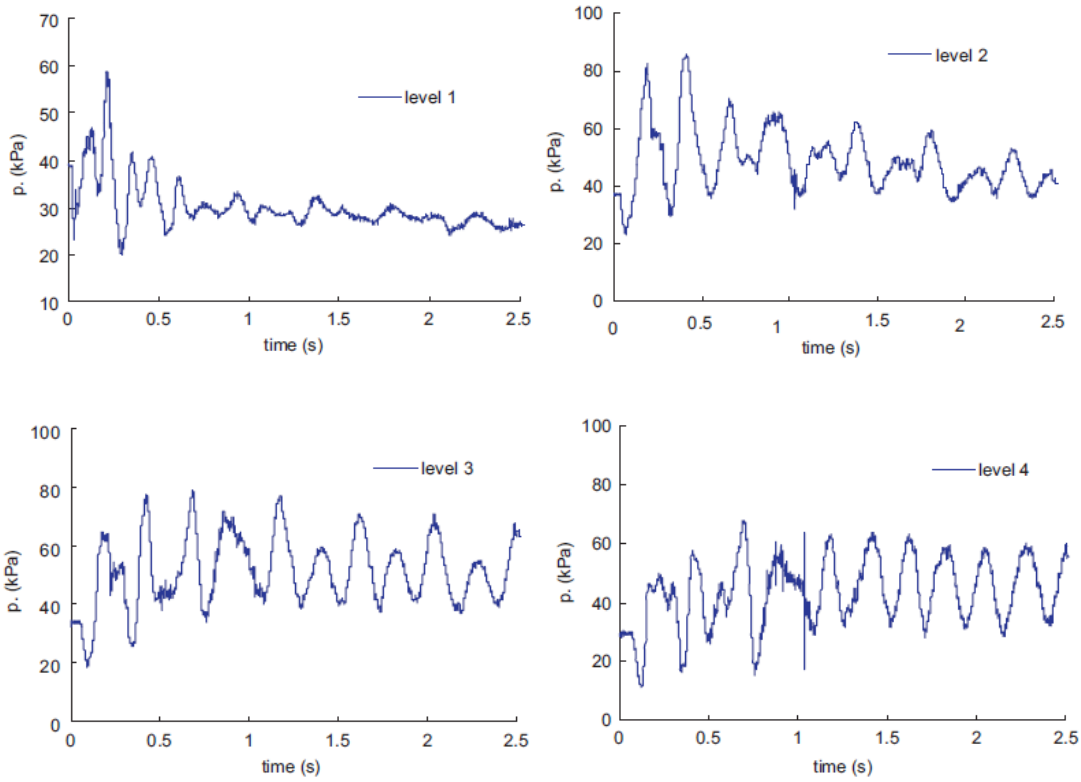

Fig. 8-11 Evolutions of wall normal pressures versus discharge time at different levels of the steep hopper with considering the non-coaxiality (after Yang et al., 2011)

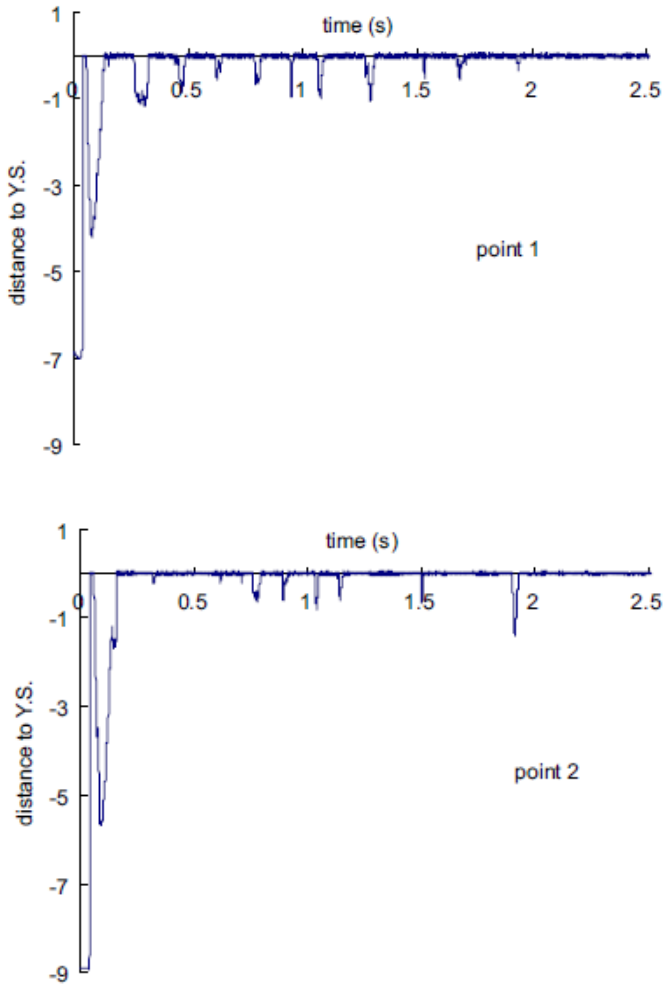

Fig. 8-12 Evolutions of principal stress orientations versus discharge time at different locations of the steep hopper (after Yang et al., 2011)

Fig. 8-10 and Fig. 8-11 show the time evolutions of predicted wall normal pressure at different levels of the hopper with and without considering the non-coaxiality. It indicates the start of discharge at the time axis of 0s. Comparisons between them indicate that the use of non-coaxial model generally predicts larger wall pressures, and the tendency is more evident at lower heights. The non-coaxiality model exhibits more sensitive response of normal stress with respect to shear strain under volumetric

constraint. At lower levels, the volumetric constraint of granular solids in the hopper is more stringent than that at upper levels. Coupled with the tendency of shear dilatancy, the normal pressure was increased when non-coaxiality was considered. Because the non-coaxial deformation only takes place on the yield surface where the ratio of shear stress to normal stress equals 0.7, the non-coaxiality should mainly come into effect some time after the onset of discharge as indicated by the time evolution of the shear stress ratio at two different locations of the steep hopper (see Fig. 8-12). The shear stress ratio is also used to judge where shear failure zones occur, which has been defined in Chapter 4, by plotting the distribution of shear stress ratio within the solid. The shear failure zone is characterized by the light yellow colour, as shown in Fig. 8-13. Identically, the contours also reveal that the solid does not yield until some time after discharge.

In addition, the time evolution of predicted wall pressure oscillates. The oscillations can be explained by studying evolution of the shear zone and the slip-stick wall motion during discharge. In Fig. 8-13, the contours of shear stress ratio indicate that an intermittent shear failure zone occurs at t=1.0s, 1.5s and 2.0s after discharge, which are located in the middle part of the hopper. Associated with that, the time history of displacement of the solid adjacent to the wall shows a slip-stick motion (see Fig. 8-14).

Simulations with smooth wall were also performed and there was less shear and resulting principal stress rotation without wall friction. Comparing to the case using rough wall, the wall pressure difference with and without considering non-coaxiality

was smaller and pressure oscillations were alleviated significantly. This can be attributed to the disappearance of the slip-stick wall motion.

The same procedure and material are employed to analyse the granular behaviour in the flat-bottomed silo. Detailed numerical results can be found in the work of Yang et al. (2011). There was an overall similarity in response between the flat-bottomed silo and the steep hopper. Less influence on the wall pressures at the lowest level in the flat-bottomed silo was observed. This is due to the existence of stagnant zone in the semi-mass flow, and the static zone at the lowest level. In addition, the amplitude of oscillations of wall pressures is smaller than that in the steep hopper. More increase of wall pressures was, however, observed in the flat-bottomed silo due to more volumetric constraint imposed by less discharge.

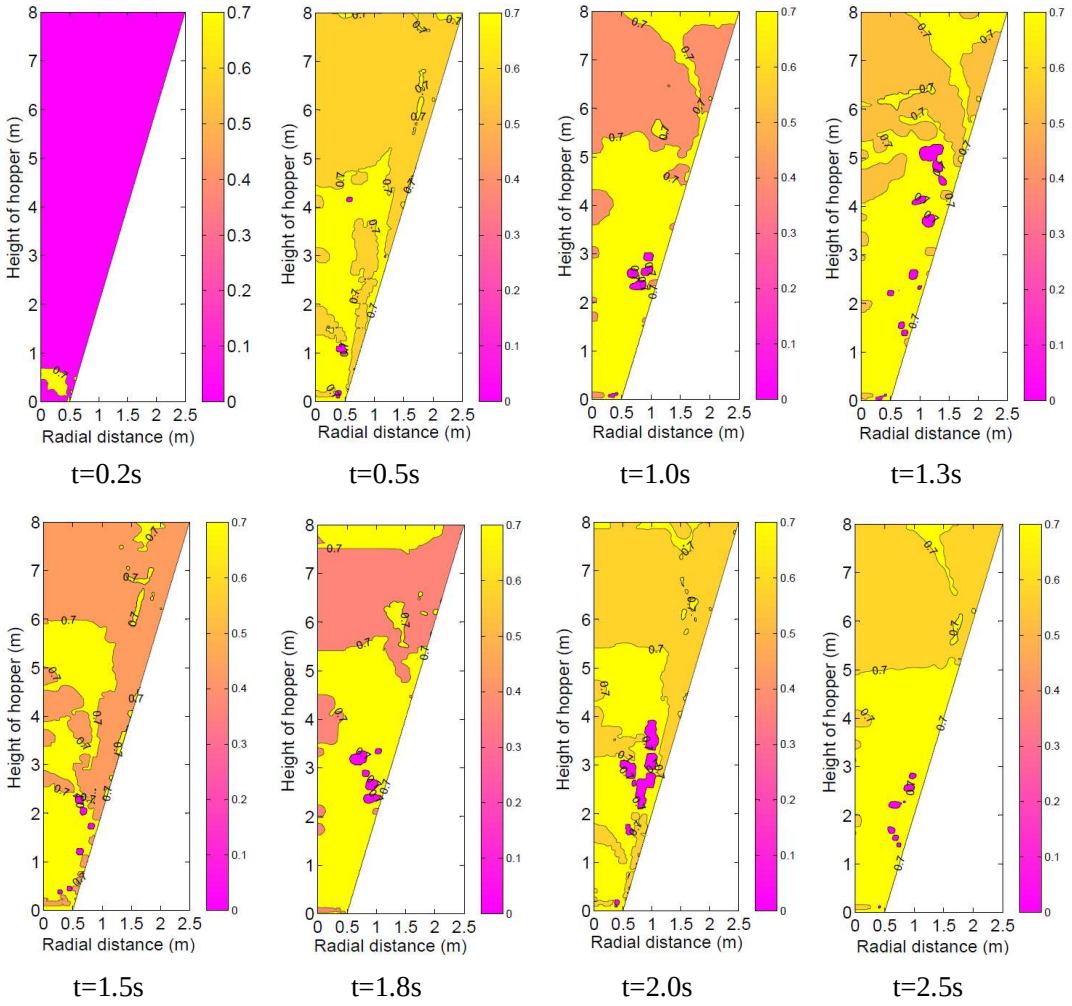

Fig. 8-13 Contours of shear stress ratio at two locations of the steep hopper at different discharge time points

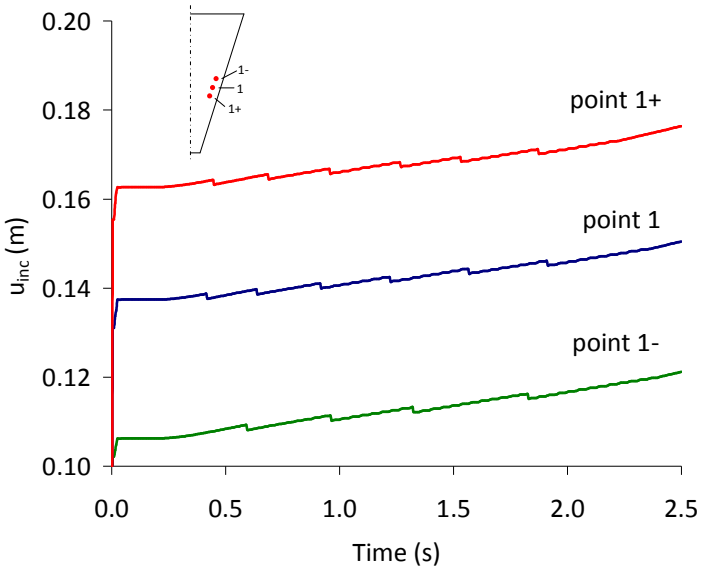

Fig. 8-14 Time history of displacements of solid versus discharge time, of point 1 and its two neighbouring points (point 1+ and 1-) against hopper wall

8.5 Concluding remarks

In most cases, there is a noticeable difference between the coaxial and the non-coaxial model. The use of the non-coaxial model decreases the hardening or softening in shear stress ratio evolution. The decease in hardening or softening becomes smaller with the increase in shear strain, and the predictions with both models tend to converge at large shear strain. According to the investigation, it has been seen that the difference between the two models increases as the elastic stiffness of the material increases and is also a function of static lateral pressure ratio. Specially, there is no significant difference when the coefficient equal to 1.0.

All these characteristics of simulations with the non-coaxial model can be attributed to the amount of the principal stress rotation and the relative directions of the coaxial and

non-coaxial components of plastic strain rate. Overall, greater rotation of principal stress leads to greater influence by the non-coaxial modelling.

The influence of non-coaxial model on predicted wall pressures in a steep hopper and a flat-bottomed silo has also been studied in detail in this chapter. The results indicate that the non-coaxial model does not affect the filling wall pressure. However, a significant difference was observed in discharge where larger wall pressure was predicted by the non-coaxial model. This tendency is more evident at lower heights of the steep hopper. In addition, the predicted wall pressure experience oscillations in time after the onset of discharge. These oscillations can be explained by studying evolution of the shear zone and the slip-stick wall motion during discharge.

Simulations with smooth wall have also been performed and there is no noticeable difference between the predictions by the coaxial and the non-coaxial model because of the less shear stress along the wall resulting in less principal stress rotation. The same procedure and material were employed to analyze the granular behaviour in the flat-bottomed silo. There was an overall similarity of responses between flat-bottomed silo and steep hopper. It has been indicated that there was some difference between the flat-bottomed silo and the steep hopper. The non-coaxiality does not influence the time history of wall pressures at the lowest level in the flat-bottomed silo （Yang et al., 2011）. This is due to the existence of stagnant zone in the semi-mass flow, and the lowest level is in the static zone.

Chapter 9

Conclusions and future work

The research in this thesis has been carried out primarily to investigate the granular flow and discharge pressure in hoppers and silos by means of the finite element (FE) method in comparison with experimental investigations and analytical models. The thesis has explored significantly the underlying mechanisms of the dynamic pressure phenomenon and also its implications on dynamic events in silos. This chapter summarizes the main conclusions drawn from previous chapters, and makes some suggestions on relevant topics for future study.

9.1 Key conclusions of this study

This study first develops an effective strategy for the finite element (FE) method to model material discharging process in silos using the uncoupled Arbitrary Langrangian-Eulerian formulation (ALE). To ensure the accuracy of calculation in this method, a wide range of numerical aspects and factors involved have been investigated in modelling of silo behaviour. The proposed FE model using the ALE formulation is found to be an effective technique for the simulation of silo discharge process which is featured by large deformation.

Using the ALE technique, almost the entire silo discharge process can be simulated without mesh distortion problems. The mass flow rate and discharge pressures predicted

using the FE model are in close agreement with the theoretical solutions. The transient dynamic phenomena induced by the silo discharge, in particular the dynamic fluctuations of pressure, are found to exhibit two primary frequencies (about 5 Hz and less than 1 Hz). Their governing mechanisms are identified such that the relatively high frequency event (about 5 Hz) is attributable to the stress wave propagation within the stored granular silos, while the event with relatively low frequency (less than 1 Hz) and much larger amplitude is associated with the intermittent shear zones within the flowing material and the associated slip-stick motion between the granular solid and the walls.

A one-dimensional dynamic model of granular columns subject to Coulomb friction has been developed to investigate the propagation of stress wave, which plays an important role in silo wall pressure distribution and silo quaking phenomenon. The stress impulse set off by incipient discharge at the outlet grows with the distance travelled up the columns, however the rate is shown to depend on the half-angle of the taper.

After the successful application of the ALE technique for a conical hopper, the FE model has been extended to simulate the granular flow in two types of silos, i.e., a flat-bottomed silo and a silo consisting of a cylindrical bin with a conical hopper. The good agreement in wall pressure distributions and flow pattern with the experimental observations for these two silos validates the applicability of the FE model using the ALE formulation.

Finally, a novel material constitutive model, i.e. non-coaxial model, has been introduced to show the non-coincidence between principal stresses and principal plastic strain rates

due to the principal stress rotation in granular material at the beginning of silo discharge. Through the numerical investigation for two silos, it is found that the non-coaxial model does not affect the filling wall pressure. But for discharge, there is a significant difference in that the use of non-coaxial model generally predicts larger wall pressure, and the tendency is more evident near the lower part of silos.

9.2 Future work

The study presented in this thesis has improved the understanding of dynamic pressure phenomenon. Further progress of studies that may be required and beneficial are suggested as follows.

As for silo experiments, a further investigation on the wall pressure are required to obtain data at a high sampling rate. This investigation can serve to study the mechanism of dynamic pressure with a certain frequency during silo discharge.

Although various constitutive models for granular solid based on continuum mechanics have been employed in FE modelling of silo discharge, it is still a great challenge to find a realistic set of constitutive model which is able to capture the many characteristics of granular flow. Since the influence of packing is very important for silo phenomena, the constitutive models, which consider the directional dependency of material mechanical properties, are required. In some situations where the time-dependent response of stress is crucial, a rate-dependent plasticity model is needed to generalise the viscous characteristics of granular solid, associated with different stress path. Micro-mechanical

models, which incorporate essential information on material parameters to model the various interactions between different particles or particles with their surrounding environment, are required to obtain phenomena such as particle size segregations, degradation/breakage or aggregation/caking. To describe the rheological behaviour of granular flow in silos, the fluid-like constitutive relations may be required with the hypothesis that the granular material, intrinsically multiphasic, can be treated as a pseudo-fluid.

Dynamic effects in bulk solids are an inherent characteristic for each silo discharge. Strong dynamic effects should be avoided for many reasons. Thus, it becomes very crucial for bulk solid handling to study their excitation mechanism. Unfortunately, the numerous conflicting studies based on various theories do not reach a consensus on the cause of the dynamic effects. The theory of pressure waves in granular material has been studied using a one-dimensional dynamic model in this thesis. Due to the inadequacies of the one-dimensional approach for columns with large half-angle, a more complex two-dimensional version of the dynamic model is required. This two-dimensional model could provide an effective means of studying pressure wave propagation in hoppers and silos, by combining the FE model which does not have the limitation of one-dimensional assumption. Beside, the behaviour of compression waves, whose wave fronts tend to form a shock within the non-linear elastic material, is also worth studying.

Various experimental measurements and theoretical analysis have been carried out to study slip-stick behaviour between the sliding particles and silo walls, which is considered to be responsible for silo music with a fundamental frequency of several

hundred Hz. Few numerical simulations are performed to investigate the slip-stick behaviour. Although FE simulations in this thesis have presented some characteristics of slip-stick behaviour, further calculations incorporating the realistic interface conditions between the bulk solid and silo walls, hence, presenting more characteristics of this behaviour, such as its shear velocity dependence, its material stiffness dependence, and its friction coefficient dependence, are suggested.

References

Ai, J. (2010). Particle scale and bulk scale investigation of granular piles and silos (PhD thesis). The University of Edinburgh, Edinburgh, UK.

Ai, J., Chen, J.F., Rotter, J.M., and Ooi, J.Y. (2011). "Numerical and experimental studies of the base pressures beneath stockpiles." *Granular Matter*, 13(2): 133-141.

Armero, F. and Love, E. (2003). "An arbitrary Lagrangian-Eulerian finite element method for finite strain plasticity." *Int. J. Numer. Methods Eng*, 57: 471-508.

Artoni, R., Santomaso, A., and Canu, P. (2009). "Simulation of dense granular flows: dynamics of wall stress in silos." *Chemical Engineering Science*, 64: 4040-4050.

Artoni, R., Zugliano, A., Primavera, A., Canu, P., and Santomaso, A. (2011). "Simulation of dense granular flows: Comparison with experiments." *Chemical Engineering Science*, 66: 548-557.

Ayuga, F., Guaita, M., and Aguado, P. (2001). "Static and dynamic silo loads using finite element models." *J.Agric. Engng Res*., 78 (3): 299-308.

Ayuga, F., Guaita, M., Aguado, P., and Couto, A. (2001). "Discharge and eccentricity of the hopper influence on the silo wall pressures." *Journal of Engineering Mechanics*, 127 (10): 1067-1074.

Bagnold, R.A. (1954). "Experiments on a gravity free dispersion of large solid spheres in a Newtonian fluid under shear." *Proc. R. Soc. Lond. A*, 225: 49-63.

Bagnold, R.A. (1966). “The shearing and dilation of dry sand and the ‘singing’ mechanism.” *Proc. R. Soc. Lond. A*, 295: 219-232.

Belytschko, T., and Kennedy, J.M. (1978). “Computer methods for subassembly simulation.” *Nucl. Eng*. Des, 49: 17-38.

Beni, Y.T., Movahhedy, M.R., and Farrahi, G.H. (2009). “Rate-dependent dynamic ALE analysis of finite deformation of elasto-viscoplastic solids.” *Materials and Design*, 30: 2995-3004.

Ben-Dor, G., Britan, A., Elperin, T., Igra, O., and Jiang, J. (1997). “Experimental investigation of the interaction between weak shock waves and granular layers”. *Exp. Fluids*., 22: 432-443.

Benson, D.J. (1989). “An efficient, accurate, simple ALE method for non-linear finite element programs.” *Applied Mechanics and Engineering*, 72: 305-350.

Berezin, Y.A., Osinov, V.A., and Hutter, K. (2001). “Evolution of plane disturbances in hypoplastic granular materials”. *Continuum Mech. Thermodyn*., 13: 79-90.

Beuth, L. et al. (2007). *Proc. of the 10th Int. Symp. on Numerical Models in Geomechanics NUMOG 10* (Eds: Pande, G., Pietruszczak, S.), Taylor & Francis Group, Rhodes: 189.

Beverloo, W.A., Leniger, H.A., and Van de Velde, J. (1961). “The flow of granular solids through orifices.” *Chemical Engineering Science*, 15: 260.

Bishara, A.G., El-Azazy, S.S., and Huang, T.D. (1981). “Practical analysis of cylindrical farm silos based on finite element analysis.” *ACI Journal* proceedings, 78: 456-462.

Bishara, A.G., Mahmoud, M.H., and Chandrangsu, K. (1977). “Finite element formulation for farm silo analysis.” *Journal of the Structural Division. ASCE*, 103: 1903-1919.

Bjorkman, G.S., and Piotter, J.M. (2008). “Finite element mesh considerations for reduced integration elements.” *ASME Pressure Vessels and Piping Conference.* Chicago, USA.

Blair-Fish, P.M., and Bransby, P.L. (1973). “Flow patterns and wall stresses in a mass-flow bunker”. *Journal of Engineering for Industry*. *Trans. ASME*, 95: 17-26.

Böhrnsen, J.U., Antes, H., Ostendorf, M., and Schwedes, J., (2004). “Silo discharge: measurement and simulation of dynamic behaviour in bulk solids.” *Chem. Eng. Technol.*, 27(1): 71-76.

Borzsonyi, T., and Kovacs, Z. (2011). “High-speed imaging of travelling waves in a granular material during silo discharge.” *Physical Review E*, 83, 032301: 1-4.

Boutreux, T., Raphael, E., and De Gennes, P.G. (1997). “Propagation of a pressure step in a granular material: the role of wall friction.” *Physical Review E*, 55: 5759-5773.

Brillhart, L.V., and Dally, J.W. (1968). “A Dynamic Photoelastic Investigation of Stress-wave Propagation in Cones.” *Experimental Mechanics*, 8: 145-153.

Brockley, C.A., and Davis, H.R. (1968). *Trans. ASME*, Ser. F, 90(1): 35.

Brown, C.J., Jarrett, N.D., and Moore, D.B. (1996). “Pressures in a square planform silo during discharge.” Proceedings of the Institution of Mechanical Engineers, Part E: *Journal of Process Mechanical Engineering*, 210(E2): 101-108.

Brown, C.J., and Nielsen, J. (1998). Silos: Fundamentals of theory, behaviour and design. London, E & FN Spon.

Buick, J.M., Chavez-Sagarnaga, J., Zhong, Z., Ooi, J.Y., Pankaj, Cambell, D.M., and Greated, C.A. (2005). "Investigation of silo-honking: slip-stick excitation and wall vibration." *Journal of Engineering Mechanics ASCE*, 131(3): 299-307.

Buick, J.M., Pankaj, Ooi, J.Y., Chavez-Sagarnaga, Pearce, A. and Houghton, G. (2004). "Motion of granular particles on the all of a model silo and the associated wall vibration." *J. Phys. D: App. Phys*., 37: 2751-2760.

Chen, J.F., Yu, S.K., Ooi, J.Y., and Rotter, J.M. (2010). "Finite-element modelling of filling pressure in a full-scale silo." *Journal of Engineering Mechanics ASCE*, 127(10): 1058-1066.

Chester, C. (1971). Techniques in partial differential equations. McGraw-Hill, New York.

Chowdhury, M.A., and Helali, M.M. (2008). "The effect of amplitude of vibration on the coefficient of friction for different materials." *Tribology International*, 41: 307-314.

Derjagin et al. (1957). *Proc. Conf. Lubrication and Wear*, London, pp: 265.

Dhoriyani, M.L., Jonnalagadda, K.K., Kandikatla, R.K., and Rao, K.K. (2006). "Silo music: sound emission during the flow of granular materials through tubes." *Powder Technology*, 167: 55-71.

Ding, S. (2004). Investigations of flow and pressure in silos during filling and discharging in presence of inserts (PhD thesis). The University of Edinburgh, Edinburgh, UK.

Ding, S., Wojcik, M., Jecmenica, M., and De Silva, S.R. (2003). "Load on walls and inserts in mass-flow silos." *TASK QUARTERLY*, 7(4): 525-538.

Dodds, R. H. (1982). "Effects of reduced integration on the 2-D quadratic isoparametric element in plane strain plasticity." *Int. Journal of Fracture*, 19: 75-82.

Donea, J, Fasoli-Stella, P., and Giuliani, S. (1977). "Lagrangian and Eulerian finite element techniques for transient fluid-structure interaction problems." *Transactions of the 4th SMIRT Conference*, Vol.B, San Francisco: 15-19.

Donea, J., and Huerta, A. (2003). Finite element methods for flow problems. John Wiley & Sons Ltd, Chichester, West Sussex, England.

Donea, J., Huerta, A., Ponthot, J.-Ph., and Rodriguez-Ferran, A. (2004). "Arbitrary Lagrangian-Eulerian methods." *Encyclopedia of Computational Mechanics*, 1969: 1-38.

Drucker, D.C., and Prager, W. (1952). "Soil mechanics and plastic analysis on limit design." *Quarterly Applied Mathematics*, 10 (2): 157-165.

Eibl, J., and Rombach, G. (1988). "Numerical investigations on discharge silos." In ICONMIG, Innsbruck, Austria, April.

EN 1991-4 (2006). Eurocode 1: Actions on Structures. Silos and Tanks. Brussel: CEN.

Fleishman, B. (1963). Wave propagation in non-simple media, Nonlinear Differential Equations and Nonlinear Mechanics. Academic, New York.

Gadala, M.S. and Wang, J. (1998). “ALE formulation and its application in solid mechanics.” *Comput. Methods Appl. Mech. Eng*, 167: 33-55.

Gadala, M. S. (2004). “Recent trends in ALE formulation and its applications in solid mechanics.” *Comput. Methods Appl. Mech. Eng*, 193: 4247-4275.

Ghosh. S., and Kikuchi, N. (1991). “An arbitrary Lagrangian-Eulerian finite element method for large deformation analysis of elastic-viscoplastic solids.” *Comput. Methods Appl. Mech. Eng*, 86: 127-188.

Ghosh, S., and Raju, S. (1996). “R-S adapted arbitrary Lagrangian-Eulerian finite element method of metal-forming with strain localization.” *Int. J. Numer. Methods Eng*., 39: 3247-3272.

Goodey, R.J., Brown, C.J., Rotter, J.M. (2003). “Verification of a 3-dimensional model for filling pressures in square thin-walled silos.” *Engineering Structures*, 25: 1773-1783.

Goodey, R.J., Brown, C.J., and Rotter, J.M. (2006). “Predicted patterns of filling pressure in thin-walled square silos.” *Engineering Structures*, 28: 109-119.

Gregor, W., and Rumpf, H. (1975). “Velocity of sound in two-phase media”. *Int. J. Multiphase Flow*, 1: 753-769.

Haber, R.B. (1984). “A mixed Eulerian-Lagrangian displacement model for large deformation analysis in solid mechanics.” *Comput. Methods Appl. Mech. Eng*., 43: 277-292.

Halleux, J.P., and Casadei, F. (1984). “Transient large strain analysis of plane and axisymmetric structures by means of biquadratic finite elements.” *Engineering Computations*, 1: 351-358.

Hardin, B., and Richart, F. (1963). *J. Soil Mech. Found. Div*., 89: 33.

Hardow, B., Schulze, D., and Schwedes, J. (1998). “An experimental analysis of the ‘silo quaking’ phenomenon.” *Proc. of the 3rd World Congress on Particle Technology*, England.

Härtl, J. (2008). A study of granular solids in silos with and without an insert (PhD thesis). University of Edinburgh, Edinburgh, UK.

Hartlen, J. Nielsen, J., Ljunggren, L., Martensson, G., and Wigram, S. (1984). “The wall pressure in large grain silos.” *Swedish Council for Building Research*, Document D2, Stockholm.

Hashiguchi, k., and Tsutsumi, S. (2001). “Elastoplastic constitutive equation with tangential stress rate effect. *Int. J. Plast*., 17: 117-145.

Haussler, U., and Eibl, J. (1984). “Numerical investigations on discharging silos.” *J. Eng. Mech. ASCE*, 110(6): 957-971.

Hirt, C.W., Amsden, A.A., and Cook, J.L. (1974). “An Arbitrary Lagrangian-Eulerian computing method for all flow speeds.” *J.Comput. Phys*., 14(3): 227-253.

Hostler, S.R., and Brennen, C.E. (2005). “Pressure wave propagation in a granular bed.” *Physical Review E*, 72, 031303: 1-13.

Howe, P.G., et al. (1955). *Canadian Jour. Chem*., 33: 1375.

Hu, Y., and Randolph, M.F. (1998). “A practical numerical approach for large deformation problems in soil.” *Int. J. Numer. Anal. Meth. Geomech*., 22(5): 327-350.

Huerta, A., and Casadei, F. (1994). “New ALE applications in non-linear fast-transient solid dynamics.” *Engineering Computations*, 11: 317-345.

Hughes, T.J.R., Liu, W.K., and Zimmermann, T.K. (1978). “Lagrangian-Eulerian finite element formulation for incompressible viscous flows.” U.S.-Japan Seminar on Interdisciplinary Finite Element Analysis, Cornell University, Ithaca, NY.

Ibrahim, R. (1994). “Friction-induced vibration, chatter, squeal, and chaos. Part 2. Dynamics and modelling.” *Appl. Mech. Rev.*, 47: 227-253.

Jaeger, H.M., and Nagel, S.R. (1992). “Physics of the granular state.” *Science*, 255: 1523-1531.

Jaeger, H.M., Nagel, S.R., and Behringer, R.P. (1996). “Granular solids, liquids, and gases.” *Rev. Mod. Phys.*, 68: 1259-1273.

Janseen, H.A. (1895). “Versuche uber getreidedruck in silozellen.” *Zeitschrift des Vereines Deuischer Ingenieure*, 39 (35): 1045-1049.

Jenike, A.W., and Johanson, J.R. (1968). “Bins loads.” *ASCE Journal of the Structural Division*, 94(ST4), April: 1011-1041.

Jenike, A.W., Johanson, J.R., and Carson, J.W. (1973). “Bin loads-part3: mass flow bins.” *Jnl. Engen Industry, Trans ASME*, 95 (Ser. B, No. 1): 6-12.

Jenkins, J.T., and Savage, S.B. (1983). “A theory for the rapid flow of identical, smooth, nearly elastic particles.” *J. Fluid Mech*., 130: 187-202.

Kamrin, K. (2010). “Nonlinear elasto-plastic model for dense granular flow.” *International Journal of Plasticity*, 26: 167-188.

Karlsson, T, Klisinski, M., and Runesson, K. (1998). Finite element simulation of granular material flow in plane silos with complicated geometry. *Powder Technology*, 99: 29-39.

Kato, S., and Matsubayashi, T. (1970). “On the dynamic behaviour of machine tool slideway-Characteristics of static friction in stick-slip motion.” *Bulletin of the JSME*., 13: 55.

Keiter, T.W.R., and Rombach, G.A. (2001). “Numerical aspects of FE simulations of granular flow in silos.” *Journal of Engineering Mechanics*, 127(10): 1044-1050.

Kenner, V.H., and Goldsmith, W. (1968). “Elastic Waves in Truncated Cones.” *Experimental Mechanics*, 8: 442-449.

Ketterhagen, W.R., Curtis, J.S., Wassgren, C.R., and Hancock, B.C. (2009). “Predicting the flow mode from hoppers using the discrete element method.” *Powder Technology*, 195: 1-10.

Khoei, A.R., Anahid, M., and Shahim, K. (2008). “An extended arbitrary Lagrangian – Eulerian finite element method for large deformation of solid mechanics.” *Finite Elements in Analysis and Design*, 44: 401 - 416.

Khoei, A.R., Anahid, M., Shahim, K., and DorMohammadi, H. (2008). “Arbitrary Lagrangian-Eulerian method in plasticity of pressure-sensitive material. Application to powder forming processes.” *Comput. Mech.*, 42: 13-38.

Kolymbas, D. (1988). “Generalized hypoplastic constitutive equation.” In Saada and Bianchini. *Constitutive equations for granular non-cohesive soils*. 349-366.

Konuk, I., Yu, S. and Gracie, R. (2005). “A 3-Dimensional continuum ALE Model for Ice Scour: Study of Trench effects.” *ASME 24th International Conference for offshore Mechanics and Arctic Engineering*, Vol. 2.

Konuk, I., Yu, S., and Gracie, R. (2005). “An ALE FE model of ice scour.” *The 11th International Conference of the International Association of Computer Methods and Advances in Geomechanics*, Turin, Italy, June: 19-21.

Kragelskii, I.V. (1965). Friction and Wear. Butterworths, Washington, DC.

Kvapil, R. (1959). Theorie der Schuttgutbewegung. Berlin: VEB-Verlag Technik.

Lenczner, D. (1963). “An investigation into the behaviour of sand in a model silo.” *Struct. Engng*, 41, 389-398.

Lewis, J.L., Goldsmith, W., and Cunningham, D.M. (1969). “Internal strain measurement of longitudinal pulses in conical bars.” *Experimental Mechanics*, 9: 313-320.

Le Veque, R.J. (1992). Numerical methods for conservation laws. Lectures in Mathematics, ETH Zurich, Birkhauser Verlag, Basel.

Li, H., and Kwauk, M. (1989). “Vertical pneumatic moving-bed transport-2. Experimental findings”. *Chemical Engineering Science*, 44(2): 261-271.

Litwiniszyn, A. (1963). “The model of a random walk of particles adapted to researches on problems of mechanics of loose media.” *Bull. Academe Polonaise Sci. Ser. Sci. Technique*, 11: 61-70.

Liu, C., and Nagel, S.R. (1992). “Sound in sand”. *Physical Review Letters*, 68: 2301.

Liu, W.K., Belytschko, T., and Chang, H. (1986). “An arbitrary Lagrangian-Eulerian finite element method for path-dependent materials.” *Comput. Methods Appl. Mech. Eng*., 58: 227-245.

Li, X.S., and Dafalias, Y.F. (2004). “A constitutive framework for anisotropic sand including non-proportional loading.” *Géotechnique*, 54: 41-55.

Martinez, M.A., Alfaro, I., and Doblare, M. (2002). “Simulation of axisymmetric discharging in metallic silos. Analysis of the induced pressure distribution and comparison with different standards.” *Engineering Structures*, 24: 1561-1574.

McLean, A.G. (1985). “Initial stress field in converging channels.” *Bulk Solids Handling*, 5(2): 49-53.

McLean, A.G., and Arnold, P.C. (1976). “Prediction of cylinder flow pressures in mass-flow bins using minimum strain energy.” *Journal of Engineering for Industry ASME*, Nov.: 1370-1374.

Melin, S. (1994). “Wave propagation in granular assemblies”. *Physical Review E*, 49(3): 2353.

Michalowski, R.L. (1987). “Flow of granular media through a plane parallel/converging bunker”. *Chemical Engineering Science*, 42(11): 2587-2596.

Michalowski, R.L. (1990). “Strain localization and period fluctuations in granular flow processes from hopper.” *Géotechnique*, 40 (3): 389-403.

Midi, GDR. (2004). “On dense granular flows.” *Eur. Phys. J. E*, 14: 341-365.

Moore, D.F. (1975). Principles and Applications of Tribology. Pergamon Press, Oxford.

Moriyama, R., and Jimbo, G. (1988). “Reduction of pulsating wall pressure near the transition point in a bin”. *Bulk Solid Handling*, 8: 421-425.

Motzkus, U. (1974). “Belastung von Siloboden und Auslauftrichtern durch kornige Schuttguter.” Dr.-Ing Dissertation, Technical University of Braunschweig, Braunschweig, Germany.

Mouraille, O., Herbst, O., and Luding, S. (2009). “Sound propagation in isotropically and uni-axially compressed cohesive, frictional granular solids.” *Engineering Fracture Mechanics*, 76: 781-792.

Muite, B.K., Quinn, F.S., Sundaresan, S., and Rao, K.K. (2004). “Silo music and silo quake: granular flow-induced vibration”. *Powder Technology*, 145: 190-202.

Mullins, W.W. (1972). “Stochastic theory of particle flow under gravity.” *J. Appl. Phys*., 43: 665-678.

Munch-Andersen, J., Askegaard, V. and Brink, A. (1992). Silo model tests with sand. Bulletin No. 91, Danish Building research institute.

Musmarra, D., Polletto, M., Vaccaro, S., and Clift, R. (1995). “Dynamic waves in fluidized beds.” *Powder Technology*, 82: 255-268.

Nagy, N., Mohamed, M., and Boot, J.C. (2010). “Nonlinear numerical modelling for the effects of surface explosions on buried reinforced concrete structures.” *Geomechanics and Engineering*, 2(1): 1-18.

Nedderman, R.M. (1992). Statics and Kinematics of Granular Materials. Cambridge University Press, Cambridge.

Niedostatkiewicz, M., and Tejchman, J. (2003). “Experimental and theoretical studies on resonance dynamic effects during silo flow.” *Powder Handling and Processing*, 15 (1): 36-42.

Nielsen, J. (1998). “Pressures from flowing granular solids in silos.” *Phil. Tran. R. Soc. Lond. A*, 356: 2667-2684.

Nielsen, J., and Ruckenbrod, C. (1988). “A note on dynamic phenomena in silos.” *Proc. Int. Conf.: Silos- Forschung und Praxis*, Karlsruhe, pp: 191-209.

Noh, W.F. (1964). “Cel: A time-dependent, two-space-dimensional, coupled eulerian-lagrange code.” in B. Alder, S. Fernbach and M. Rotenberg, eds, Methods in computational physics. Advances in research and applications. Fundamental methods in hydrodynamics, Vol. 3, Academic Press, New York, pp: 117-179.

Norton, F.H. (1929). The creep of steel at high temperature. McGraw-Hill, New York.

Ocone, R., and Astarita, G. (1995). “Compression and rarefaction waves in granular flow.” *Powder Technology*, 82: 231-237.

Oden, J.T., and Martins, J.A.C. (1985). “Models and computational methods for dynamic friction phenomena.” *Comput. Methods Appl. Mech. Eng*, 52: 527-634.

Ooi, J.Y. (1990). Bulk solids behaviour and silo wall pressures. PhD thesis. School of Civil and Mining Engineering, University of Sydney, Sydney.

Ooi, J.Y., and Rotter, J.M. (1990). “Wall pressures in squat steel silos from finite element analysis.” *Computers & Structures*, 37(4): 361-374.

Ooi, J.Y., and Rotter, J.M. (1991). “Elastic prediction of pressures in conical silo hoppers.” *Engineering Structures*, 13(1): 2-12.

Ooi, J.Y., Chen, J.F., Lohnes, R.A., and Rotter, J.M., (1996). “Predictions of static wall pressures in coal silos.” *Construction and Building Materials*, 10(2): 109-116.

Ostendorf, M., Schwedes, J., Böhrnsen, J.U., and Antes, H. (2003). “Dynamic measurement and simulation of bulk solids during silo discharge.” *TASK QUARTERLY*, *7*(4): 611-621.

Oveisy, A., Hall, K., Soltanpour, M., and Shibayama, T. (2009). “Two-dimensional horizontal wave propagation and mud mass transport model.” *Continental Shelf Research*, 29: 652-665.

Philips, C.E.S. (1910). “Electrical and other properties of sand.” *Proceedings of the Royal Institution of Great Britain*, 19: 742.

Pijaudier-Cabot, G., Bode, L., and Huerta, A. (1995). “Arbitrary Lagrangian-Eulerian finite element analysis of strain localization in transient problems.” *Int. J. Numer, Meth. Eng.*, 38: 4171-4191.

Potts DM, Dounias, G.T., and Vaughan, P.R., (1987). “Finite element analysis of the direct shear box test.” *Géotechnique*, 37(1): 11-23.

Prakash, S. (1981). Soil dynamics, McGraw-Hill, New York.

Rabinowicz, E. (1951). “The nature of the static and kinetic coefficients of friction.” *J. Appl. Phys.*, 22(11): 1373-1379.

Rabinowicz, E. (1965). Friction and Wear of Matericals. Wiley, New York.

Renner, M. (1996) Theoretische and experimentelle Untersuchungen zum schnellen Fliessen von Schuttgutern in konvergenten Geometrien (PhD thesis). Karlsruhe University, Germany.

Roberts, A.W. (1990). Unpublished experimental data, TUNRA Bulk Solids, The University of Newcastle, Australia.

Roberts, A.W. (1995). “Shock loads in silos due to flow pulsations.” *Proc. Int. Conf. PARTEC* 95, Nurnberg: 131-141.

Roberts, A.W. (1996). “Factors influencing load pulsations in silos during discharge flow.” *Bulk Solids Handling*, 16: 59-73.

Roberts, A.W., and Wensrich, C.M. (2002). “Flow dynamics or ‘quaking’ in gravity discharge from silos.” *Chemical Engineering Science*, 57: 295-305.

Roberts, I. (1882). “Pressure of stored grain.” *Engineering*, 34: 399.

Roberts, I. (1884). “Determination of the vertical and lateral pressures of granular substances.” *Proceedings of the Royal Society of London*, 36: 225-240.

Rodriguez-Ferran, A., Casadei, F., and Huerta, A. (1998). “ALE stress update for transient and quasistatic processes.” *Int. J. Numer, Meth. Eng.*, 43: 241-262.

Rodriguez-Ferran, A., Perez-Foguet, A., and Huerta, A. (1998). “Arbitrary Lagrangian-Eulerian (ALE) formulation for hyperelastoplasticity.” *Int. J. Numer, Meth. Eng.*, 53: 1831-1851.

Rogge, T. (1971). “Longitudinal wave propagation in bars with variable cross section.” *Zeitschrift für Angewandte Mathematik und Physik*, 22: 299-307.

Rombach, G., and Eibl, J. (1998). A dynamic finite element model for silo pressure and solids flow, *Silos, Fundamentals of theory behaviour and design*, Edited by C.J. Brown and J. Nielsen, E&FN SPON: 481-494.

Rose, H.F., and Tanaka, T. (1956). The Engineer (London) 208, Oct.23.

Roscoe, K.H., Bassett, R.H., and Cole, E.R. (1967). “Principal axes observed during simple shear of a sand.” *Proceedings of the Geotechnical Conference*, vol. 1, Oslo, pp: 231-237.

Rotter, J.M. (2001). Guide for the economic design of circular metal silos, Spon Press, London and New York.

Rotter, J.M., Brown, C.J., and Lahlouh, E.H. (2002). “Patterns of wall pressure on filling a square planform steel silo.” *Engineering Structures*, 24: 135-150.

Rotter, J.M., Holst, J.M.F.G., Ooi, J.Y., and Sanad, A.M. (1998). “Silo pressure predictions using discrete-element and finite-element analyses.” *Philosophical Transactions of the Royal Society A: Mathematical, Physical and Engineering Sciences*, 356(1747): 2685-2712.

Rotter, J.M., Ooi, J.Y., and Zhong, Z. (2004). “Danish silo experiment: Unsymmetrical wall pressure measurements.” Internal Report. School of Engineering, University of Edinburgh.

Ruckenbrod, C. (1995). Statische und dynamische Phanomene bei der Entleerung von Silozellen (PhD thesis). Karlsruhe University, Germany.

Rudnicki, J.W., and Rice, J.R., (1975). “Conditions for the localization of the deformation in pressure sensitive dilatant materials.” *J. Mech. Phys. Solids*, 23: 371-394.

Rusinek, R., Molenda, M., and Horabik, J. (2009). “Performance of membrane pressure transducers in granular materials of various particle sizes”. *Powder Technology*, 190 (3): 410-414.

Rycroft, C.H., Kamrin, K., and Bazant, M.Z. (2009). “Assessing continuum postulates in simulations of granular flow.” *Journal of the Mechanics and Physics of Solids*, 57: 828-839.

Savidis, S.A., Aubram, D., and Rackwitz, F. (2008). “Arbitrary Lagrangian-Eulerian finite element formulation for geotechnical construction processes.” *Journal of Theoretical and Applied Mechanics*, 38(1-2): 165-194.

Schaeffer, D.G. (1987). “Instability in the evolution equations describing incompressible granular flow.” *Journal of differential equation*, 66:19-50.

Schofield, A., and Wroth, C. (1968). Critical state soil mechanics. McGraw-Hill, New York.

Schulze, D. (1998). “Silo quaking.” Silos-fundamentals and theory, behaviour and design, in: Brown, C.J. and Nielsen, J. (Eds.), EFN Spon: 171-182.

Schulze, D. (2003). “Time and velocity dependent properties of powders effecting slip-stick oscillations.” *Chem. Eng. Technol*., 26: 1047-1051.

Schulze, D. (2007). Powders and Bulk Solids: Behaviour, Characterization, Storage and Flow. Springer Berlin Heidelberg New York.

Sielamowicz, I., Blonski, S., and Kowalewski, T.A. (2006). “Digital particle image velocimetry (DPIV) technique in measurements of granular material flows, Part 2 of 3-converging hopper.” *Chemical Engineering Science*, 61: 5307-5317.

SIMULIA (2008). Abaqus analysis: User’s Manual, Dassault Systèmes.

Suh, N.P. (1968). “On stress pulse amplification ratio in truncated solid cones.” *Journal of Applied Mechanics*, 35: 831–833.

Susila, E., and Hryciw, R.D. (2003). “Large displacement FEM modelling of the cone penetration test (CPT) in normally consolidated sand.” *International Journal for Numerical and Analytical Methods in Geomechanics*, 27: 585-602.

Symes, M.J.P.R., Gen, A., and Hight, D.W. (1984). “Undrained anisotropy and principal stress rotation in saturated sand.” *Géotechnique*, 34: 11-27.

Tardos, G.I. (1997). “A fluid mechanics approach to slow, frictional powder flows.” *Powder Technology*, 92: 61-74.

Tejchman, J. (1987). “Dynamic phenomena in model silos.” *Int. Report of Institute for Rock and Soil Mechanics*, Karlsruhe University.

Tejchaman, J. (1998). “Numerical simulation of filling in silos with a polar hypoplastic constitutive model.” *Powder Technology*, 96: 227-239.

Tejchman, J. (1998). “Silo-quake-measurements, a numerical polar approach and a way for its suppression.” *Thin-Wall Structure*, 31(1-3): 137-158.

Tejchman, J. (1999). “Technical concept to prevent the silo honking.” *Powder Technology*, 106: 7-22.

Tejchaman, J. (1998). “Numerical simulation of filling in silos with a polar hypoplastic constitutive model.” *Powder Technology*, 96: 227-239.

Tejchman, J., and Gudehus, G. (1993). “Silo-music and silo-quake, experiments and a numerical Cosserat approach.” *Powder Technology*, 762: 201-212.

Tournat, V., Gusev, V.E., and Castagnède, B. (2004). “Subharmonics and noise excitation in transmission of acoustic wave through unconsolidated granular medium.” *Physics Letters A*, 326: 340-348.

Tuzun, U., and Nedderman, R.M. (1979). “A kinematic model for the flow of granular materials.” *Powder Technology*, 22: 243-253.

Vidal, P., Guaita, M., and Ayuga, F. (2005). “Analysis of dynamic discharge pressures in cylindrical slender silos with a flat bottom or with a hopper: comparison with Eurocode 1.” *Biosystems Engineering*, 91(3): 335-348.

Walker, D.M. (1966). “An approximate theory for pressures and arching in hoppers.” *Chemical Engineering Science*, 21: 975-997.

Wang, Y., Lu, Y., and Ooi, J.Y. (2011). “Numerical calculations of dynamic pressure during hopper discharge using an uncoupled ALE-formulation.” *Proceedings of the 19th UK Conference of the Association for Computational Mechanics in Engineering*, Edinburgh.

Wang, Y., Wensrich, C.M., and Ooi, J.Y. (2012). “Rarefaction wave propagation in tapered granular columns.” *Chemical Engineering Science*, 71: 32-38.

Watson, G.R. and Rotter, J.M. (1996). “A finite element kinematic analysis of planar granular solids flow.” *Chemical Engineering Science*, 51 (16): 3967-3978.

Weir, G.J. (2001). “Sound speed and attenuation in dense, non-cohesive air-granular systems”. *Chemical Engineering Science*, 56: 3699-3717.

Wensrich, C.M., and Roberts, A.W. (2000). “The role of slip-stick motion in silo quaking.” *IMech Conf. Transactions* “From Powder to Bulk”, London.

Wensrich, C. (2002). “Dissipation, dispersion, and shocks in granular media.” *Powder Technology*, 126: 1 - 12.

Wensrich, C. (2002). “Experimental behaviour of quaking in tall silos.” *Powder Technology*, 127: 87-94.

Wensrich, C. (2003). “Numerical modelling of quaking in tall silos.” *International Journal of Mechanical Sciences*, 45: 541-551.

Wensrich, C. (2006). “Slip-stick motion in harmonic oscillator chains subject to Coulomb friction.” *Tribology International*, 39: 490-495.

Wieckowski, Z. (2000). *Proc. of the 8th Int. Conf. on Computing in Civil and Building Engineering* (Eds: Fruchter, R., Pena-Mora, F., Roddis, K.), ASCE, Stanford, 764.

Wieckowsk, Z. (2003). “Modelling of silo discharge and filling problems by the material point method.” *TASK QUARTERLY*, 7(4): 701-721.

Wilde, K., Rucka, M., and Tejchman, J. (2008). “Silo music-Mechanism of dynamic flow and structure interaction.” *Powder Technology*, 186: 113-129.

Wilde, K., Tejchman, J., Rucka, M., and Niedostatkiewicz, M. (2010). “Experimental and theoretical investigations of silo music.” *Powder Technology*, 198: 38-48.

Wojcik, M., Enstad, G.G., and Jecmenica, M. (2003). “Numerical calculations of wall pressures and stresses in steel cylindrical silos with concentric and eccentric hoppers.” *Particulate Science and Technology*, 21: 247-258.

Wojcik, M., Hartl, J., Ooi, J.Y., Rotter, J.M., Ding, S., and Enstad, G.G. (2007). “Experimental Investigation of the Flow Pattern and Wall Pressure Distribution in a Silo with a Double-Cone Insert.” *Particle & Particle Systems Characterization*, 24(4-5): 296-303.

Wojcik, M., and Tejchman, J. (2009). “Modeling of shear localization during confined granular flow in silos within non-local hypoplasticity.” *Powder Technology*, 192: 298-310.

Wu, Y.H., and Schmidt, L.C. (1992). “A boundary element method for prediction of silo pressures” *Comput. Struct*., 45(2): 315.

Yamada, T., and Kikuchi, F. (1993). “An arbitrary Lagrangian-Eulerian finite element method for incompressible hyperelasticity.” *Comput. Methods Appl. Mech. Eng.*, 102: 149-177.

Yang, J.C.S., and Hassett, R.J. (1972). “Transient Stresses in Axisymmetric Bodies of Varying Area.” *Experimental Mechanics*, 12: 304-310.

Yang, Y., Ooi, J.Y., Rotter, J.M., and Wang, Y. (2011). “Numerical analysis of silo behavior using non-coaxial models.” *Chemical Engineering Science*, 66: 1715-1727.

Yang, Y., Rotter, J.M., Ooi, J.Y., and Wang, Y. (2011). “Flow channel boundaries in silos.” *Chemical Engineering Technology*, 34(8): 1295-1302.

Yang, Y., and Yu, H.S., (2006). “Numerical simulations of simple shear with non-coaxial soil models.” *Int. J. Numer. Anal. Methods*, 30: 1-19.

Yu, H.S., and Yuan, X. (2006). “On a class of non-coaxial plasticity models for granular soils.” *Philos. T. Roy. Soc. A.*, 462(2067): 725-748.

Zhong, Z., Ooi, J.Y., and Rotter, J.M. (2001). “The sensitivity of silo flow and wall stresses to filling method.” *Engineering Structures*, 23: 756-767.

Zhu, H., Mehrabadi, M.M., and Massoudi, M. (2006). “Three-dimensional constitutive relations for granular materials based on the dilatant double shearing mechanism and the concept of fabric.” *Int. J. Plast*., 22: 826-857.

Zhu, H., Mehrabadi, M.M., and Massoudi, M. (2007). “The frictional flow of a dense granular material based on the dilatant double shearing model.” *Comput. Math. Appl.*, 53: 244-259.

Zienkiewicz, O.C. (1979). The finite element method. McGRAW-Hill, Maidenhead, UK.